

# **SYNTHESIS OF NANOMATERIALS AND THEIR APPLICATIONS IN BIOSENSOR**

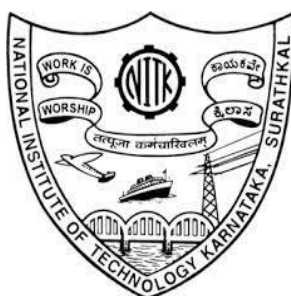
Thesis

Submitted in partial fulfilment of the requirements for the degree of

DOCTOR OF PHILOSOPHY

by

LAVANYA RAO V R



DEPARTMENT OF CHEMISTRY

NATIONAL INSTITUTE OF TECHNOLOGY KARNATAKA

SURATHKAL, MANGALURU – 575025

OCTOBER, 2024



## DECLARATION

I hereby declare that the Research Thesis entitled **“SYNTHESIS OF NANOMATERIALS AND THEIR APPLICATIONS IN BIOSENSOR”** which is being submitted to the **National Institute of Technology Karnataka, Surathkal** in partial fulfilment of the requirements for the award of the Degree of **Doctor of Philosophy in Chemistry** is a bonafide report of the research work carried out by me. The material contained in this Research Thesis has not been submitted to any University or Institution for the award of any degree.

*Lavanya Rao*

**LAVANYA RAO V R**

Reg. No.: 197057CY004

Department of Chemistry

Place: NITK, Surathkal

Date: 28-10-2024.



## C E R T I F I C A T E

This is to certify that the Research Thesis entitled  
**“SYNTHESIS OF NANOMATERIALS AND THEIR  
APPLICATIONS IN BIOSENSOR”** submitted by  
**LAVANYA RAO V R** (Register Number: 197057CY004)  
as the record of the research work carried out by her, is  
accepted as the Research Thesis submission in partial  
fulfilment of the requirements for the award of Degree of  
Doctor of Philosophy.




**Dr. B. RAMACHANDRA BHAT**  
Professor

Department of Chemistry  
National Institute of Technology Karnataka  
Surathkal, Sreeyeshpur, MANGALURU - 575 026  
**Research Guide**

Place: NITK, Surathkal

Date: 28.10.2024



**Chairman - DRPC**

विभागाध्यक्ष / H.O.D.  
रसायन शास्त्र विभाग / Department of Chemistry  
राष्ट्रीय प्रौद्योगिकी संस्थान, कर्नाटक, सुरथकल  
NITK, Sreeyeshpur  
मंगलूरु / Mangaluru  
MANGALURU-575 026, KARNATAKA



## ACKNOWLEDGEMENT

A successful Ph.D. journey is a collaborative endeavour, supported by the unwavering encouragement and assistance of many individuals. In this brief space, I wish to extend my heartfelt gratitude to all those who have contributed to the completion of this work.

The role of a research supervisor in shaping a Ph.D. is of paramount importance, and it is my privilege to acknowledge the unwavering support and generosity of Prof. B. Ramachandra Bhat. He has been a constant source of inspiration and guidance. His insightful direction, patience, and thoughtfulness have greatly benefited our research group, fostering a positive and productive environment. It has been an immense fortune to have him as an advisor, allowing me the freedom to explore and evaluate ideas independently. I hold him in the highest regard, not only as an exceptional teacher but also as an exemplary human being. His mentorship has been invaluable, and his support has been instrumental in the successful completion of this dissertation.

I extend my gratitude to my RPAC members Prof. Arun M. Isoor, Department of Chemistry, Prof. Muralidhar Kulkarni, Department of Electronics and Communication Engineering, and Prof. H.S. Nagaraj, Department of Physics. Their encouragement, perceptive comments, and insightful discussions have been pivotal in the successful progress and completion of my research objectives.

I would like to express my sincere gratitude to Prof. Arun M. Isoor, Prof. Udaya Kumar D., and Prof. Darshak R. Trivedi for providing the necessary administrative support for my Ph.D. work during their respective tenures as Heads of the Department of Chemistry. Their assistance has been instrumental in facilitating the progress of my research.

I extend my sincere gratitude to the National Institute of Technology Karnataka (NITK), Surathkal, for providing the invaluable opportunity to conduct my research. My heartfelt thanks also go to the esteemed faculty members of the Department of Chemistry for their unwavering support and well-wishes.

I am profoundly appreciative of the assistance rendered by Sprint Mumbai, SRMIST Chennai, Sathyabama University Chennai, Alagappa University Kozhikode, the Department of Physics at NITK, PSGTECHS COE INDUTECH, STIC Cochin and the Central Research Facility (CRF) at NITK, for their sophisticated experimental and characterization facilities, which were crucial to the advancement of my research.

Furthermore, I wish to acknowledge the indispensable support provided by the non-teaching staff of the Department of Chemistry at NITK Surathkal. Their diligent assistance in all official matters has been immensely helpful. In particular, I express my deepest appreciation to Mrs.

Rashmi, Mrs. Vikhitha, Mr. Santhosh, Mr. Prashanth, Mrs. Sharmila, Mr. Pradeep, Mr. Harish, Mrs. Deepa, Mrs. Divya, Mrs. Ashwija and Ms. Chitrashree for their dedicated support and contributions to the department.

Throughout the course of research, one inevitably encounters challenges, yet the presence of a supportive and dynamic group of laboratory colleagues proves invaluable in navigating these obstacles. I extend my profound gratitude to Dr. Praveen Mishra, Dr. Anuma Saroja, Dr. Madhukar Nimalbakar, Mrs. Fiona Joyline Mascarenhas, Mr. Shreeganesh Hegde, Ms. Sushmitha S., and Mr. Mahesh Nayak for their unwavering camaraderie and steadfast encouragement during my doctoral journey. I wish to convey heartfelt appreciation to Dr. John D. Rodney, our esteemed collaborator, whose guidance has been instrumental in guiding me through every phase of this scholarly pursuit. His mentorship has not only fortified my research endeavors but also facilitated significant strides in scholarly publications. I am deeply grateful for his consistent support and invaluable counsel. Additionally, I extend special recognition to Mrs. Fiona Joyline Mascarenhas, my steadfast colleague and confidante throughout this academic pursuit. Her unwavering presence has offered invaluable perspectives, unwavering motivation, and essential emotional sustenance, which have proven indispensable in overcoming challenges and achieving milestones in this scholarly endeavor.

I am grateful to my supportive friends Mrs. Anupriya James, Mr. Sindhur U Joshi, Ms. Subhasmita Ray, Mr. Laxmisagar G, Mr. Mukesh P, Mr. Avinash I Ingle, Mrs. Anupama Sebastian, Ms. Archana, Mrs. Sammitha Hebbar, and others who have been steadfast companions through all challenges and triumphs.

I am profoundly thankful for the unwavering support and understanding of my father, whose guidance has been a beacon of strength in my life's journey. My mother's nurturing love and endless encouragement have filled my heart with resilience and determination. The understanding and companionship of my sister have been a source of comfort and solidarity in both joyful and difficult moments. The warm embrace and acceptance of my in-laws have made me feel cherished and part of a loving family. Above all, my husband's unwavering belief in me and his constant support have been my rock, inspiring me to face challenges with courage and to cherish moments of joy with gratitude.

Finally, I express my heartfelt gratitude to all individuals who have contributed, whether directly or indirectly, to the realization of this dissertation.

LAVANYA RAO V R

## ABSTRACT

Technology plays an indispensable role in daily life, streamlining processes and addressing multifaceted challenges. Within healthcare, advanced diagnostics significantly enhance treatment efficacy. The emergence of reliable biosensors holds the potential to augment testing precision, surpassing conventional limitations. This thesis, titled "**Synthesis of Nanomaterials and their Applications in Biosensors**" delves into the intricate domain of biosensing utilizing metal oxide nanomaterials, with a specific focus on monitoring glucose and cholesterol levels. The research initiates with meticulous synthesis and detailed characterization of various nanomaterials, including V-doped TiO<sub>2</sub>, Ce-doped ZnO, and Pd/C-decorated SnO<sub>2</sub>. Advanced analytical techniques and electrochemical methods are employed to study non-enzymatic biosensor activity.

In the domain of glucose biosensing, V-doped TiO<sub>2</sub> nanoparticles, notably V<sub>0.03</sub>Ti<sub>0.97</sub>O<sub>2</sub>, emerge as highly promising candidates. This material exhibits exceptional sensitivity, detecting glucose at a rate of 1129.31  $\mu\text{A mM}^{-1}\text{cm}^{-2}$  with a remarkably low detection limit of 1.8  $\mu\text{M}$ . Moreover, its response time of 2.1 s in 0.1 M KOH solution underscores its rapid analytical capabilities, validated through testing with human samples. Further optimization via varying vanadium concentrations identifies V<sub>0.07</sub>Ti<sub>0.93</sub>O<sub>2</sub> as an even more efficient biosensing material, achieving a heightened sensitivity of 1482.8  $\mu\text{A mM}^{-1}\text{cm}^{-2}$  and a detection limit of 488  $\mu\text{M}$ . In exploring cholesterol biosensing, the research focuses on synthesizing and characterizing ZnO and cerium-doped ZnO (Zn<sub>0.03</sub>Ce<sub>0.97</sub>O-CZO3) nanomaterials. CZO3 emerges as a particularly effective photoelectrochemical non-enzymatic cholesterol biosensor, demonstrating a sensitivity of 2.81  $\text{mA.mM}^{-1}.\text{cm}^{-2}$  and a detection limit of 17  $\mu\text{M}$ , validated through testing with human samples. Additionally, the study investigates Pd/C-decorated SnO<sub>2</sub> nanoparticles for their cholesterol biosensing capabilities, showing sensitivity of 1.50  $\text{mA.mM}^{-1}.\text{cm}^{-2}$  and a rapid response time of 2 s, validated through testing with human samples.

These findings underscore significant advancements in leveraging metal oxide nanomaterials for biosensing applications. By elucidating the development, thorough

characterization, and practical applications of these innovative biosensors, this thesis contributes valuable insights poised to enhance biomedical research and clinical diagnostics in the foreseeable future.

**Keywords:** Non-enzymatic Biosensor; Metal-Oxide; Glucose; Cholesterol; Electrochemistry.

## Table of Contents

CHAPTER 1 .....	1
INTRODUCTION TO BIOSENSORS AND NANOMATERIALS .....	1
1. INTRODUCTION .....	1
1.1 Constituents of Biosensing Devices .....	3
1.2 Fundamental Characteristics of Biosensing Devices .....	4
1.3 Comprehensive Overview of Biosensor Classification.....	5
1.3.1 Electrochemical Biosensor.....	6
1.3.1.1 Potentiometric Biosensor .....	7
1.3.1.2 Amperometric Biosensor.....	8
1.3.1.3 Conductometric Biosensor .....	10
1.3.2 Enzymatic Biosensor .....	10
1.3.3 Non-enzymatic Biosensor .....	11
1.4 Nanomaterials and Various Synthesis Techniques .....	12
1.4.1 Bottom-up Approach .....	13
1.4.2 Top-down Approach .....	14
1.4.1.1 Hydrothermal Method.....	14
1.4.1.2 Co-precipitation Method.....	15
1.5 Significance of Nanomaterials in Advancing Electrochemical Biosensor....	15
1.6 Electrochemical Cell .....	19
1.6.1 Electrolyte Solution .....	19
1.6.2 Reference Electrode .....	20
1.6.3 Counter Electrode .....	20
1.6.4 Working Electrode .....	20
1.7 Electrochemical Techniques .....	21
1.7.1 Voltammetric measurements .....	21
1.7.1.1 Cyclic Voltammetry (CV) .....	22
1.7.1.2 Chronoamperometry (CA) .....	24
1.7.1.3 Differential Pulse Voltammetry (DPV) .....	25
1.7.1.4 Electrochemical Impedance Spectroscopy (EIS) .....	26
1.8 Applications of Biosensor .....	27

1.8.1	Clinical Diagnosis .....	27
1.8.2	Environmental Applications .....	28
1.8.3	Food Safety .....	29
1.9	Summary .....	29
CHAPTER 2	.....	31
LITERATURE REVIEW, RESEARCH SCOPE AND OBJECTIVE	.....	31
2.1	Glucose Biosensor Utilizing Metal Oxide-Based Materials .....	34
2.2	Cholesterol Biosensor Utilizing Metal Oxide-Based Materials .....	38
2.3	Scope of the Work.....	40
2.4	Objectives.....	41
CHAPTER 3	.....	43
EXPERIMENTAL PROCEDURES AND METHODOLOGY	.....	43
3.1	Chemical reagents .....	45
3.2	Real-Time Samples .....	45
3.3	Preparation of Nickel Foam for Fabrication .....	45
3.4	Preparation of Glucose Stock Solution .....	46
3.5	Preparation of Cholesterol Stock Solution .....	46
3.6	Electrochemical Characterization .....	46
3.7	Characterization Techniques .....	47
CHAPTER 4	.....	51
SYNTHESIS OF MESOPOROUS $M_xTi_{1-x}O_2$ (M=V, Ni, OR Co) (x=0.00, 0.01, 0.02, OR 0.03) AS AN EFFECTIVE ELECTROCHEMICAL NON-ENZYMATIC BLOOD GLUCOSE SENSOR	.....	51
4.1	Introduction .....	53
4.2	Experimental Section .....	54
4.2.1	Chemical Reagents .....	54
4.2.2	Synthesis of $M_xTi_{1-x}O_2$ (x = 0.00, 0.01, 0.02, 0.03) Nanoparticles .....	55
4.2.3	First Principle Study (Density Functional Theory) .....	56
4.3	Results and Discussion.....	57
4.3.1	X-ray diffraction (XRD) Analysis .....	57
4.3.2	Cyclic Voltammetry (CV) Analysis .....	59
4.3.3	Morphological Analysis .....	62

4.3.4 UV-Visible Spectra and Bandgap Study .....	66
4.3.5 Raman Analysis .....	67
4.3.6 Electrochemical Active Surface Area (ECSA) Analysis .....	68
4.3.7 Electrochemical Impedance Spectra (EIS) Analysis .....	69
4.3.8 Density Functional Theory (DFT) Study .....	71
4.3.9 X-ray photoelectron spectroscopy (XPS) Analysis .....	73
4.3.10 Electrochemical Studies .....	75
4.3.11 Post-Glucose Oxidation Characterization .....	82
4.3.12 Real-sample Study .....	84
4.4 Conclusions .....	85
CHAPTER 5 .....	87
SYNTHESIS OF MESOPOROUS $V_xTi_{1-x}O_2$ ( $x=0.03, 0.05, 0.07$ AND $0.09$ ) AS AN EFFECTIVE ELECTROCHEMICAL NON-ENZYMATIC GLUCOSE SENSOR ..	87
5.1 Introduction .....	89
5.2 Experimental Section .....	91
5.2.1 Synthesis of $V_xTi_{1-x}O_2$ .....	91
5.3.1 X-ray diffraction (XRD) Analysis .....	92
5.3.2 Cyclic Voltammetry (CV) Analysis .....	93
5.3.3 Field Emission Scanning Electron Microscopy (FE-SEM) Analysis .....	95
5.3.4 UV-Visible Spectra and Bandgap Study .....	96
5.3.5 Electrochemical Active Surface Area (ECSA) Analysis .....	98
5.3.6 High-Resolution Transmission Electron Microscopy (HR-TEM) Analysis .....	99
5.3.7 Electrochemical Analysis .....	100
5.3.8 Post-Glucose Oxidation Characterization .....	103
5.4 Conclusions .....	104
CHAPTER 6 .....	105
CERIUM-MODULATED ZINC OXIDE FOR PHOTOELECTROCHEMICAL NON-ENZYMATIC BIOSENSING OF CHOLESTEROL: EXPERIMENTAL AND FIRST PRINCIPLE ANALYSIS .....	105
6.1 Introduction .....	107
6.2 Experimental Method .....	110
6.2.1 Chemicals Reagents .....	110

6.2.3	Illumination Setup .....	111
6.2.4	Computational Studies .....	111
6.3	Results and Discussion.....	112
6.3.1	X-ray diffraction (XRD) Analysis.....	112
6.3.2	Raman Analysis.....	115
6.3.3	UV-Visible Analysis and Bandgap Study .....	116
6.3.4	Photoluminescence (PL) Spectra Analysis.....	117
6.3.5	Field Emission Scanning Electron Microscopy (FE-SEM) and Energy-dispersive X-ray Spectroscopy (EDS) Analysis.....	118
6.3.6	Cyclic Voltammetry (CV) Analysis .....	120
6.3.7	Electrochemical Active Surface Area (ECAS) Analysis.....	121
6.3.8	Electrochemical Impedance Spectra (EIS) Analysis .....	122
6.3.9	High-Resolution Transmission Electron Microscopy (HR-TEM) Analysis .....	123
6.3.10	Photoelectrochemical Analysis of CZO3 .....	125
6.3.11	X-ray photoelectron spectroscopy (XPS) Analysis .....	127
6.3.12	Density Functional Theory (DFT) Analysis.....	129
6.3.13	Mechanism of PEC cholesterol biosensor of CZO3.....	131
6.3.14	Electrochemical Analysis .....	132
6.3.15	High-Resolution Liquid Chromatography Mass Spectrometry (HR-LCMS) Analysis .....	141
6.3.16	Real-Sample Analysis.....	142
6.3.17	Eco-Friendly Properties.....	145
6.4	Conclusions .....	146
CHAPTER 7 .....		147
ENHANCED NON-ENZYMATIC CHOLESTEROL BIOSENSING USING Pd/C-DECORATED SnO <sub>2</sub> : SYNTHESIS, CHARACTERIZATION, AND ANALYTICAL PERFORMANCE IN CLINICAL BLOOD SPECIMENS .....		147
7.1	Introduction .....	149
7.2	Experimental Method.....	151
7.2.1	Chemical reagents.....	151
7.2.2	Synthesis of SnO <sub>2</sub> and SnO <sub>2</sub> -Pd/C.....	151
7.3	Results and Discussions .....	152

7.3.1 X-Ray Diffraction (XRD) Analysis.....	152
7.3.2 Raman Analysis.....	153
7.3.3 Cyclic Voltammetry (CV) and Electrochemical Active Surface Area (ECAS) study.....	154
7.3.4 Electrochemical Impedance Spectra (EIS) Study.....	157
7.3.5 Field Emission Scanning Electron Microscopy (FE-SEM) Analysis.....	158
7.3.6 High-Resolution Transmission Electron Microscopy (HR-TEM) Analysis .....	160
7.3.7 X-ray photoelectron spectroscopy (XPS) Analysis .....	161
7.3.8 Electrochemical Study .....	163
7.3.9 Post-Cholesterol Oxidation Characterization .....	172
7.3.10 High-Resolution Liquid Chromatography Mass Spectrometry (HR-LCMS) .....	173
7.3.11 Real Sample Analysis.....	175
7.4 Conclusions .....	175
CHAPTER 8 .....	177
SUMMARY AND CONCLUSIONS .....	177
8.1 Summary .....	179
8.2 Conclusions .....	184
8.3 Future Work .....	185
REFERENCES .....	187

## NOMENCLATURE

### ABBREVIATIONS

AA	Ascorbic Acid
CA	Chronoamperometry
CNTs	Carbon Nanotubes
CV	Cyclic Voltammetry
DFT	Density Functional Theory
DP	Dopamine
DPV	Differential Pulse Voltammetry
ECAS	Electrochemical Active Surface Area
EDS	Energy-dispersive X-ray spectroscopy
EIS	Electrochemical Impedance Spectroscopy
FE-SEM	Field Emission Scanning Electron Microscopy
GCE	Glassy Carbon Electrode
HR-LCMS	High-Resolution Liquid Chromatography Mass Spectrometry
HR-TEM	High-Resolution Transmission Electron Microscopy
LOD	Limit of Detection
LOQ	Limit of Quantification
LSV	Linear Sweep Voltammetry
MO	Metal Oxide
MWCNTs	Multiwalled Carbon Nanotube
NF	Nickel Foam
NMs	Nanomaterials
NPs	Nanoparticles
PEC	Photoelectrochemical
PL	Photoluminescence
PVDF	Polyvinylidene Fluoride
UA	Uric Acid
XPS	X-ray Photoelectron Spectroscopy
XRD	X-ray Diffraction

## **CHAPTER 1**

---

---

### **INTRODUCTION TO BIOSENSORS AND NANOMATERIALS**

---

---



---

---

***Abstract:** Chapter 1 describes the basic features, methods of functioning, and classifications of biosensors are explained. Special attention is paid to the electrochemical methods. It discusses the importance of nanomaterials and outlines their essential functions in biosensor applications. In addition, the chapter explores the complexities of electrochemical cells and methods, providing a thorough grasp of them.*

---

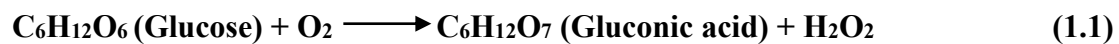
---

## **1. INTRODUCTION**

In today's world, technology is deeply ingrained in every aspect of our daily lives, showcasing its vital role in navigating the complexities of modernity. Its widespread presence underscores its significance in simplifying processes and addressing various challenges faced by humanity through innovation, application, and information exchange. Nowhere is its impact more profound than in healthcare, where advancements in diagnostic technologies have brought about transformative changes. These innovations enhance the efficiency of life-saving treatments by enabling healthcare professionals to swiftly identify and address health issues. Consequently, the availability of reliable analytical tools capable of conducting tests rapidly and accurately is indispensable (Monošík et al. 2012). Given these circumstances, the meticulous development and implementation of biosensors emerge as a promising solution to mitigate the limitations of traditional techniques.

According to the National Institutes of Health's criteria, as per IUPAC regulations from 1999, "**A biosensor is an independent integrated receptor transducer device that can provide specific information from a biological recognition method that is a quantitative or semi-quantitative element**" (Bhalla et al. 2016). Biosensors serve a broad range of purposes aimed at enhancing quality of life. These include identifying diseases, ensuring food quality and safety, safeguarding against threats, monitoring environmental conditions, and aiding in developing medicines, among others. A key role of biosensors is to detect biomolecules that can serve as targets for pharmaceutical interventions or as indicators of disease. In clinical settings, biomarkers are often identified using electrochemical biosensing techniques. These applications typically rely on disposable, cost-effective sensing platforms known as "single shot" analytical instruments (Jolly et al. 2015a; b).

Dr. Leland C. Clark's pioneering work in 1960 led to the development of the first biosensor, marking a significant advancement in biomedical technology. This milestone achievement involved developing a prototype "enzyme electrode" glycemia sensor, designed to accurately monitor glucose concentration in blood samples. The constructed device incorporated a thin layer of immobilized glucose oxidase onto an electrode, which was safeguarded by a semipermeable membrane. This configuration facilitated the measurement of oxygen consumption during enzyme-catalyzed reactions. This innovative technology revolutionized various industries, including biotechnology and medical diagnostics, laying the foundation for further advancements in biosensing techniques.



During the process of monitoring oxygen, Dr. Leland Clark observed something remarkable: the enzyme could convert inactive substrates into active products. He observed a reduction in the signal that exhibited a direct correlation with the oxygen concentration relative to the glucose concentration in the solution. Another approach involved monitoring the levels of hydrogen peroxide ( $\text{H}_2\text{O}_2$ ), which is generated when glucose undergoes oxidation, as a means of gauging the glucose quantity (**Eq. 1.1**) (Santoro and Ricciardi 2016).

## 1.1 Constituents of Biosensing Devices

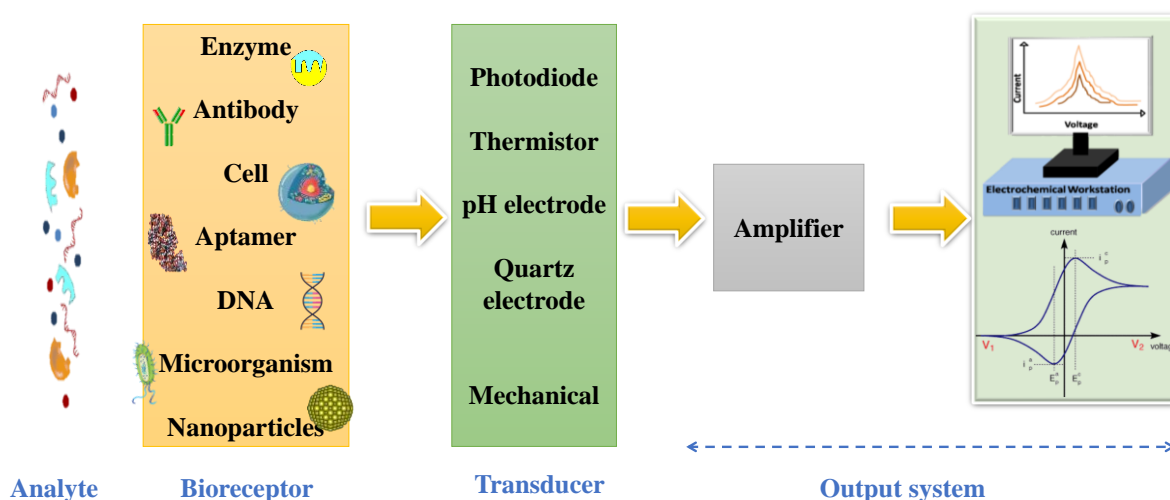


*Figure 1.1. Schematic diagram of a typical biosensor.*

A biosensor comprises a transducer coupled with bioreceptors or other biosensing constituents. Upon interaction with the analyte, the bioreceptor initiates a biological response, which the transducer then converts into an electrical signal. This electrical signal is directly proportional to the concentration of the analyte. In biosensing applications, bioreceptors encompass a diverse array of molecules, including antibodies, DNA, phage, proteins, enzymes, Peptide Nucleic Acids (PNA), and aptamers (Bhalla et al. 2016; Monošík et al. 2012). A schematic diagram of a typical biosensor is illustrated in **Fig 1.1**.

- i. **Analyte:** In the realm of biosensing, the term "analyte" denotes a substance of particular significance targeted for detection within a specific environment. (Chakraborty and Hashmi 2017).
- ii. **Bioreceptor:** In the realm of biosensing, a bioreceptor, also termed a molecular recognition element, is characterized by its specific affinity for the target analyte. Bio-recognition delineates the process whereby the bioreceptor interacts with the analyte, leading to the generation of a discernible signal, which may manifest as light emission, heat release, pH alteration, charge modulation, or mass variation (Bhalla et al. 2016).
- iii. **Transducer:** The transducer, an indispensable component of a biosensor, plays a pivotal role in converting one form of energy into another. The optical or

electrical signals generated by transducers are frequently indicative of the magnitude of analyte-bioreceptor interactions (Bhalla et al. 2016).

## 1.2 Fundamental Characteristics of Biosensing Devices

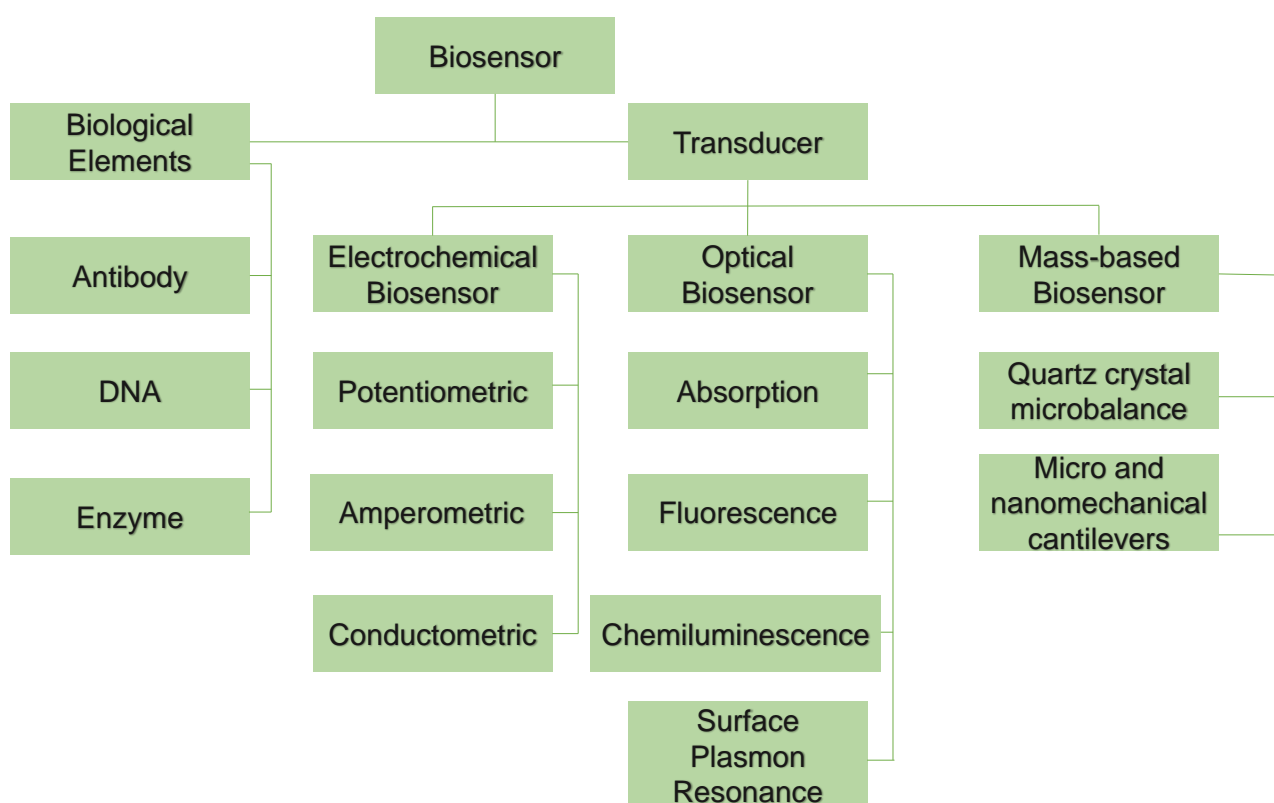
An optimal biosensor should exhibit the following essential characteristics: (Bhalla et al. 2016; Grattarola and Massobrio 1998; Malhotra and Ali 2018).

- i. **Sensitivity:** A key consideration for biosensors is the lowest concentration of the analyte that can be detected, often known as the sensitivity. A high degree of sensitivity is essential in biosensing technology because medical and environmental analytes can occur at extremely low concentrations, often as little as nanograms per milliliter.
- ii. **Selectivity:** The ability to identify and distinguish a specific analyte from a complex combination of many analytes without interference or disruption.
- iii. **Reproducibility:** The reproducibility of a biosensor is the ability to generate identical results under the same experimental settings.
- iv. **Response time:** The reaction's kinetics control how quickly a biosensor generates a response. The kinetics of enzymatic activities are usually quicker, which means that biosensors that use these mechanisms will respond more quickly.
- v. **Lifetime:** The bioreceptor may degrade over time, which would reduce its capacity for biosensing. As such, an optimal biosensor needs to have a long working life in order to guarantee its continued efficacy.
- vi. **Linearity:** The precision of the data obtained, especially when represented on a linear scale, is referred to as linearity within a biosensor. This feature clarifies the sensor's capacity to deliver precise readings over a variety of analyte concentrations. Moreover, linearity defines the lowest incremental change in analyte concentration required for detection, which helps the biosensor achieve resolution.

### 1.3 Comprehensive Overview of Biosensor Classification

The two main types of biosensors are those that depend on the biological component used in the analysis and those that depend on the transduction mechanism applied. The transduction mechanism type used in the sensor, which is related to the physiochemical changes that arise from the sensing event, is the primary factor that determines the categorization of biosensors (Karunakaran et al. 2015). All of the different kinds of biosensors are listed in detail in **Table 1.1**.

*Table 1.1. Comprehensive list of different types of biosensors*



Biosensors are categorized based on the types of transducers they utilize:

- i. Electrochemical Biosensors
- ii. Optical-based Biosensors
- iii. Mass-based Biosensor

### 1.3.1 Electrochemical Biosensor

Electrochemical biosensors, characterized by their utilization of oxidation and reduction processes to monitor electrical signals, feature an electrochemical transducer as their distinguishing component. These molecular sensing devices enable the conversion of biological recognition events into detectable electrical signals by meticulously immobilizing a biological recognition element onto solid electrode surfaces or arrays that respond to applied electrical stimuli. The capacity of electrochemical biosensors to accurately determine analyte concentrations in biological samples renders them highly desirable. Notably, the primary advantage of electrochemical transduction lies in its compatibility with complex and opaque media, enabling the development of miniaturized and cost-effective devices (Karunakaran et al. 2015; Mohankumar et al. 2021).

Electrochemical sensors are frequently employed for the quantitative assessment of bioactive substances, leveraging catalytic enhancements to facilitate potential-driven redox reactions in biofluids. These sensors boast high accuracy and rapid response rates, maintaining linearity even at lower analyte concentrations. Operating on affinity-based principles, they detect voltage or current changes, offering promise for cost-effective applications due to their energy efficiency, affordability, and ease of miniaturization. Given their remarkable sensitivity, affordability, and ability to provide swift and precise results, electrochemical biosensors have garnered significant interest in recent years (Griffin et al. 2014).

Three primary categories of Electrochemical Biosensors are:

- i. **Potentiometric biosensors** employ ion-selective electrodes to detect variations in the concentration of targeted ions.
- ii. **Amperometric biosensors** quantitate the electric current arising from electron transfer during redox reactions.
- iii. **Conductometric biosensors** gauge alterations in the conductivity of a medium caused by enzyme-mediated reactions, which subsequently alter its ionic composition.

### 1.3.1.1 Potentiometric Biosensor

The electrochemical biosensor under consideration operates at a consistent current level and employs potentiometry to gauge the ionic activity involved in electrochemical reactions. Potentiometric biosensors assess the potential difference between two solutions across an ion-selective membrane. Notably, ion-selective electrodes, exemplified by the pH electrode, serve as valuable tools for monitoring alterations in ionic concentrations. Furthermore, selective electrodes designed for detecting substances like ammonia and carbon dioxide play significant roles in biosensing applications (Chakraborty and Hashmi 2017; Santoro and Ricciardi 2016).

Potentiometric sensors typically necessitate both a reference electrode and an indication (working) electrode to interface with the test sample solution effectively. Upon integration with ion-selective electrodes, these sensors exhibit sensitivity to a spectrum of ions, encompassing hydrogen, fluorine, iodine, chlorine, as well as gases like carbon dioxide and ammonia (Alarcon-Angeles et al. 2018; Ronkainen et al. 2010; Thévenot et al. 2001). **Fig 1.2** illustrates the schematic diagram of a potentiometric biosensor.

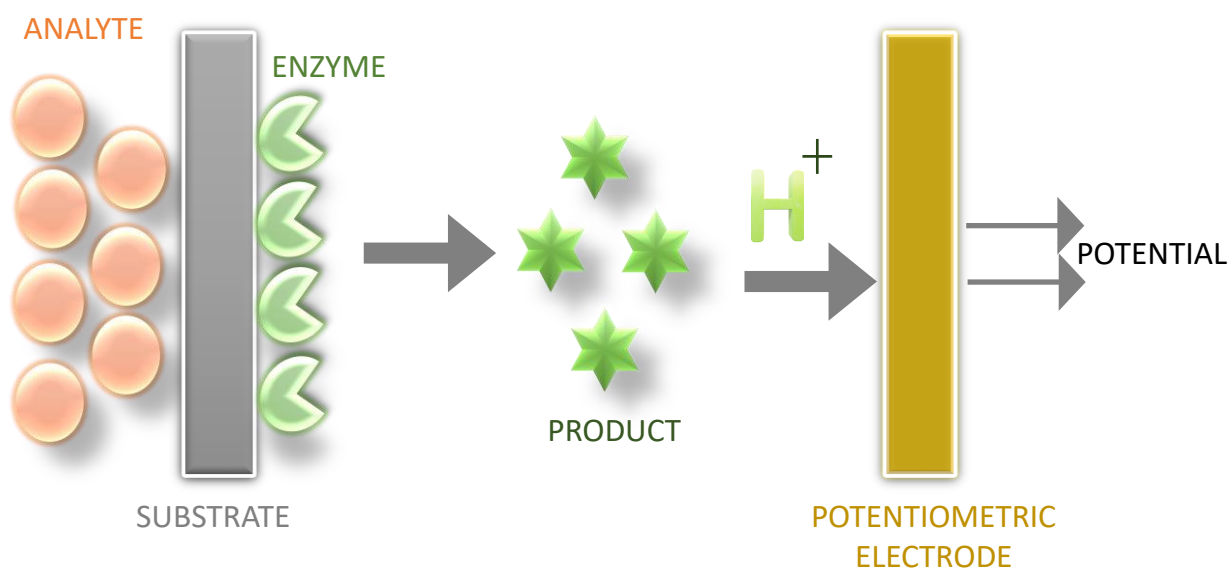


*Figure 1.2. Schematic diagram of typical Potentiometric biosensor.*

**Advantages:**

- i. The biosensor demonstrates the capability to detect ions over a broad dynamic range, typically spanning concentrations from 1  $\mu\text{M}$  to 0.1M.
- ii. Due to its capacity for continuous measurement, the biosensor is particularly suited for environmental monitoring and clinical diagnostics applications. Inexpensive and portable (Zhu et al. 2002).

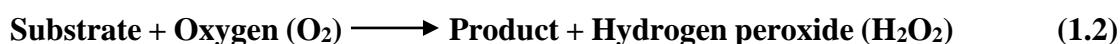
**Disadvantages:**

- i. In enzyme-based sensors, maintaining optimal enzyme activity often necessitates the use of pH buffers, which can sometimes restrict the range over which analytes can be detected (Zhu et al. 2002).

**1.3.1.2 Amperometric Biosensor**

Amperometric systems, belonging to the realm of electrochemical devices, continuously measure current during biological reactions by detecting the redox reaction of electroactive molecules at the electrode surface. Notably, a linear relationship exists between the target concentration and the resultant current. Amperometry, the method utilized for measuring changes in current over time while maintaining a constant voltage between the working and reference electrodes, determines the current by either sustaining the potential at the desired level or promptly reaching it. Consequently, a strong correlation emerges between the bulk concentration of the analyte in the solution and the peak current value measured within a linear potential range (Davis 1985).

Numerous enzymatic assays involving hydrogen peroxide generation during the reaction process commonly employ amperometry. Subsequently, hydrogen peroxide undergoes oxidation at a constant voltage to yield oxygen molecules, eliciting an electron flow that generates a discernible current directly correlated with the concentration of hydrogen peroxide (**Eq. 1.2**) (Santoro and Ricciardi 2016; Zhu et al. 2002).



Amperometric biosensors generate signals through electron transfer occurring between an electrode and the biological system situated within the bioreceptor layer. In the context of amperometric biosensors, the analyte typically undergoes a redox reaction, resulting in an observable current within the electrochemical cell, thus determining the outcome. Through a (bio)chemical process, the analyte or its associated species modulates the oxidation state of the electrode. Subsequently, the measured electron flow is directly proportional to the quantity of species electrochemically altered at the electrode (Belluzo et al. 2008). The fundamental workings of an amperometric biosensor are depicted in **Fig 1.3**.

The working electrode material in biosensors varies, with options including carbon nanotubes and noble metals such as gold, titanium, nickel, or titanium tin oxide, which are commonly employed. An illustrious instance of an amperometric biosensor is the Clark electrode, renowned for its simplicity and often utilized to measure the partial pressure of dissolved oxygen in blood or other substances (Monošík et al. 2012).

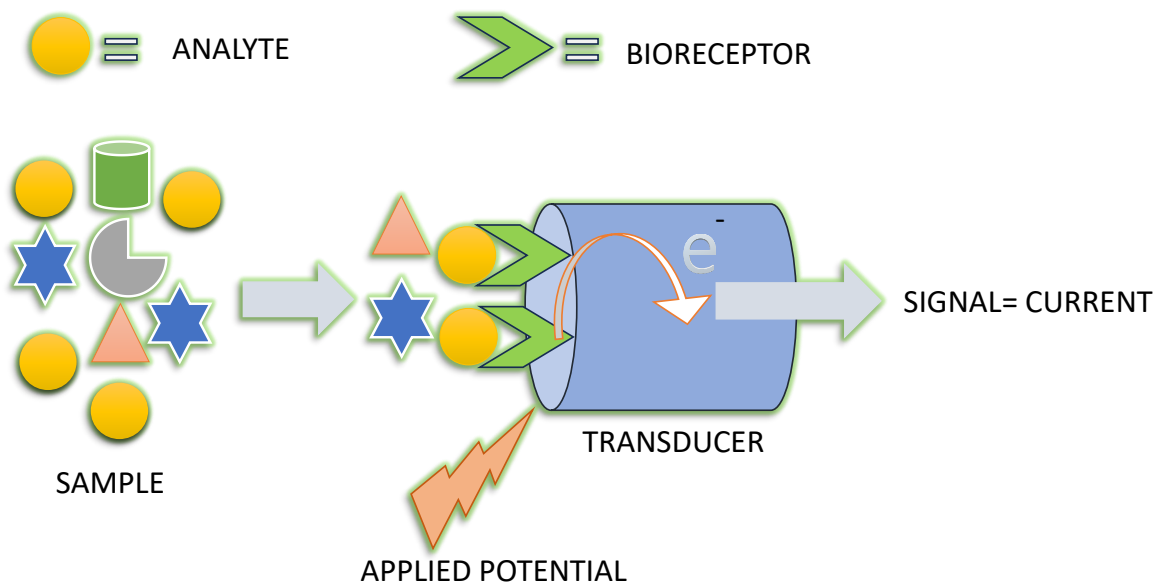


**Figure 1.3.** Schematic diagram of typical Amperometric biosensor.

**Advantages:**

- i. Utilization of economically feasible and disposable electrodes.
- ii. The instrumentation required for these biosensors is cost-effective and compact, facilitating the feasibility of conducting on-site measurements.
- iii. The amperometric biosensor responds quickly, has a broad linear range, and is very sensitive.

**Disadvantages:**

- i. The signal may be obstructed by other electroactive materials. The biosensor is therefore not selective (Zhu et al. 2002).

**1.3.1.3 Conductometric Biosensor**

The generation of ions or electrons during biological processes causes variations in the solution's overall conductivity or resistivity. Since many processes result in changes to the concentration of ions in a medium, conductance which is closely correlated with ion concentration serves as a good parameter for conductometric biosensors. When using this transducer, the electrical conductance or resistance of the solution is the measured parameter. The sensitivity of conductance measurements is usually rather poor. On the other hand, to counteract unwanted effects including concentration polarization, double-layer charging, and Faradaic processes, an electric field is produced when an AC sinusoidal voltage is used. These biosensors are used to detect drugs in human urine and track environmental pollution levels (Monošík et al. 2012).

Biosensors are categorized into distinct groups according to the type of bioreceptor utilized.

**1.3.2 Enzymatic Biosensor**

Enzymes are the basis of enzymatic biosensors; they require the right environment for maximum activity. Local chemical and temperature variables may have an impact on the stability of the enzymes. The kind of transducer, the physicochemical characteristics of the analyte, the function of the bioreceptor, and other variables all affect the enzyme's maximal activity. High selectivity towards particular analytes is another feature of enzymatic biosensors (Revathi and Rajendra Kumar 2019).

Enzymes are immobilized through various methods:

- i. Adsorption:** Stronger bonding, defined by the formation of covalent bonds, is involved in chemisorption, whereas physical sorption includes weaker connections mediated by van der Waals forces.
- ii. Covalent bonding:** It occurs at the interface between a functional group and the transducer.
- iii. Cross-linking:** To improve the stability of the adsorbed biomaterial, the biomaterial and the supporting material are chemically linked during this procedure.

The selectivity and sensitivity of enzyme-based electrochemical biosensors are remarkable; on the other hand, there are drawbacks, such as the enzyme's sensitivity to temperature, pH, and hazardous chemicals, and its vulnerability to denaturation during immobilization. Furthermore, improvements are needed to make enzyme-based sensors more reproducible. Non-enzymatic sensors have been developed in response to these limits, and they provide benefits such as increased stability, ease of manufacturing, greater repeatability, and affordability (Revathi and Rajendra Kumar 2019).

### 1.3.3 Non-enzymatic Biosensor

Enzyme immobilization on transducers and short shelf life are major obstacles to enzyme-based biosensors, regardless of their great selectivity towards analytes. Their use is further complicated by compound interference issues. As a result, non-enzymatic biosensors have become a viable substitute. Non-enzymatic biosensors can achieve improved simplicity, repeatability, and stability by using nanomaterials. The large surface area, particular shape, and effective electron transport of nanomaterials make them essential for enhancing electrocatalytic activity and selectivity (Revathi and Rajendra Kumar 2019).

A variety of materials are used to alter the functioning electrode of biosensors to overcome these difficulties. For high-performance nonenzymatic electrochemical sensors, nanomaterials, such as graphene, quantum dots, and noble metals like Au and Pt, as well as carbon-based materials like CNTs, act as efficient conductive supports. In addition, metal oxide nanoparticles (ZnO, Cu<sub>2</sub>O, NiO, SiO<sub>2</sub>, Fe<sub>2</sub>O<sub>3</sub>, MnO<sub>2</sub>,

Co<sub>3</sub>O<sub>4</sub>, etc.) are used because of their high catalytic activity and affordability. Composite materials are commonly used to improve both chemical and physical properties by mixing several nanomaterials (Revathi and Rajendra Kumar 2019). Non-enzymatic can be further classified into subcategories according to the manner the particular analyte binds:

- i. Immunosensors:** High-affinity interactions between antibodies and the corresponding antigens are the basis of immunosensor function, producing measurable signals. Antibodies interact with antigens by immobilization on a solid surface, triggering a signaling reaction. These biosensors show remarkable selectivity and have the potential to be improved by generating new recombinant antibodies.
- ii. DNA:** The unique property of DNA that these biosensors, designed to replace immunosensors, utilize the ability of a single DNA strand (or any nucleic acid) to recognize its corresponding strand in the analyte, made possible by hydrogen bonding between the two strands. They are extremely selective and stable due to their fundamental quality while maintaining cost-effectiveness.
- iii. Organelle-based:** These biosensors are very stable since they are made of biological organelles such as microsomes, mitochondria, chloroplasts, and cell membranes. They are distinguished by extended detection times (Alhadrami 2018; Malhotra and Ali 2018).

#### **1.4 Nanomaterials and Various Synthesis Techniques**

The origins of nanotechnology may be attributed to a revolutionary speech given in December 1959 at the American Physical Society annual conference by Nobel winner Richard P. Feynman, a physicist. In his address titled 'There's Plenty of Room at the Bottom', Feynman envisioned the possibility of miniaturization on an unprecedented scale. He proposed that the complete Encyclopaedia Britannica might be replicated on the head of a pin to demonstrate the idea (Nasrollahzadeh et al. 2019).

Numerous techniques may be used to synthesize different kinds of nanomaterials, such as thin films, colloidal nanoparticles, nanowires, nanotubes, nanorods, and nanoclusters. These techniques combine conventional procedures with modifications to attain nanoscale dimensions. Currently, physical, chemical, biological, and hybrid

methods may be used to synthesize nanomaterials. The particular material or nanomaterial to be synthesized—zero-dimensional (0D), one-dimensional (1D), or two-dimensional (2D), as well as factors like size and quantity requirements, all influence the synthesis process choice (Malhotra and Ali 2018).

Top-down and bottom-up approaches are the two ways to approach the nanoscale as shown in **Fig 1.4**. Reducing the structure to the nanoscale is the top-down approach. Using a bottom-up method, smaller atoms and molecules are used to build larger nanostructures (Malhotra and Ali 2018).

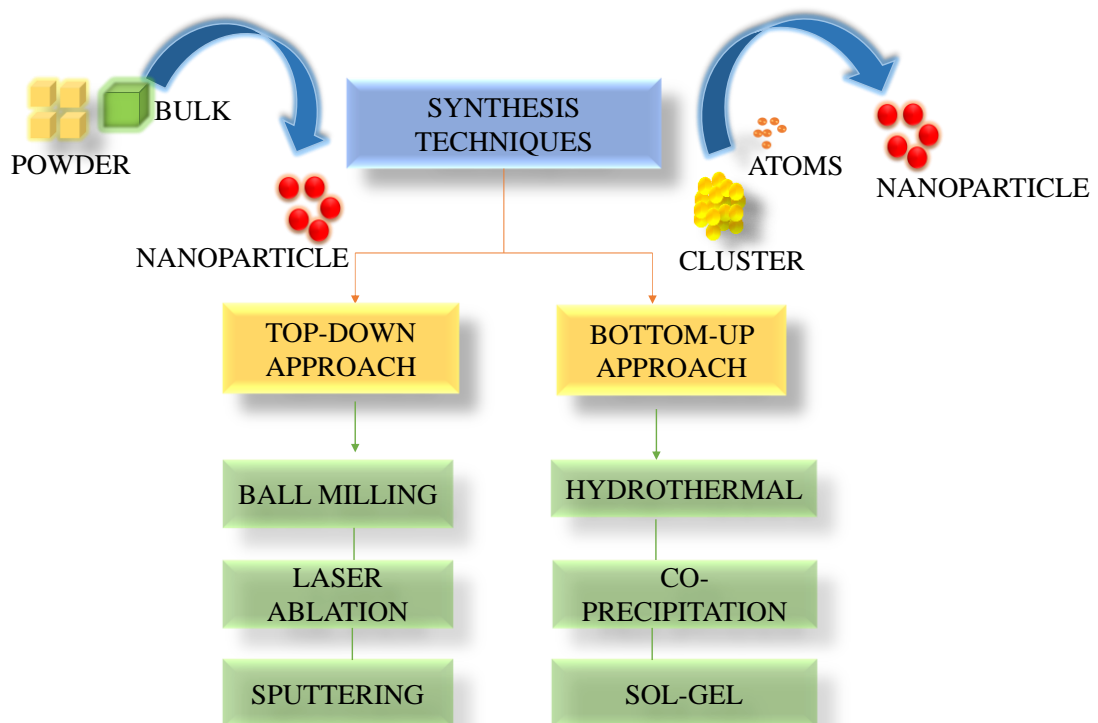


*Figure 1.4. General techniques for synthesizing nanostructures employing top-down and bottom-up approaches.*

### 1.4.1 Bottom-up Approach

According to this process, material constituents are reduced to the atomic level and then allowed to self-assemble to develop nanostructures. During the process of self-assembly, larger components are constructed from nanostructured materials. Using this method, quantum dots have been produced during epitaxial growth, and nanoparticles

from colloidal dispersions have been produced. Using this method yields materials with a more homogeneous chemical structure and fewer defects (Malhotra and Ali 2018).

#### **1.4.2 Top-down Approach**

With this technology, desirable nanostructures may be fabricated and the macroscopic structure can be externally manipulated. Methods like ball milling, large plastic deformation, and mask-based etching are examples of this method. However, a significant disadvantage of this technique is that the resultant nanostructures have surface imperfections. These surface imperfections can have a substantial effect on the physical properties of the nanoparticles because of the high aspect ratio that is characteristic of this technique (Malhotra and Ali 2018).

##### **1.4.1.1 Hydrothermal Method**

Hydrothermal synthesis involves the precipitation of microscopic particles from a solid reacting with an aqueous solution under elevated pressure and temperature conditions within a steel autoclave. This method, using water as a solvent, enables precise control over parameters like temperature and pressure, surpassing the boiling point to achieve vapor saturation. Renowned for its consistent yield, cost-effectiveness, environmental sustainability, scalability, and capacity to produce high-purity end products, hydrothermal synthesis has made significant contributions to contemporary scientific and technological advancements. Its diverse applications span material synthesis, crystallization, organic waste treatment, and the production of refined ceramic powders (Abid et al. 2022).

#### **Advantages:**

- i. Controlling the size of nanoparticles with accuracy.
- ii. Produce nanocrystals with high crystallinity.

#### **Disadvantages:**

- i. High-priced autoclave.

### 1.4.1.2 Co-precipitation Method

The co-precipitation method is a widely utilized wet chemistry approach for synthesizing nanomaterials. It involves initiating a precipitation process in a homogeneous solution containing two or more cations, resulting in nanomaterials with small diameters and narrow size distributions. pH adjustment using solutions like sodium hydroxide or ammonia is common. Filtration or centrifugation is then used to collect precipitates, followed by secondary washing with solvents like ethanol or distilled water to ensure high purity by removing impurities. Post-processing techniques such as sintering, annealing, or calcination are often employed to achieve desired morphologies and crystal structures in the synthesized nanomaterials (Abid et al. 2022).

#### **Advantages:**

- i. Several choices for modifying the particle surface condition and overall homogeneity.
- ii. Low temperature and energy efficiency.
- iii. Easy and quick preparation.

#### **Disadvantages:**

- i. If the precipitation rates of the reactants differ considerably, this method will not work.

## 1.5 Significance of Nanomaterials in Advancing Electrochemical Biosensor

It is possible to categorize nanomaterials (NMs) according to dimensionality, shape, condition, and chemical composition, among other factors. Their size is a major determining factor in this classification; they are often between 1 and 100 nanometers in at least one dimension. These criteria are usually used to classify nanomaterials into discrete groups, which are further subdivided by dimensionality and general structural arrangement, allowing for more thorough categorization (Nasrollahzadeh et al. 2019). NMs can be further divided into four classes:

- i. **Zero-dimensional NMs (0D):** Every object in the 0-dimensional (0D) category has all three dimensions in nanoscale, which are generally less than 100

nanometers. The structures that fall under this category include hollow spheres, spherical nanomaterials, cubes, polygons, metal and core-shell nanoparticles, and quantum dots (QDs).

- ii. **One-dimensional NMs (1D):** The materials classified as 1-dimensional (1D) have two dimensions at the nanoscale and one dimension that is not in the nanoscale. This category includes a wide range of materials, such as metallic, ceramic, and polymeric structures, in addition to different types of nanowires, nanofibers, nanorods, and nanotubes.
- iii. **Two-dimensional NMs (2D):** In the 2-dimensional (2D) category, materials only have one dimension at the nanoscale; the other two dimensions are not in the nanoscale. This class includes a range of shapes with crystalline or amorphous components, such as single-layered and multi-layered structures. Nanocoating, nanoplates, and thin films are a few examples of such structures.
- iv. **Three-dimensional NMs (3D):** Materials that are classified as 3-dimensional (3D) extend over 100 nanometers in size. These materials sometimes consist of many nanocrystals arranged in different orientations, generating complex three-dimensional structures. Foams, fibers, carbon nanobuds, nanotubes, fullerenes, pillars, polycrystals, honeycombs, and layered skeletons are a few examples of these structures.

NMs are categorized into many groups according to their varied chemical properties. Single constituent nanoparticles (NPs) and nanocomposites are among these classes; each is further split into several varieties according to the composition of its constituent chemicals as shown in **Fig 1.5**. Carbon-based substances including fullerenes, carbon nanotubes (CNTs), and graphenes make up the majority of carbonaceous nanomaterials. Alumina, zinc, titania, silver, copper, iron, and silica are some of the metals that are used to make metallic nanostructures. Branched dendrimers are a subclass of nanomaterials that exhibit nanoscale branch-like features. Quantum dots (QDs) are very small semiconductor particles with special optical and electrical characteristics that come from quantum mechanics. These particles are usually just a few nanometres in size (Nasrollahzadeh et al. 2019; Santoro and Ricciardi 2016).

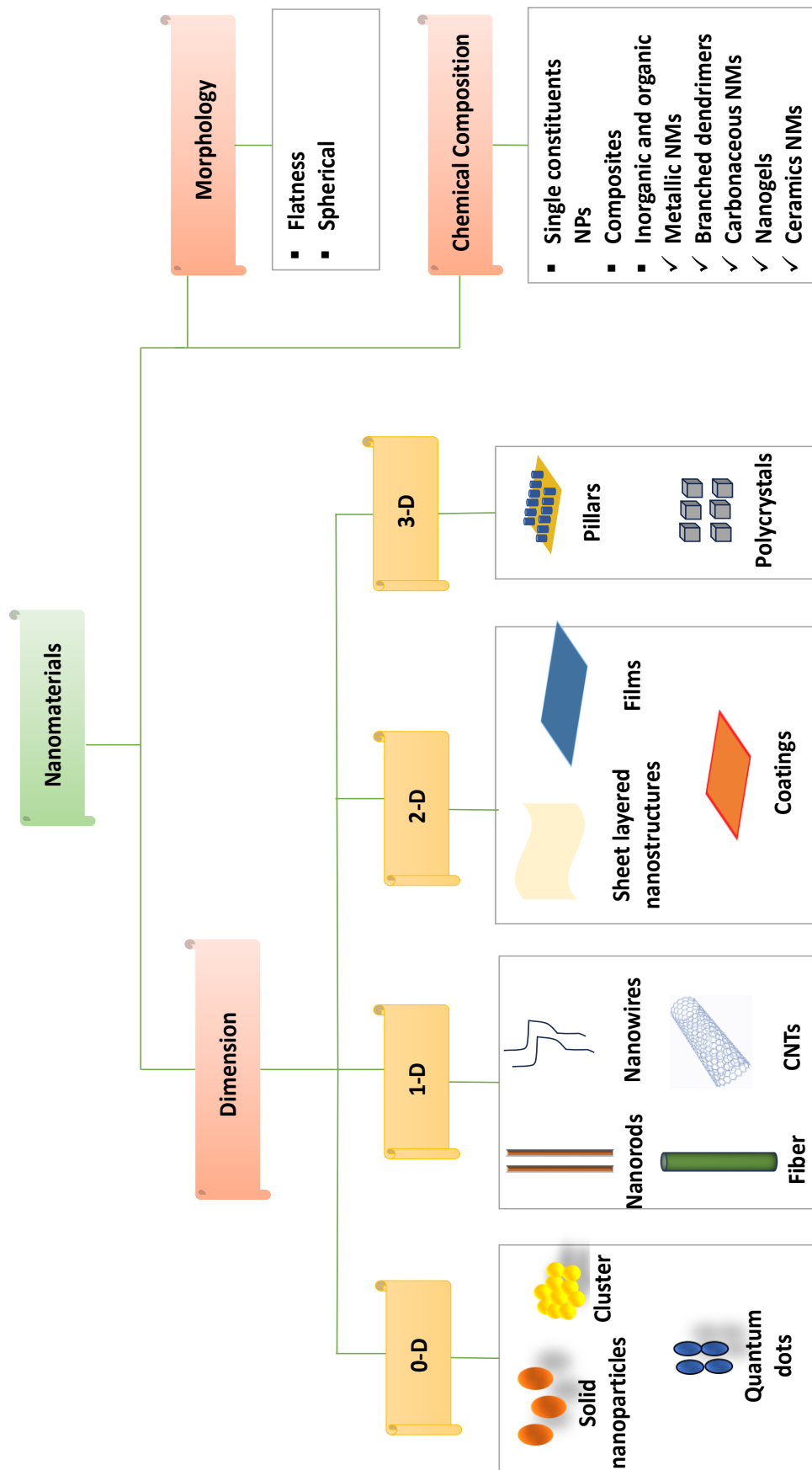


Figure 1.5. Classification of nanoparticles.

Ultrasensitive electrochemical biosensor development appears to have a bright future because of nanotechnology. As a result of their nanometric size, exceptional electrical characteristics, large surface area, and electrocatalytic activity qualities that improve signal detection. Nanotechnology is a growing contributor to the development of biosensors. The field of nanomaterials research has made significant progress recently, resulting in a wide range of innovative materials that have the potential to be used in many other contexts, such as biosensor integration. A remarkable range of inorganic nanomaterials have been synthesized and characterized. These include nanoparticles, which include Ti, Zn, Cu, and iron nanocrystals, which include quantum dots (QDs); nanorods, nanowires; and different carbon nanostructures, such as single and multiwalled carbon nanotubes and nanofibers (Griffin et al. 2014).

Nanomaterials have unique physical characteristics that make them ideal scaffolds for biosensing applications because of their small size. These capabilities include electrical conductivity, unique optical properties, special structural features with very high surface area-to-volume ratios, and particular biological properties that are a result of their nanoscale size. The integration of microfabrication and nanofabrication techniques facilitates the creation of materials and devices with dimensions generally less than 100 nanometers (Griffin et al. 2014; Santoro and Ricciardi 2016). The advantages of this smaller-scale approach are further substantiated by the potential to

- i. Lowering unit costs through the implementation of large-scale production methods.
- ii. Reduce sample volumes to microliters or less.
- iii. Reduced costs associated with reagents.
- iv. Employ microfluidics to mitigate sample processing duration and streamline analysis time.
- v. Reduce the dependency on power consumption.
- vi. Enhance the portability of electronic systems while simultaneously augmenting the sensitivity of biosensors (Santoro and Ricciardi 2016).

## 1.6 Electrochemical Cell

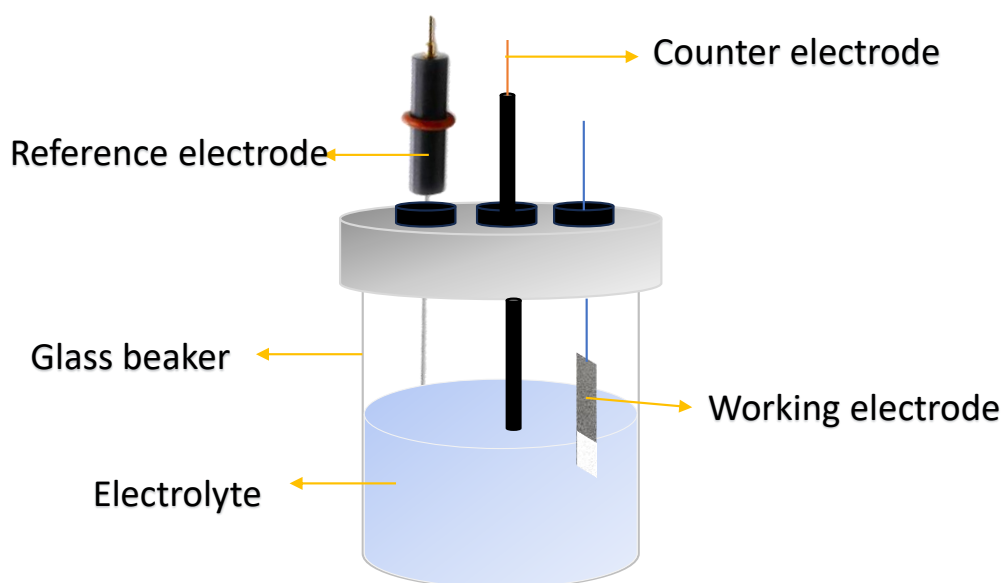


*Figure 1.6. Schematic diagram of a typical electrochemical cell for electrochemical techniques.*

### 1.6.1 Electrolyte Solution

In cyclic voltammetry (CV) experiments, ions in the solution facilitate electron transfer, maintaining electrical balance. When electrons move from the electrode to the analyte, ions in the solution shift positions to balance the charge and complete the electrical circuit. To decrease solution resistance, a salt known as a supportive electrolyte is dissolved in the solvent. This combination of solvent and supporting electrolyte is often termed the "electrolyte solution." The schematic three-electrode system is depicted in **Fig 1.6**.

In a liquid medium, the electrical conductivity of the analyte can undergo alterations. Consequently, the electrolyte solution imparts conductivity to the analyte solution and impedes the migration of charged ions toward their respective electrodes. Such ion migration can potentially obstruct ion diffusion processes. Supporting electrolytes, such as strong acids, bases, and buffer solutions, furnish the necessary  $\text{H}^+$  and  $\text{OH}^-$  ions essential for electrochemical reactions. Commonly employed supporting electrolytes include ions like  $\text{H}^+$ ,  $\text{Li}^+$ ,  $\text{Na}^+$ ,  $\text{Cl}^-$ ,  $\text{Br}^-$ , and  $\text{PF}_6^-$  (Elgrishi et al. 2018).

### **1.6.2 Reference Electrode**

A reference electrode possesses a distinct and consistent equilibrium potential, serving as a benchmark for comparing the potentials of other electrodes within an electrochemical cell. Often denoted by "vs" alongside a designated reference, the applied potential can be precisely determined. Several electrode configurations are renowned for maintaining their potential irrespective of the electrolyte composition within the cell. Notable examples of reference electrodes frequently employed in aqueous environments include the saturated calomel electrode (SCE), standard hydrogen electrode (SHE), and AgCl/Ag electrode. (Elgrishi et al. 2018; Lefrou et al. 2010).

### **1.6.3 Counter Electrode**

The initiation of current flow occurs when an electrical potential is applied to the working electrode, facilitating the reduction or oxidation of the analyte. The role of the counter electrode is to complete the electrical circuit. The counter electrode, which is usually made of platinum wire or disk but may alternatively be made of carbon, helps with an oxidation process when reduction takes place at the working electrode. To reduce any unintended reactions, it is crucial to select a counter electrode with inert qualities. Counter electrodes may develop byproducts depending on the experiment, in which case they must be isolated via a fritted compartment from the rest of the system (Elgrishi et al. 2018; Lefrou et al. 2010).

### **1.6.4 Working Electrode**

Electrochemical processes are significantly enhanced by the working electrode, whose potential is precisely regulated by a potentiostat relative to the reference electrode. A key feature of the working electrode is its composition of redox-inert materials, matched to the appropriate potential range. Common materials include glassy carbon, Nickel Foam (NF), serving as indicators of the reaction of interest. Prior to experiments, the working electrode undergoes meticulous preparation: it is polished with abrasive materials like alumina or diamond paste, rinsed with solvents such as water or ethanol, and subjected to ultrasonic treatment to remove residual particles, ensuring uniform surface conditions (Dekanski et al. 2001).

- i. **Glassy Carbon Electrode:** A polymer composed of benzene units is utilized to produce a glassy carbon electrode. This material is robust, chemically inert, and exhibits a non-porous, glass-like structure when fractured. The electrode's properties are significantly influenced by the production temperature and the initial polymer composition. Notably, the glassy carbon electrode demonstrates exceptional resistance to chemical corrosion and gas permeability, enhancing the reversibility of various redox processes. Additionally, it presents a cost-effective alternative to platinum and gold electrodes while offering an extended potential window (Dekanski et al. 2001).
- ii. **Nickel Foam:** Nickel foam (NF) is widely used in electrochemical applications due to its uniformity, high porosity, and lightweight nature. Its strong mechanical strength, excellent corrosion resistance, moderate ionic diffusion resistance, and high electrical and thermal conductivity make NF an ideal current collector. These attributes enhance the stability of electrodes by maximizing contact surfaces between charged species, active materials, and the NF substrate, thereby improving electrochemical performance (Ratsoma et al. 2023).

## 1.7 Electrochemical Techniques

Electrochemical processes are essentially dependent on reactions occurring at an electrode surface. Electrochemical detection refers to the monitoring of changes in an electrical signal that results from these processes, which are frequently caused by an applied voltage or current. Significant approaches in this field are voltammetric techniques such as Differential Pulse Voltammetry (DPV), Chronoamperometry, and Cyclic Voltammetry (Rezaei and Irannejad 2019).

### 1.7.1 Voltammetric measurements

Voltammetry, derived from "volt" and "amperometry," measures current as a function of electrode potential. It encompasses methods that evaluate current in relation to electrode potential, divided into controlled potential and controlled current techniques. Controlled potential techniques use potentiostats to regulate electrode potential, while current measurements assess the system's response to potential changes. This makes

voltammetry a fundamental technique for studying electrode/electrolyte interface processes (Scholz 2015).

### 1.7.1.1 Cyclic Voltammetry (CV)

Cyclic Voltammetry (CV) is a widely used electrochemical technique for investigating oxidation and reduction processes of molecular species. It is essential for analyzing electron transport-mediated chemical processes, providing estimates of redox potentials, electron transfer rates, and analyte stability during oxidation. In CV, a stationary working electrode is immersed in a quiescent solution with an excess of supporting electrolyte, ensuring that electroactive species exchange with the electrode surface occurs solely through diffusion. This method operates by measuring the current generated and adjusting the applied voltage at a working electrode at a predetermined scan rate. Initially, the first scan moves away from the switching potential in one direction, then reverses and proceeds upward. A cycle can be completed fully, partially, or over multiple rounds, depending on specific analytical requirements (Bontempelli et al. 2016; Scholz 2015). The Cyclic voltammogram is represented in **Fig 1.7**.

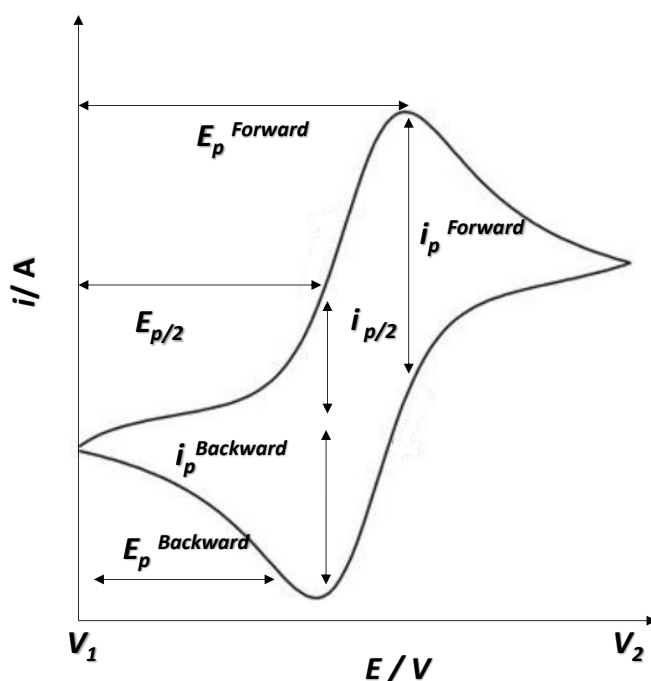


**Figure 1.7.** Cyclic Voltammogram for reversible reaction

Electrochemical reactions typically entail the following sequential steps:

- i. Reactants and products migrate in opposing directions from the bulk solution to the electrode surface in the first stage.
- ii. Reaction of charge transfer.
- iii. Significant changes in structure and/or chemical composition might occur before, after, or simultaneously with the charge transfer phase, as well as in the times between subsequent charge transfer events (Scholz 2015).

In addition, adsorption and other surface reactions might get involved. Depending on the chosen scan rate, each of these phases might have different effects on voltammetric responses, which define the experimental window for monitoring the electrochemical process. Several tens of millivolts per second to hundreds of volts per second are the ranges within which scan rates may be varied. This allows for flexibility in timeframes, ranging from  $10^{-5}$  to  $10^2$  seconds (Bontempelli et al. 2016).

As shown in **Fig. 1.7**, this approach involves the voltage undergoing a scanning process from a starting point ( $V_1$ ) to a specified point ( $V_2$ ) and then back to its initial level. A crucial parameter in this approach is the scan rate  $(V_2 - V_1) / (t_2 - t_1)$ , as significant chemical reactions need sufficient time to take place. As a result, changing the scan rate produces different results. The working electrode's potential changes caused by the reference electrode are controlled during this process, and the current between the working and counter electrodes is observed. These observations yield voltage-versus-current plots or voltammograms.

Additionally, when the voltage becomes closer to the analyte's electrochemical reduction potential, the current generated by the electrochemical process experiences an increment. A peak on the voltammogram when the voltage increases toward  $V_2$  and the current drops, indicating that the high oxidation potential of the electrode is reducing the analyte concentration close to the electrode surface. The reaction then starts to reoxidize the main reaction product as the voltage drops back to starting point of  $V_1$  to finish the CV. In this phase, voltage scan moves toward  $V_1$ , and the current shows a polarity reversal from the forward scan before dropping once more. As such,

for a certain scan rate, a reverse scan provides relevant information on the reversibility of the reaction (Bontempelli et al. 2016).

### 1.7.1.2 Chronoamperometry (CA)

Chronoamperometry (CA) is a recognized electrochemical technique that involves applying a pulsed potential to a functional electrode and monitoring the resulting current over time. This method tracks changes in the current caused by variations in the analyte's diffuse layer near the electrode surface. The diffuse layer, where analyte concentrations differ from the bulk solution, forms due to analyte diffusion from higher concentration regions (bulk solution) to the electrode surface under an applied voltage, reducing the local analyte concentration to zero (Kamat et al. 2010; Rezaei and Irannejad 2019).

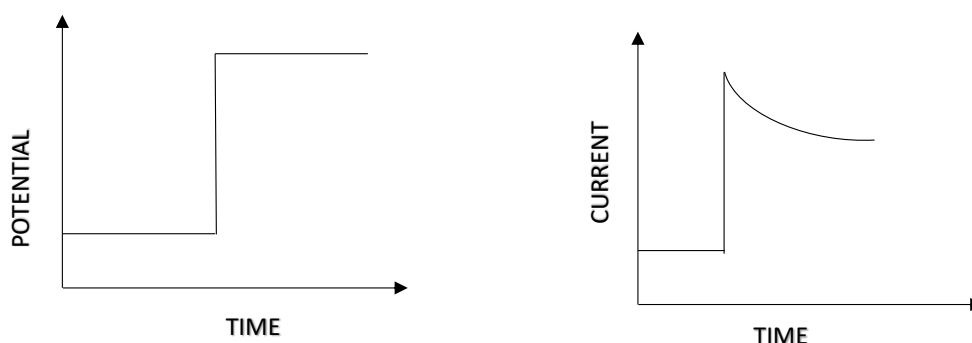


*Figure 1.8. Single potential chronoamperometry processes*

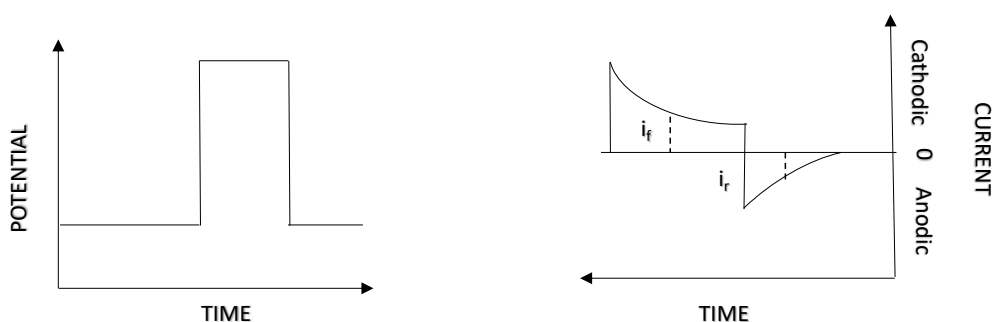


*Figure 1.9. Double potential step chronoamperometry process*

Chronoamperometric experiments can be of two main types: single potential steps (**Fig 1.8**), in which a forward potential is applied and the current that results are recorded, or double potential steps (**Fig 1.9**), in which a forward potential is applied and the initial value is returned within a predetermined amount of time. Cottrell's equation (**Eq. 1.3**) controls the current in reversible redox processes at every time point that follows a significant single potential step (Evans and Kelly 1982).

$$it = \frac{nFAC_0D_0^{1/2}}{\pi^{1/2}t^{1/2}} \quad (1.3)$$

Cottrell's equation is utilized in chronoamperometric analysis to evaluate the current data following a significant single potential step. This formula includes parameters like 'n', which is the stoichiometric number of electrons in the redox reaction; 'F' stands for Faraday's constant; 'A' is the electrode surface area; and 'C' and 'D' are the concentration and diffusion constant of the electroactive species respectively in the solution.

Chronoamperometry enables the measurement of electrode surface area (A) via a redox reaction (n, C, and D). Once the electrode area is known, quantifying electroactive species in solution becomes straightforward. Particularly in product absorption systems, the double potential step approaches offer an extremely thorough insight into the chemical reaction's rate constants (Bontempelli et al. 2016; Rezaei and Irannejad 2019).

### 1.7.1.3 Differential Pulse Voltammetry (DPV)

Using amplitude potential pulses on a linear ramp potential, DPV is an electrochemical method used to measure the concentrations of ions in a solution. An electrode in DPV is adjusted to a base potential where no faradaic reaction takes place. The base potential is then gradually increased in between pulses. Immediate current measurements are collected before and after each pulse is applied, and the difference between these readings is noted. When the voltage is raised, the current rises, peaks, and then falls as expected. The magnitude of this peak is indicative of the concentration of the electroactive substance present in the sample (Simões and Xavier 2017). **Fig 1.10** depicts the typical DPV plot.

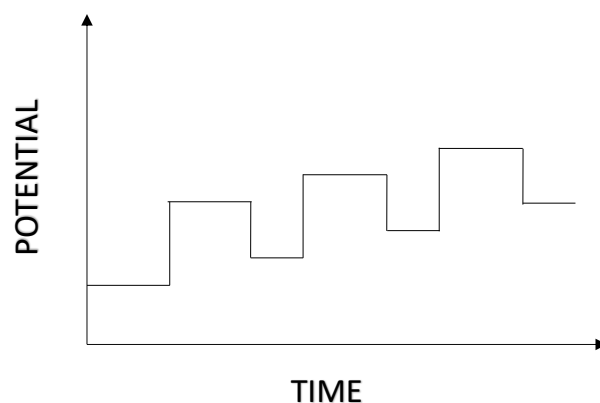


*Figure 1.10. Differential pulse voltammetry graph*

#### 1.7.1.4 Electrochemical Impedance Spectroscopy (EIS)

Electrochemical Impedance Spectroscopy (EIS) is a fast, inexpensive, and non-invasive technique widely used in biological system studies. Impedance examines the resistance properties of an electrical circuit under an alternating current. By applying a small sinusoidal voltage, EIS measures current flow responses and detects frequency variations over a broad range. This response, represented as a complex number with real and imaginary components, is analyzed through mathematical relations adjusted for excitation frequency. EIS plays a crucial role in material characterization and biosensor transductions, enabling the investigation of conductivity, resistivity, capacitance, and other intrinsic material properties in electrochemical systems. Electrolyte-based systems are analyzed using EIS, which involves key components: ohmic resistance ( $R_s$ ), capacitance (C), constant phase element (CPE), and Warburg impedance (W). Selecting an appropriate circuit is crucial for impedance analysis, with equivalent circuits providing detailed descriptions of impedance components in parallel or series configurations (Rezaei and Irannejad 2019). **Fig 1.11** depicts the typical EIS graph and its equivalent circuit.

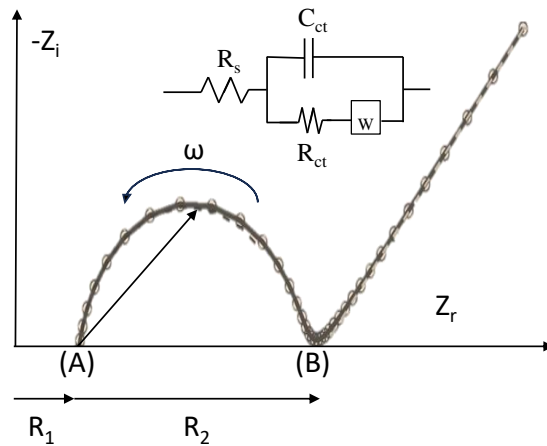


**Figure 1.11.** The Nyquist plot of an electrochemical cell and its Randles' equivalent circuit

## 1.8 Applications of Biosensor

Scientific and medical institutions increasingly rely on affordable biosensors for diverse applications, including detecting pollutants in food and water, monitoring biological processes in humans, and facilitating precise health diagnostics. This trend reflects the academic and healthcare sectors' demand for reliable, cost-effective tools to advance research, safeguard public health, and deliver personalized healthcare solutions. Biosensors provide a straightforward, economical means to address these challenges effectively (Haleem et al. 2021).

### 1.8.1 Clinical Diagnosis

Advances in biosensor technology are increasingly crucial in modern medicine, pivotal for disease diagnosis including viral screening, chronic illness management, early detection, and mental health monitoring. Recent innovations have enhanced early disease detection, characterization, treatment monitoring, and efficacy assessment. There is a rising demand in clinical settings for affordable, reliable biosensors empowering patients, notably those with conditions like diabetes. Low-cost biosensors show promise across diverse settings, from home to hospital, given the cost considerations of laboratory equipment upkeep. Meeting varied healthcare needs requires advanced biomolecular sensor development, research, and commercialization, emphasizing material exploration for surface immobilization and integration to enhance

usability and effectiveness in medical and health monitoring applications.(Monošík et al. 2012).

- i. **Detection of glucose:** To effectively manage diabetes mellitus, a chronic metabolic condition, blood glucose levels must be continuously monitored. In the past, sample destruction and heavy equipment were involved in this tedious monitoring procedure. However, the development of biosensors has completely changed the process of determining glucose levels, providing increased simplicity and dependability. Although finger-prick biosensors are widely used in commercial applications, they are invasive and require frequent replacement even if they yield quick findings. More long-term stability is provided by implanted biosensors, which are the result of advancements in the area. Furthermore, the use of nanomaterials has improved glucose detection's sensitivity and selectivity even further (Gouvea 2011; Monošík et al. 2012).
- i. **Detection of cholesterol:** As a precursor to several important compounds, including steroids, hormones, and vitamin D, cholesterol plays a crucial structural role in biological cells, including nerve cells and plasma. High cholesterol levels can cause cholesterol to accumulate on artery walls, which leads to diseases including myocardial infarction, arteriosclerosis, and coronary heart disease. As such, there is a significant public health issue with respect to the identification and measurement of cholesterol levels. While conventional techniques like spectrometry, colorimetry, and HPLC have been used historically for this purpose, their time-consuming and procedurally complex nature highlights the need for more effective alternatives. Biosensors have become an appropriate choice since they can detect cholesterol levels quickly and accurately, allowing for prompt action and control of any related health problems (Gouvea 2011; Nandini et al. 2016).

### **1.8.2 Environmental Applications**

Public concern has increased as a result of the increasing amount of contaminants in the environment, which highlights the urgent need for improved environmental supervision. As a result, there is an increasing need to selectively monitor and evaluate these contaminants. Conventional approaches have excellent sensitivity and accuracy,

but they are also associated with long processing times, high costs, and the need for specialist staff (Rogers 2006; Sassolas et al. 2012; Serra 2011).

The substances that can be detected are:

- i. Heavy metals:** Even in low quantities, heavy metals such as zinc, mercury, copper, lead, and cadmium are exceptionally hazardous to individuals and the environment. To precisely detect the quantities of heavy metals, bacterial and enzyme biosensors are frequently employed to overcome this challenge.
- ii. Nitrogen compounds:** Nitrogen materials, such as nitrites, which frequently serve as soil fertilizers, are highly dangerous to individuals and may lead to several diseases. Therefore, they must be found and observed. For this, amperometric biosensors are employed, whereby cytochrome c serves as the electrochemical bioreceptor.
- iii. Pesticides:** Pesticides are extremely harmful to both individuals and the environment, and that is the reason that enzymatic biosensors are utilized in their detection.

### 1.8.3 Food Safety

The identification of allergens and pathogens in food is a major challenge for the food processing industry. Biosensors offer a promising solution by enabling rapid detection of these contaminants. They are effective for various aspects of food quality control, such as monitoring raw materials, detecting pollutants, authenticating products, and evaluating freshness. Unlike traditional tests that require time-consuming procedures, biosensors provide efficient, non-destructive analytical techniques, potentially revolutionizing quality control in the food and agriculture industries (Anand et al. 2013).

## 1.9 Summary

Nanomaterials and biosensors play crucial roles across various disciplines in modern society. Nanomaterials, distinguished by their extensive surface area and distinct chemical properties, significantly enhance the sensitivity and reliability of biosensors. This advancement enables precise detection of minute molecules critical for environmental monitoring, food safety, and medical diagnostics. In healthcare,

biosensors facilitate real-time measurement of biomarkers such as glucose and cholesterol levels, thereby improving patient outcomes and treatment efficacy. Their adaptability for decentralized testing and integration into portable devices further enhances their utility in diverse applications, including healthcare. Together, biosensors and nanomaterials exemplify scientific progress that upholds essential standards of environmental sustainability, health, and safety, while also enhancing operational efficiency in contemporary society.

\*\*\*\*\*

## **CHAPTER 2**

---

---

### **LITERATURE REVIEW, RESEARCH SCOPE AND OBJECTIVE**

---

---



---

---

**Abstract:** Chapter 2 delves into the historical progression of non-enzymatic biosensors designed for the detection of glucose and cholesterol. Various metal oxide and nanocomposite materials are investigated within this context and thoroughly examined throughout the chapter. Additionally, the chapter outlines the scope and objectives of the current research endeavour.

---

---

In the domain of nano biosensors, metal oxides are essential and have attracted a lot of interest from environmental science, analytical chemistry, and biological sciences. Their extraordinary properties, including a large surface area, unique nanomorphology, excellent biocompatibility, non-toxicity, chemical stability, and catalytic activity, precisely make them appealing. These nanomaterials provide strong adsorption and improved electron-transfer kinetics, which create ideal microenvironments for biomolecule immobilization and improve biosensor performance. Metal oxide-based biosensors are especially appealing for broad use because they provide accessible and affordable substitutes for metal alloys. The mesoporous frameworks of transition metal oxide nanoparticles, in particular, have been the subject of much investigation due to their exceptional electrocatalytic and photocatalytic characteristics, which are determined by their size, shape, and large surface area. Moreover, metal and metal oxide nanostructures are frequently combined with semiconducting materials like some dopants, carbon nanotubes, graphene, and quantum dots to improve optical, electrical, and magnetic properties, which improves biosensor qualities. Semiconducting metal oxide nanoparticles are used as tracers and markers in electrochemical research, whereas biocompatible transition metal oxide nanoparticles are useful in immobilizing biomolecules for the construction of immunosensors, DNA sensors, and enzyme sensors (Agnihotri et al. 2021; Dong et al. 2021; Liu and Liu 2019; Rahman et al. 2010).

## 2.1 Glucose Biosensor Utilizing Metal Oxide-Based Materials

Over the years, glucose biosensors have come across several difficulties, including low stability, pH sensitivity, and enzyme dependence. Although promising at first, enzymatic glucose sensors have drawbacks such as expensive production and environmental sensitivity that need disposable use. Emerging as a possible fourth-generation solution, non-enzymatic glucose biosensors provide direct glucose oxidation independent of enzymes. These biosensors offer increased sensitivity, stability, and cost-effectiveness by using a variety of electrode materials, such as metals, metal oxides, alloys, and carbon-based substrates. By adding nanomaterials to electrode modifications, catalytic activity is increased and heightened sensitivity is achieved in glucose detection. Despite being widely used, noble metal electrodes have slow kinetics and are susceptible to biological substances. Wide linearity and low detection limits are two advantages of using nanostructured materials, such as metal oxides and carbon composites, in enhancing electrode performance. Non-enzymatic glucose biosensors have the potential to deliver improved performance and reliability in glucose monitoring by precisely optimizing the shape and composition of the electrodes (Fahmy Taha et al. 2020; Mohamad Nor et al. 2022).

Prasad and Bhat et al. synthesized self-assembled cobalt oxide-multiwalled carbon nanotube composites using a simple and effective wet chemical method (Prasad and Bhat 2015a). A modified glassy carbon electrode was subsequently fabricated and evaluated for enzyme-free glucose sensor applications. The sensor demonstrated an impressive sensitivity of  $5089.1 \mu\text{A}\cdot\text{mM}^{-1}\text{cm}^{-2}$  with LOD of  $10.42 \mu\text{M}$  across a glucose concentration range of 0.05-12 mM. Additionally, the sensor exhibited desirable features such as stability, selectivity, and rapid detection capabilities.

Zhou et al. synthesized CuO-Cu nanospheres electrodeposited on a  $\text{TiO}_2$  nanotube array are employed in a non-enzymatic glucose sensor that demonstrates promising performance (Zhou et al. 2020). The sensor exhibits a broad linear range of 0.2-90 mM, LOD of 19 nM, a high sensitivity of  $234 \mu\text{A}\cdot\text{mM}^{-1}\text{cm}^{-2}$ , and a typical operating voltage of 0.65 V in 0.1 M NaOH solution. These results emphasize the promise of the CuO-Cu nanosphere/TNT array electrode for sensitive and selective glucose detection in

biosensing applications. Moreover, the sensor shows selectivity against interfering substances.

Prasad et al. developed a solvent-free method to decorate multi-walled carbon nanotubes (MWCNTs) with nickel oxide NPs (NiO-NPs) (Prasad and Bhat 2015b). Utilizing the synthesized composite material, an enzyme-free modified carbon paste electrode was fabricated and evaluated for glucose sensing applications. The sensor incorporating 10% NiO-MWCNTs composites exhibited excellent electro-catalytic activity towards direct glucose oxidation. The sensor demonstrated a sensitivity of 1696  $\mu\text{A}\cdot\text{mM}^{-1}\text{cm}^{-2}$  and 122.1  $\mu\text{A}\cdot\text{mM}^{-1}\text{cm}^{-2}$ , with LOD of 11.04 nM and 31  $\mu\text{M}$  for linear responses over glucose concentration ranges of 1-200  $\mu\text{M}$  and 0.5-9.0 mM, respectively. Additionally, the 10% NiO-MWCNTs sensor showcased excellent anti-interference capability, high stability, and good reproducibility.

Grochowska et al. developed titanium dioxide nanotubes coated in gold that have superior qualities for detecting glucose (Grochowska et al. 2019). Anodization and magnetron sputtering were used in the fabrication process to develop a homogeneous architecture with gold collars forming at the edges of the nanotubes. Electrochemical analysis showed the sensitivity of 540 and 185  $\mu\text{A}\cdot\text{cm}^{-2}\text{mM}^{-1}$ , a LOD of 10  $\mu\text{M}$  in NaOH, and 45  $\mu\text{A}\cdot\text{cm}^{-2}\text{mM}^{-1}$  sensitivity with LOD of 50  $\mu\text{M}$  in PBS. Even with human serum diluted in NaOH, the sensor's sensitivity is lowered to 124  $\mu\text{A}\cdot\text{cm}^{-2}\text{mM}^{-1}$ , yet it is still appropriate for non-enzymatic glucose detection within physiological limits. The developed electrodes show remarkable resistance to repetitive bending and extended use, demonstrating their dependability and endurance in practical applications.

Prasad et al. (2015) synthesized plant root nodule-like NiO-MWCNT nanocomposites using a simple, rapid, and solvent-free method with nickel formate as a precursor (Prasad et al. 2015). The resulting NiO-MWCNT composite was employed to fabricate a modified non-enzymatic Carbon paste electrode for glucose sensing. Electrochemical investigations revealed that the fabricated sensor exhibited an outstanding sensitivity of 6527  $\mu\text{A}\cdot\text{mM}^{-1}\text{cm}^{-2}$ , with LOD of 19  $\mu\text{M}$  and a linear response range of 0.001-14 mM for glucose concentration at an applied potential of 0.5V. The sensor also demonstrated superior stability, selectivity, and reproducibility.

Khosroshahi et al. presented a porous structure composed of three-dimensional graphene decorated with Cu-based nanoparticles (Cu or Cu-Cu<sub>2</sub>O) to develop an enzyme-free electrochemical glucose sensor (Khosroshahi et al. 2020). Cu-Cu<sub>2</sub>O NPs@3DG foam showed linear range of 0.8-10 mM (R=0.9951) and LOD of 16 μM. This electrode attained a high sensitivity of 230.86 μA.mM<sup>-1</sup>cm<sup>-2</sup>. The sensor was noteworthy for its great selectivity and strong repeatability, and no discernible interference from interfering species was found.

Ahmad et al. proposed a biosensor with outstanding analytical performance that uses a nanohybrid composition of ZnO nanorods and CuO nanoparticles (Ahmad et al. 2017). The hybrid CuO-ZnO material that resulted was then covered with Nafion. The hybrid sensor demonstrated LOD of 0.40 μM, a linear range of 8.45 mM, a sensitivity of 2961.7 μA.mM<sup>-1</sup>cm<sup>-2</sup>, and a quick response time. The sensor also showed outstanding stability, selectivity, reproducibility, and repeatability.

Viswanathan et al. developed an electrocatalyst made of Cu/CuO/Cu(OH)<sub>2</sub>, in the presence of dopamine. By reducing Cu (II) to Cu (0), dopamine improves the conductivity of metal oxides (CuO /Cu(OH)<sub>2</sub>) (Viswanathan et al. 2019). The electrode modified with composite catalyst exhibits an excellent sensitivity of 223.177 μA.mM<sup>-1</sup>cm<sup>-2</sup>, LOD of 20 μM, and a linear range that extends up to 20 mM, making it appropriate for measuring blood glucose levels. In addition, the sensor shows excellent selectivity, repeatability, stability, and application for the detection of glucose in human urine samples, with a response time of less than 3 s.

Prasad et al. (2016) developed a solvent-free method for synthesizing a NiO-carbon nanotube/graphene ternary composite, utilizing nickel formate as a green precursor through a thermal decomposition process (Prasad et al. 2016). The synthesized NiO particles were uniformly decorated on the surface of conductive carbon matrix networks, such as MWCNTs and reduced graphene oxide (rGO). Under optimal conditions, the composite containing 20 wt.% NiO-MWCNT/rGO on a glassy carbon electrode (GCE) exhibited a sensitivity of 4223.3 μA.cm<sup>-2</sup>mM<sup>-1</sup> and LOD of 0.92 μM, within a linear glucose concentration range up to 19 mM. The constructed sensor demonstrated effective performance in detecting glucose in real human blood serum samples, yielding satisfactory results.

Vinoth et al. describe a simple and affordable way for fabricating a glucose sensor using zinc oxide quantum dots (ZnO QDs) immobilized by ultrasonication on MWCNTs nanocomposites (Vinoth et al. 2021). ZnO QDs anchored on MWCNTs showed consistent findings with LOD of 0.208  $\mu\text{M}$  and a sensitivity of 9.36  $\mu\text{A}\cdot\text{mM}^{-1}\text{cm}^{-2}$ . By using nanocomposites, the reaction time was lowered to less than 3s and the linear range was increased from 0.1-2.5  $\mu\text{M}$ . The sensor's ability to detect glucose levels in human urine samples effectively highlights its potential for useful glucose monitoring applications.

Jang et al. describe the synthesis of spinel-type  $\text{NiCo}_2\text{O}_4$  (NCO) nanostructures for glucose detection by post-heating at 450°C after a chemical bath technique (Jang et al. 2021). Its characteristics include a greater sensitivity of 146.27  $\mu\text{A}\cdot\text{mM}^{-1}\text{cm}^{-2}$  and a quick current response of 5 s, all within the linear range of 0.01-6 mM. Furthermore, NCO's excellent selectivity for glucose detection is shown by its exclusive oxidation reaction with glucose, indicating possible applications in clinical diabetes diagnosis and human health monitoring systems.

Thi Phong Thu et al. work aimed at developing a non-enzymatic glucose sensor, using NiO nanoflowers that were grown directly on a commercial pencil graphite electrode (Thi Phong Thu et al. 2024). A simple and inexpensive chemical process was used to deposit NiO materials on the electrode without the need for a binder. The electrode that was developed exhibited remarkable selectivity, LOD of 4  $\mu\text{M}$ , and a high sensitivity of 337  $\mu\text{A}\cdot\text{mM}^{-1}\text{cm}^{-2}$ . Moreover, the NiO/PGE sensor successfully measured the amounts of glucose in human serum samples, demonstrating its usefulness and dependability in clinical situations.

T. et al. synthesized  $\text{CeO}_2@\text{CuO}$  core-shell nanostructures (CeCCS NSs) were utilized to develop a fourth-generation glucose biosensor (T. et al. 2018). To evaluate the conductivity and catalytic activity of CeCCS NSs toward glucose sensing, SPEs were employed. The CeCCS/SPE modified electrode, optimized at a potential of 0.4 V, showed a sensitivity of 3319.83  $\mu\text{A}\cdot\text{mM}^{-1}\text{cm}^{-2}$  and LOD of 0.019  $\mu\text{M}$ , according to amperometric measurements.

## 2.2 Cholesterol Biosensor Utilizing Metal Oxide-Based Materials

Recent developments in electrode materials, notably in metal and metal oxide nanostructures like ZnO, TiO<sub>2</sub>, WO<sub>3</sub>, SnO<sub>2</sub>, and Co<sub>3</sub>O<sub>4</sub>, have contributed to the development of effective and trustworthy cholesterol non-enzymatic biosensors. Numerous technological benefits are provided by these electrodes based on nanostructures, such as a high surface-to-volume ratio, more active sites, fast charge transfer rates, and improved electrochemical characteristics at the nanoscale. They are very competitive materials for biosensing applications because of their morphological versatility, chemical stability, and possibility for composite constructions. Typically, polymer binders are used to immobilize electrochemically active molecules onto the working electrode in cholesterol sensor composition (Ahmad et al. 2022).

Khaliq et al. used titanium (Ti) foil anodization to develop TiO<sub>2</sub> nanotubes (TNTs), which were then coated with Cu<sub>2</sub>O NPs using chemical bath deposition (Khaliq et al. 2020). In comparison to pristine electrodes, the hybrid electrode showed a remarkable sensitivity of 6034.04  $\mu\text{A}\cdot\text{mM}^{-1}\cdot\text{cm}^{-2}$ , LOD of 0.05  $\mu\text{M}$ , and a response reaction time of 3 s. Furthermore, the activity of the developed biosensor compared to commercially available cholesterol biosensors, real-time measurement of cholesterol in human blood serum showed good accuracy.

Anh et al. synthesized a highly sensitive nonenzymatic biosensor for detecting cholesterol concentrations using ZnO nanorods (NRs) was developed (Anh et al. 2018). With the addition of Ag nanoparticles (AgNPs) to the ZnO-NRs structure, the biosensor's sensitivity increased to 135.5  $\mu\text{A}\cdot\text{mM}^{-1}\cdot\text{cm}^{-2}$  from 4.2  $\mu\text{A}\cdot\text{mM}^{-1}\cdot\text{cm}^{-2}$ , and the LOD to 0.184 mM from 1.78 mM. The biosensor showed a linear response range of 1-9 mM. Investigations into the biosensor's repeatability, stability, and reusability further highlighted its potential for useful applications in the monitoring of cholesterol in-home care and clinical settings.

Alam et al. developed a cholesterol sensor using a GCE coated with ternary low-dimensional ZnO/SnO<sub>2</sub>/RuO<sub>2</sub> NMs is the main objective of this electrochemical investigation (Alam et al. 2021). The sensitivity was found to be 11.3513  $\mu\text{A}\cdot\mu\text{M}^{-1}\cdot\text{cm}^{-2}$  based on the slope of the calibration curve, and the linear range was 0.1 nM - 0.01

mM. The lowest LOD was found to be  $91.42 \pm 4.57$  pM based on a S/N=3. Real-sample detection revealed the fabricated cholesterol sensor's good reproducibility, fast response time, and ability to perform over extended sensor elapse time.

Nagarajan et al. for the objective of non-enzymatic electrochemical cholesterol detection in this study, a GCE was modified with an Au@NiO decorated polypyrrole nanocomposite (Au@NiO/PPy-GCE) (Nagarajan et al. 2023). The results showed a sensitivity of  $7.6 \mu\text{A}\cdot\text{mM}^{-1}\text{cm}^{-2}$  and LOD of  $5.8 \times 10^{-7}$  M. Interestingly, a linear detection range was found, ranging from  $1.0 \times 10^{-5}$ - $1.0 \times 10^{-4}$  M. As such, this composite material exhibits great potential for a variety of practical applications in the development of industrial sensors.

Rengaraj et al. a novel non-enzymatic cholesterol sensor developed using a composite material consisting of high-quality graphene and nickel oxide (Rengaraj et al. 2015). Electrochemical analyses of the sensor revealed a notable sensitivity of  $40.6 \text{mA}\cdot\mu\text{M}^{-1}\text{cm}^{-2}$ , a fast response time of 5 s, and LOD of 0.13  $\mu\text{M}$  for cholesterol detection. The composite electrode demonstrated robust cholesterol detection capabilities, with good reproducibility and long-term stability, due to the synergistic interactions between NiO and graphene.

Umar et al. synthesized Bismuth subcarbonate ( $\text{Bi}_2\text{O}_2\text{CO}_3$ ) nanoplates that were produced at low temperatures by means of a simple hydrothermal process (Umar et al. 2016). The resultant biosensors showed remarkable characteristics, such as LOD of 10 mM for cholesterol sensing, a wide linear detection range spanning from 0.05-7.4 mM, and a sensitivity of  $139.5 \mu\text{A}\cdot\text{Mm}^{-1}\text{cm}^{-2}$ . The biosensors also demonstrated a rapid response time of 4 s. The biosensor also demonstrated strong anti-interference properties, repeatability, and long-term stability, highlighting its potential for real-world uses.

Waleed et al. developed  $\text{Co}_3\text{O}_4$  nanosheets loaded with different concentrations of CdS NPs were prepared using a modified SILAR approach in combination with a hydrothermal procedure (Waleed et al. 2024).  $\text{Co}_3\text{O}_4$ @CdS-3 exhibited remarkable sensing capacities for cholesterol throughout an extensive linear range of 250-5000  $\mu\text{M}$ . This electrode was noteworthy for its very high sensitivity of  $13564.8 \mu\text{A}\cdot\text{mM}^{-1}\text{cm}^{-2}$ ,

which outperformed earlier nanomaterial-based, non-enzymatic cholesterol biosensors. Additionally, it demonstrated a remarkable sensitivity for the detection of cholesterol in real samples, suggesting that it could potentially have beneficial applications.

Ghorui et al. synthesized  $\text{WO}_3$  nanoflakes were deposited on hexagon-shaped ZnO nanoplates to develop a composite film ( $\text{ZnO}/\text{WO}_3$ ) using a basic galvanic deposition process (Ghorui et al. 2023). At the electrode surface, this biosensor demonstrated a remarkable sensitivity of  $176.6 \mu\text{A}\cdot\text{cm}^{-2}\cdot\text{mM}^{-1}$  and LOD of 5.5 nM. High selectivity, long-term stability, repeatability, and reproducibility were all displayed by the biosensor, indicating that it may be used with real blood samples for clinical diagnosis.

$\text{SnO}_2$ -PANI nanocomposite was synthesized by in situ chemical polymerization of aniline with ammonium persulfate functioning as the oxidizing agent (Singh et al. 2023). With LOD of 0.25  $\mu\text{M}$  (S/N=3) and a sensitivity of  $300 \mu\text{A}\cdot\text{Mm}^{-1}\cdot\text{cm}^{-2}$ , the resultant  $\text{SnO}_2$ -PANI/NF sensor showed a linear detection range of 1-100  $\mu\text{M}$  for cholesterol.  $\text{SnO}_2$ -PANI has the potential to be a flexible platform for a range of electrochemical-based bioanalytical applications, as demonstrated by the sensor's good selectivity and accuracy in determining the concentration of Cholesterol in mimicked blood serum samples.

$\text{MnO}_2$  was electrochemically deposited on a graphene-coated Pencil Graphite Electrode to develop an electrochemical sensor for measuring cholesterol (Rison et al. 2020). The linear dynamic range for determining cholesterol under optimal conditions was found to be  $12\times 10^{-10}$  -  $240\times 10^{-10}$  M. The technique's remarkable ultralow LOD of 0.42 nM highlighted its exceptional sensitivity. The achievement of ultralow levels of cholesterol determination in human blood samples by non-enzymatic means provided additional evidence of the effectiveness of the built technology.

### **2.3 Scope of the Work**

In the application of non-enzymatic biosensors aimed at identifying important analytes such as glucose and cholesterol, metal oxides have several functions that are essential to the overall performance of the sensors. Metal oxides play a key role in these biosensors because of their catalytic activity, which allows target analytes to be directly

detected electrochemically without the need for enzyme mediation. This catalytic ability is especially useful since it lowers related expenses and simplifies sensor design.

In addition, metal oxides have a remarkable surface-to-volume ratio and offer a wide range of active sites for analyte adsorption and subsequent electron transfer, particularly when designed at the nanoscale (Ratnam et al. 2020). Because of its increased surface area, the biosensor is more sensitive and can detect even minute levels of the target analyte. Furthermore, by functionalizing or doping metal oxides, one may modify their ability to interact with certain molecules, improving the selectivity of the biosensor and reducing interference from other elements found in complicated biological media.

Metal oxides contribute to the stability and longevity of the biosensor in addition to their catalytic and selectivity-enhancing qualities. They provide chemical and mechanical resistance, protecting the sensor interaction from degradation and ensuring steady performance even after frequent usage. Moreover, metal oxide-based non-enzymatic biosensors can be easily incorporated into portable point-of-care systems due to their compatibility with microfabrication processes. Due to their compactness, biosensors are currently able to be readily analyzed on-site, making them essential instruments for rapid diagnosis in a variety of environmental and biological settings. Fundamentally, metal oxides are adaptable and essential parts of the design of non-enzymatic biosensors, and they are essential to extending the boundaries of biosensing technology (Malhotra and Ali 2018).

## **2.4 Objectives**

In the current chapters, we aim to achieve the following objectives:

- i.** To synthesize metal oxide/ doped-metal oxide/ metal oxide nanocomposite via hydrothermal or co-precipitation method.
- ii.** To characterize the synthesized nanoparticles to ascertain their chemical and structural composition utilizing appropriate techniques, including XRD, XPS, FE-SEM, HR-TEM, UV-Vis spectroscopy, PL study, and Raman spectroscopy.
- iii.** To assemble the electrochemical cell utilizing the synthesized active electrode materials to facilitate electrochemical analysis.

- iv. To investigate the constructed electrode for detecting biologically active molecules such as Glucose and Cholesterol.
- v. To investigate the capability to detect analytes in real samples collected in compliance with ethical standards.

\*\*\*\*\*

## **CHAPTER 3**

---

### **EXPERIMENTAL PROCEDURES AND METHODOLOGY**

---



---

---

***Abstract:** Chapter 3 describes the chemicals employed, electrode fabrications, and tools used in this research*

---

---

### **3.1 Chemical reagents**

Loba supplied the following chemicals (AR grade): Potassium chloride (KCl), Sodium chloride (NaCl), dopamine (C<sub>8</sub>H<sub>11</sub>NO<sub>2</sub>) (DP), Uric Acid (C<sub>5</sub>H<sub>4</sub>N<sub>4</sub>O<sub>3</sub>) (UA), N-methyl pyrrolidone (NMP), Cholesterol (C<sub>27</sub>H<sub>46</sub>O), and Ascorbic Acid (C<sub>6</sub>H<sub>8</sub>O<sub>6</sub>) (AA). D-glucose (C<sub>6</sub>H<sub>12</sub>O<sub>6</sub>), Triton X 100 and Polyvinylidene fluoride (PVDF) were purchased from Sigma. We purchased a 0.5 mm thick piece of nickel foam (NF) from Global Nanotech in Mumbai. Each solution was made using ultrapure Milli-Q water (18.2 MΩ). Due to the high purity of the ingredients used, further purification procedures were not performed.

### **3.2 Real-Time Samples**

According to the study protocol sanctioned by the Ethical Committee of the National Institute of Technology Karnataka, Surathkal (Reference No. NITK/Bioethics/2023/02 dated 24/04/2023), blood serum samples were voluntarily donated by consenting patients for the purpose of this research. To verify the concentrations of the analytes, commercially available biosensors were utilized. The analytical performance of these commercial biosensors was subsequently compared to that of the electrodes developed in our investigation.

### **3.3 Preparation of Nickel Foam for Fabrication**

The nickel foam, cut into dimensions of 3x1 cm<sup>2</sup>, underwent a meticulous cleaning protocol prior to fabrication. Initially, the foam was immersed in a 3 N HCl solution, followed by sequential immersion in acetone and distilled water. Each immersion step was accompanied by sonication for a duration of five minutes to ensure thorough cleaning. After the three-step cleaning process, the foam was dried in an oven at 90°C.

A predetermined quantity of synthesized material was mixed in a 9:1 ratio with PVDF binder and then mixed with NMP until homogeneity was achieved, resulting in a uniform paste. Following that, the final paste was coated over a 1 cm<sup>2</sup>

area of NF. Following application, the electrode was allowed to dry at 80°C for 24 hr. It was determined that the loading capacity was 10±0.2 mg.

### 3.4 Preparation of Glucose Stock Solution

To prepare the glucose stock solution, 18 mg of glucose was dissolved in 50 mL of standard flask water and then filled up to the mark. Subsequently, the stock solution was kept at 4°C and used as needed.

### 3.5 Preparation of Cholesterol Stock Solution

To make the cholesterol stock solution, dissolve 0.040 g of cholesterol in 1 mL of Triton X 100 and heat it to 60°C while stirring constantly. The 0.1 M KOH solution was then added in an amount of 9 mL. Following that, the stock solution was kept at 4°C and subsequently diluted with KOH to get the desired range of cholesterol concentrations.

### 3.6 Electrochemical Characterization

The electrochemical studies were performed for coated electrodes using an Autolab PGSTAT204 electrochemical workstation. The electrochemical cell was constructed using three electrode system having modified nickel foam as the working electrode, platinum foil (Pt) as the counter electrode, and Ag/AgCl electrode with the ceramic frit as a reference electrode with 0.1 M KOH as a supporting electrolyte. The entire experimental part was carried out with stirring conditions and without purging any inert gases. The data obtained here are not iR compensated. The CV studies were carried out with a potential range for all the modified electrodes with different scan rates from 5-120 mV/s. The CA study was conducted by applying peak potential within a certain period. The DPV was performed with the applied potential with a scan rate of 5 mV/s and pulse amplitude of 50 mV. The Electrochemical Impedance Spectra (EIS) was carried out with the frequency range of 1-1000 kHz at zero-bias voltage. Electrochemical Active Surface Area (ECAS) was carried out for different scan rates from 5-120 mV/s. The double-layer capacitance ( $C_{dl}$ ) was calculated by plotting  $\Delta j = j_a - j_c$  vs. scan rate, half the slope is equivalent to the  $C_{dl}$  value (Kim et al. 2020). Further, the real surface area is calculated using the formula  $C_{dl}/C_s$ , where  $C_s$  is capacitance of

an automatically smooth surface ( $40 \mu\text{F}\cdot\text{cm}^{-2}$ ) (Junita et al. 2023). The sensitivity calculated with the calibration curve vs. concentration graph is given as;

$$\text{Sensitivity} = \frac{\text{Slope of the calibration curve}}{\text{Surface area}} \quad (3.1)$$

LOD and LOQ are calculated using the formula;

$$\text{LOD} = \frac{3 \times \text{Standard deviation}}{\text{Slope of the calibration curve}} \quad (3.2)$$

$$\text{LOQ} = \frac{10 \times \text{Standard deviation}}{\text{Slope of the calibration curve}} \quad (3.3)$$

### 3.7 Characterization Techniques

Understanding the structural, morphological, and chemical characteristics of biosensor materials is essential, as these attributes directly impact their functionality and performance. Researchers can gain profound insights into the composition, surface chemistry, electronic structure, and other critical properties of biosensor materials by employing a comprehensive array of advanced characterization techniques. These techniques, encompassing spectroscopy, diffraction, and microscopy, each provide complementary and distinct insights into the biosensors, thereby facilitating a thorough evaluation and optimization of their performance.

- a) **Field Emission Scanning Electron Microscopy (FE-SEM):** Field Emission Scanning Electron Microscopy (FE-SEM) was employed to investigate the morphology and topography of the synthesized material using a Carl Zeiss instrument (USA). The sample was meticulously prepared, mounted on a conductive substrate, and coated with gold or carbon to enhance conductivity. Following calibration, multiple regions were scanned to acquire high-resolution images, which were subsequently analyzed to determine particle size, shape, surface texture, and distribution.
- b) **Energy-dispersive X-ray spectroscopy (EDS):** Energy-dispersive X-ray Spectroscopy (EDS) was utilized to ascertain the elemental composition and distribution within the synthesized materials, employing a Nano XFlash

Detector from BRUKER (Germany). This technique involves bombarding the sample with an electron beam in a Scanning Electron Microscope (SEM), inducing the emission of characteristic X-rays. These X-rays were then detected and analyzed to reveal the material's elemental composition.

- c) **X-ray diffraction (XRD):** X-ray Diffraction (XRD) was employed to analyze the phase composition and crystalline structure of materials using the Rigaku Miniflex 600 instrument. This technique involves exposing the sample to X-rays to measure the diffraction pattern, which reveals information about the atomic arrangement and crystallographic phases present. The experimental process included preparing the sample as a thin film or powder, positioning it in the X-ray beam path, and analyzing the resultant diffraction pattern using specialized software to identify crystallographic phases and extract structural parameters such as lattice constants and grain size.
- d) **High-Resolution Transmission Electron Microscopy (HR-TEM):** High-Resolution Transmission Electron Microscopy (HR-TEM), specifically utilizing the Jeol JM 2100 model in this study, enabled a detailed examination of nanomaterials, elucidating their morphology, crystal structure, and atomic-scale defects. This technique involved the preparation of ultrathin, electron-transparent samples subjected to a focused electron beam. Analysis of the transmitted electrons yielded high-resolution images that unveiled precise structural characteristics at the atomic level. HR-TEM played a pivotal role in comprehending essential properties of nanomaterials, crucial for advancing scientific and technological applications.
- e) **X-ray photoelectron spectroscopy (XPS):** X-ray Photoelectron Spectroscopy (XPS), utilizing the Thermo Fischer Scientific ESCALAB Xi+, was employed to analyze the elemental composition, chemical bonding, and electronic state of material surfaces. This technique involves X-ray irradiation to induce photoelectron emission, which is then analyzed by kinetic energy to determine surface elemental composition and chemical states. XPS provided crucial insights into surface chemistry, facilitating understanding of reactions, oxidation states, and compositional dynamics with exceptional sensitivity and resolution.

- f) Lambda 950 UV-Vis spectrometer:** The Lambda 950 UV-Vis spectrometer was utilized to investigate the electronic structure and purity of substances through their absorption of ultraviolet and visible light. This involved preparing samples, measuring absorbance spectra from 190 to 1100 nm, and analyzing electronic transitions, concentration, and optical properties.
- g) Photoluminescence (PL) spectroscopy:** Photoluminescence (PL) spectroscopy examined material energy band structures, electronic configurations, and defects by exposing them to specific wavelength light, often from lasers or filtered lamps. This excitation caused electrons to transition to higher energy states, emitting photons that revealed details about electronic transitions, band gaps, and structural imperfections such as vacancies or impurities. The Fluoromax-4 TCSPC spectrophotometer by Horiba Jobin Yvon was used for precise PL measurements.
- h) Raman spectroscopy (Renishaw Raman spectrometer):** The Renishaw Raman spectrometer was employed to analyze molecular composition, chemical bonding, and crystal structure through the measurement of inelastic scattering of monochromatic light. This technique involved illuminating the sample with a laser beam and analyzing the scattered light to identify unique vibrational modes associated with various molecular structures. These analyses provided critical insights into the chemical composition and structural properties of the materials studied.
- i) Liquid Chromatography-Mass Spectrometry (LC-MS):** Liquid Chromatography-Mass Spectrometry (LC-MS) enabled the thorough analysis of polar and non-polar compounds through chromatographic separation, ionization, and precise mass-to-charge ratio detection. The Xevo QToF system from Waters, USA, employed in this research, ensured high-resolution mass analysis for accurate compound identification and quantification.

The fabrication of electrodes and the assessment of biosensing activity require precise chemical reagents and preparation methods. These are crucial for improving the performance and sensitivity of biosensors. Additionally, meticulous preparation

of analyte solutions is essential for accurate biosensor evaluation, collectively enhancing sensor efficacy.

\*\*\*\*\*

## CHAPTER 4

---

---

**SYNTHESIS OF MESOPOROUS  $M_xTi_{1-x}O_2$  (M=V, Ni, OR Co)  
(x=0.00, 0.01, 0.02, OR 0.03) AS AN EFFECTIVE  
ELECTROCHEMICAL NON-ENZYMATIC BLOOD GLUCOSE  
SENSOR**

---

---



---

---

**Abstract:** *The synthesis of  $M_xTi_{1-x}O_2$  ( $M = \text{Vanadium, Nickel, or Cobalt}$ ) with different doping levels ( $x=0.00, 0.01, 0.02, \text{ or } 0.03$ ) is described in detail in this chapter along with a comprehensive characterization that is intended to make the electrochemical detection of glucose levels in human serum simpler.*

---

---

## 4.1 Introduction

The International Diabetes Federation (IDF) lists lack of insulin and hyperglycemia as two of the top 10 deadly conditions in the world for diabetes mellitus. It is the most common chronic disease and has a high risk of cardiovascular consequences, kidney problems, retinal vascular diseases, and peripheral neuropathy, among other health issues. According to recent statistics, diabetes is projected to be the cause of over 4 million deaths worldwide, with 300 million people expected to be impacted by the disease by 2045. The significant financial cost of USD 727 billion in 2017 emphasizes the significance of regularly monitoring and controlling blood glucose levels, which may be made easier with the use of electrochemical glucose sensors, to reduce the health risks related to diabetes (Chiu et al. 2021; Fox 2004; Wang 2008).

In recent years, glucose sensors incorporated with nanomaterials helped in the enhancement of electron transfer, where the nanomaterials can be mono-metallic (Luo et al. 2012; Ye et al. 2015), bi-metallic (Karimi-Maleh et al. 2020; Li et al. 2015), metal oxide (MO) based (Guo et al. 2013; Liu et al. 2013; Qi et al. 2022; Tian et al. 2018; Zhuang et al. 2008), mixed M-M based nanomaterials (Chiu et al. 2020; Ding et al. 2010; Su et al. 2018; Zheng et al. 2014). These nanomaterials have a larger surface area and some of the important physical properties that help to increase the efficiency of the sensor such as sensitivity, response time, and accuracy. Especially, transition metals like Ni, Co, Cu, Au, and metal-oxides help to detect glucose as they help in the oxidation of glucose (Duan et al. 2019; Prasad et al. 2015b; Sehit and Altintas 2020).

Few research has been conducted to study the catalytic nature of  $TiO_2$  by embracing metal oxides, metals and it is used as it has a metal-semiconductor property with low cost, innocuous, and biocompatible nature (Schneider et al. 2014; Si et al. 2011). It has

a larger surface area and higher active sites which makes this material suitable for biosensing, with the properties of porosity, crystalline nature, the morphology of the material, and depends on dopant elements used for doping TiO<sub>2</sub>. Importantly, the usage of pure TiO<sub>2</sub> is restricted due to the wide band gap (3.2 eV), which will obstruct the rapid electrochemical response to the analyte. Thus, the incorporation of the metal dopant will make the TiO<sub>2</sub> inspect rapid electrochemical response (Rajendran et al. 2018).

Here, vanadium, nickel, and cobalt have been incorporated into TiO<sub>2</sub> in varied molar ratios as the three distinct dopants respectively. To discover more about each material's electrocatalytic properties, it is all coated on the NF. The best material is then subjected to further electrochemical testing for its biosensing capacity toward glucose utilizing CV, CA, and DPV. In the meanwhile, we additionally looked at material choice using a Density Functional Theory (DFT) approach. The results of the model, which were in agreement with the experimental data, indicated the charge transfer of the D-Glucose adsorbed on the material surface. Actual blood glucose samples will also be evaluated in the content.

## **4.2 Experimental Section**

### **4.2.1 Chemical Reagents**

Titanium isopropoxide (TIP), Vanadium (III) chloride (VCl<sub>3</sub>), and Cobalt (II) chloride hexahydrate (CoCl<sub>2</sub>.6H<sub>2</sub>O) were purchased from Sigma. Nickel chloride hexahydrate (NiCl<sub>2</sub>.6H<sub>2</sub>O), isopropyl alcohol (IPA), and Acetic acid (CH<sub>3</sub>COOH) was purchased from Loba.

#### 4.2.2 Synthesis of $M_xTi_{1-x}O_2$ ( $x = 0.00, 0.01, 0.02, 0.03$ ) Nanoparticles

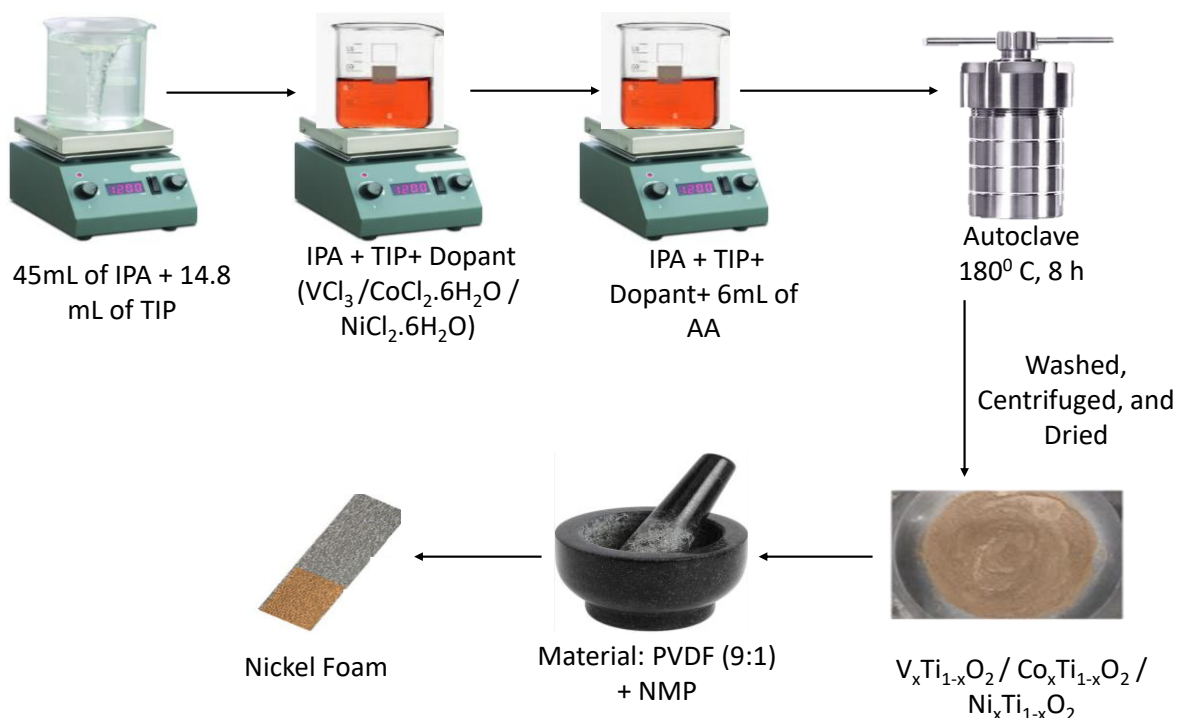


**Figure 4.1.** Schematic diagram of the synthesis of the  $TiO_2 / V_xTi_{1-x}O_2 / Co_xTi_{1-x}O_2 / Ni_xTi_{1-x}O_2$

$M_xTi_{1-x}O_2$  ( $M=V, Ni, Co$ ) ( $x = 0.00, 0.01, 0.02, 0.03$ ) nanoparticles were synthesized by incorporating a specified amount of the precursor Titanium Isopropoxide (TIP) into 50 mL of an IPA solution and stirred for 10 min. The dopants  $VCl_3$ ,  $CoCl_2 \cdot 6H_2O$ , and  $NiCl_2 \cdot 6H_2O$ , respectively, were calculated in considerable molar concentration (i.e.,  $x=0.01, 0.02$ , and  $0.03$ ) and dissolved in a known volume of diluted HCl (0.01 M). To synthesize the corresponding  $M_xTi_{1-x}O_2$ , each dopant solution was individually added to the aforementioned TIP solution and agitated for 10 min.  $TiO_2$  is prepared using a similar process without the addition of any dopants. To regulate the hydrolysis, a known volume of  $CH_3COOH$  acid was added dropwise, and the mixture was rapidly agitated for 2 h. The obtained solution is then placed in a 100 mL autoclave and heated at  $180^\circ C$  for 8 h. The resulting materials were washed twice with ethanol and Milli-Q water and dried at  $80^\circ C$  for 36 h. The dried materials were ground to a fine powder and then employed for further investigation. **Fig 4.1** represents the schematic diagram of the synthesis of  $TiO_2 / V_xTi_{1-x}O_2 / Co_xTi_{1-x}O_2 / Ni_xTi_{1-x}O_2$ .

### **4.2.3 First Principle Study (Density Functional Theory)**

In this study, we focused on the tetragonal crystallographic structure of anatase with a space group of I41/amd and lattice parameters of  $a = b = 3.785\text{\AA}$  and  $c = 9.514\text{\AA}$ . The surface under investigation was derived from the anatase crystallographic structure through cleavage. To delve into its properties, we conducted Density Functional Theory (DFT) calculations on a basal (3x3) supercell of the anatase (1 0 1) slab, comprising four O-Ti-O trilayers. Our computational work was carried out using Material Studio 20.1.0, specifically the Forcite tool. For structural optimization, we employed a sophisticated algorithm along with the COMPASS force field and the Ewald summation method. Subsequently, we conducted adsorption studies using the Adsorption Locator tool of Material Studio 20.1.0.

## 4.3 Results and Discussion

### 4.3.1 X-ray diffraction (XRD) Analysis

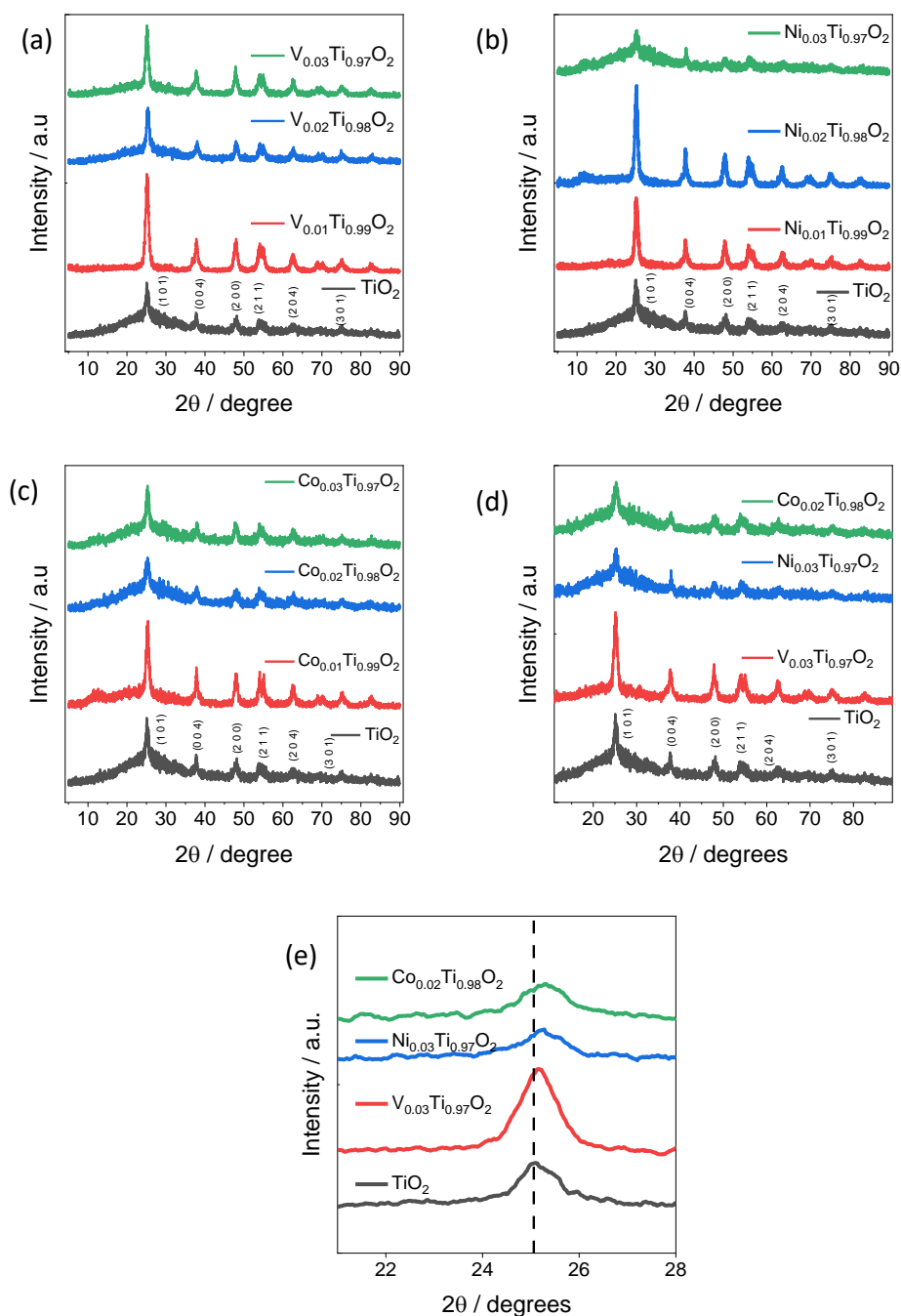


**Figure 4.2.** XRD analysis of (a)  $V_xTi_{1-x}O_2$ ; (b)  $Ni_xTi_{1-x}O_2$ ; (c)  $Co_xTi_{1-x}O_2$ ; (d) XRD analysis of  $TiO_2$ ,  $V_{0.03}Ti_{0.97}O_2$ ,  $Ni_{0.03}Ti_{0.97}O_2$ , and  $Co_{0.02}Ti_{0.98}O_2$ ; (e) XRD (101) peak shift towards higher diffraction angle with different dopants.

The structure and phase purity of each produced  $M_xTi_{1-x}O_2$  ( $M=V, Ni, Co, x=0.00, 0.01, 0.02, 0.03$ ) material were determined by the XRD analysis, as shown in **Fig 4.2 (a-c)**. From XRD, the anatase phase with a tetragonal structure of both doped and undoped  $TiO_2$  is well matched with the JCPDS number 71-1168. V, Ni, and Co ions were incorporated into  $TiO_2$  without affecting the material's composition as there is no impurity peaks observed as all of the dopants' ionic radii are equal to those of the Ti ion and may readily replace the Ti ion when doped into a  $TiO_2$  lattice.

As shown in **Fig 4.2 (d-e)** all selected best materials  $V_{0.03}Ti_{0.97}O_2$ ,  $Ni_{0.03}Ti_{0.97}O_2$ , and  $Co_{0.02}Ti_{0.98}O_2$  subjected to XRD investigation exhibit a minor shift in the diffraction peak to the higher diffraction angle and a change in peak intensity reflecting the confirmation of doping in their respective hosts. This result is further substantiated in **Fig 4.3 (e)**. The increased crystalline nature of the substance, as seen in **Table 4.1**, causes further defects in the  $TiO_2$  structure that aid in increasing the electron transfer rate, which explains the higher activity of  $V_{0.03}Ti_{0.97}O_2$ . Contrary to pure  $TiO_2$ , **Table 4.1** displays materials incorporating Ni/Co that have larger ionic radii (i.e., Ni = 0.69 Å, Co = 0.65 Å) than Ti (0.61 Å), which causes a difference in the lattice parameters owing to doping, but there is no variation in the crystalline structure.

**Table 4.1.** XRD Parameters and Crystalline size of the  $TiO_2$ , and doped  $TiO_2$ .

SAMPLES	a=b (Å)	c (Å)	D (nm)
$TiO_2$	3.795	9.528	9.104
$V_{0.03}Ti_{0.97}O_2$	3.833	9.398	9.469
$Ni_{0.03}Ti_{0.97}O_2$	3.800	12.99	7.823
$Co_{0.02}Ti_{0.98}O_2$	3.783	11.317	7.479

### 4.3.2 Cyclic Voltammetry (CV) Analysis

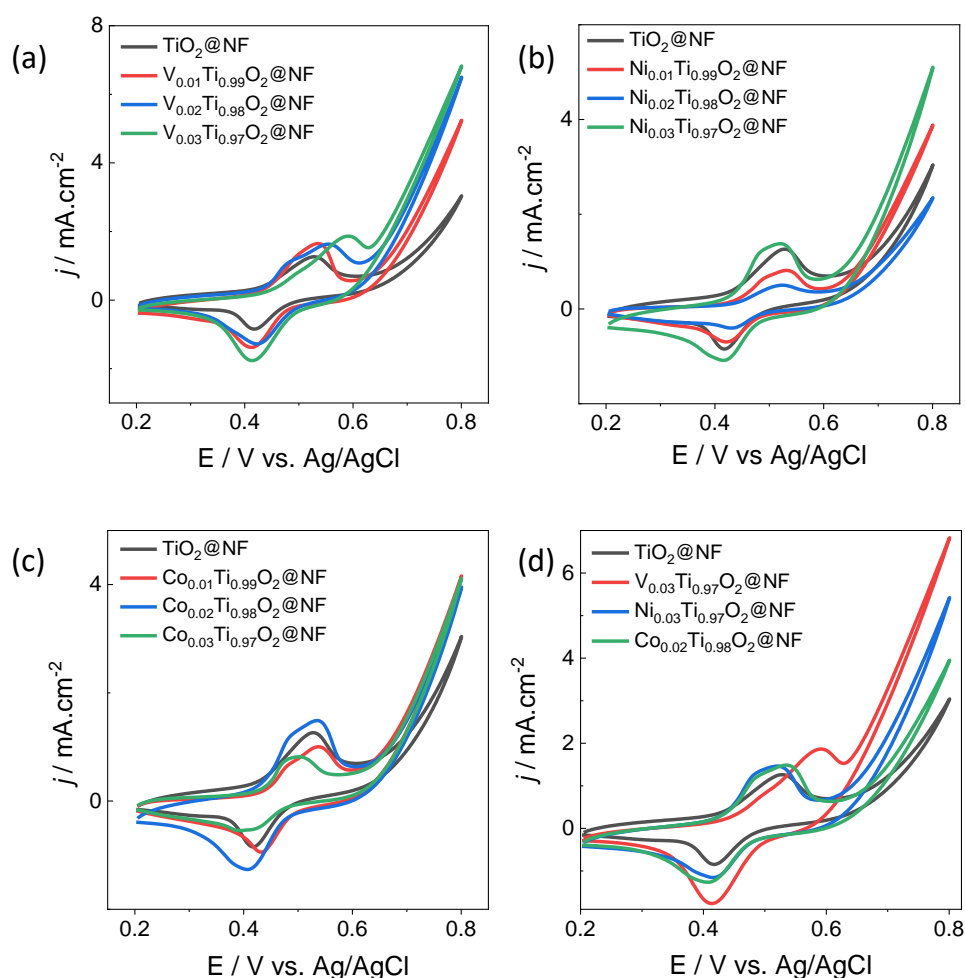


**Figure 4.3.** Cyclic voltammogram of (a)  $V_xTi_{1-x}O_2@NF$ ; (b)  $Ni_xTi_{1-x}O_2@NF$ ; (c)  $Co_xTi_{1-x}O_2@NF$  compared to  $TiO_2$  at a scan rate of 25 mV/s in 0.1 H KOH; (d) Comparison of cyclic voltammograms for  $V_{0.03}Ti_{0.97}O_2@NF$ ,  $Ni_{0.03}Ti_{0.97}O_2@NF$ , and  $Co_{0.02}Ti_{0.98}O_2@NF$ , demonstrating superior activity relative to pure  $TiO_2@NF$ .

The CV additionally worked to find the best active material in the potential window of 0.2-0.8 V vs Ag/AgCl at a scan rate of 25 mV/s for the coated  $TiO_2@NF$  and  $M_xTi_{1-x}O_2@NF$  as displayed in **Fig 4.3 (a-c)**, where  $V_{0.03}Ti_{0.97}O_2@NF$ ,  $Ni_{0.03}Ti_{0.97}O_2@NF$ , and  $Co_{0.02}Ti_{0.98}O_2@NF$ , were showing superior activity compared to all other varied molar concentration doped  $TiO_2@NF$  shown in **Fig 4.3 (d)**. According to the CV analysis,  $V_{0.03}Ti_{0.97}O_2@NF$  exhibits much greater anodic and cathodic peaks than pure  $TiO_2@NF$  and Ni/Co- $TiO_2$ .

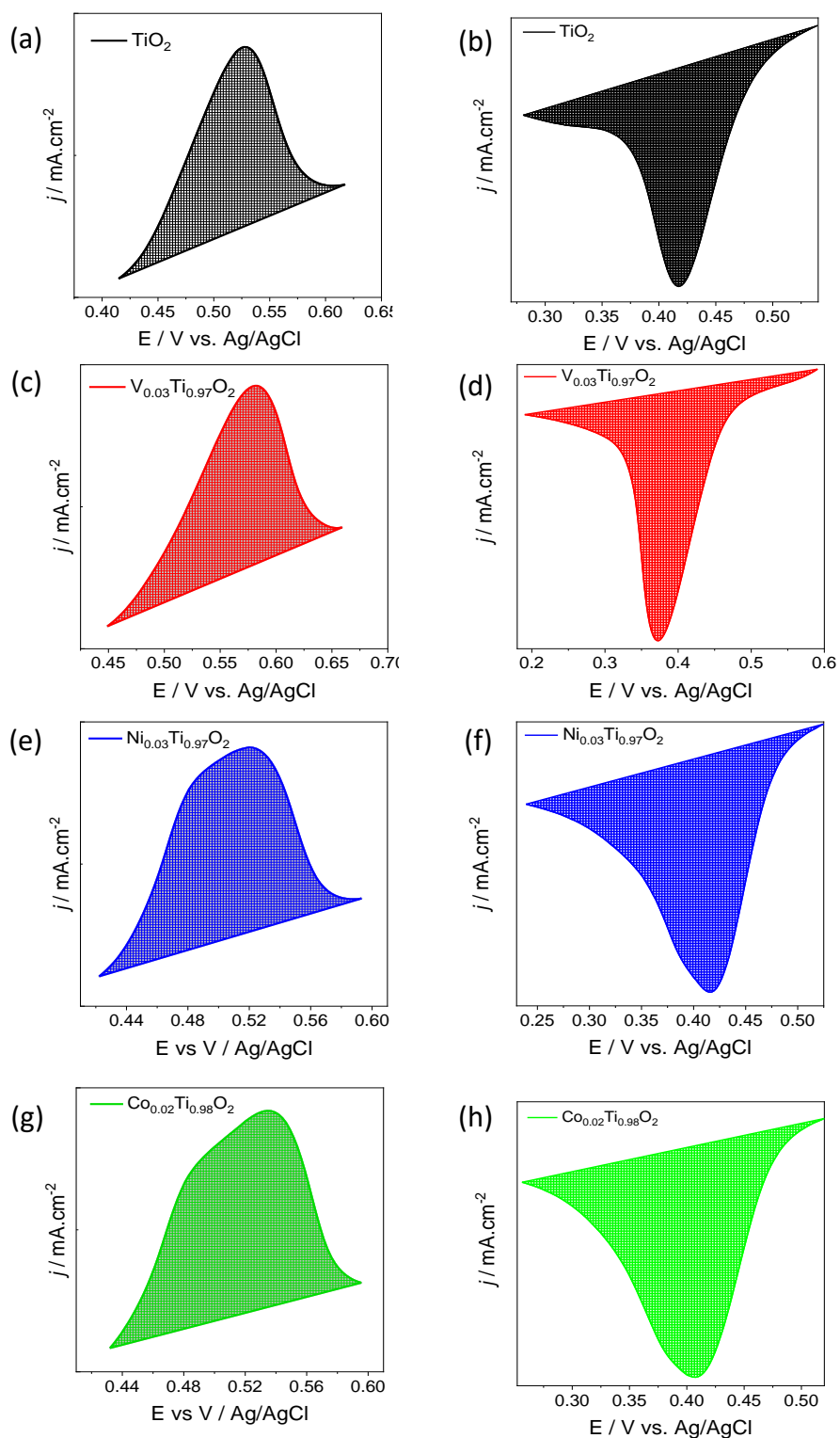


**Figure 4.4.** Redox peak study for the determination of the number of electrons of (a), (b)  $\text{TiO}_2@NF$ ; (c), (d)  $\text{V}_{0.03}\text{Ti}_{0.97}\text{O}_2@NF$ ; (e), (f)  $\text{Ni}_{0.03}\text{Ti}_{0.97}\text{O}_2@NF$ , and (g), (h)  $\text{Co}_{0.02}\text{Ti}_{0.98}\text{O}_2@NF$  at a scan rate of 25 mV/s.

An examination of surface-active sites using redox peak current data as shown in **Fig 4.4 (a–h)** supports the choice of  $V_{0.03}Ti_{0.97}O_2@NF$  as the best material. When the number of electrons transported in the oxidation and reduction peaks were computed,  $TiO_2@NF$ ,  $V_{0.03}Ti_{0.97}O_2@NF$ ,  $Ni_{0.03}Ti_{0.97}O_2@NF$ , and  $Co_{0.02}Ti_{0.98}O_2@NF$  resulted in values of  $1.59 \times 10^{19}$ ,  $5.0 \times 10^{19}$ ,  $2.17 \times 10^{19}$ , and  $2.24 \times 10^{19}$  for oxidation peak and  $0.775 \times 10^{19}$ ,  $4.26 \times 10^{19}$ ,  $1.19 \times 10^{19}$  and  $1.31 \times 10^{19}$  for reduction peak respectively. These numbers show that  $V_{0.03}Ti_{0.97}O_2@NF$  is the most efficient material since it has the largest electron transport in its anodic and cathodic peaks respectively.

### 4.3.3 Morphological Analysis

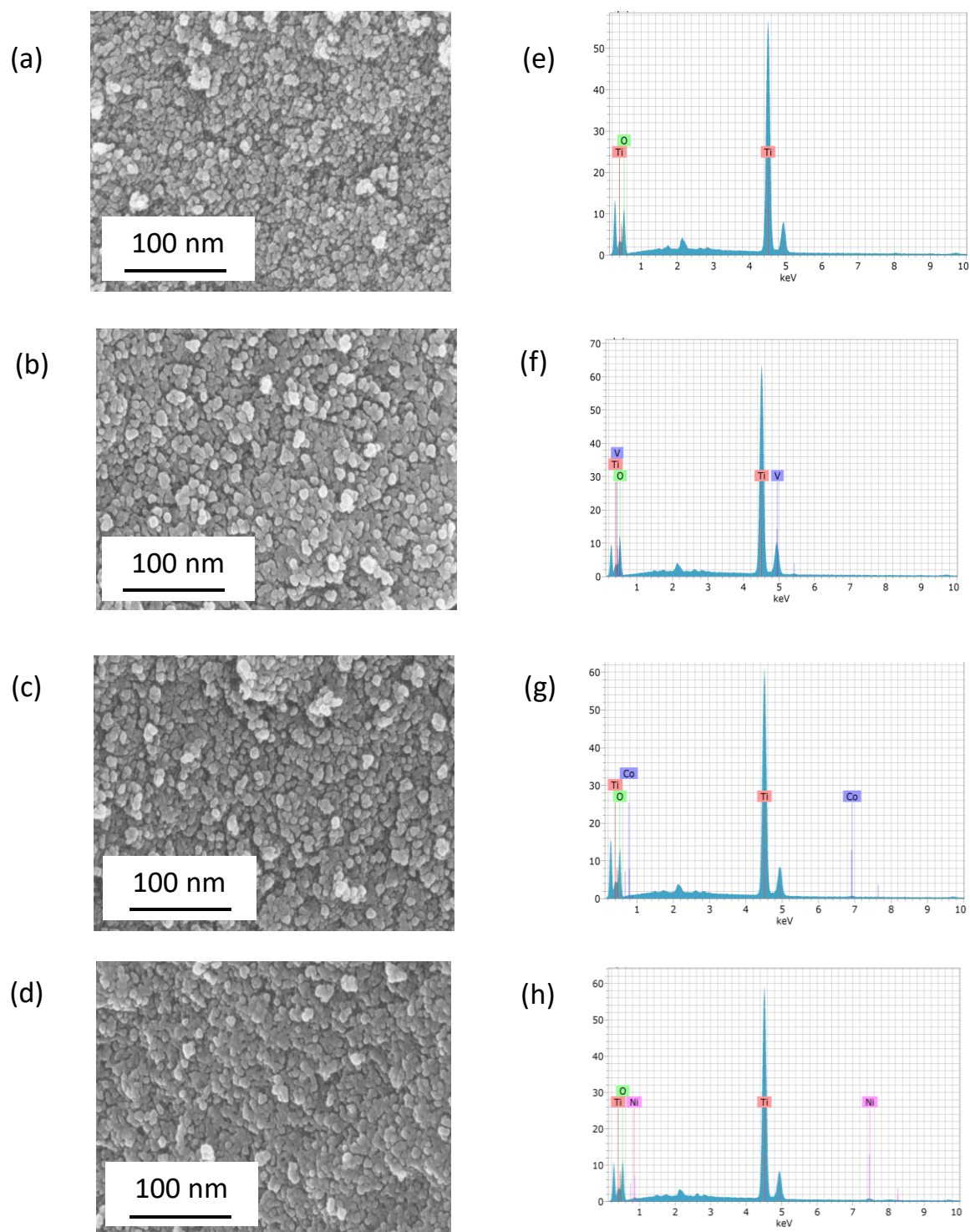


**Figure 4.5.** FE-SEM images (a)  $\text{TiO}_2$ ; (b)  $\text{V}_{0.03}\text{Ti}_{0.97}\text{O}_2$ ; (c)  $\text{Co}_{0.02}\text{Ti}_{0.98}\text{O}_2$ ; (d)  $\text{Ni}_{0.03}\text{Ti}_{0.97}\text{O}_2$ ; EDS images of (e)  $\text{TiO}_2$ ; (f)  $\text{V}_{0.03}\text{Ti}_{0.97}\text{O}_2$ ; (g)  $\text{Co}_{0.02}\text{Ti}_{0.98}\text{O}_2$ ; (h)  $\text{Ni}_{0.03}\text{Ti}_{0.97}\text{O}_2$ .

The morphological structures of  $\text{TiO}_2$ ,  $\text{V}_{0.03}\text{Ti}_{0.97}\text{O}_2$ ,  $\text{Co}_{0.02}\text{Ti}_{0.98}\text{O}_2$ , and  $\text{Ni}_{0.03}\text{Ti}_{0.97}\text{O}_2$  were analyzed using FE-SEM, as depicted in **Fig 4.5 (a-d)**.  $\text{TiO}_2$  exhibited a mesoporous morphology, which was largely retained upon the addition of V, Ni, and Co, with only minor variations in particle size and degree of agglomeration observed. EDS was employed to confirm the elemental composition of the samples. As shown in **Fig 4.5 (e-h)**, the presence of Ti and O in the pure  $\text{TiO}_2$  sample was verified, along with the successful incorporation of Co, Ni, and V as dopants in the  $\text{TiO}_2$  matrix, confirming effective doping.

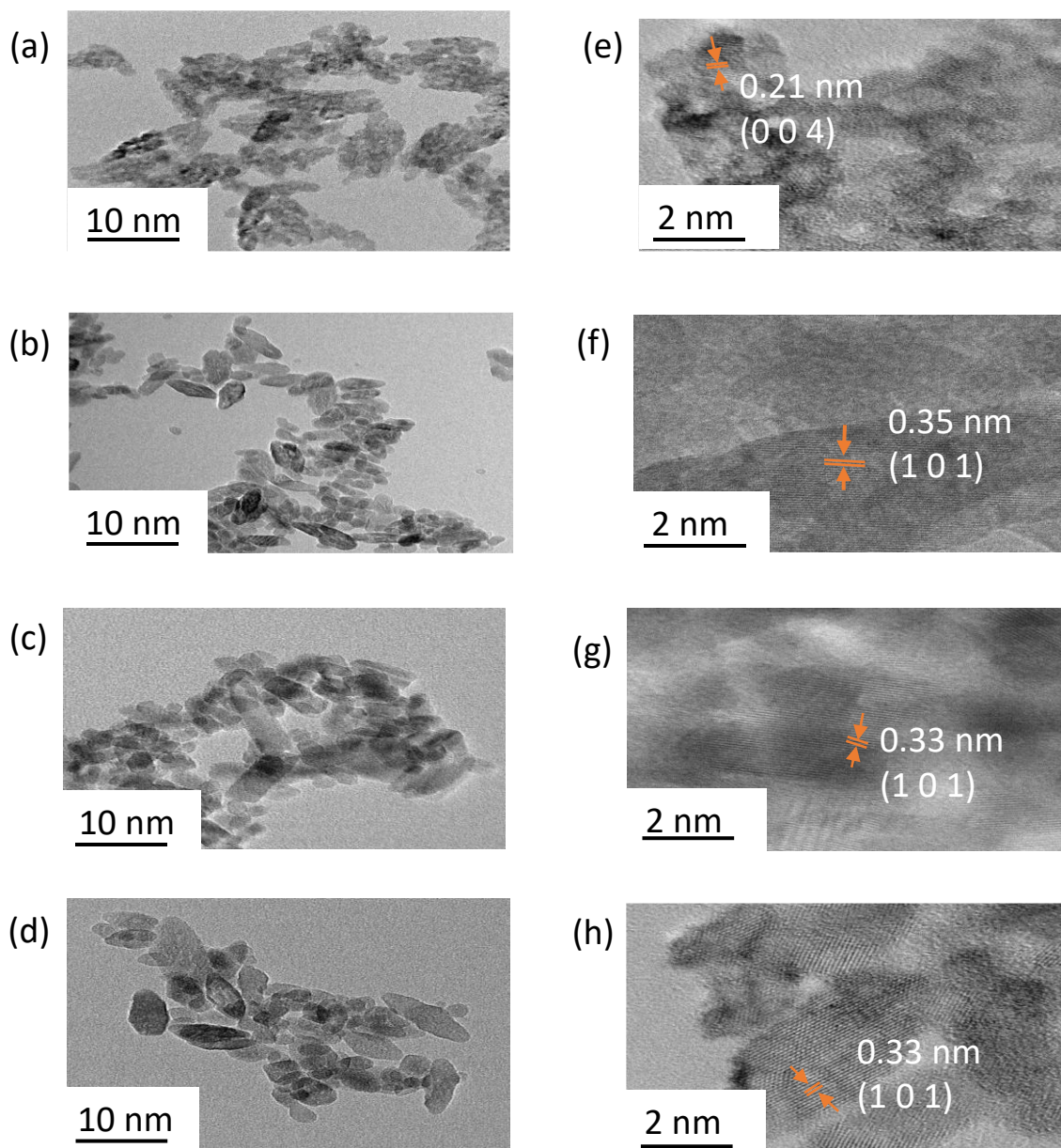


**Figure 4.6.** HR-TEM images (a), (e)  $\text{TiO}_2$ ; (b), (f)  $\text{V}_{0.03}\text{Ti}_{0.97}\text{O}_2$ ; (c) (g)  $\text{Co}_{0.02}\text{Ti}_{0.98}\text{O}_2$ ; (d), (h)  $\text{Ni}_{0.03}\text{Ti}_{0.97}\text{O}_2$ .

HR-TEM images of  $\text{TiO}_2$ ,  $\text{V}_{0.03}\text{Ti}_{0.97}\text{O}_2$ ,  $\text{Co}_{0.02}\text{Ti}_{0.98}\text{O}_2$ , and  $\text{Ni}_{0.03}\text{Ti}_{0.97}\text{O}_2$ , exhibiting uniform lattice fringes, are presented in **Fig 4.6 (a-h)**. It confirms the agglomerated particle distribution of all chosen materials as observed in FE-SEM. As per **Fig 4.7 (a-d)**, these material exhibits a mesoporous nature with an irregular spherical shape, ranging in diameter from 10 to 30 nm. HR-TEM reveals uniform fringes with a 0.21 nm spacing, corresponding to the (0 0 4) plane of  $\text{TiO}_2$ , as shown in **Fig 4.6 (e)**. The d-

spacing values determined from HR-TEM confirm the anatase phase with a tetragonal structure, matching JCPDS card no: 71-1168. Notably, for the dopant  $M_xTi_{1-x}O_2$  ( $M=V, Ni, Co$ ), uniform fringes with an approximate 0.3 nm spacing corresponding to the (1 0 1) plane of the anatase phase with the tetragonal structure are observed, indicating the retention of the host material.

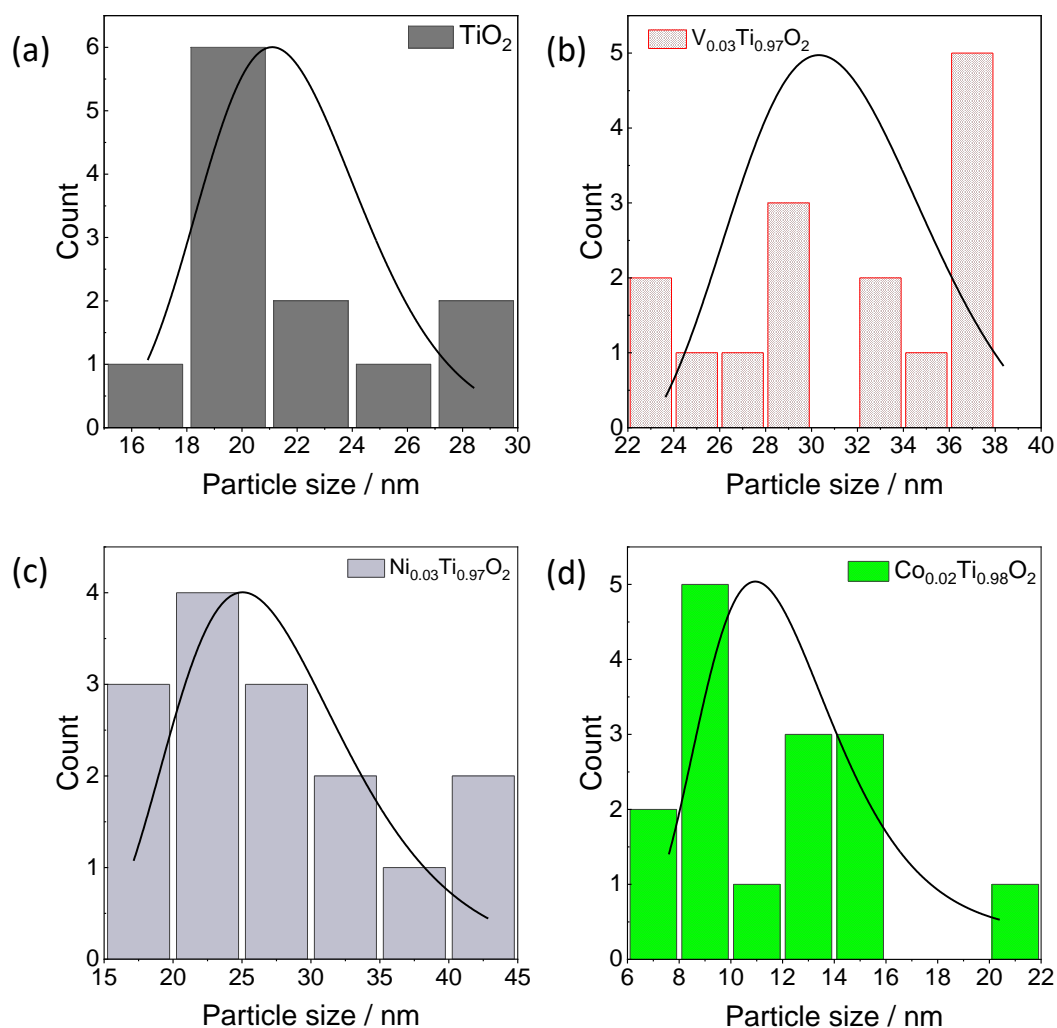


**Figure 4.7.** Particle size analysis of (a)  $TiO_2$ ; (b)  $V_{0.03}Ti_{0.97}O_2$ ; (c)  $Ni_{0.03}Ti_{0.97}O_2$ ; and (d)  $Co_{0.02}Ti_{0.98}O_2$ .

### 4.3.4 UV-Visible Spectra and Bandgap Study

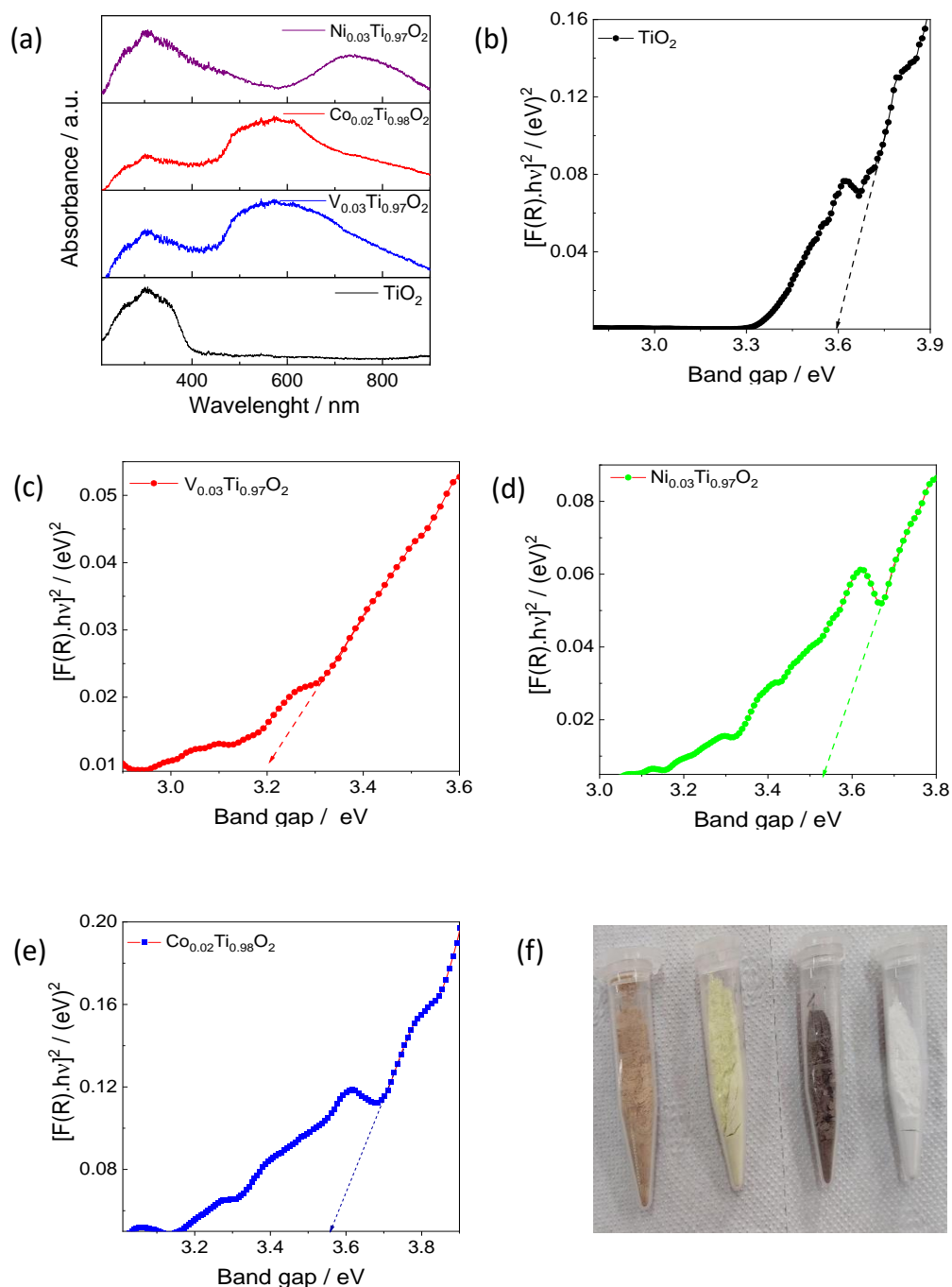


**Figure 4.8.** (a) UV-Vis spectra of  $\text{TiO}_2$ ,  $\text{V}_{0.03}\text{Ti}_{0.97}\text{O}_2$ ,  $\text{Co}_{0.02}\text{Ti}_{0.98}\text{O}_2$ , and  $\text{Ni}_{0.03}\text{Ti}_{0.97}\text{O}_2$ ; Optical band-gap energy of (b)  $\text{TiO}_2$ ; (c)  $\text{V}_{0.03}\text{Ti}_{0.97}\text{O}_2$ ; (d)  $\text{Ni}_{0.03}\text{Ti}_{0.97}\text{O}_2$ ; and (e)  $\text{Co}_{0.02}\text{Ti}_{0.98}\text{O}_2$ ; (f) Image of the synthesized compounds  $\text{TiO}_2$ ,  $\text{V}_{0.03}\text{Ti}_{0.97}\text{O}_2$ ,  $\text{Ni}_{0.03}\text{Ti}_{0.97}\text{O}_2$ , and  $\text{Co}_{0.02}\text{Ti}_{0.98}\text{O}_2$  (Right to left).

UV-Vis absorption spectra of pure  $\text{TiO}_2$ ,  $\text{V}_{0.03}\text{Ti}_{0.97}\text{O}_2$ ,  $\text{Ni}_{0.03}\text{Ti}_{0.97}\text{O}_2$ , and  $\text{Co}_{0.02}\text{Ti}_{0.98}\text{O}_2$  are presented in **Fig 4.8 (a)**. The absorption spectrum of pure  $\text{TiO}_2$  predominantly shows a peak in the range of 200-330 nm. Upon doping with V, Ni, and Co, a broad peak is observed between 400-800 nm, indicating the presence of dopants in the  $\text{TiO}_2$  host lattice.

The band gap of the materials was further determined by plotting the square of the Kubelka-Munk function  $f(R)^2$  versus energy in electron volts as shown in **Fig 4.8 (b-e)**. Pure  $\text{TiO}_2$  has a band gap of 3.60 eV, whereas  $\text{V}_{0.03}\text{Ti}_{0.97}\text{O}_2$ ,  $\text{Co}_{0.02}\text{Ti}_{0.98}\text{O}_2$ , and  $\text{Ni}_{0.03}\text{Ti}_{0.97}\text{O}_2$  have a band gap of 3.2 eV, 3.56 eV and 3.54 eV respectively. All materials exhibit different colours where pure  $\text{TiO}_2$  is white,  $\text{V}_{0.03}\text{Ti}_{0.97}\text{O}_2$  is dark brown,  $\text{Ni}_{0.03}\text{Ti}_{0.97}\text{O}_2$  is light brown, and  $\text{Co}_{0.02}\text{Ti}_{0.98}\text{O}_2$  is pale yellow as shown in **Fig 4.8 (f)**.

#### 4.3.5 Raman Analysis

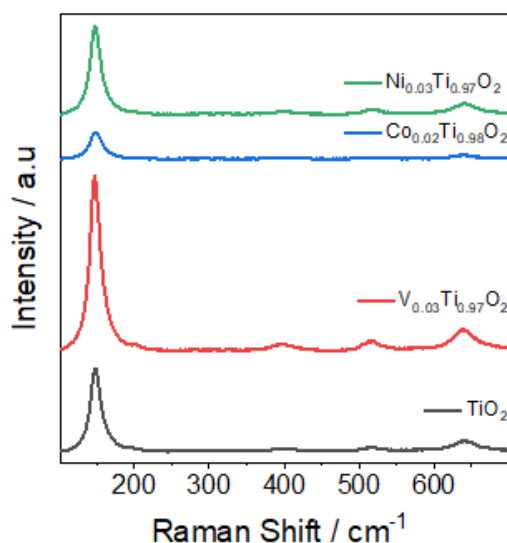


**Figure 4.9.** Raman spectra of  $\text{TiO}_2$ ,  $\text{V}_{0.03}\text{Ti}_{0.97}\text{O}_2$ ,  $\text{Ni}_{0.03}\text{Ti}_{0.97}\text{O}_2$ , and  $\text{Co}_{0.02}\text{Ti}_{0.98}\text{O}_2$ .

The Raman spectra of pure  $\text{TiO}_2$  and  $\text{V}_{0.03}\text{Ti}_{0.97}\text{O}_2$ ,  $\text{Ni}_{0.03}\text{Ti}_{0.97}\text{O}_2$ , and  $\text{Co}_{0.02}\text{Ti}_{0.98}\text{O}_2$  samples were analysed as shown in **Fig 4.9**, revealing four distinct Raman-active peaks centred around  $143\text{ cm}^{-1}$  ( $E_g$ ),  $395\text{ cm}^{-1}$  ( $B_{1g}$ ),  $513\text{ cm}^{-1}$  ( $A_{1g}$ ), and  $637\text{ cm}^{-1}$  ( $E_g$ ) for pure  $\text{TiO}_2$ . These peaks were found to be located at  $144\text{ cm}^{-1}$ ,  $399\text{ cm}^{-1}$ ,  $516\text{ cm}^{-1}$ , and  $639\text{ cm}^{-1}$  respectively, for doped  $\text{TiO}_2$ . The close alignment of the peaks with those of pure  $\text{TiO}_2$  indicates the formation of the pure anatase phase in the doped samples. The slight

broadening of the Raman spectra at  $144\text{ cm}^{-1}$  suggests a partial breakdown of the long-range translational crystal symmetry, which can be attributed to the incorporation of dopant ions into the  $\text{TiO}_2$  lattice.

#### 4.3.6 Electrochemical Active Surface Area (ECSA) Analysis

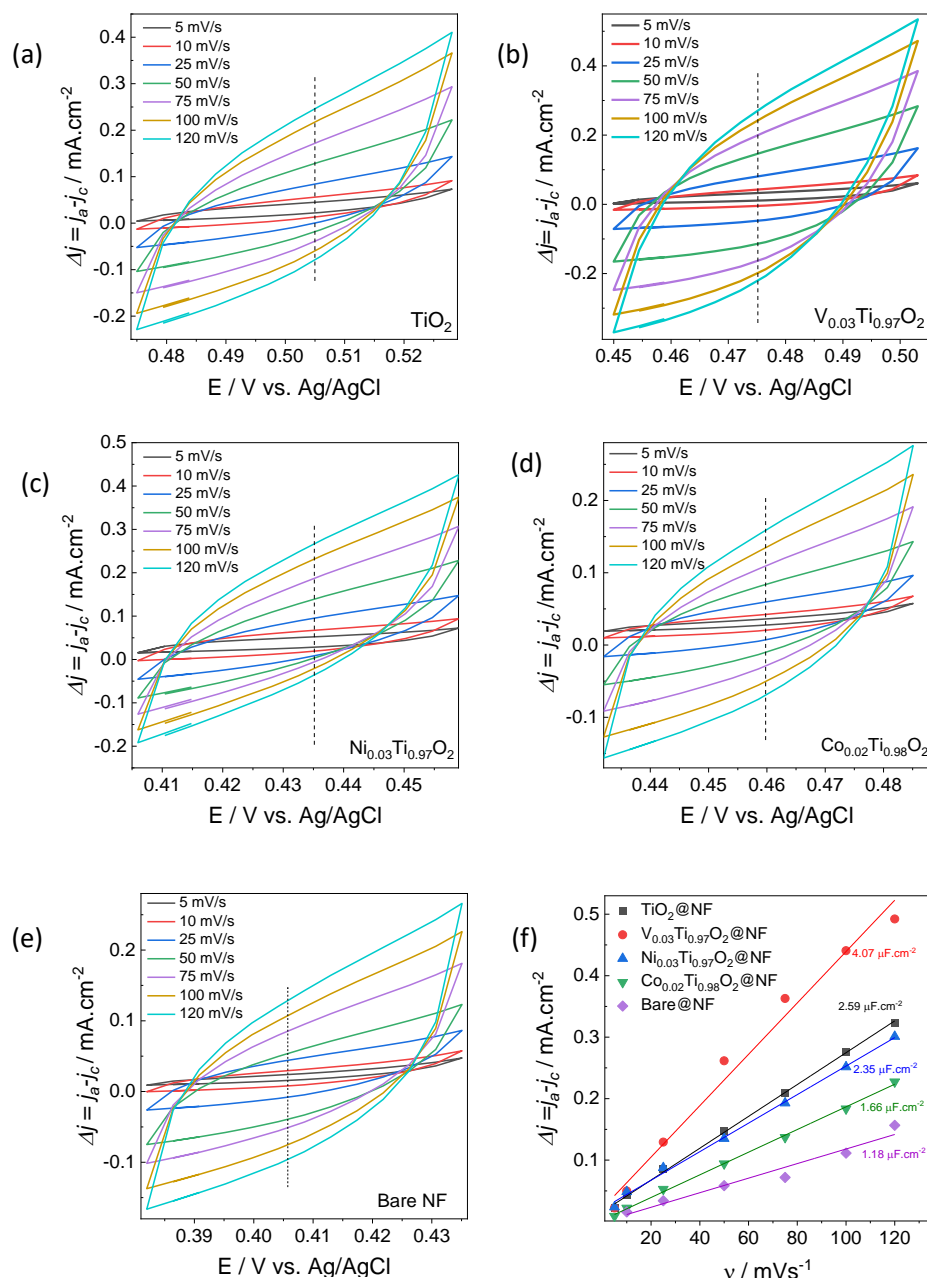


**Figure 4.10.** CV study for ECSA plot of (a)  $\text{TiO}_2@NF$ ; (b)  $V_{0.03}\text{Ti}_{0.97}\text{O}_2@NF$ ; (c)  $Ni_{0.03}\text{Ti}_{0.97}\text{O}_2@NF$ ; (d)  $Co_{0.02}\text{Ti}_{0.98}\text{O}_2@NF$ ; (e) Bare NF; and (f) ECSA plot of  $\text{TiO}_2@NF$ ,  $V_{0.03}\text{Ti}_{0.97}\text{O}_2@NF$ ,  $Ni_{0.03}\text{Ti}_{0.97}\text{O}_2@NF$ ,  $Co_{0.02}\text{Ti}_{0.98}\text{O}_2@NF$  and bare NF.

According to **Fig 4.10 (a-e)**, the ECSA compares the activity of  $\text{TiO}_2@\text{NF}$  and  $\text{V}_{0.03}\text{Ti}_{0.97}\text{O}_2@\text{NF}$ ,  $\text{Ni}_{0.03}\text{Ti}_{0.97}\text{O}_2@\text{NF}$ ,  $\text{Co}_{0.02}\text{Ti}_{0.98}\text{O}_2@\text{NF}$  and bare NF electrodes. Unlike the BET research, this particular study fully immerses the material in the electrolyte, allowing us to determine the material's accurate surface area activity. According to **Fig 4.10 (f)**, the  $2C_{dl}$  values for  $\text{TiO}_2@\text{NF}$ ,  $\text{V}_{0.03}\text{Ti}_{0.97}\text{O}_2@\text{NF}$ ,  $\text{Ni}_{0.03}\text{Ti}_{0.97}\text{O}_2@\text{NF}$ ,  $\text{Co}_{0.02}\text{Ti}_{0.98}\text{O}_2@\text{NF}$  and bare NF are  $2.59 \mu\text{F}\cdot\text{cm}^{-2}$ ,  $4.07 \mu\text{F}\cdot\text{cm}^{-2}$ ,  $2.35 \mu\text{F}\cdot\text{cm}^{-2}$ ,  $1.66 \mu\text{F}\cdot\text{cm}^{-2}$ , and  $1.18 \mu\text{F}\cdot\text{cm}^{-2}$  respectively. For  $\text{TiO}_2@\text{NF}$ ,  $\text{V}_{0.03}\text{Ti}_{0.97}\text{O}_2@\text{NF}$ ,  $\text{Ni}_{0.03}\text{Ti}_{0.97}\text{O}_2@\text{NF}$ , and  $\text{Co}_{0.02}\text{Ti}_{0.98}\text{O}_2@\text{NF}$ , the electrochemically active surface areas were determined to be  $0.032 \text{ cm}^2$ ,  $0.051 \text{ cm}^2$ ,  $0.029 \text{ cm}^2$ ,  $0.021 \text{ cm}^2$ , and  $0.0147 \text{ cm}^2$  respectively. Due to the improvement of the active sites in comparison to the other electrodes, it is confirmed unequivocally that  $\text{V}_{0.03}\text{Ti}_{0.97}\text{O}_2@\text{NF}$  is the optimum material.

#### 4.3.7 Electrochemical Impedance Spectra (EIS) Analysis

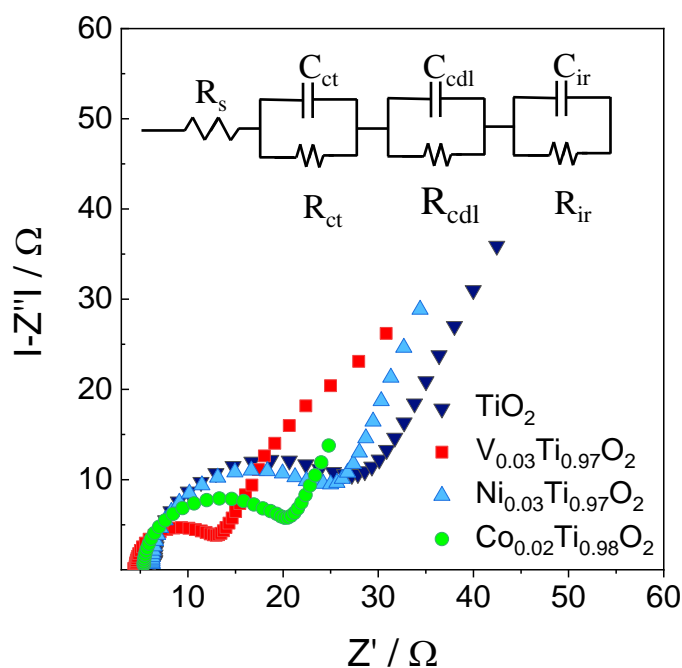


**Figure 4.11.** Nyquist Plot of  $\text{TiO}_2@\text{NF}$ ,  $\text{V}_{0.03}\text{Ti}_{0.97}\text{O}_2@\text{NF}$ ,  $\text{Ni}_{0.03}\text{Ti}_{0.97}\text{O}_2@\text{NF}$  and  $\text{Co}_{0.02}\text{Ti}_{0.98}\text{O}_2@\text{NF}$ .

Using the same three-electrode setup we conducted EIS, the conductivity and interference properties of  $\text{TiO}_2@\text{NF}$  and  $\text{V}_{0.03}\text{Ti}_{0.97}\text{O}_2@\text{NF}$ ,  $\text{Ni}_{0.03}\text{Ti}_{0.97}\text{O}_2@\text{NF}$ , and

$\text{Co}_{0.02}\text{Ti}_{0.98}\text{O}_2@\text{NF}$  were investigated. The corresponding circuit is fitted to the Nyquist plot in **Fig 4.11**. It has a solution resistance of ( $R_s$ ), double layer resistance of ( $R_{\text{cdl}}$ ), charge transfer resistance of ( $R_{\text{ct}}$ ), and internal resistance of ( $R_{\text{ir}}$ ), which are all parallel to the corresponding double layer capacitance ( $C_{\text{cdl}}$ ), charge transfer capacitance ( $C_{\text{ct}}$ ), and internal capacitance ( $C_{\text{ir}}$ ). The charge transfer resistance for  $\text{V}_{0.03}\text{Ti}_{0.97}\text{O}_2@\text{NF}$  was found to be very low, which validates the material's high activity. **Table 4.2** displays the electrochemically fitted parameter.

**Table 4.2.** EIS parameters for the fitted circuit

Samples	$R_s$ ( $\Omega$ )	$C_{\text{ct}}$ (F)	$R_{\text{ct}}$ ( $\Omega$ )	$C_{\text{cdl}}$ (F)	$R_{\text{cdl}}$ ( $\Omega$ )	$C_{\text{ir}}$ (F)	$R_{\text{ir}}$ ( $\Omega$ )
$\text{TiO}_2$	6.41	$5.99 \times 10^{-5}$	7.545	$1.66 \times 10^{-6}$	21.52	$4.5 \times 10^{-5}$	156.3
$\text{V}_{0.03}\text{Ti}_{0.97}\text{O}_2$	3.12	$1.42 \times 10^{-5}$	3.673	$3.86 \times 10^{-4}$	1.279	$2.8 \times 10^{-4}$	17.84
$\text{Ni}_{0.03}\text{Ti}_{0.97}\text{O}_2$	6.15	$2.39 \times 10^{-6}$	19.19	$5.84 \times 10^{-5}$	187.7	$9.8 \times 10^{-5}$	5.355
$\text{Co}_{0.02}\text{Ti}_{0.98}\text{O}_2$	5.34	$3.14 \times 10^{-6}$	14.42	$1.382 \times 10^{-4}$	2.596	$1.2 \times 10^{-4}$	66.69

### 4.3.8 Density Functional Theory (DFT) Study

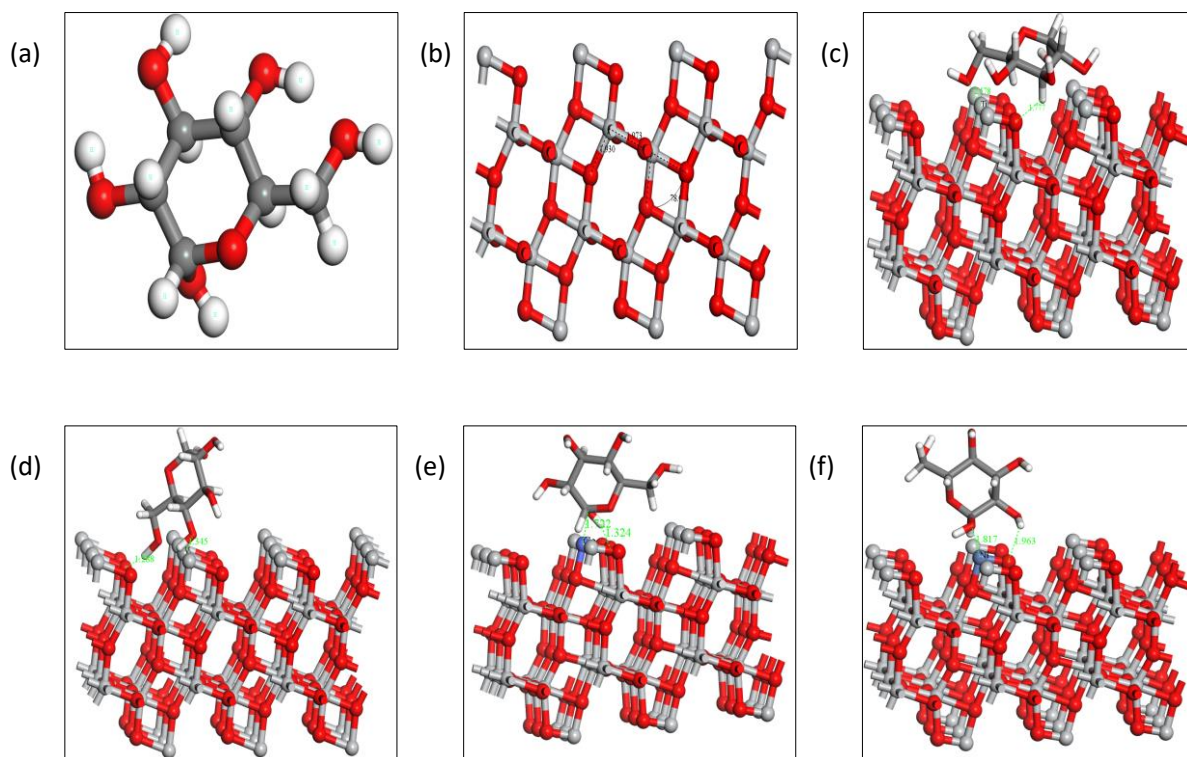


**Figure 4.12.** (a) Optimized structure of D-Glucose; (b) Optimized surface of (1 0 1) of  $\text{TiO}_2$ ; Adsorption of D-Glucose on the surface of (1 0 1) of (c)  $\text{TiO}_2$ ; (d)  $\text{V}_{0.03}\text{Ti}_{0.97}\text{O}_2$ ; (e)  $\text{Co}_{0.02}\text{Ti}_{0.98}\text{O}_2$ ; (f)  $\text{Ni}_{0.03}\text{Ti}_{0.97}\text{O}_2$ .

Geometry optimization and adsorption of glucose on pure  $\text{TiO}_2$  and doped  $\text{TiO}_2$  surfaces were studied using the DFT method.  $\text{TiO}_2$  surface (1 0 1) was optimized using the DFT method and is shown in **Fig 4.12 (b)** and the optimized structure of D-Glucose is shown in **Fig 4.12 (a)**. After optimization, the bond lengths of vertical and horizontal Ti-O were found to be 1.973 Å and 1.930 Å respectively which matches the experimental (1.95 Å) and theoretical values (1.90 Å – 1.93 Å). The angle of O-Ti-O was slightly reduced from the original 78.10° to 78.04°. To calculate the anatase doping, a Ti atom was doped with 3d transition metals such as V, Co, and Ni either by replacing the  $\text{Ti}^{+4}$  or by inserting them into the gaps and optimizing their geometry.

After optimizing the surfaces, we conducted a detailed investigation into how D-Glucose molecules adsorb onto different sites of  $\text{TiO}_2$  and metal-doped  $\text{TiO}_2$  surfaces.

D-Glucose has unique properties due to its ether oxygen and various hydroxyl groups, allowing it to bind in multiple ways to these surfaces. Specifically, we focused on end-on adsorption, where the oxygen atoms of TiO<sub>2</sub> and metal-doped TiO<sub>2</sub> interact with hydrogen atoms in D-Glucose, while metal atoms like Ti, V, Co, and Ni bind with oxygen atoms in D-Glucose, as illustrated **Fig 4.12 (c-f)**. In our analysis, we considered the energies of various configurations involving doped atoms and adjacent oxygen atoms for all optimized surfaces. The configuration with the lowest energy was used to determine the adsorption energy. We calculated the adsorption energy of D-Glucose with TiO<sub>2</sub> and TiO<sub>2</sub> doped with Vanadium, Cobalt, and Nickel using the following equation:

$$\Delta E_{\text{system}} = E_{(\text{surface-glucose})} - E_{\text{surface}} - E_{\text{glucose}} \quad (4.1)$$

Where:  $E_{(\text{surface-glucose})}$  = Energy of the optimized system containing glucose and the TiO<sub>2</sub> (101) surface.  $E_{\text{surface}}$  = Energy of the optimized pure or doped TiO<sub>2</sub> surfaces.  $E_{\text{glucose}}$  = Energy of the optimized glucose molecule.

Our results showed that the adsorption energy of D-Glucose on TiO<sub>2</sub> was -150.30 eV, with a binding distance of 2.578 Å. In contrast, for TiO<sub>2</sub> surfaces doped with V, Co, and Ni, the adsorption energies were -389.73 eV, -236.57 eV, and -228.41 eV, respectively. Similarly, the binding distances for V, Co, and Ni-doped TiO<sub>2</sub> surfaces were found to be 1.345 Å, 1.722 Å, and 1.817 Å, respectively. These results indicate that metal-doped TiO<sub>2</sub> surfaces exhibit higher adsorption energy and shorter binding distances compared to pure TiO<sub>2</sub>, making them more favourable for D-Glucose adsorption. Among the surfaces studied, the Vanadium-doped TiO<sub>2</sub> surface exhibited the best performance for sensing glucose and it will match with the experimental data. **Table 4.3** shows the adsorption energy and binding distance of the glucose with TiO<sub>2</sub>, V<sub>0.03</sub>Ti<sub>0.97</sub>O<sub>2</sub>, Co<sub>0.02</sub>Ti<sub>0.98</sub>O<sub>2</sub>, and Ni<sub>0.03</sub>Ti<sub>0.97</sub>O<sub>2</sub> respectively.

**Table 4.3.** Adsorption energy (eV) and binding distance (Å)

System	Adsorption energy (eV)	Binding distance (Å)
TiO <sub>2</sub> -Glucose	-150.30	2.578
V-TiO <sub>2</sub> -Glucose	-389.73	1.345
Co-TiO <sub>2</sub> -Glucose	-236.57	1.722
Ni-TiO <sub>2</sub> -Glucose	-228.41	1.817

### 4.3.9 X-ray photoelectron spectroscopy (XPS) Analysis

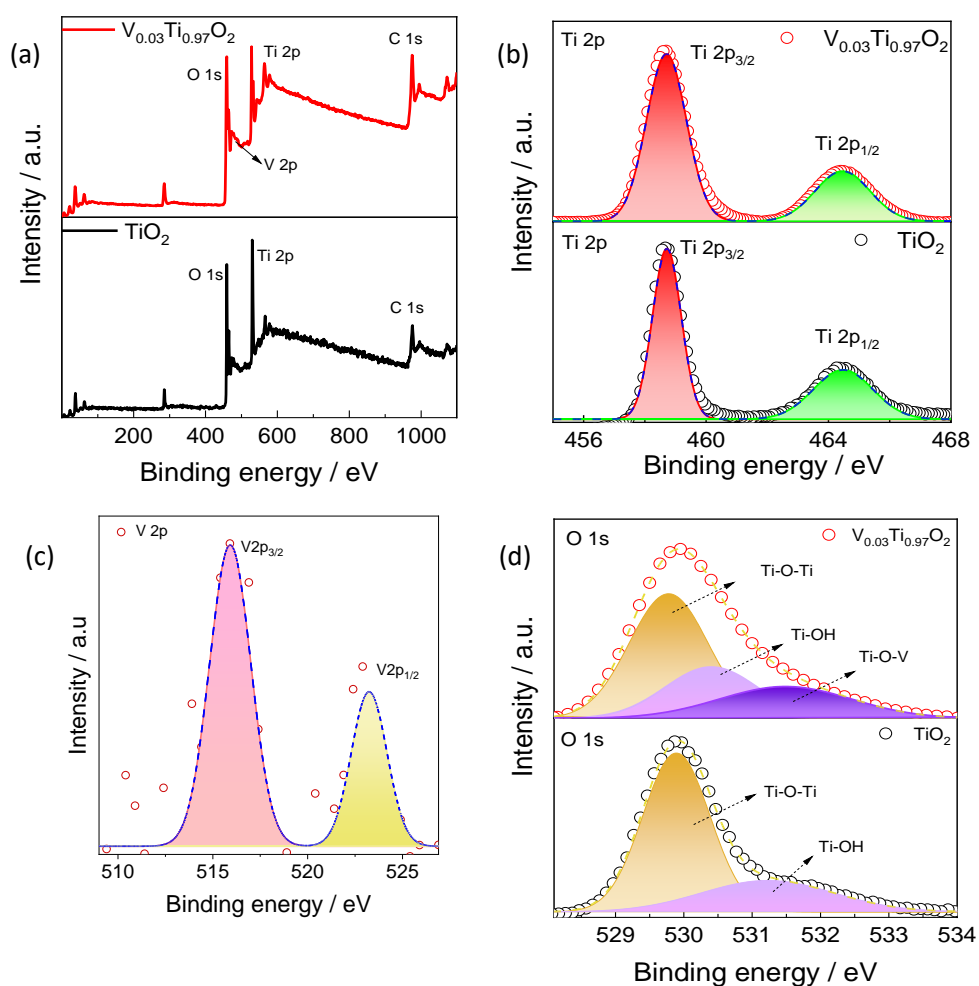


**Figure 4.13.** XPS of  $V_{0.03}Ti_{0.97}O_2$ , and  $TiO_2$  (a) Survey; (b) Ti 2p; (c) V 2p; (d) O 1s.

All of the aforementioned experiments demonstrate that  $V_{0.03}Ti_{0.97}O_2$  activity is more effective than that of  $TiO_2$  and  $M_xTi_{1-x}O_2$  ( $M = Ni, Co$ ). The  $V_{0.03}Ti_{0.97}O_2$ ,  $TiO_2$  XPS spectrum, seen in **Fig 4.13 (a-d)**, aids in the analysis of the chemical composition by determining the state of the system's constituent components. The survey spectra of the  $V_{0.03}Ti_{0.97}O_2$  and  $TiO_2$  are shown in **Fig 4.13 (a)**, and they demonstrate the existence of Ti, O, and V elements in the sample.

The XPS spectra of the Ti 2p state in  $V_{0.03}Ti_{0.97}O_2$  and  $TiO_2$  are shown in **Fig 4.13 (b)**. It consists of two peaks with binding energies of 458.6 eV and 464.5 eV, respectively, which represent the Ti 2p<sub>1/2</sub> and Ti 2p<sub>3/2</sub> states. The  $Ti^{4+}$  state is present in  $V_{0.03}Ti_{0.97}O_2$  and in  $TiO_2$  as evidenced by the Ti 2p doublet's peak position and it has a peak separation of 5.9 eV.

The doping of vanadium onto the  $TiO_2$  matrix is confirmed by the XPS spectra of the V 2p state in **Fig 4.13 (c)**. The V 2p<sub>1/2</sub> peak is partially merged with the O 1s peak, and the V 2p<sub>3/2</sub> and V 2p<sub>1/2</sub> states are also recognized. There are two states  $V^{4+}$  and  $V^{5+}$  in V 2p<sub>2/3</sub>, which are deconvoluted into two main peaks with binding energies of 515.98 eV and 523.27 eV, respectively.  $V^{4+}$  is due to the formation of Ti-O-V bonding and  $V^{4+}$  can be replaced easily into a  $TiO_2$  lattice, whereas,  $V^{5+}$  is in the form of  $V_2O_5$  on the surface of the  $TiO_2$  and  $Ti^{4+}$  is substituted by the  $V^{5+}$  ion which may cause the space charge layer at the interference with  $TiO_2$  due to delocalization of the valence electron around the  $V^{5+}$  positive centre. It is also seen that  $V_{0.03}Ti_{0.97}O_2$  existed mainly in  $V^{5+}$  ions.

Vanadium doping causes the O 1s peak to move to the higher binding energy, as seen in **Fig 4.13 (d)**, which displays the XPS spectra of the O 1s peak for  $V_{0.03}Ti_{0.97}O_2$  and  $TiO_2$  respectively. The O 1s peak in  $V_{0.03}Ti_{0.97}O_2$  has three primary peaks that correspond to binding energies of 529.75 eV, 530.5 eV, and 532.5 eV. The peak at the binding energy of 530.5 eV is attributed to the Ti-OH bond formed by the reaction between  $TiO_2$  and  $H_2O$  absorbed on the surface of the sample, and the photopeak at the binding energy of 532.5 eV is assigned to the Ti-O-V bond as it indicates that Ti has been replaced by vanadium in the  $TiO_2$  lattice. The photopeak corresponding to 529.75 eV binding energy is the Ti-O-Ti bond. Whereas, the pure  $TiO_2$  for the XPS study shows the same peaks at 531.5 eV and 530.2 eV are attributed to Ti-OH and Ti-O-Ti respectively. This shows that vanadium-doped  $TiO_2$  is confirmed.

### 4.3.10 Electrochemical Studies

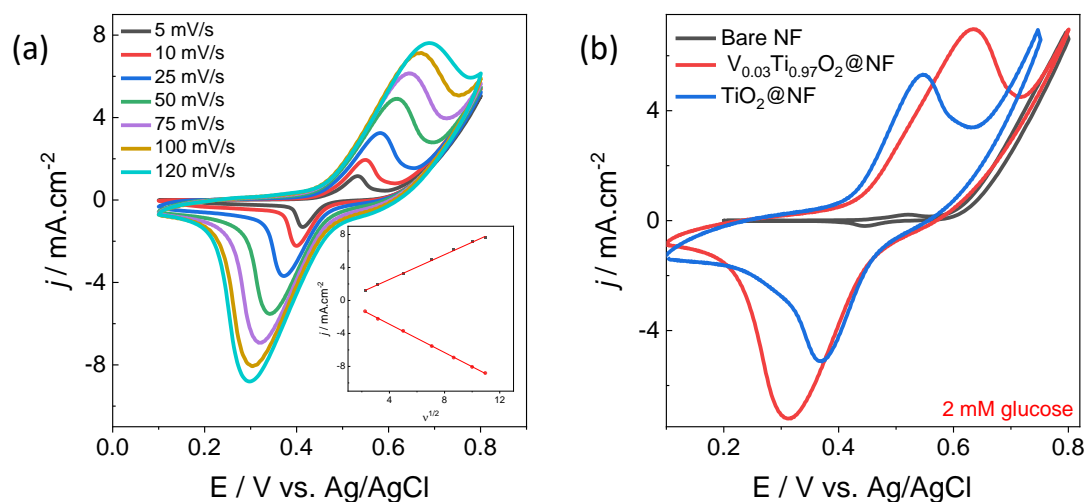


**Figure 4.14.** (a) Cyclic voltammogram of  $V_{0.03}Ti_{0.97}O_2@NF$  in 0.1 M KOH at increasing scan rates from 5-120 mV/s. The corresponding anodic peak current and cathodic peak current as a function of the square root of the scan rate (Inset); (b) Cyclic voltammogram of  $V_{0.03}Ti_{0.97}O_2@NF$ ,  $TiO_2@NF$  and bare NF in 0.1 M KOH with the presence of 2 mM glucose.

As shown in **Fig 4.14 (a)**, the fabrication of  $V_{0.03}Ti_{0.97}O_2@NF$  was subjected to a CV investigation with various scan rates ranging from 5-120 mV/s. It demonstrates the nature and reaction kinetics of the modified electrodes and the investigation of the impact of scan rate on anodic and cathodic peak current. The anodic and cathodic peaks are shown to rise as the scan rate rises. This results from the formation of a diffusion layer that reduces as the scan rate increases. When the scan rate is lower, more diffusion layer is formed, which allows lesser electroactive species to reach the electrode surface, resulting in lower cathodic and anodic peak currents. When the scan rate is higher, the reverse is valid. As the scan rate increased, the cathodic peak altered to the negative side while the anodic peak shifted to the positive side. It demonstrates that the redox behavior of the  $V_{0.03}Ti_{0.97}O_2@NF$  has a linear connection with the square root of the scan rate (Inset), demonstrating unequivocally that the diffusion layer is impermeable to the electroactive species and that an electron transfer occurs via the outer sphere mechanism. As seen in **Fig 4.14 (b)**, the material  $V_{0.03}Ti_{0.97}O_2@NF$  was tested for glucose oxidation together with bare NF and  $TiO_2@NF$  in the presence of 2 mM glucose

in 0.1 M KOH. This demonstrates clearly that in the potential range of 0.2 to 0.8 V versus Ag/AgCl, bare NF does not exhibit any discernible catalytic reaction toward the oxidation of glucose. In contrast, the TiO<sub>2</sub>@NF material responded to glucose by increasing the anodic peak current, which supported the oxidation of the glucose. Additionally, a significant increase in anodic peak current was seen for V<sub>0.03</sub>Ti<sub>0.97</sub>O<sub>2</sub>@NF at E<sub>pa</sub>= 0.634V in response to the addition of glucose at the same concentration. Compared to TiO<sub>2</sub>@NF, V<sub>0.03</sub>Ti<sub>0.97</sub>O<sub>2</sub>@NF exhibits a 1.7-fold increase in anodic peak current responsiveness. This demonstrates strongly that the vanadium-doped TiO<sub>2</sub> has higher electrochemical activity than pure TiO<sub>2</sub>, and the mechanism at play is that glucose (C<sub>6</sub>H<sub>12</sub>O<sub>6</sub>) is oxidized to gluconolactone (C<sub>6</sub>H<sub>10</sub>O<sub>6</sub>) on the working electrode, and the production of electrons causes the change in the current for a particular amount of glucose solution (Eq. 4.2).



As vanadium doping increases the activity of TiO<sub>2</sub> with an increase in adsorption energy and a decrease in binding distance as mentioned in the DFT study, along with the material's crystallinity and an increase in the number of electrons transferred, a defect produced in the mesoporous TiO<sub>2</sub>, which has a larger surface area, affects the efficiency of glucose oxidation. The number of electrons involved in the oxidation of glucose can be calculated using the Laviron equation (Eq. 4.3).

$$\text{Slope} = \frac{RT}{F\alpha n} \quad (4.3)$$

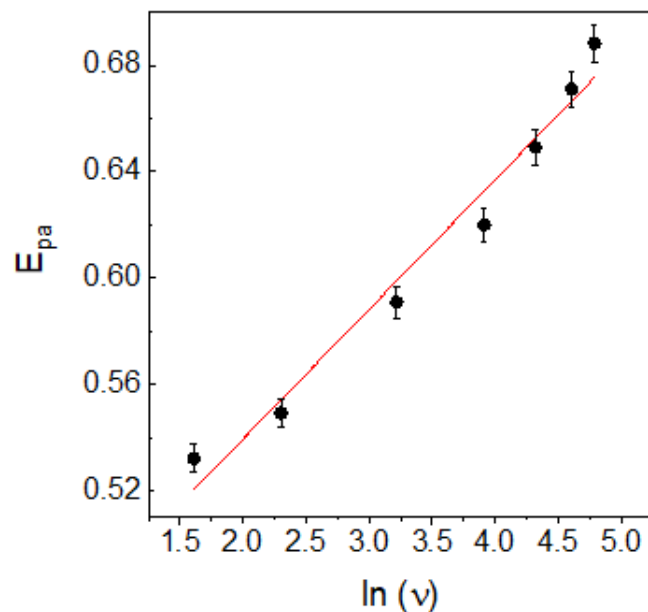


**Figure 4.15.** Laviron equation study of  $\ln v$  vs  $E_{pa}$ .

According to **Fig 4.15**, the Laviron equation is calculated using the slope of  $\ln (v)$  vs anodic peak potential in the presence of glucose addition. Here,  $R$  is the ideal gas constant ( $R=8.314 \text{ J K}^{-1}\text{mol}^{-1}$ ),  $T$  is 300 K,  $F$  is  $96\,480 \text{ C mol}^{-1}$ , is the transfer coefficient ( $\alpha=0.5$ ), and  $n$  is the number of electrons involved in glucose oxidation. Furthermore, the electro-oxidation of glucose results in the transmission of 1.055 electrons, confirming that just one electron is transmitted during the process.

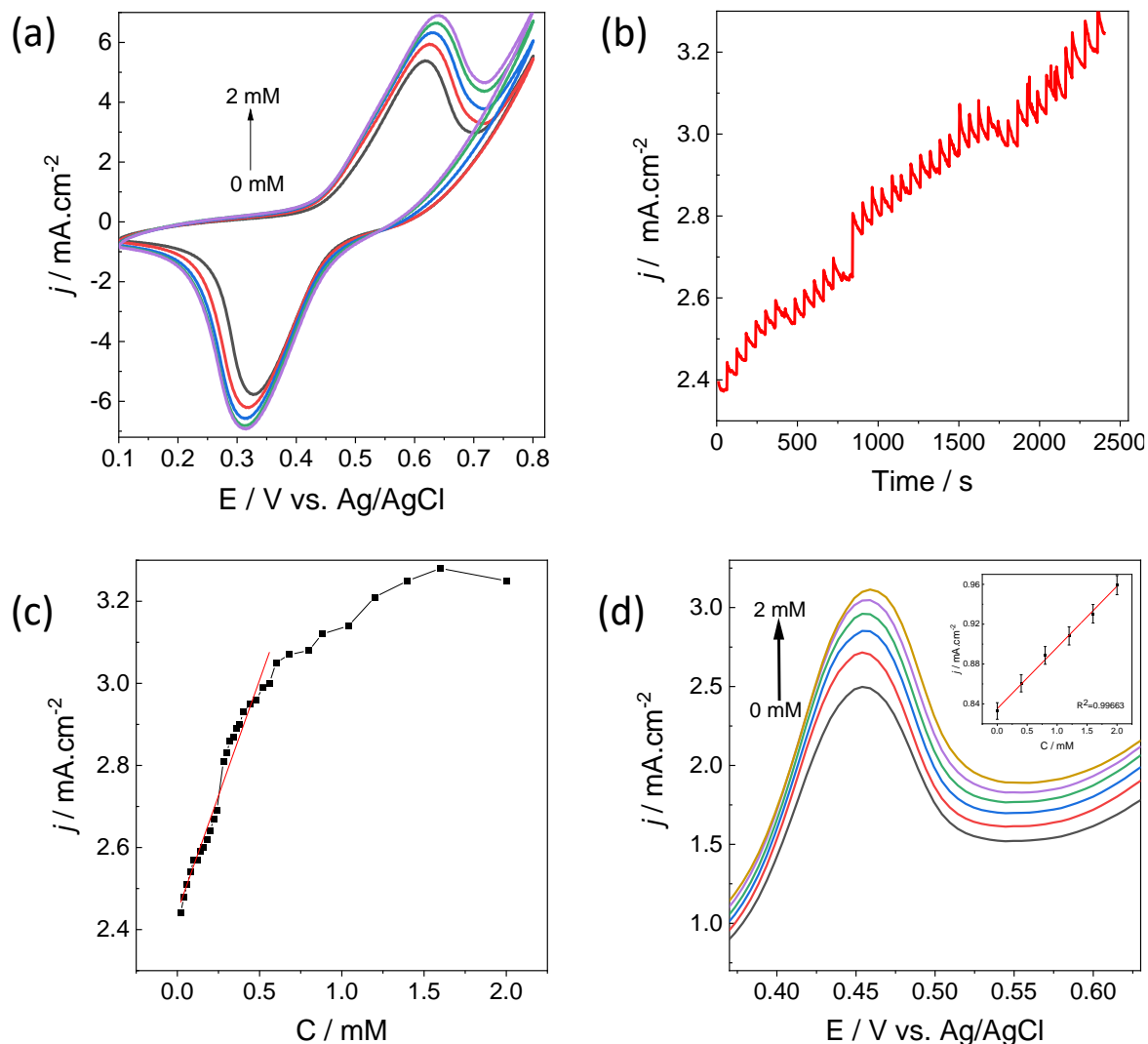


**Figure 4.16.** (a) The successive addition of glucose in 0.1 M KOH at the scan rate of 50 mV/s; (b) The CA study of  $V_{0.03}Ti_{0.97}O_2@NF$  in 0.1 M KOH with the successive addition of glucose in stirring condition. Applied potential: 0.6 V; (c) Calibration plot of the  $V_{0.03}Ti_{0.97}O_2@NF$  for the determination of the glucose; (d) DPV study of  $V_{0.03}Ti_{0.97}O_2@NF$  in 0.1 M KOH with the successive addition of glucose in stirring condition.

The successive addition study of glucose in 0.1 M KOH is shown in **Fig 4.16 (a)**, showing that as the addition of glucose increases, the anodic peak also increases gradually exhibiting the electrocatalytic oxidation of glucose. This is due to an increase in the diffusion layer of the analyte that causes an increase in the anodic peak.

Therefore, it is suited for the amperometric sensor for the determination of glucose. The enzyme-free glucose sensor is subjected to an analytical performance by carrying out CA measurements for  $V_{0.03}Ti_{0.97}O_2@NF$  with glucose addition at a varied concentration to find the linear response of glucose in a range of 20  $\mu M$  to 2 mM. For this amperometric study, a constant potential of 0.6 V and its amperometric response is noted at every 60 sec by the addition of the glucose in the stirring condition. The behavior of the material was found to increase with the increase in the current step-wise suggesting an increase in the anodic peak upon each glucose addition as shown in **Fig 4.16 (b)**. This is due to each addition of glucose being sensed by the material and current change occurs due to an increase in the diffusion layer of the analyte near the surface of the working electrode. But there was a gradual depletion in the line was observed, this is due to the stirring condition and the conversion of glucose to the respective product causing the change. The sudden hike in the current was observed at 900 sec which is due to disturbance caused because of stirring. The saturation was observed near 2500 sec for a 2 mM concentration of glucose. The calibration curve of the glucose sensor has a linear relationship for concentration in the range of 20  $\mu M$  to 2 mM as shown in **Fig 4.16 (c)**, this helps to find the sensitivity, LOD, and LOQ of the material and it is found to be 1129.31  $\mu A\ mM^{-1}\ cm^2$ , 1.8  $\mu M$  and 6.2  $\mu M$  respectively with a response time of 2.1 s.

DPV study showed much better reproducibility, thus making DPV analysis reliable. The DPV study for  $V_{0.03}Ti_{0.97}O_2@NF$  as shown in **Fig 4.16 (d)** in the linear range of 0.4 mM to 2 mM. This successive addition of glucose in 0.1 M of KOH was added at the scan rate of 5 mV/s and it is seen that the change in the current was observed for every addition of glucose concentration with the linearity obtained from the calibration curve of current vs concentration of  $R^2=0.99663$ . All the above study shows, that there is a response of  $V_{0.03}Ti_{0.97}O_2@NF$  for each addition of glucose because of its mesoporous nature along with the defects of  $TiO_2$  makes the material sense the glucose analyte.

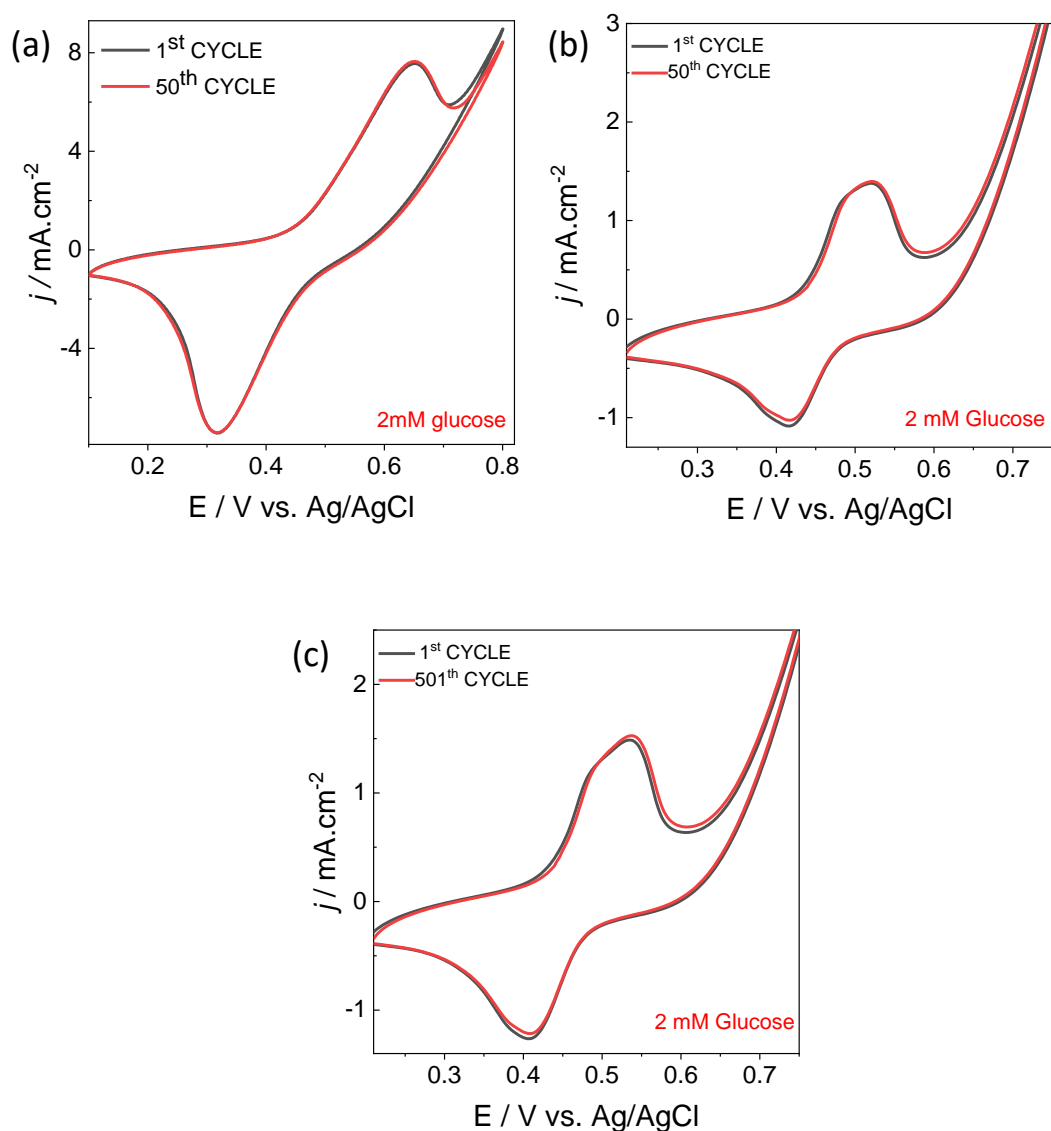


**Figure 4.17.** The CVs of (a)  $V_{0.03}Ti_{0.97}O_2@NF$ ; (b)  $Ni_{0.03}Ti_{0.97}O_2@NF$ ; (c)  $Co_{0.02}Ti_{0.98}O_2@NF$  with 2 mM glucose for 50 cycles in 0.1 M KOH at the scan rate of 50 mV/s.

The long-term stability of the  $V_{0.03}Ti_{0.97}O_2@NF$  is studied by measuring the response of the electrode for 50 cycles in the presence of the 2 mM glucose, achieving the 100% retention of anodic current as shown in **Fig 4.17 (a)**, suggesting that the material is studied for the longer analysis and shelf life found to be outstanding confirming that the ability to reuse the same electrode for the varied occasion with the very less depletion in the response. Similarly, the electrochemical studies of  $Ni_{0.03}Ti_{0.97}O_2@NF$  and  $Co_{0.02}Ti_{0.98}O_2@NF$  were also conducted by adding 2 mM glucose and running 50

cycles at a scan rate of 50 mV/s as shown in **Fig 4.17 (b-c)**. The results indicate a 99% retention rate with a stable current throughout the cycles.

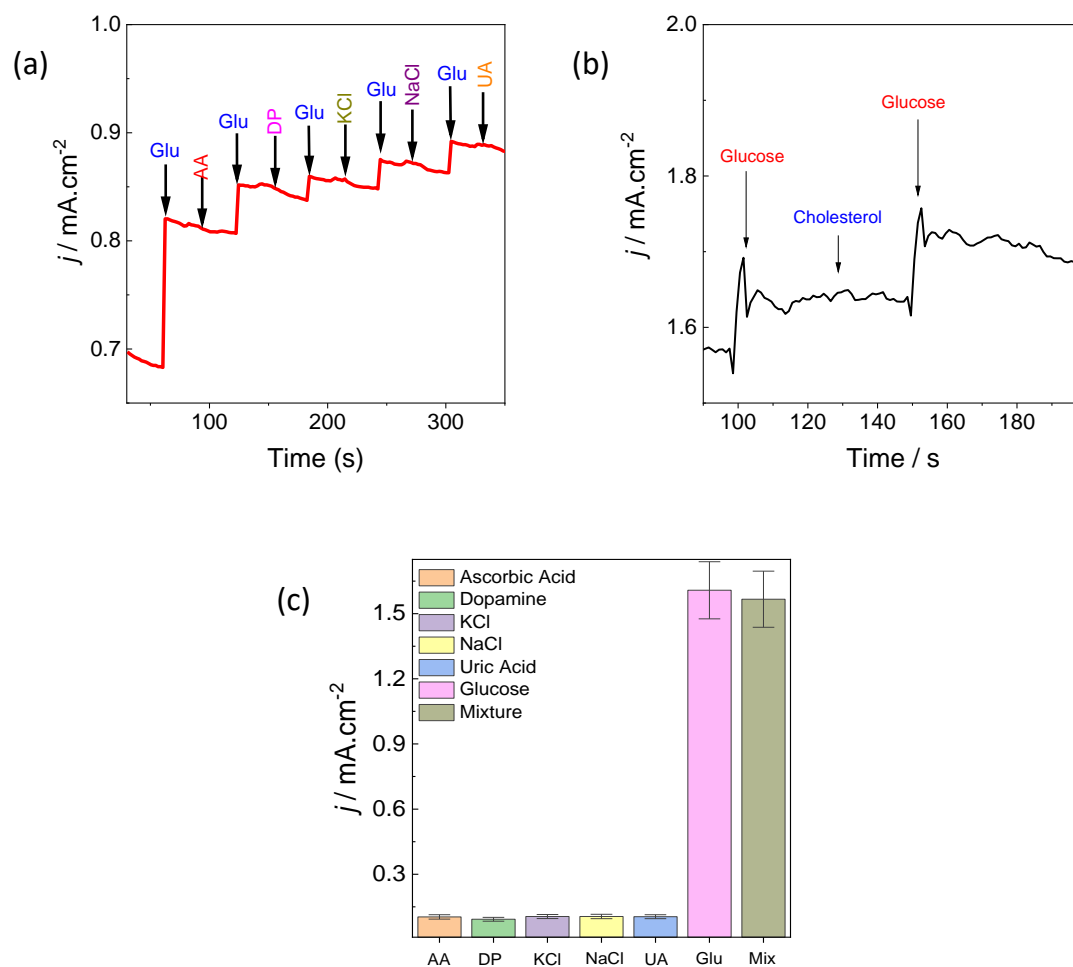


**Figure 4.18.** (a), (b) Amperometric response of  $V_{0.03}Ti_{0.97}O_2@NF$  towards the interference species under stirring condition in 0.1 M KOH. Applied potential :0.6 V; (c) DPV interference study for  $V_{0.03}Ti_{0.97}O_2@NF$  at a scan rate of 5 mV/s with the pulse amplitude of 5 mV/s.

The primary challenge when developing an electrochemical glucose sensor is the removal of interfering compounds during glucose oxidation, which speaks well of the material's selectivity for glucose detection. The CA adds various substances, such as AA, DP, NaCl, KCl, UA and Glucose to a 0.1 M KOH solution to study the selectivity of the  $V_{0.03}Ti_{0.97}O_2@NF$ . **Fig 4.18 (a-b)** depicts the interference of species at a 0.5 mM concentration, which exhibits no reaction to  $V_{0.03}Ti_{0.97}O_2@NF$  but exhibits a sharp rise

in current at the addition of 1 mM glucose. In reality, human blood has a glucose concentration of 4 mM to 7 mM, demonstrating that the response to the interference should be minimal because of its low concentration. Thus, this research demonstrates that the interference species will not affect glucose oxidation activity even at larger concentrations. This demonstrates the high selectivity of  $V_{0.03}Ti_{0.97}O_2@NF$  for glucose sensing.

Similar to the CA-based investigation, the interference study using DPV was also conducted and the findings are displayed in **Fig 4.18 (c)**. Additionally, a DPV analysis was conducted on the mixture that included 1 mM glucose and all of the interference species at a concentration of 0.5 mM. The lack of a significant shift in the material's activity confirms that the interfering species won't change the  $V_{0.03}Ti_{0.97}O_2@NF$ 's sensitivity to glucose. This further demonstrates the high selectivity and potential of  $V_{0.03}Ti_{0.97}O_2@NF$  as a material for the oxidation of glucose.

#### 4.3.11 Post-Glucose Oxidation Characterization

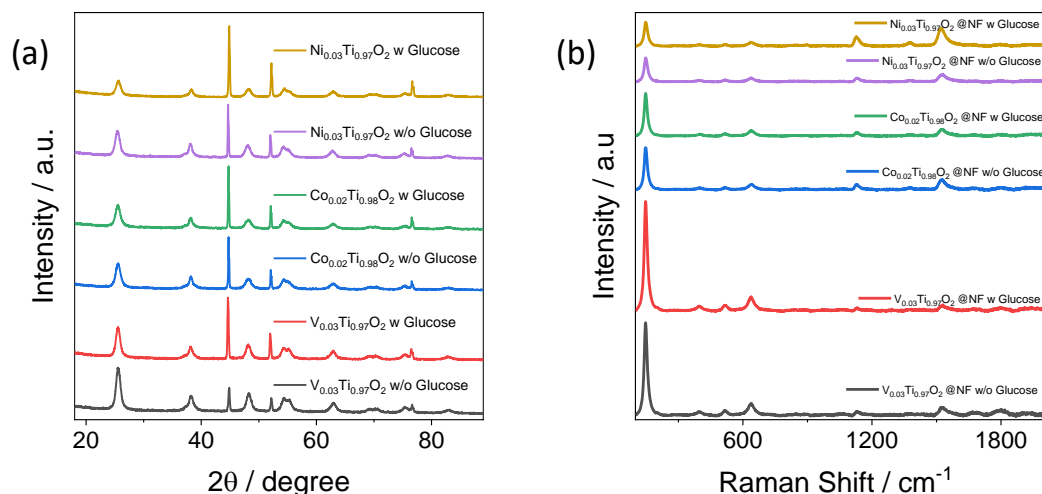


**Figure 4.19.** (a) XRD analysis of  $V_{0.03}Ti_{0.97}O_2@NF$ ,  $Co_{0.02}Ti_{0.98}O_2@NF$ , and  $Ni_{0.03}Ti_{0.97}O_2@NF$  before and after glucose oxidation ; (b) Raman analysis of  $V_{0.03}Ti_{0.97}O_2@NF$ ,  $Co_{0.02}Ti_{0.98}O_2@NF$  and  $Ni_{0.03}Ti_{0.97}O_2@NF$  before and after glucose oxidation .

The materials underwent XRD and Raman spectroscopy before and after glucose oxidation, as depicted in **Fig 4.19 (a-b)**. The XRD analysis revealed peaks at  $44^\circ$  and

53°, attributable to the NF, with the remaining peaks indicative of  $V_{0.03}Ti_{0.97}O_2@NF$ , as illustrated in **Fig 4.19 (a)**. Similarly, the other two materials,  $Co_{0.02}Ti_{0.98}O_2@NF$  and  $Ni_{0.03}Ti_{0.97}O_2@NF$ , underwent the same treatment, with no observed change in composition. This suggests that the material configuration remains consistent even after glucose oxidation. In the Raman spectra, peaks at 1132, 1376, and 1572  $cm^{-1}$  correspond to the NF, with the remaining peaks matching the Raman spectra of  $V_{0.03}Ti_{0.97}O_2@NF$ , as shown in **Fig 4.19 (b)**. Again, the other two materials,  $Co_{0.02}Ti_{0.98}O_2@NF$  and  $Ni_{0.03}Ti_{0.97}O_2@NF$ , showed no change in composition when subjected to the same analysis. Therefore, there is no evidence of additional peaks, indicating that the material remains unchanged following glucose oxidation.

As demonstrated in **Table 4.4**, the observed biosensing characteristics are equivalent to and superior to those of published glucose biosensors. For the first time, a non-enzymatic vanadium-doped  $TiO_2$  glucose biosensor has been proposed and confirmed utilizing theoretical and experimental research techniques.

**Table 4.4.** List of Electrochemical performance of non-enzymatic glucose sensors

Electrodes	Linear Range	Sensitivity ( $\mu\text{AmM}^{-1}\text{cm}^{-2}$ )	LOD $\mu\text{M}$	Response time (s)	Ref.
Cu NPs-LIG	1 $\mu\text{M}$ -6 mM	495	0.39	<0.5	(Zhang et al. 2020)
NF/AuNPs/CuO-MoS <sub>2</sub>	0.5 $\mu\text{M}$ -5.67 mM	872.71	0.5	-	(Bao et al. 2019)
NiCo <sub>2</sub> O <sub>4</sub>	5 $\mu\text{M}$ -0.25 mM	806.17	2.75	-	(Jo et al. 2020)
AuNi/NX/MWCNT/GCE	1-1900 $\mu\text{M}$	662.93	0.063	-	(Amiripour et al. 2021)
Pd-Ni@f-MWCNT	0.01-1.4 mM	71	0.026	-	(Karimi-Maleh et al. 2020)
V <sub>0.03</sub> Ti <sub>0.97</sub> O <sub>2</sub> @NF	20 $\mu\text{M}$ -2 mM	1129.31	1.8	2.1	This work

#### 4.3.12 Real-sample Study

V<sub>0.03</sub>Ti<sub>0.97</sub>O<sub>2</sub>@NF was used to measure the amount of glucose in human blood serum. The human serum was collected from hospitals with glucose concentrations ranging from 4 mM to 24 mM. Since the serum acquired further was not altered and was utilized directly for the examination of the genuine sample, the values closely matched the estimated values. As can be shown in **Table 4.5**, the V<sub>0.03</sub>Ti<sub>0.97</sub>O<sub>2</sub>@NF electrode, therefore, provides an acceptable range for determining the glucose from the actual sample. **Fig 4.20** displays the blood serum that was utilized in real sample investigations.

**Table 4.5.** Analysis of human blood sample

Patient	Gender	Clinically tested (mg/dL)	Found	Deviation
			(mg/dL)	
1	M	85	79.2	5.8
2	F	187	184.3	2.7
3	M	266	261.2	4.8
4	F	441	423	18

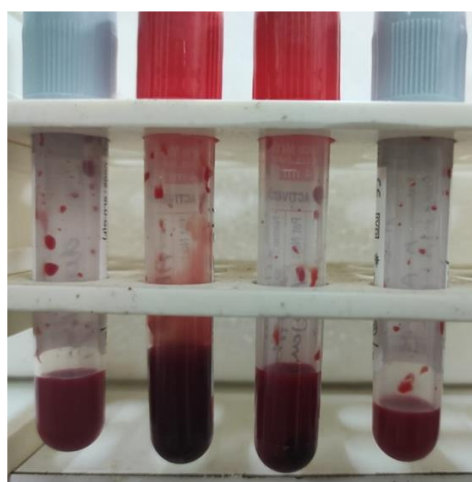


**Figure 4.20.** The blood samples used for real sample study.

#### 4.4 Conclusions

- In summary,  $\text{TiO}_2$  and  $\text{M}_x\text{Ti}_{1-x}\text{O}_2$  ( $\text{M}=\text{V}, \text{Ni}, \text{Co}$ ) nanoparticles were synthesized and electrochemically studied.
- Among them,  $\text{V}_{0.03}\text{Ti}_{0.97}\text{O}_2@\text{NF}$  exhibited superior performance, attributed to its crystalline structure, mesoporous nature, higher surface area, faster electron mobility, and fast charge transfer.
- We explored the potential of  $\text{TiO}_2$  and doped  $\text{TiO}_2$  ( $\text{V}, \text{Ni}, \text{Co}$ ) as glucose sensors using Density Functional Theory (DFT) simulations.

- Our research revealed that  $V_{0.03}Ti_{0.97}O_2@NF$  showed enhanced chemical reactivity, forming a chemical bond with glucose oxygen.  $V_{0.03}Ti_{0.97}O_2@NF$ , in particular, demonstrated a remarkable sensitivity of  $1129.31 \mu A mM^{-1}cm^{-2}$ , a detection limit of  $1.8 \mu M$ , and a rapid response of  $2.1 s$  in  $0.1 M KOH$ .
- It has demonstrated efficacy in the analysis of human blood samples, underscoring its potential as a glucose biosensor suitable for industrial applications. The material's quick synthesis, cost-effectiveness, and diverse medical applications highlight its commercialization potential, providing an affordable solution for glucose sensing in various medical contexts.

\*\*\*\*\*

## **CHAPTER 5**

---

---

**SYNTHESIS OF MESOPOROUS  $V_xTi_{1-x}O_2$  ( $x=0.03, 0.05, 0.07$  AND  
 $0.09$ ) AS AN EFFECTIVE ELECTROCHEMICAL NON-  
ENZYMATIC GLUCOSE SENSOR**

---

---



---

---

**Abstract:** *This chapter provides a detailed explanation of the synthesis of  $V_xTi_{1-x}O_2$  at various doping concentrations ( $V=0.03,0.05,0.07$ , and  $0.09$ ) as well as in-depth characterization. The main goal is to simplify the electrochemical method of measuring glucose levels by providing a simpler approach.*

---

---

## 5.1 Introduction

Researchers have paid a great deal of attention to mesoporous materials because of their large volume, uniform size, large surface area, and regulated pore structure. Their flexibility is due to the fact that they consistently interact with particles on the surface of the material as well as within it. In the case of mesoporous  $TiO_2$ , which has a large surface area and well-organized pores, is known to exhibit improved biosensing characteristics, such as high sensitivity, wide linear response, low detection limits, and excellent repeatability. As a result, mesoporous  $TiO_2$  has been used in biosensor development much more frequently in recent years.

The anatase phase of  $TiO_2$  exhibits considerable potential in many applications due to its enhanced electron mobility, superior electron transfer capacity, reduced density and dielectric constant, and increased surface stability and reactivity. Moreover, the process with which the anatase phase forms at lower temperatures reduces the possibility of adverse consequences on the mesoporous structure (Amri et al. 2021).

Several dopants have been introduced into the  $TiO_2$  lattice, including metal (Mo, Fe, V etc.) and nonmetal (S, N, C, etc.) elements. Vanadium (V) is a promising choice for  $TiO_2$  addition among the evaluated dopants since it can be doped into  $TiO_2$  with ease due to their almost identical ionic radii ( $V^{4+}/Ti^{4+} = 0.72/0.75$  Å). Furthermore,  $TiO_2$  doped with vanadium not only alters its band gap, it also enhances electrical conductivity and promotes effective charge transfer mechanisms. The material's sensitivity and selectivity are improved by this change, which is important for biosensing applications (Yu et al. 2016).

Additionally, the surface area of vanadium-doped  $TiO_2$  is higher, offering more sites for biomolecule adsorption and enhancing detection sensitivity. Improved electron

transfer kinetics allow for faster and more precise glucose level measurement, which further maximizes biosensor performance. All things considered, vanadium doping in  $\text{TiO}_2$  provides a versatile way to improve biosensor performance, guaranteeing accurate and dependable glucose detection for biomedical applications.

Vanadium doping levels ( $V = 0.03, 0.05, 0.07, \text{ and } 0.09$ ) were varied in the  $\text{V}_x\text{Ti}_{1-x}\text{O}_2$  materials that we synthesized and deposited on NF in the present study. The electrocatalytic characteristics of each produced material were investigated. After the first screening, the most promising material was chosen to undergo further electrochemical characterization, with a particular emphasis on its glucose biosensing abilities. CV, CA, and DPV methodologies were used in this comprehensive assessment. To further the development of electrochemical biosensing technologies, these investigations aimed to gain an understanding of the selected material's biosensing ability toward glucose.

## 5.2 Experimental Section

### 5.2.1 Synthesis of $V_xTi_{1-x}O_2$

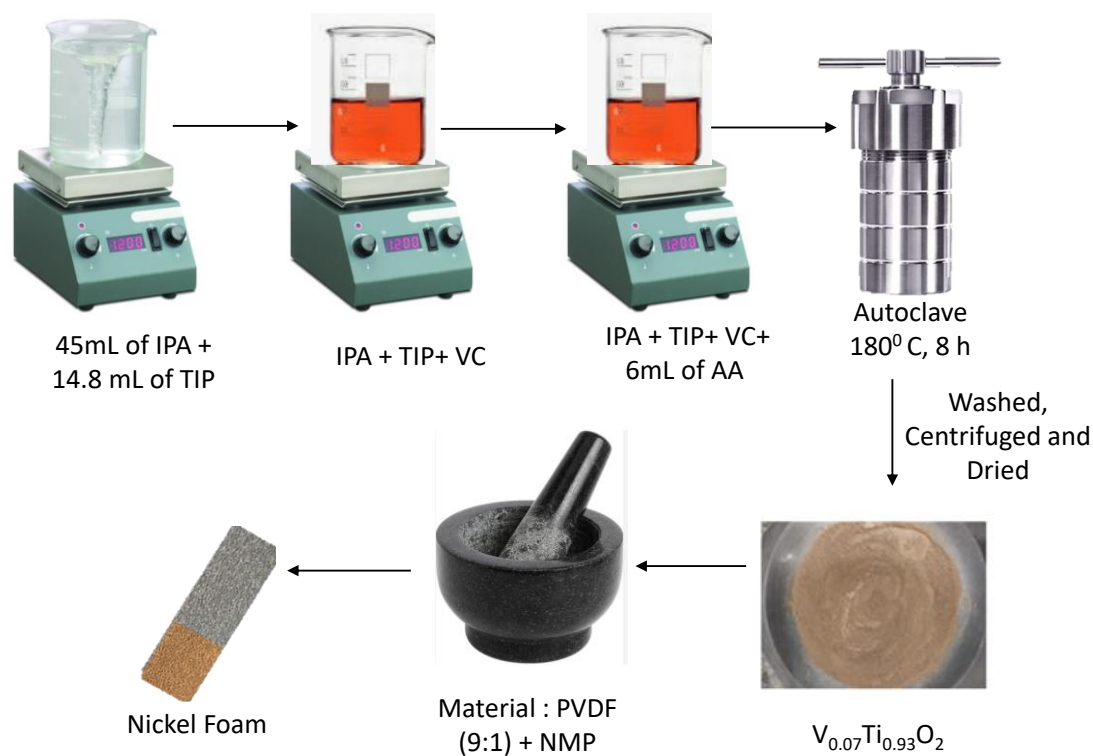


**Figure 5.1.** Schematic diagram of synthesis of the  $V_xTi_{1-x}O_2$ .

Combine 14.8 mL of TIP with 45 mL of IPA, then stir for 10 minutes to synthesize the  $V_xTi_{1-x}O_2$  nanoparticles.  $VCl_3$  should be weighed according to 0.03, 0.05, 0.07 and 0.09 molar percentage and dissolved in a small amount of dil. HCl before being added dropwise to the TIP/IPA mixture and stirred for ten minutes. 6 mL of acetic acid is added, and the mixture is aggressively stirred for two hours. The resultant solution is heated in a 100 mL autoclave at 180°C for 8 hours. The product should be dried for 36 hours at 80°C after being cleaned twice with ethanol and Milli-Q water. For additional investigation, finely powder the dry materials. The experimental procedure diagram is shown in **Fig 5.1**.

## 5.3 RESULTS AND DISCUSSION

### 5.3.1 X-ray diffraction (XRD) Analysis

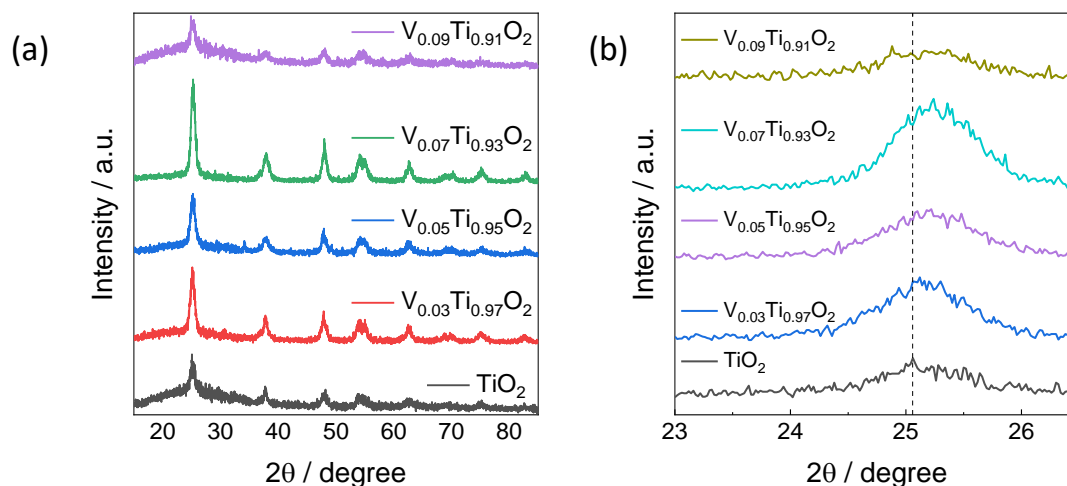


**Figure 5.2.** (a) XRD plot  $\text{TiO}_2$  and  $\text{V}_x\text{Ti}_{1-x}\text{O}_2$  ( $x = 0.03, 0.05, 0.07$  and  $0.09$ ); (b) A shift in the (101) peak towards a higher diffraction angle.

XRD examination was used to evaluate the phase purity and crystalline structure of all materials, as shown in **Fig 5.2 (a)**. In accordance with JCPDS card number 71-1168, the  $\text{TiO}_2$  sample showed six unique diffraction peaks, suggesting its existence in the tetragonal Anatase phase. Apart from the pure  $\text{TiO}_2$  and  $\text{V}_x\text{Ti}_{1-x}\text{O}_2$  ( $x = 0.03, 0.05, 0.07$ , and  $0.09$ ) phases, which showed no variation in composition. Slight differences in peak intensity and diffraction patterns were found by XRD analysis; these differences were most pronounced in the (1 0 1) plane, as shown in **Fig 5.2 (b)**. These modifications verify that host material has been successfully doped. Additionally, the dopant and Ti ionic radii are similar, suggesting that the doping mechanism is substitutional and only involves the replacement of Ti ions in the  $\text{TiO}_2$  lattice.

### 5.3.2 Cyclic Voltammetry (CV) Analysis

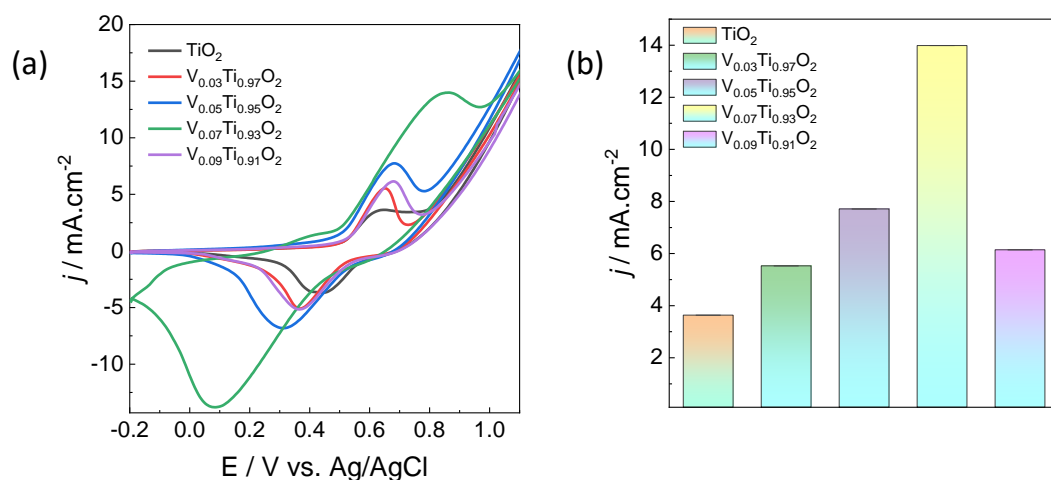


**Figure 5.3.** (a) CV analysis of  $\text{TiO}_2$  and  $\text{V}_x\text{Ti}_{1-x}\text{O}_2$  ( $x = 0.03, 0.05, 0.07$  and  $0.09$ ) in  $0.1 \text{ M KOH}$  at scan rate of  $50 \text{ mV/s}$ ; (b) Comparison of all the electrode in bar graph.

Using CV at a scan rate of  $50 \text{ mV/s}$ , all synthetic materials,  $\text{TiO}_2@\text{NF}$  and  $\text{V}_x\text{Ti}_{1-x}\text{O}_2$  ( $x = 0.03, 0.05, 0.07$  and  $0.09$ ), were investigated in a potential range of  $-0.2$  to  $1.1 \text{ V}$  vs  $\text{Ag/AgCl}$ . The findings, as shown in **Fig 5.3 (a-b)**, show that  $\text{V}_{0.07}\text{Ti}_{0.93}\text{O}_2@\text{NF}$  exhibits much greater activity than  $\text{TiO}_2@\text{NF}$ .  $\text{V}_{0.07}\text{Ti}_{0.93}\text{O}_2@\text{NF}$  exhibits significantly enhanced anodic and cathodic peaks, according to the analysis of the CV data. The increased crystallinity of the material, which adds additional defects to the  $\text{TiO}_2$  structure, is responsible for this improved performance. Because of such defects, the resulting higher electron transfer rates indicate higher activity for  $\text{V}_{0.07}\text{Ti}_{0.93}\text{O}_2@\text{NF}$  compared to  $\text{TiO}_2@\text{NF}$ .

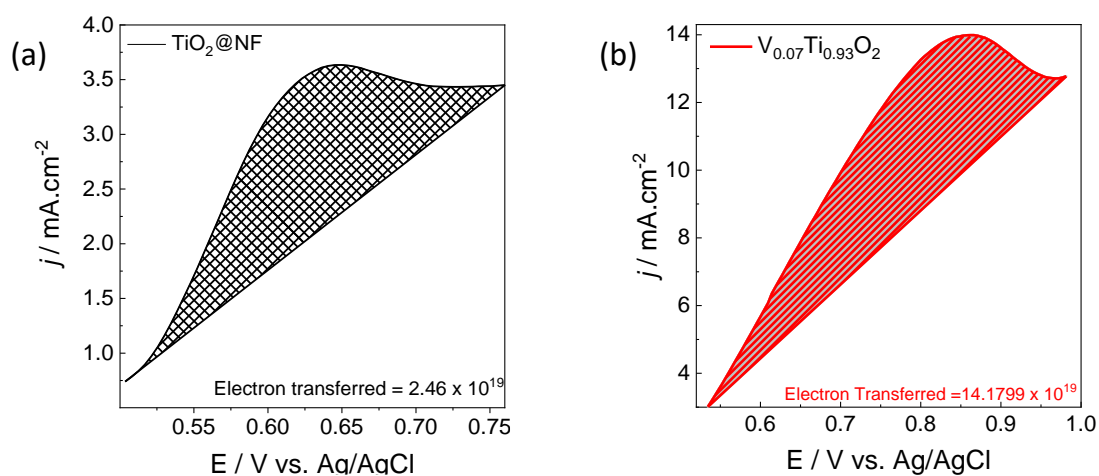


**Figure 5.4.** Oxidation peak of (a)  $\text{TiO}_2@\text{NF}$ ; (b)  $\text{V}_{0.07}\text{Ti}_{0.93}\text{O}_2@\text{NF}$  in 0.1 M KOH

Moreover, the selection of  $\text{V}_{0.07}\text{Ti}_{0.93}\text{O}_2$  may be further demonstrated by determining the surface-active sites from the redox peak current shown in **Fig 5.4 (a-b)**. The best materials' recorded CV will be useful in determining the surface-active sites, in addition to the quantity of electrons transported in the redox peak. The oxidation peak is taken into account in this work to determine the number of electrons transported, which is determined to be  $2.46 \times 10^{19}$  for  $\text{TiO}_2@\text{NF}$  and  $14.1799 \times 10^{19}$  for  $\text{V}_{0.07}\text{Ti}_{0.93}\text{O}_2@\text{NF}$ , as shown in **Fig 5.4 (a-b)** respectively. This shows unequivocally that  $\text{V}_{0.07}\text{Ti}_{0.93}\text{O}_2@\text{NF}$  is the best material and has the highest number of electron transfers in its anodic peak.

### 5.3.3 Field Emission Scanning Electron Microscopy (FE-SEM) Analysis

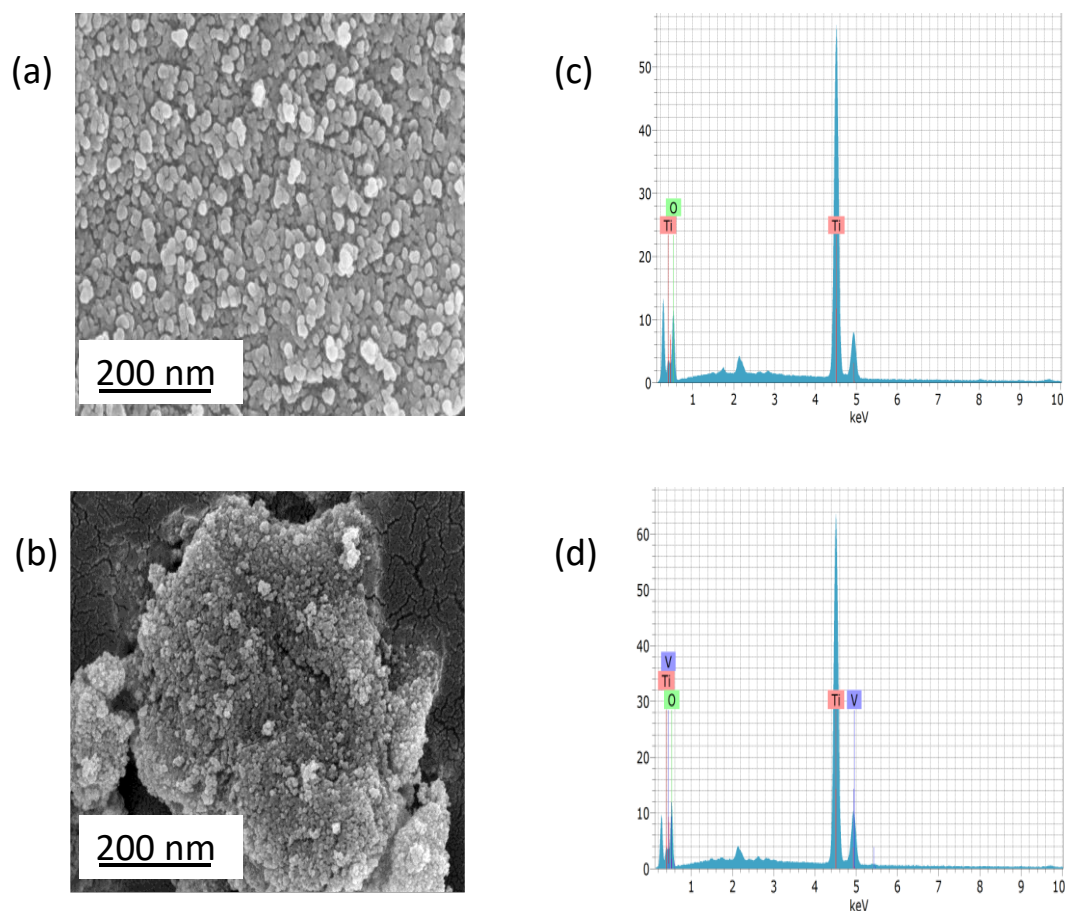


**Figure 5.5.** FE-SEM analysis of (a)  $\text{TiO}_2$ ; (b)  $\text{V}_{0.07}\text{Ti}_{0.93}\text{O}_2$ ; EDS of (c)  $\text{TiO}_2$ , (d)  $\text{V}_{0.07}\text{Ti}_{0.93}\text{O}_2$ .

The morphological properties of  $\text{V}_{0.07}\text{Ti}_{0.93}\text{O}_2$  and  $\text{TiO}_2$  materials were examined using FE-SEM analysis; the findings are shown in **Fig. 5.5 (a-b)**. The analysis showed that the mesoporous structure that both materials displayed was unaffected by the addition of V. However, observable variations in agglomeration levels and particle size were noted. Significantly, **Fig 5.5 (a)** showed less agglomeration than its pure  $\text{TiO}_2$  equivalent, suggesting that V doping could cause more agglomeration, as shown by **Fig 5.5 (b)**. Furthermore, as shown in **Fig 5.5 (c-d)**, EDS verified the elemental composition, demonstrating that Ti and O were present in the pure sample and that the addition of V dopant in  $\text{TiO}_2$  validated the doping process within the system.

### 5.3.4 UV-Visible Spectra and Bandgap Study

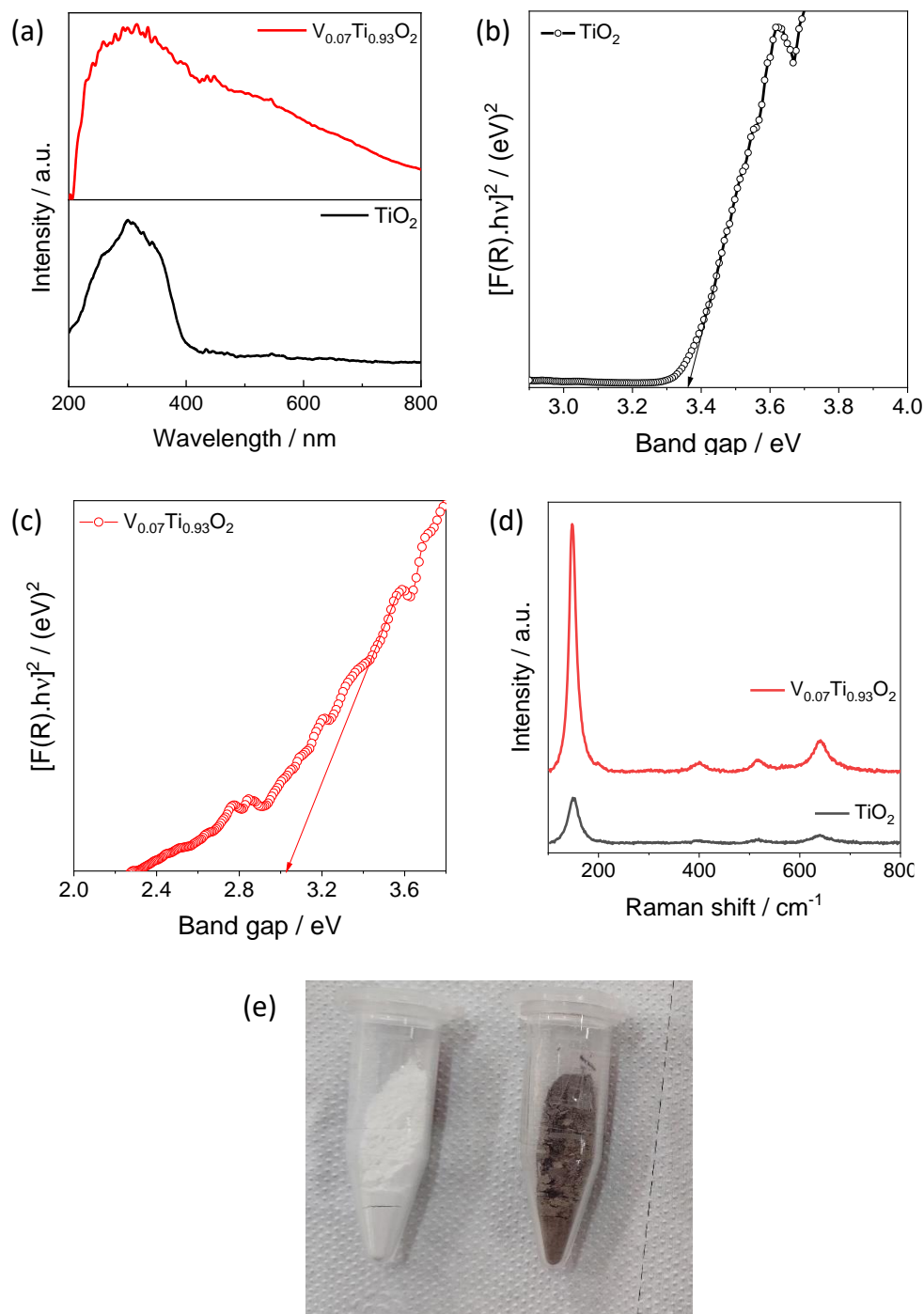


**Figure 5.6.** UV-Vis analysis of (a)  $TiO_2$  and  $V_{0.07}Ti_{0.93}O_2$ ; Optical band-gap energy of (b)  $TiO_2$ ; (c)  $V_{0.07}Ti_{0.93}O_2$ ; Raman analysis of (d)  $V_{0.07}Ti_{0.93}O_2$  and  $TiO_2$ ; (e) The synthesized  $TiO_2$  and  $V_{0.07}Ti_{0.93}O_2$ .

UV-Vis absorption spectra of  $V_{0.07}Ti_{0.93}O_2$  and pure  $TiO_2$  are represented in **Fig 5.6 (a)**. The 200–330 nm region exhibits a strong peak in the pure  $TiO_2$  spectra. Then, as shown in **Fig 5.6 (b-c)**, the band gaps of the materials were calculated by graphing the square of the Kubelka-Munk function,  $f(R)^2$ , versus energy in electron volts. The band gap of pure  $TiO_2$  is 3.36 eV, but the band gap of  $V_{0.07}Ti_{0.93}O_2$  is 3.03 eV less. Moreover, the visual difference between the materials is seen in **Fig 5.6 (e)**, where  $V_{0.07}Ti_{0.93}O_2$  appears as dark brown and pure  $TiO_2$  is white in colour. The changes in optical characteristics brought about by the doping procedure are reflected in this visual differentiation.

Raman spectra analysis of  $V_{0.07}Ti_{0.93}O_2$  and pure  $TiO_2$  are displayed in **Fig 5.6 (d)**. Four distinct Raman-active peaks are seen. In pure  $TiO_2$ , these peaks are centered at approximately  $147\text{ cm}^{-1}$  ( $E_g$ ),  $395\text{ cm}^{-1}$  ( $B_{1g}$ ),  $516\text{ cm}^{-1}$  ( $A_{1g}$ ), and  $640\text{ cm}^{-1}$  ( $E_g$ ). Upon doping with vanadium, the peaks exhibit shifts to  $150\text{ cm}^{-1}$ ,  $400\text{ cm}^{-1}$ ,  $516\text{ cm}^{-1}$ , and  $639\text{ cm}^{-1}$ . The observed light blue shift of the peak at  $150\text{ cm}^{-1}$  indicates the incorporation of vanadium into  $TiO_2$  host sites, possibly attributed to oxygen defects. This observation confirms the successful incorporation of vanadium into the  $TiO_2$  host site (Kashale et al. 2019; Kunnamareddy et al. 2021; Thuy et al. 2012).

### 5.3.5 Electrochemical Active Surface Area (ECSA) Analysis

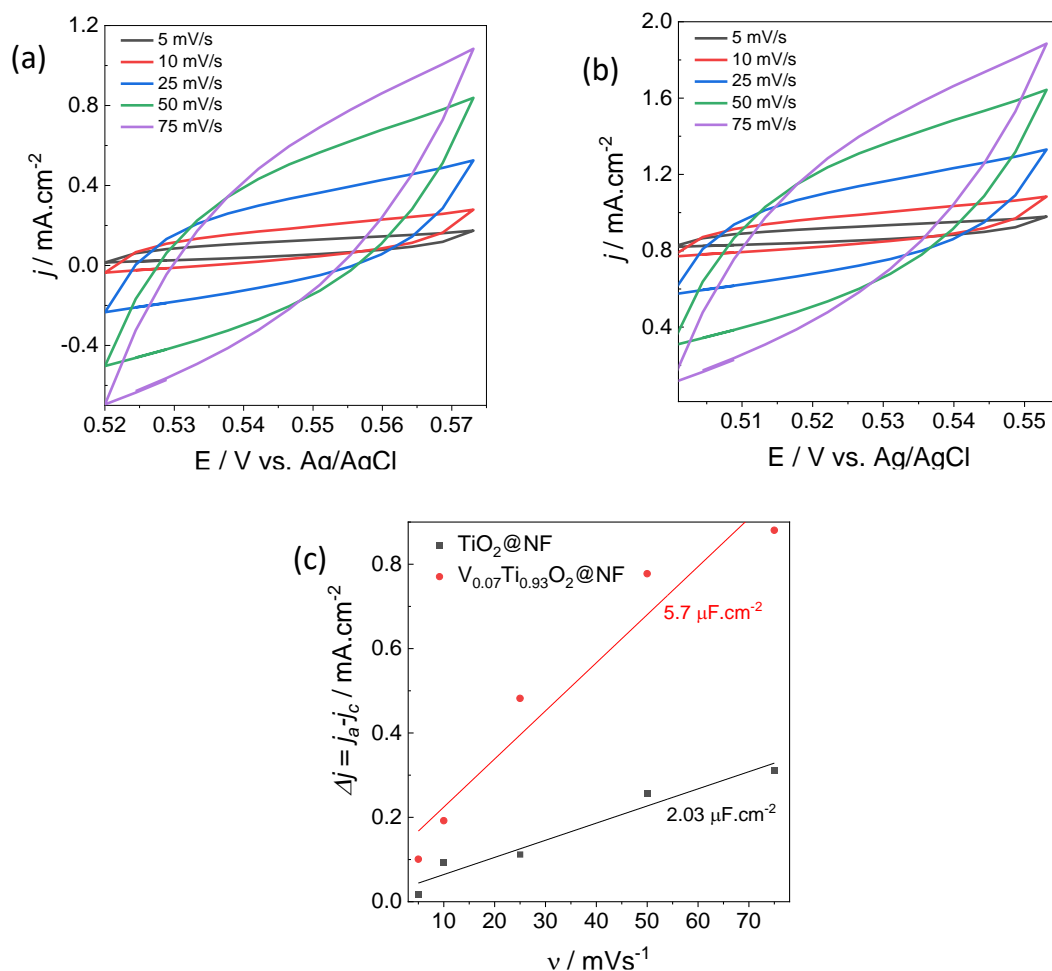


**Figure 5.7.** CV curve at different scan rates of (a)  $\text{TiO}_2@\text{NF}$ ; (b)  $\text{V}_{0.07}\text{Ti}_{0.93}\text{O}_2@\text{NF}$ ; (c) ECSA plot of  $\text{TiO}_2@\text{NF}$  and  $\text{V}_{0.07}\text{Ti}_{0.93}\text{O}_2@\text{NF}$ .

Using CV study for different scan rates, the  $\text{TiO}_2@\text{NF}$  and  $\text{V}_{0.07}\text{Ti}_{0.93}\text{O}_2@\text{NF}$  electrode comparison are shown in **Fig 5.7 (a-b)**, whereas, the ECSA study accurately calculates the material's surface area activity as shown in **Fig 5.7 (c)**, unlike BET research, the material is entirely immersed in the electrolyte.  $\text{V}_{0.07}\text{Ti}_{0.93}\text{O}_2$  and  $\text{TiO}_2$  had  $C_{dl}$  values of  $5.7 \mu\text{F}\cdot\text{cm}^{-2}$  and  $2.03 \mu\text{F}\cdot\text{cm}^{-2}$ , respectively.  $\text{V}_{0.07}\text{Ti}_{0.93}\text{O}_2$  and  $\text{TiO}_2$  were found to have electrochemically active surface areas of  $0.1425 \text{ cm}^2$  and  $0.0507 \text{ cm}^2$ , respectively.  $\text{V}_{0.07}\text{Ti}_{0.93}\text{O}_2@\text{NF}$  is the material that stands out as being ideal since it has more active sites than  $\text{TiO}_2@\text{NF}$  electrodes.

### 5.3.6 High-Resolution Transmission Electron Microscopy (HR-TEM) Analysis

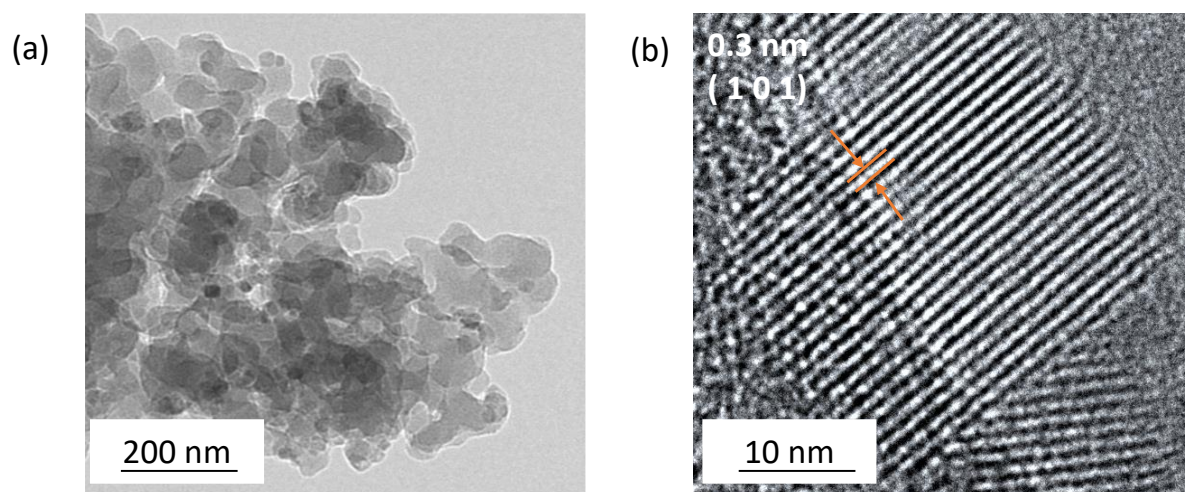


**Figure 5.8.** (a) TEM and (b) HR-TEM images of  $V_{0.07}Ti_{0.93}O_2$

The HR-TEM images in Fig. 5.8 (a-b) show the morphology of  $V_{0.07}Ti_{0.93}O_2$ , with uniform fringes and particle agglomeration which aligns with the results from the FE-SEM analysis. Notably, the doped material  $V_{0.07}Ti_{0.93}O_2$  exhibits uniform fringes with an approximate 0.3 nm spacing, corresponding to the (1 0 1) plane of the anatase phase with tetragonal structure, in accordance with JCPDS card no: 71-1168. This observation suggests the retention of the host material within the synthesized sample.

### 5.3.7 Electrochemical Analysis

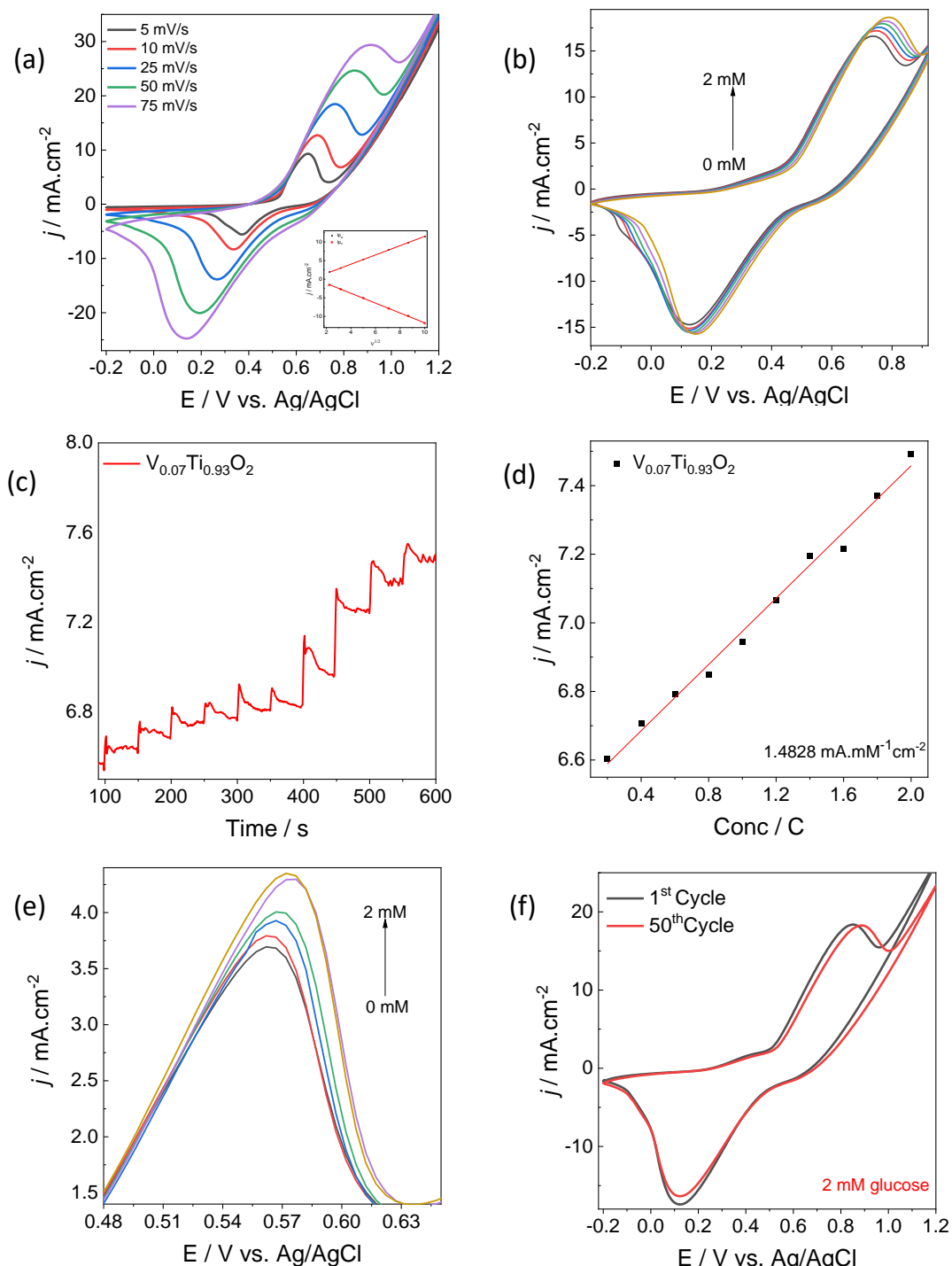


**Figure 5.9** (a) Cyclic voltammogram of  $V_{0.07}Ti_{0.93}O_2@NF$  in 0.1 M KOH with the scan rate of 5-75 mV/s. The corresponding anodic and cathodic peak current as the function of the square root of the scan rate (Inset); (b) The successive addition of

*glucose in 0.1 M KOH at the scan rate of 50mV/s; (c) The CA study of  $V_{0.07}Ti_{0.93}O_2@NF$  in 0.1 M KOH with the successive addition of glucose in stirring condition. Applied potential: 0.75 V; (d) Calibration plot of the  $V_{0.07}Ti_{0.93}O_2@NF$  for the determination of the glucose; (e) DPV study of  $V_{0.07}Ti_{0.93}O_2@NF$  in 0.1 KOH with the successive addition of glucose; (f) Cyclic stability of the  $V_{0.07}Ti_{0.93}O_2@NF$  in 0.1 KOH with the presence of 2 mM glucose.*

The synthesized  $V_{0.07}Ti_{0.93}O_2@NF$  was evaluated by doing a CV analysis on it at various scan rates, ranging from 5-75 mV/s, as shown in **Fig 5.9 (a)**. This research explains the characteristics and response kinetics of the modified electrodes and examines how scan rate affects anodic and cathodic peak currents. The formation of the diffusion layer explains why anodic and cathodic peaks rise in proportion to an increase in scan rate. As the scan rate rises, the diffusion layer grows thinner. Conversely, a decreased scan rate results in a wider diffusion layer, which in turn reduces the peak currents of the anodic and cathodic phases. This result implies that the size of the diffusion layer has a major role in regulating the accessibility of electroactive materials to the electrode surface. At elevated scan rates, the opposite trend is observed. The anodic peak rises toward the positive side and the cathodic peak toward the negative side as the scan rate rises. As shown in the inset, the redox properties of  $V_{0.07}Ti_{0.93}O_2@NF$  show a linear correlation with the square root of the scan rate. This signifies that electron transfer via the outer sphere mechanism demonstrates that electroactive species are unable to move through the diffusion layer.

The analysis of successive glucose additions in 0.1 M KOH is shown in **Fig 5.9 (b)**. As glucose is introduced, the trend indicates a steady increase in the anodic peak, indicating the electrocatalytic oxidation of glucose. The observed increase in the anodic peak can be attributed to the expansion of the diffusion layer of the analyte. As a consequence, its electrochemical activity makes it effective when used as an amperometric sensor to monitor glucose.  $V_{0.07}Ti_{0.93}O_2@NF$  was used as the sensing material in CA experiments to assess the analytical performance of an enzyme-free glucose sensor as shown in **Fig 5.9 (c)**. A range of quantities of glucose, from 0.2 mM to 2 mM, was applied in order to evaluate the sensor's linear response. A fixed potential of 0.75 V was used for the amperometric investigation, and stirring conditions were

maintained. The amperometric response was measured every 60 s after each addition of glucose. The material had a progressively rising behavior upon the addition of glucose, as seen by the stepwise increase in current, which suggested an improvement in the anodic peak. This effect is caused by the material's capacity to detect each addition of glucose, which leads to variations in current that are attributed to an increased analyte diffusion layer close to the working electrode's surface.

The calibration curve of the glucose sensor shows a linear range between 0.2 mM and 2 mM, as shown in **Fig 5.9 (d)**. This corresponds to the analysis of the material's sensitivity, LOQ, and LOD, which show values of  $1482.8 \mu\text{A mM}^{-1} \text{cm}^{-2}$ , 488  $\mu\text{M}$ , and 1.629  $\mu\text{M}$  respectively. The sensor has a notable rapid response time of 2 sec.

The DPV study demonstrated significantly improved reproducibility, thereby enhancing the reliability of DPV analysis. The linear range of 0.4 mM to 2 mM, the DPV analysis of  $\text{V}_{0.07}\text{Ti}_{0.93}\text{O}_2@\text{NF}$ , depicted in **Fig 5.9 (e)**, revealed successive additions of glucose in 0.1 M KOH solution at a scan rate of 5 mV/s. Remarkably, a change in current was observed with each addition of glucose. This collective evidence underscores the responsive nature of  $\text{V}_{0.07}\text{Ti}_{0.93}\text{O}_2@\text{NF}$  to glucose, attributable to its mesoporous characteristics coupled with defects within the  $\text{TiO}_2$  structure, enabling the material to detect the glucose analyte.

The long-term stability of  $\text{V}_{0.07}\text{Ti}_{0.93}\text{O}_2@\text{NF}$  was evaluated by subjecting the electrode to 50 cycles in the presence of 2 mM glucose. The results, illustrated in **Fig 5.9 (f)**, revealed a remarkable 98% retention of anodic current. This finding suggests that the material is well-suited for extended analysis, with outstanding shelf life, indicating the ability to reuse the same electrode across various occasions with minimal depletion in response.

### 5.3.8 Post-Glucose Oxidation Characterization

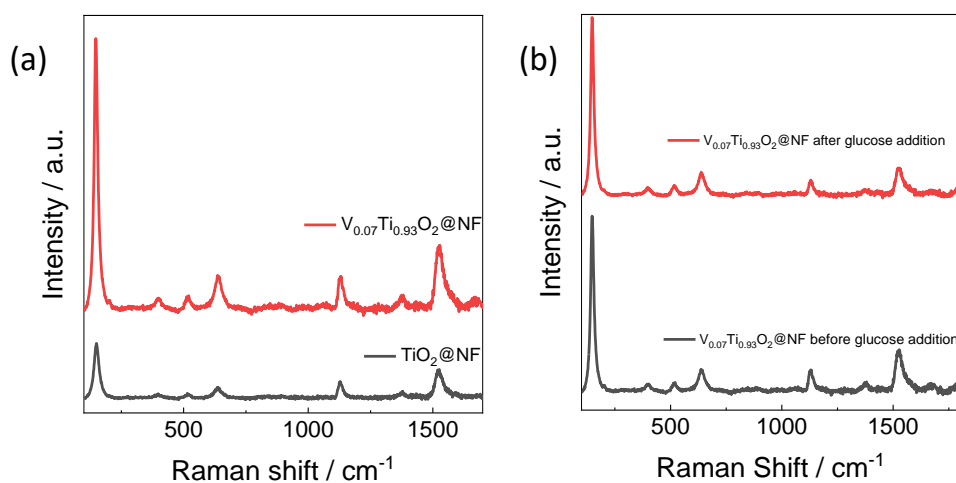


**Figure 5.10.** (a) Raman analysis of  $\text{TiO}_2@\text{NF}$  and  $\text{V}_{0.07}\text{Ti}_{0.93}\text{O}_2@\text{NF}$ ; (b) Raman analysis of  $\text{V}_{0.07}\text{Ti}_{0.93}\text{O}_2@\text{NF}$  before and after glucose addition.

Raman analysis of the  $\text{TiO}_2@\text{NF}$  and  $\text{V}_{0.07}\text{Ti}_{0.93}\text{O}_2@\text{NF}$  are illustrated in **Fig 5.10 (a)**, respectively. The material is confirmed by the remaining peak of  $\text{TiO}_2@\text{NF}$ , which fits the Raman spectra of  $\text{V}_{0.07}\text{Ti}_{0.93}\text{O}_2@\text{NF}$ . The peaks at 1132, 1376, and 1572  $\text{cm}^{-1}$  correspond to the NF. **Fig 5.10 (b)** shows the Raman spectra before and after the glucose addition of  $\text{V}_{0.07}\text{Ti}_{0.93}\text{O}_2@\text{NF}$ . It demonstrates the fact that, even with the addition of glucose, there is no such alteration in the other peaks. As demonstrated in **Table 5.1**, the observed biosensing characteristics are equivalent to and superior to those of published glucose biosensors.

**Table 5.1.** List of Electrochemical performance of non-enzymatic glucose sensors

<b>ELECTRODE</b>	<b>LINEAR RANGE</b>	<b>SENSITIVITY (<math>\mu\text{A. mM}^{-1}\text{cm}^{-2}</math>)</b>	<b>Ref.</b>
Co <sub>2</sub> P/NPCNT	0 – 7 mM	388.8	(Das et al. 2017)
Au@Cu(OH) <sub>2</sub> /CFC	100 $\mu\text{M}$ – 3.30 mM	7350	(Jiang et al. 2019)
PLA/GR/Pani/Cu	1 – 7 mM	-	(Estadulho et al. 2021)
AuNPs/PANI	10.26 $\mu\text{M}$ – 10 mM	150	(Xu et al. 2017)
V <sub>0.07</sub> Ti <sub>0.93</sub> O <sub>2</sub> @NF	0.2-2 mM	1482.8	This work

#### 5.4 Conclusions

- In summary, this work involved the synthesis, fabrication, and electrochemical analyses of TiO<sub>2</sub> and V<sub>x</sub>Ti<sub>1-x</sub>O<sub>2</sub> (x = 0.03, 0.05, 0.07, and 0.09) nanoparticles. Among other things, V<sub>0.07</sub>Ti<sub>0.93</sub>O<sub>2</sub>@NF performed better in electrochemical tests than the basis material.
- This material has a crystalline form, mesoporous behavior, greater surface area, and improved electron mobility.
- In particular, the V<sub>0.07</sub>Ti<sub>0.93</sub>O<sub>2</sub> @NF electrode showed impressive characteristics, with a detection limit of 488  $\mu\text{M}$  a sensitivity of 1482.8  $\mu\text{A mM}^{-1}\text{cm}^{-2}$ , and a quick response of 2 secs.
- The rapid, low-cost synthesis and potent medicinal benefits of V<sub>0.07</sub>Ti<sub>0.93</sub>O<sub>2</sub>@NF support its commercial potential. Its efficient glucose-sensing properties make it suitable for various medical applications.

\*\*\*\*\*

## **CHAPTER 6**

---

---

### **CERIUM-MODULATED ZINC OXIDE FOR PHOTOELECTROCHEMICAL NON-ENZYMATIC BIOSENSING OF CHOLESTEROL: EXPERIMENTAL AND FIRST PRINCIPLE ANALYSIS**

---

---



---

---

**Abstract:** *This chapter explores the synthesis and characterization of Cerium-modulated Zinc Oxide (CZOx) at doping levels of  $x = 1, 2,$  or  $3$  to improve electrochemical cholesterol measurement. The CZO3 materials are used to develop a novel photoelectrochemical cholesterol biosensor. Detailed structural, morphological, and electrochemical analyses highlight their potential for efficient biosensing applications.*

---

---

## 6.1 Introduction

Cholesterol, a crucial component in living organisms, plays a vital role in synthesizing bile acids, vitamin D, and steroid hormones, while also forming cell membranes (Levitan et al. 2010; Sulimovici and Boyd 1970). Lipoproteins, compounds of lipids and proteins, facilitate cholesterol transport in the blood, including chylomicrons, very low-density lipoproteins (VLDL), low-density lipoproteins (LDL), and high-density lipoproteins (HDL). Maintaining a healthy blood cholesterol level below 5.17 mM (200 mgdL<sup>-1</sup>) is crucial, as levels exceeding 6.21 mM (240 mgdL<sup>-1</sup>) are linked to disorders like hypertension and coronary heart disease (Narwal et al. 2019; Yadav et al. 2021). Accurate cholesterol detection is vital in medical diagnostics, given its association with cardiovascular issues.

Quick and accurate cholesterol measurement is essential for disease prevention. Traditional methods, though sensitive, are costly and slow. Nanotechnology improves biosensors with nanomaterials offering better selectivity, simplicity, cost-effectiveness, and quick response times, ideal for point-of-care diagnostics (Bai and Zhou 2014; Wang 2005). Advanced electrochemical cholesterol sensors are particularly promising. Since Becquerel's 1839 (Devadoss et al. 2015) explanation of the photoelectric effect, photoelectrochemistry has gained interest for its applications in various fields, including sensor technologies (Han et al. 2013).

Photoelectrochemistry primarily investigates the way light influences photoelectrodes and the subsequent photoelectric conversion process (Grätzel 2001; Kang et al. 2016). The primary emphasis is on the way photoelectric materials absorb photons, resulting

in an excited state and eventual charge separation, which ultimately turns light energy into electric energy via this process (Hagfeldt et al. 2010; Peter 1990). As separated electron-hole pairs approach the junction between the electrode surface and the electrolyte solution, they initiate an oxidation-reduction process that results in a photovoltaic or photocurrent during photoelectrochemical (PEC) reactions (Ge et al. 2019; Ham et al. 2010; Zhao et al. 2015).

PEC biosensors use the above technique for quantitative analysis of the analyte based on current measurements, this photocurrent acts as the detection signal. This makes PEC sensors popular due to their quick response, increased sensitivity, affordability, and mobility, and they outperform traditional electrochemical counterparts by reducing background signals and enhancing sensitivity through light-induced photocurrent (Shu and Tang 2017; Wang et al. 2023; Yang et al. 2020). PEC sensors are distinguished by their ease of use, and versatility in terms of miniaturization and known for ease of use and versatility in miniaturization, employ various nanomaterials in electrode preparation, such as inorganic, organic, or composites, to achieve ultrasensitive and selective sensing platforms (Yu et al. 2023).

Photoelectric sensing materials that are often used include metal-based materials like metal nanoparticles, metal oxides, and quantum dots, as well as carbon-based nanomaterials like graphene, fullerene, and carbon nanotubes, and organic-inorganic based perovskites (Feng et al. 2022). Rapid electron transit and greater surface area of nanoparticles provide improved sensitivity, while functionalized nanomaterials enhance selectivity and increase effectiveness through their ability to compact and incorporate into portable electronics. The use of nanomaterials improves the overall performance of cholesterol biosensors (Lee and Park 2010; Phetsang et al. 2019; Yadav et al. 2021).

Zinc oxide (ZnO) is a pivotal semiconductor known for its versatility in high-performance electronics, energy applications, and environmental solutions. With its unique properties, including high stability, binding energy, and a wide band gap, ZnO finds applications in optoelectronics, laser technology, ceramics, and biomedicine, photocatalysis, sensing, and energy generation in hydrogen production (Beitollahi et al. 2020; Reinert et al. 2013). The nanostructured form of ZnO amplifies its advantages,

making it an ideal compound for efficient sensors and biosensors, with features like a wide band gap, large excitation binding energy, non-toxicity, and biocompatibility (Beitollahi et al. 2020; Chaudhary et al. 2018). In our study, we synthesized Cerium-doped ZnO ( $\text{Ce}_x\text{Zn}_{1-x}\text{O}$ ,  $x = 0.00, 0.01, 0.02, \text{ and } 0.03$ ) through a wet chemical method and deposited it onto Nickel Foam (NF). The synthesized material underwent PEC-based analyses, including Cyclic Voltammetry (CV), Chronoamperometry (CA), and Differential Pulse Voltammetry. Our investigation focuses on the impact of cerium incorporation on enhancing photocatalytic properties, improving sensitivity, increasing optical properties, reducing the bandgap, enhancing stability, minimizing electron-hole recombination, and decreasing interference. Concurrently, we explored material selection using a Density Functional Theory (DFT) approach. The DFT results, aligned with experimental data, revealed cholesterol adsorption-induced charge transfer on the material surface. Additionally, the study involves the evaluation of actual blood cholesterol samples.

## 6.2 Experimental Method

### 6.2.1 Chemicals Reagents

Zinc nitrate hexahydrate ( $\text{Zn}(\text{NO}_3)_2$ ), Cerous nitrate hexahydrate ( $\text{Ce}(\text{NO}_3)_3 \cdot 6\text{H}_2\text{O}$ ), Sodium hydroxide ( $\text{NaOH}$ ) from Loba. The materials were employed with great purity and no additional purification was needed.

### 6.2.2 Synthesis of $\text{ZnO}$ and $\text{Ce}_x\text{Zn}_{1-x}\text{O}$

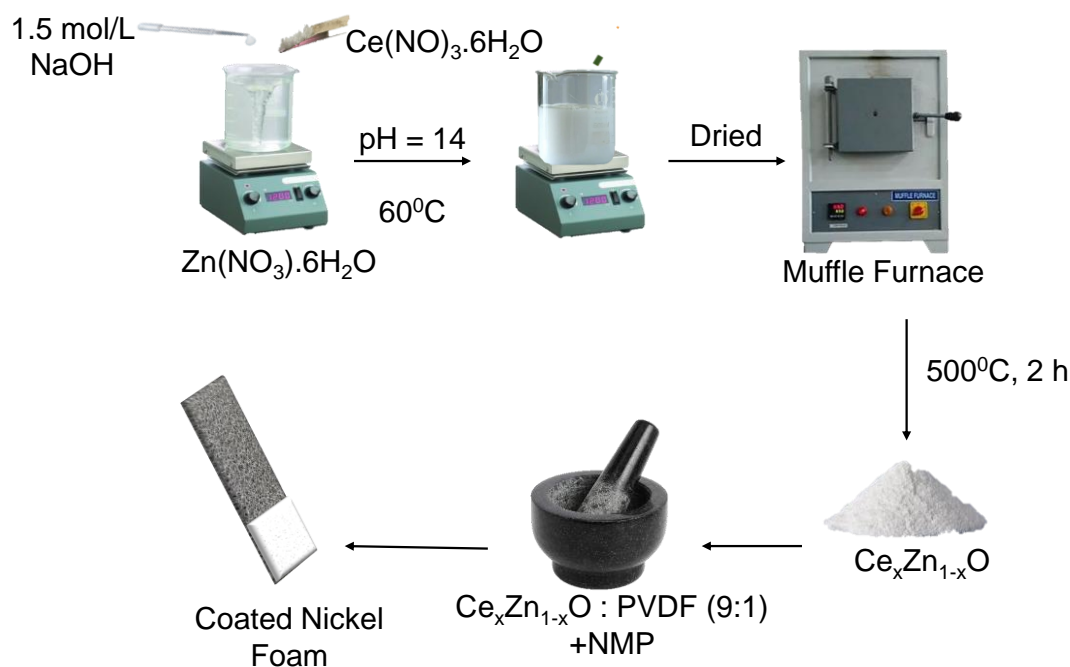


**Figure 6.1.** Schematic diagram of synthesis of the  $\text{ZnO}$  and  $\text{Ce}$  doped  $\text{ZnO}$

Cerium-doped  $\text{ZnO}$  nanoparticles were synthesized by digesting 29.748 g of  $\text{Zn}(\text{NO}_3)_2 \cdot 6\text{H}_2\text{O}$  in 100 ml of Milli-Q water. To attain a light white solution, let it warm to  $60^\circ\text{C}$  while stirring constantly, then the aforementioned solution was subsequently enriched with the calculated quantities of  $\text{Ce}$  ( $x = 0.01, 0.02$ , and  $0.03$ ), and the mixture was agitated until uniform. Add the 1.5 mol/L  $\text{NaOH}$  solution progressively dropwise until the pH of the solution reaches 14. Then, mix while heating the above-formed solution for 2 H, then without heating for 12 hours.  $\text{ZnO}$  is produced through a similar process without the incorporation of any dopant. The produced solution then needs to

have some time to stand before being repeatedly washed with deionized water twice and then with ethanol. The product obtained was 12 hours of drying at 120°C in the oven and 2 hours of calcination at 500°C in the muffle furnace. ZnO and Ce<sub>x</sub>Zn<sub>1-x</sub>O (x = 0.01, 0.02, and 0.03) nanoparticles will appear as it cools. **Fig 6.1** represents the schematic diagram of the synthesis.

### 6.2.3 Illumination Setup

Utilizing a Philips Master Colour CDM-R PAR30L 70W light source, the investigation was carried out in total darkness and with illumination.

### 6.2.4 Computational Studies

The electronic structures of pristine and Ce-doped ZnO were examined using Density Functional Theory (DFT) calculations, implemented in the Vienna Ab initio Simulation Package (VASP) (Kresse and Furthmüller 1996). The calculations employed the Projected Augmented Wave (PAW) method (Blöchl 1994), with the Generalized Gradient Approximation (GGA) and the Perdew–Burke–Ernzerhof (PBE) parameterization scheme for exchange and correlation potential estimation (Lu et al. 2016). To ensure accurate results, a large energy cut-off of 520 eV for wave functions was utilized in all calculations. The initial step involved optimizing the bulk unit cell geometry for both systems by performing a complete relaxation of the cell parameters and atomic positions based on reported experimental structures. Ce-doped ZnO models was constructed by substituting two Zn atoms with two Ce atoms in a 3 × 3 × 2 wurtzite ZnO supercell, corresponding to a dopant concentration of 3.13%, which closely matches our experimental conditions. Subsequently, (101) surface slab was generated from the optimized bulk geometry. Atomic positions in the surface-slab structure unit cell, comprising 72 atoms, were further relaxed to understand the surface properties of the pristine semiconductor. A vacuum of 15 Å along the surface-normal direction was included within the unit cell to prevent interactions between periodic images. The relaxation of all atoms inside the fixed unit cell was performed using a force convergence criterion of 0.01 eV Å<sup>-1</sup>. Brillouin zone integrations were carried out using a 2 × 3 × 1 Monkhorst *K*-point sample for all surface-based cases. Band dispersion analysis was investigated along the *K*-path G, X, H<sub>1</sub>, C, H, Y, and G for all structures

to investigate their electronic properties. The adsorption energy was calculated by using the following formula (Eq. 6.1);

$$E_a = E_{system+analyte} - E_{system} - E_{analyte} \quad (6.1)$$

### 6.3 Results and Discussion

#### 6.3.1 X-ray diffraction (XRD) Analysis

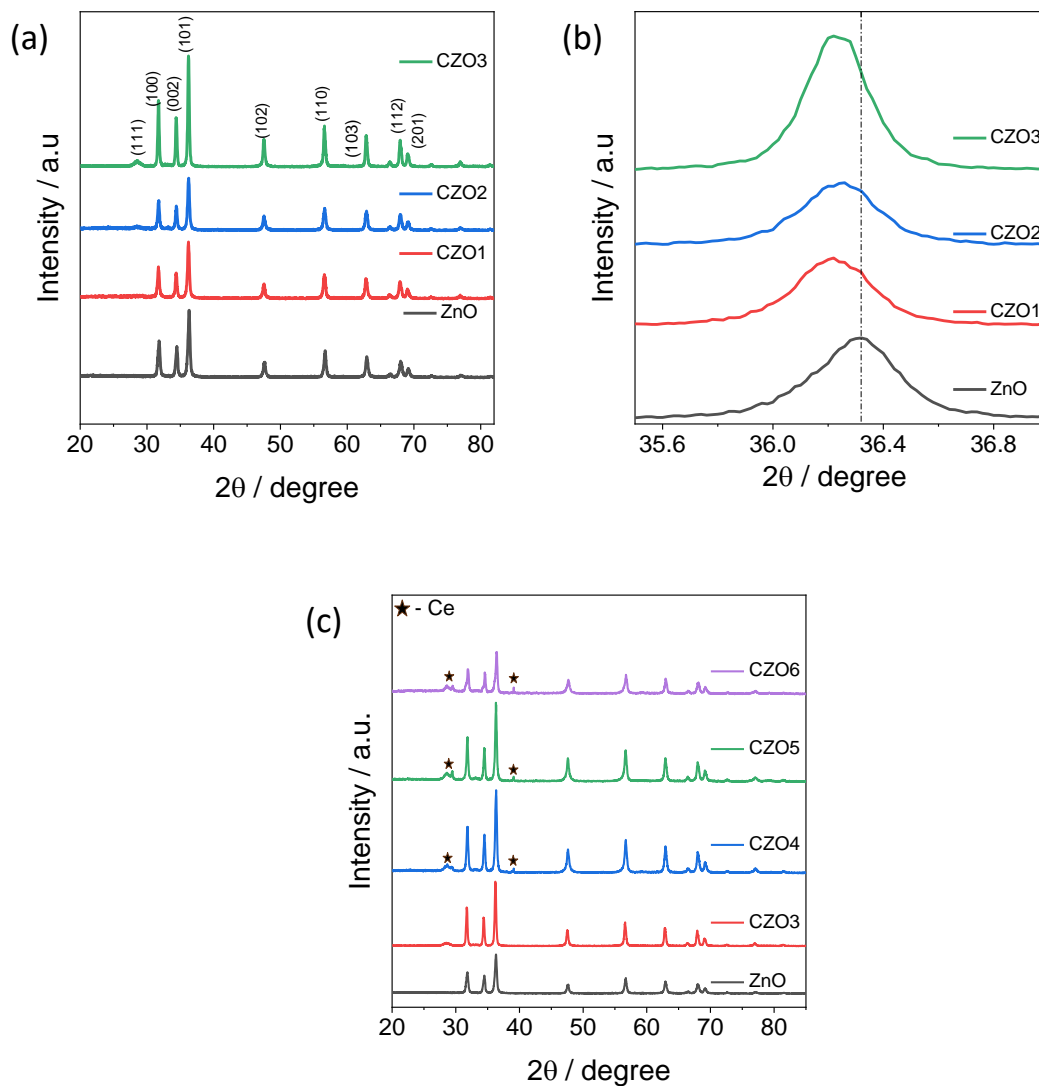


**Figure 6.2.** (a) XRD analysis of ZnO, CZO1, CZO2, and CZO3; (b) (101) XRD peak shift towards lower diffraction angle with the dopant; (c) XRD analysis of ZnO, CZO3, CZO4, CZO5 and CZO6.

According to **Fig 6.2 (a)**, it confirms the hexagonal wurtzite crystal structure of ZnO, CZO1, CZO2, and CZO3, with their respective crystalline sizes and lattice parameters, as outlined in **Table 6.2**, showing good alignment with JCPDS standards 089-0510. In **Fig 6.2 (b)**, the XRD analysis of the (101) plane reveals a subtle shift in peak position towards smaller  $2\theta$  angles in comparison to pure ZnO, indicative of Ce incorporation into the ZnO lattice and substitution of Zn ion host sites (Liu et al. 2018). This phenomenon can be ascribed to the larger ionic radii of  $\text{Ce}^{4+}$  (0.092 nm) and  $\text{Ce}^{3+}$  (0.103 nm) relative to  $\text{Zn}^{2+}$  (0.074 nm) (Faisal et al. 2013; Jung et al. 2012). We also investigated the effects of cerium doping on the structural integrity of ZnO using CZOx materials with cerium concentrations ranging from 4% to 6%, as shown in **Fig 6.2 (c)**. XRD analysis revealed the appearance of additional peaks at approximately  $28^\circ$  and  $39^\circ$  in samples with higher doping levels (4-6%), suggesting the formation of impurity phases due to cerium oxide segregation, which disrupts the ZnO lattice. This structural degradation correlates with the decline in PEC performance at doping levels above 3%. Additionally, microstrain analysis further supports this conclusion as shown in **Table 6.1** Williamson-Hall (W-H) method. As shown in the table, there is a decrease in microstrain as cerium concentrations increase from 1% to 3%, indicating the ZnO lattice can accommodate the dopant, enhancing PEC performance. However, at cerium levels above 3%, the microstrain rises again, reflecting increased lattice strain and structural disruption. These findings suggest 3% cerium doping as the optimal concentration for maintaining structural integrity and maximizing PEC efficiency, with excess doping leading to performance degradation.

**Table 6.1** Microstrain study of ZnO and CZO<sub>x</sub> ( $x = 1, 2, 3, 4, 5,$  and  $6$ ).

SAMPLES	MICROSTRAIN ( $10^{-3}$ )
ZnO	0.67
CZO1	1.73
CZO2	1.5
CZO3	1.36
CZO4	1.51
CZO5	1.8
CZO6	2.79

Additionally, introduction of Ce dopants led to an increase in crystalline size, thereby facilitating more rapid electron charge transfer (Xiao et al. 2011). Notably, **Table 6.2** highlights CZO3 as displaying the most pronounced crystalline nature, indicative of superior electron charge transfer properties compared to the other investigated materials.

**Table 6.2** XRD Parameters and Crystalline Size of the ZnO and Ce<sub>x</sub>Zn<sub>1-x</sub>O ( $x = 0.01, 0.02,$  and  $0.03$ ).

SAMPLES	a=b (Å)	c (Å)	D (nm)
ZnO	3.24	5.199	24.38
CZO1	3.25	5.21	28.39
CZO2	3.25	5.21	30.93
CZO3	3.25	5.21	39.5

### 6.3.2 Raman Analysis

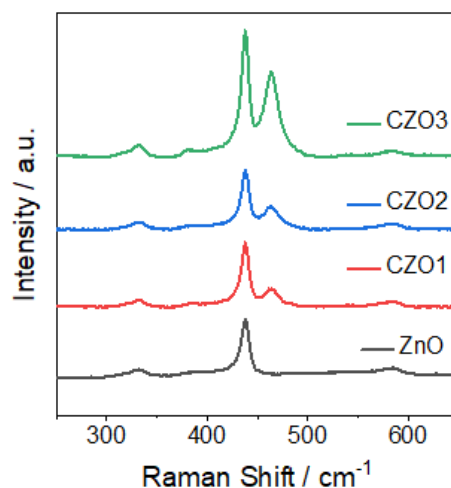


**Figure 6.3.** Raman analysis of ZnO, CZO1, CZO2 and CZO3

The Raman spectroscopy depicted in **Fig 6.3** reveals negligible distinctions among the spectra of pure ZnO, CZO1, CZO2, and CZO3. However, a discernible low-intensity absorption band at approximately  $463.5\text{ cm}^{-1}$  in all doped ZnO samples serves as confirmation of cerium presence. This band corresponds to the  $F_{2g}$  Raman active mode, indicative of the symmetric breathing motion of oxygen atoms surrounding cerium ions, elucidating their bond within the lattice (Liu et al. 2014). Furthermore, three additional vibrational modes observed at  $331.4\text{ cm}^{-1}$ ,  $437.6\text{ cm}^{-1}$ , and  $582.3\text{ cm}^{-1}$  are attributed to the crystalline structure of ZnO. Notably, the  $437.6\text{ cm}^{-1}$  peak signifies the Raman-active optical phonon  $E_2H$  vibration mode characteristic of the wurtzite hexagonal ZnO structure, consistent across all investigated  $Ce_xZn_{1-x}O$  and pure ZnO samples (Bechambi et al. 2015; Umar and Hahn 2008). This coherence with XRD findings underscores the crystalline nature of the samples, corroborating their structural integrity (Fifere et al. 2018). Noteworthy is the superior performance of CZO3, attributed to its enhanced propensity for crystallization, facilitating expedited electron transmission. The observation of a second-order Raman spectrum at  $332\text{ cm}^{-1}$ , traditionally associated with single-crystal ZnO, suggests a minor frequency shift with increased cerium content, potentially indicative of lattice distortions and oxygen vacancy formation. Additionally, the presence of a weak band at  $582\text{ cm}^{-1}$  implicates the generation of

defects such as oxygen vacancies and interstitial Zn, further contributing to the understanding of the material's structural properties (Fifere et al. 2018).

### 6.3.3 UV-Visible Analysis and Bandgap Study

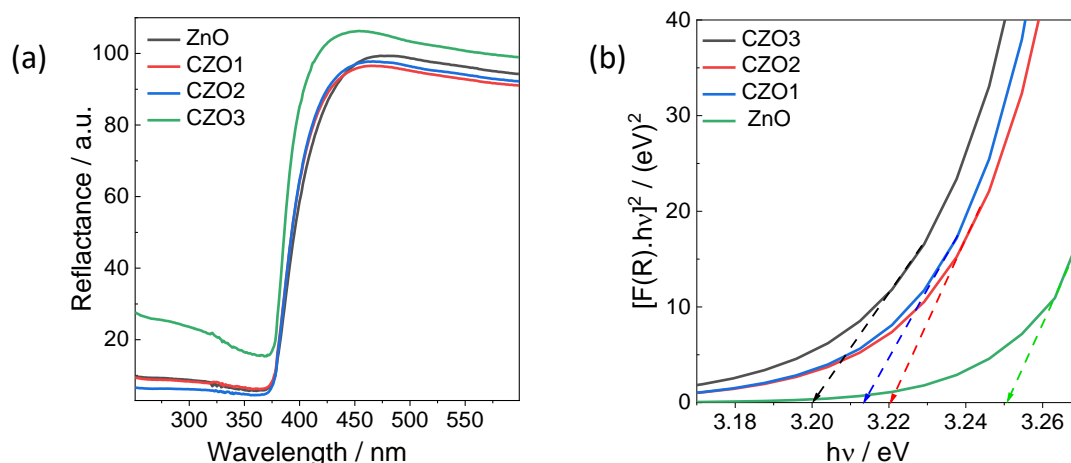


**Figure 6.4.** (a) UV-Visible spectra of ZnO, CZO1, CZO2, and CZO3; (b) Optical band-gap energy of ZnO, CZO1, CZO2, and CZO3

The optical characteristics of pure ZnO, CZO1, CZO2, and CZO3 were systematically investigated through UV-Visible spectroscopy, in conjunction with band gap analyses depicted in **Fig 6.4 (a-b)**. Notably, all synthesized materials exhibit response to visible light, as evidenced by the reflectance spectra, which manifest light-induced inter-band electronic transitions spanning from 380 to 550 nm. Utilizing the Kubelka-Munk function  $f(R)^2$  plotted against energy in electron volts, the band gap energies of these materials were discerned. Employing linear extrapolation with  $f(R)^2 = 0$ , the band gap values were determined as follows: ZnO (3.25 eV) > CZO2 (3.22 eV) > CZO1 (3.21 eV) > CZO3 (3.20 eV). This observation elucidates the phenomenon whereby the absorption edge transitions to longer wavelengths, thereby amplifying the absorption of incident light (Djaja and Saleh 2013). Notably, the CZO3 sample exhibits superior activation under visible light illumination, emerging as the most promising material for applications involving visible light. Cerium doping induces the formation of localized states, effectively generating a new lowest unoccupied molecular orbital and reducing the band gap. Consequently, electron states are introduced within ZnO's band gap,

which is closer to the conduction band's bottom edge, leading to a red shift in UV emission (Djaja and Saleh 2013).

### 6.3.4 Photoluminescence (PL) Spectra Analysis

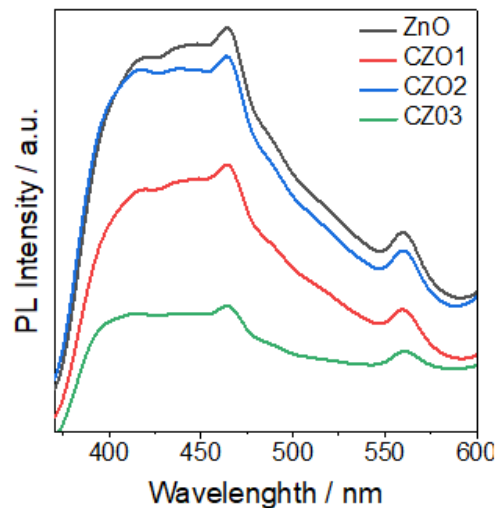


*Figure 6.5. PL spectra of ZnO, CZO1, CZO2, and CZO3*

As illustrated in **Fig 6.5**, PL spectra were recorded between 350 and 600 nm to assess the charge carrier separation efficiency. Upon excitation at a wavelength of 315 nm, broad emission spectra were observed for the samples. Notably, the emission peak intensity significantly decreased in the doped samples in the order of  $\text{ZnO} > \text{CZO1} > \text{CZO2} > \text{CZO3}$ , with the intensity maxima located at 466 nm. The emission spectra intensity, resulting from the radiative recombination of excited charge carriers, clearly indicated the degree of charge carrier separation. Among the samples, CZO3 exhibited the lowest peak intensity, indicating the least charge carrier recombination. This reduced recombination can be attributed to the additional energy sites introduced by Ce doping, which effectively trap the excited electrons, thereby preventing recombination. Consequently, CZO3 demonstrates a smaller emission peak and inhibits charge carrier recombination.

### 6.3.5 Field Emission Scanning Electron Microscopy (FE-SEM) and Energy-dispersive X-ray Spectroscopy (EDS) Analysis

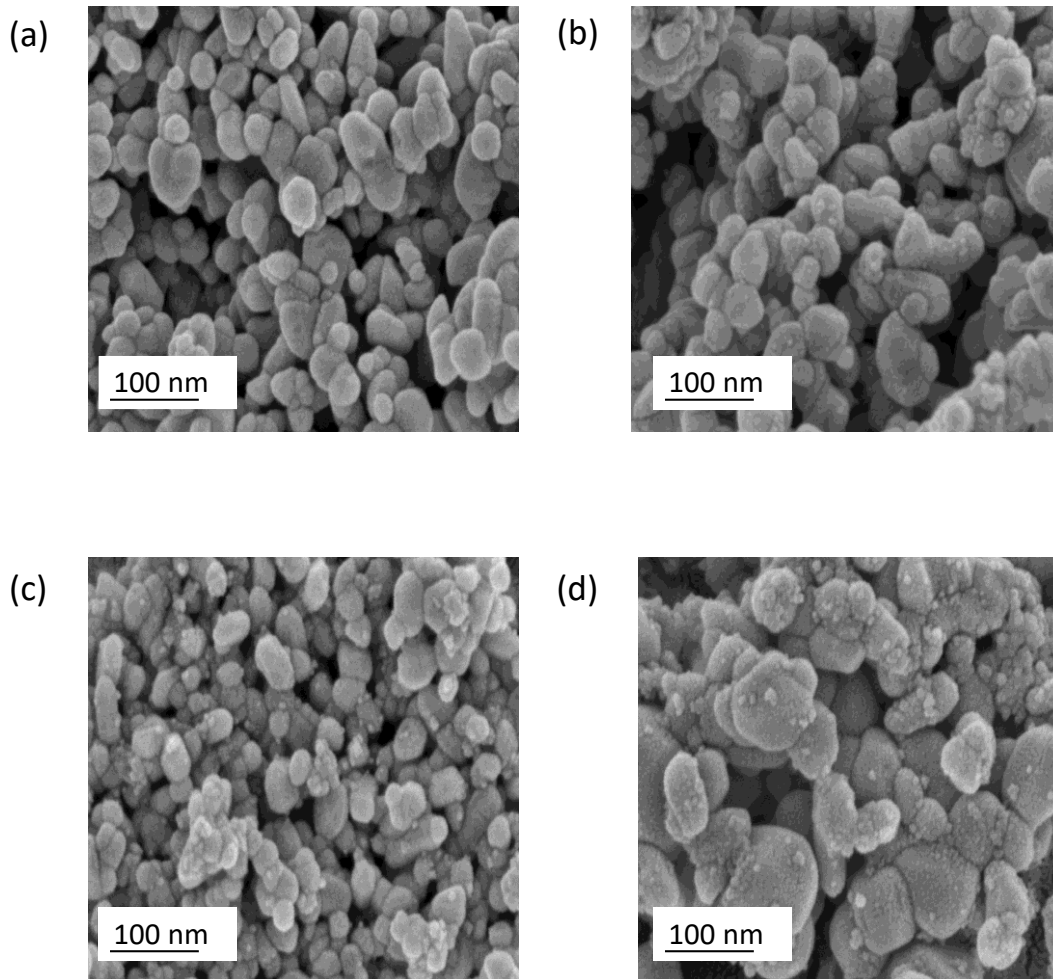


**Figure 6.6.** FE-SEM analysis of (a) ZnO; (b) CZO1; (c) CZO2; and (d) CZO3.

The morphological attributes of ZnO, CZO1, CZO2, and CZO3 are depicted in **Fig 6.6 (a-d)**. Undoped ZnO exhibits a spherical morphology characterized by a smooth surface and uniform pattern. Notably, lower concentrations of Ce doping correspond to diminished morphological degradation of the resulting products. With increasing concentrations of the dopant Ce, small granules emerge on the surfaces of CZO1, CZO2, and CZO3, exhibiting rough textures (Wen et al. 2020). The discernible variation in ionic radii between Ce and Zn facilitates the substitution of Ce for Zn within the ZnO lattice. As the concentration of Ce within ZnO increases, it has the potential to

disrupt the crystal lattice structure, thereby possibly compromising the integrity of ZnO (Liang et al. 2015).

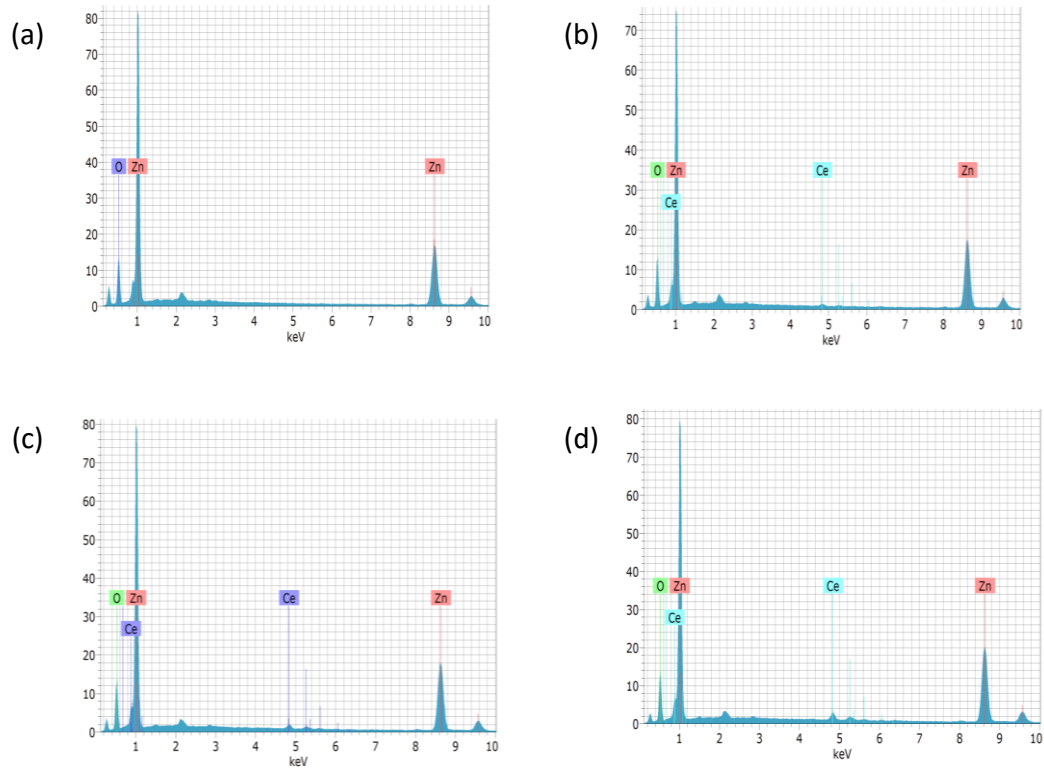


**Figure 6.7.** EDS analysis of (a) ZnO; (b) CZO1; (c) CZO2; and (d) CZO3.

Elemental composition validation via EDS corroborates the presence of Zn and O in the pure sample, alongside Ce as a dopant within the doped ZnO system, as depicted in **Fig 6.7 (a-d)**. This substantiates the incorporation of the dopant within the system, thereby confirming successful doping.

### 6.3.6 Cyclic Voltammetry (CV) Analysis

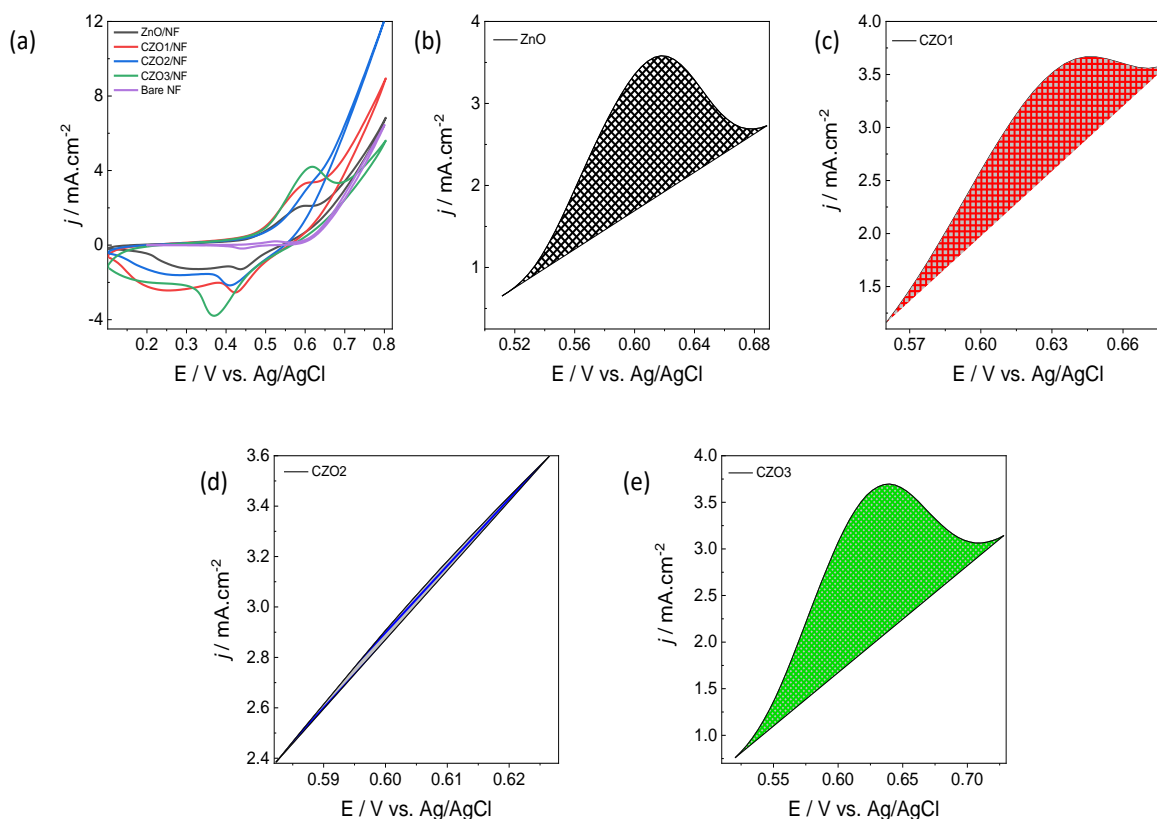


**Figure 6.8.** (a) Cyclic voltammogram of ZnO, CZO1, CZO2, CZO3 and Bare NF; Oxidation peak analysis of (b) ZnO; (c) CZO1; (d) CZO2; (e) CZO3.

Moreover, CV analyses were conducted on the synthesized ZnO samples, including ZnO, CZO1, CZO2, CZO3, and bare NF, within a potential window spanning from 0.1 to 0.8 V vs Ag/AgCl, at a scan rate of 25 mV/s, as depicted in **Fig 6.8 (a)**. Notably, CZO3 exhibits remarkable activity relative to the other materials, evidenced by both its cathodic and anodic peaks surpassing those of its counterparts. Furthermore, the selection of the electrode material can be rationalized by elucidating the electrochemical surface-active sites inferred from the redox peak current, as illustrated in **Fig 6.8 (b-e)**. The determination of surface-active sites, corresponding to the number of electrons transferred during the redox peak (Anantharaj et al. 2018), can be achieved through analysis of the recorded CV data for the optimal materials. In this investigation, the oxidation peak was utilized to quantify the electron transfers, resulting in values of  $1.79 \times 10^{19}$ ,  $0.76 \times 10^{19}$ ,  $1.33 \times 10^{19}$ , and  $2.1 \times 10^{19}$  for ZnO, CZO1, CZO2, and CZO3,

respectively. This analysis underscores CZO3 as the superior material, given its notably higher electron transfer rate during the oxidation peak.

### 6.3.7 Electrochemical Active Surface Area (ECAS) Analysis

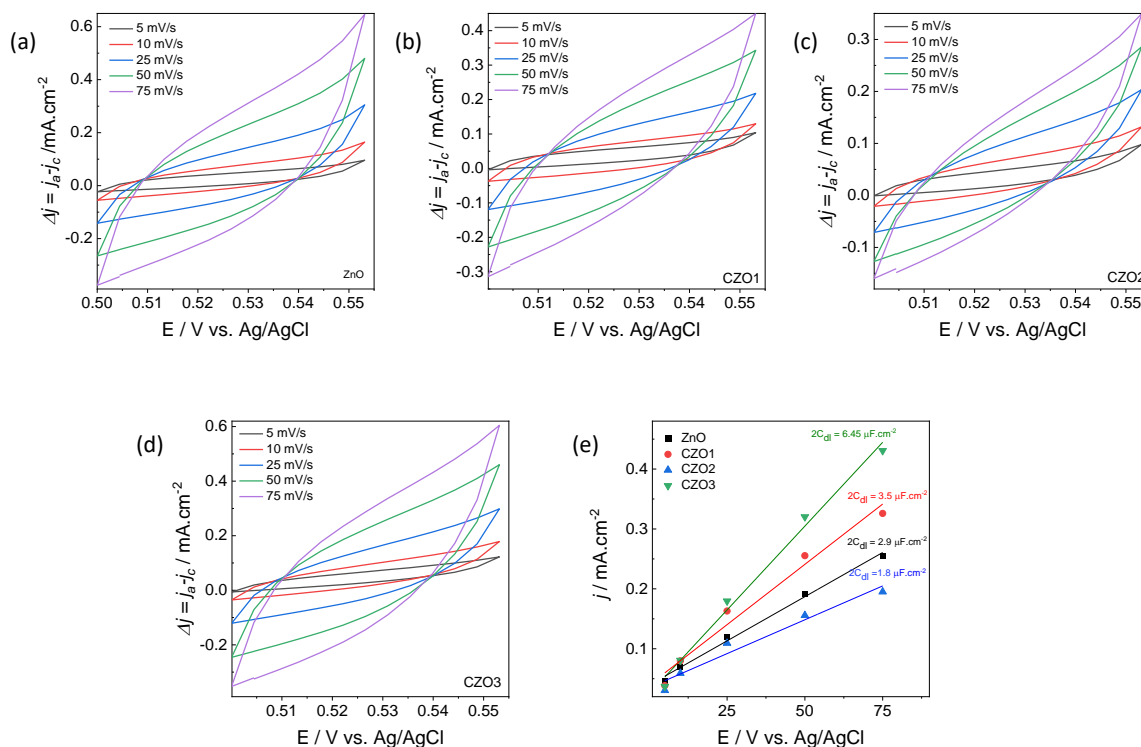


**Figure 6.9.** CV plot of (a) ZnO; (b) CZO1; (c) CZO2; and (d) CZO3; (e) ECSA plot of ZnO, CZO1, CZO2 and CZO3.

As depicted in **Fig 6.9 (a-d)**, the ECSA analysis offers a comparative assessment of the activity exhibited by ZnO, CZO1, CZO2, and CZO3. Diverging from the methodology of BET research, this study provides a more precise evaluation of the material's surface area activity by maintaining complete immersion in the electrolyte (Anantharaj et al. 2018). Notably, the  $2C_{dl}$  values for ZnO, CZO1, CZO2, and CZO3 are recorded as  $2.9 \mu\text{F}\cdot\text{cm}^{-2}$ ,  $3.5 \mu\text{F}\cdot\text{cm}^{-2}$ ,  $1.8 \mu\text{F}\cdot\text{cm}^{-2}$ , and  $6.48 \mu\text{F}\cdot\text{cm}^{-2}$ , respectively, as illustrated in **Fig 6.9 (e)**. The augmented performance of active sites relative to other electrodes confirms CZO3 as the optimal material. Estimations of the actual surface areas for ZnO, CZO1, CZO2, and CZO3 are determined to be  $0.0365 \text{ cm}^2$ ,  $0.0437 \text{ cm}^2$ ,  $0.0225 \text{ cm}^2$ , and  $0.081 \text{ cm}^2$ , respectively. This unequivocally underscores CZO3 as the superior material among the tested samples.

### 6.3.8 Electrochemical Impedance Spectra (EIS) Analysis

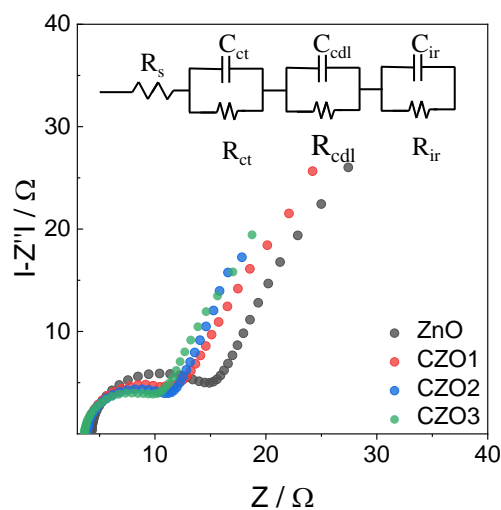


**Figure 6.10.** Nyquist Plot of ZnO and ZnO, CZO1, CZO2, and CZO3.

The conductivity and interference characteristics of ZnO, CZO1, CZO2, and CZO3 were systematically investigated through Electrochemical Impedance Spectroscopy (EIS), employing a consistent three-electrode configuration. The Nyquist plot was analyzed by fitting it to the equivalent circuit depicted as illustrated in **Fig 6.10**. This circuit comprises solution resistance ( $R_s$ ) in conjunction with double layer resistance ( $R_{cdl}$ ) and charge transfer resistance ( $R_{ct}$ ), supplemented by internal resistance ( $R_{ir}$ ). The electrochemically derived parameters, delineated in **Table 6.3**, provide crucial insights into the materials' performance. Notably, CZO3 exhibits markedly lower charge transfer resistance and solution resistance compared to the other materials, as evidenced in **Table 6.3**. This observation serves to confirm its heightened activity relative to all other tested materials.

**Table 6.3.** EIS parameters for the fitted circuit

Samples	$R_s$ ( $\Omega$ )	$C_{ct}$ (F)	$R_{ct}$ ( $\Omega$ )	$C_{cdl}$ (F)	$R_{cdl}$ ( $\Omega$ )	$C_{ir}$ (F)	$R_{ir}$ ( $\Omega$ )
ZnO	4.296	$4.059 \times 10^{-6}$	10.55	0.0001182	78.62	0.0001577	3.508
CZO1	3.681	$1.0515 \times 10^{-6}$	7.947	0.00017	77.42	0.0002611	2.529
CZO2	4.290	$4.059 \times 10^{-6}$	19.55	0.0001102	78.63	0.0001576	3.509
CZO3	3.336	$6.639 \times 10^{-6}$	6.586	0.0001512	60.34	0.0001253	4.748

### 6.3.9 High-Resolution Transmission Electron Microscopy (HR-TEM) Analysis

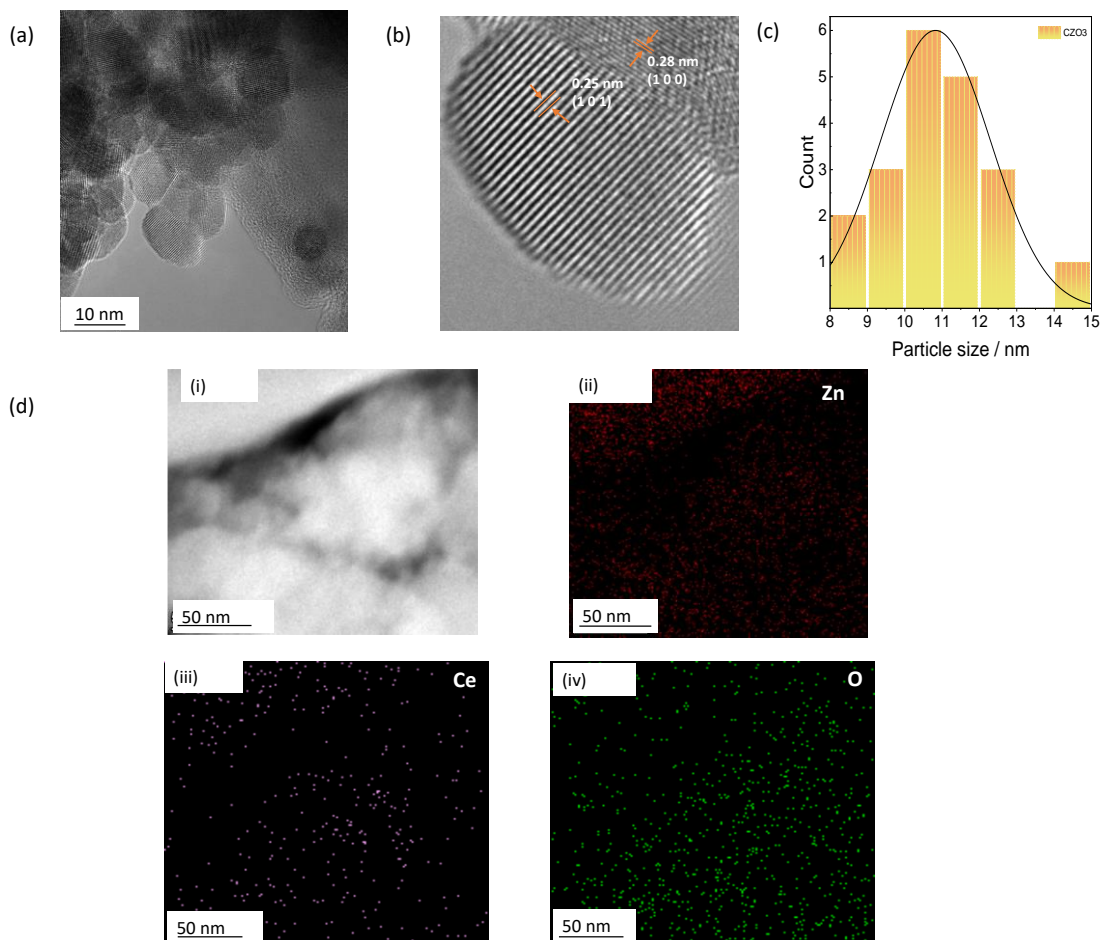


**Figure 6.11.** (a) TEM; (b) HR-TEM; (c) Particle size analysis of CZO3; and (d)(i-iv) STEM analysis of CZO3 respectively.

So, according to all the examinations, CZO3 has the highest activity compared to ZnO, CZO1, and CZO2. The HR-TEM for CZO3 shown in **Fig 6.11 (a-b)** has a spherical shape and lattice space between adjacent planes has uniform fringe with the approximate interval of 0.25 nm corresponding to (1 0 1) plane and 0.28 nm corresponding to (1 0 0) plane of ZnO and it confirms the hexagonal wurtzite structure that well matches with the JCPDS card no: 089-0510. As observed in **Fig 6.11 (c)**, it has particles that are typically between 8-15 nm in size. STEM analysis confirms successful doping in CZO3, revealing a uniform distribution of Ce, Zn, and O elements as depicted in **Fig 6.11 (d) (i-iv)**.

### 6.3.10 Photoelectrochemical Analysis of CZO3

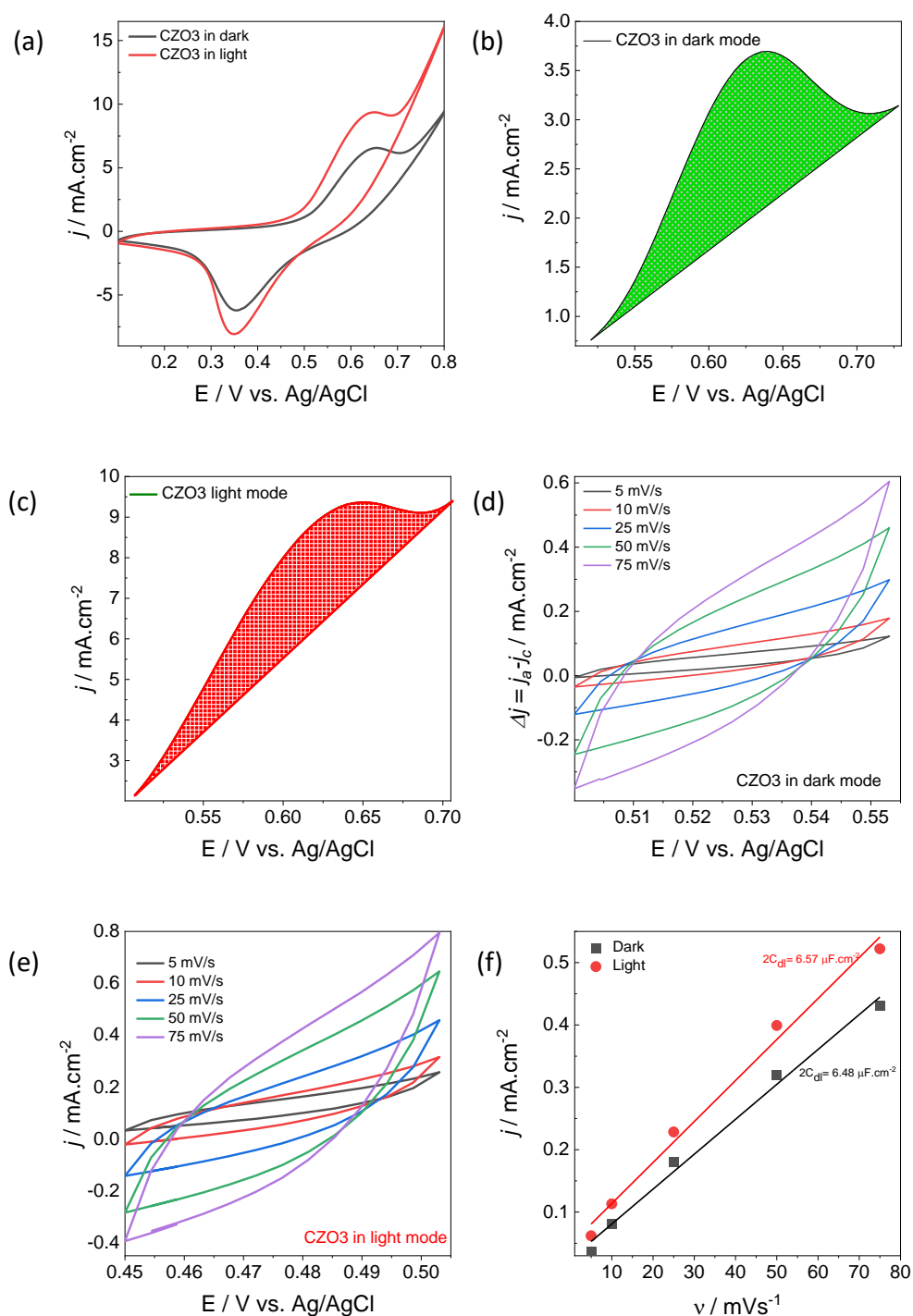


**Figure 6.12.** (a) CV analysis of CZO3 in dark and illuminated environments; Oxidation peak analysis of CZO3 in (b) dark and (c) illuminated mode respectively; ECSA CV analysis of CZO3 in (d) dark and (e) illuminated mode; (f) ECSA plot of CZO3 of dark and illuminated mode.

The selected material is subjected to CV analysis in a dark and illuminated mode and the changes in the activity are observed in **Fig 6.12 (a)**. Light illumination significantly boosted the photoelectrochemical activity of CZO3/NF films synthesized in this work compared to dark condition. The aforementioned findings emphasize the enhanced electrical conductivity or chemical catalytic activity of the coatings upon illumination. When comparing their relative ionic radii, a possible explanation for this occurrence is the substitution of  $Zn^{2+}$  ions in the ZnO lattice by  $Ce^{4+}$  ions. The following reaction **Eq. 6.2** may be used to illustrate this substitution:



In this case,  $O_o^x$  stands for the defect caused by oxygen ions in the interstices, while  $Ce_{Zn}^{oo}$  signifies the defect caused by the substitution of  $Zn^{2+}$  ions with  $Ce^{4+}$  ions inside the ZnO lattice. The increased photoelectrochemical properties shown in these thin films might be attributed to the presence of a greater number of electrons and holes, as well as the comparatively high mobility of bulk oxygen species and the simple production of labile oxygen vacancies (Yousefi et al. 2011). When light interacts with cerium-doped ZnO (CZO), it generates free electrons more efficiently, which significantly enhance the photoelectrochemical activity (**Eq. 6.3**). Effect the Ce doping reduces the carrier charge carrier recombination and improves the photoelectrochemical performance of pristine ZnO. As a result, the material exhibits improved photoelectrochemical properties due to the effective suppression of recombination processes and the promotion of efficient electrochemical reactions. The mechanism can be represented by the equation:



where  $h\nu$  denotes the incident photon energy,  $e^{-*}$  are the generated conduction band electrons, and  $h^+$  are the valence band holes.

Significantly, the photoelectrochemical activity of CZO3 material demonstrates a notable augmentation in an illuminated environment compared to a dark setting, as evidenced in **Fig 6.12 (a)**. These findings underscore the influence of light exposure on

enhancing electron transfer within the material, consequently amplifying its photoelectrochemical reactivity. Moreover, the quantification of electron transfers during the redox peak reveals a conspicuous increase from  $2.1 \times 10^{19}$  to  $3.51 \times 10^{19}$  upon illumination, as depicted in **Fig 6.12 (b-c)**. This notable elevation in electron transfer rate attributed to illumination can be attributed to the generation of a new lowest unoccupied molecular orbital and reduction in the band gap. These excited electrons effectively sustain charge separation, thereby mitigating electron-hole recombination, consequently indicating a significant enhancement in the material's redox activity. The light-induced electrochemical active sites of the material were investigated using electrical double-layer capacitance ( $C_{dl}$ ). The results, as illustrated in **Fig 6.12 (d-e)**, demonstrate an enhancement in the active surface area from  $0.0806 \text{ cm}^2$  to  $0.0821 \text{ cm}^2$ . The ECSA plot is represented in **Fig 6.12 (f)**.

### 6.3.11 X-ray photoelectron spectroscopy (XPS) Analysis

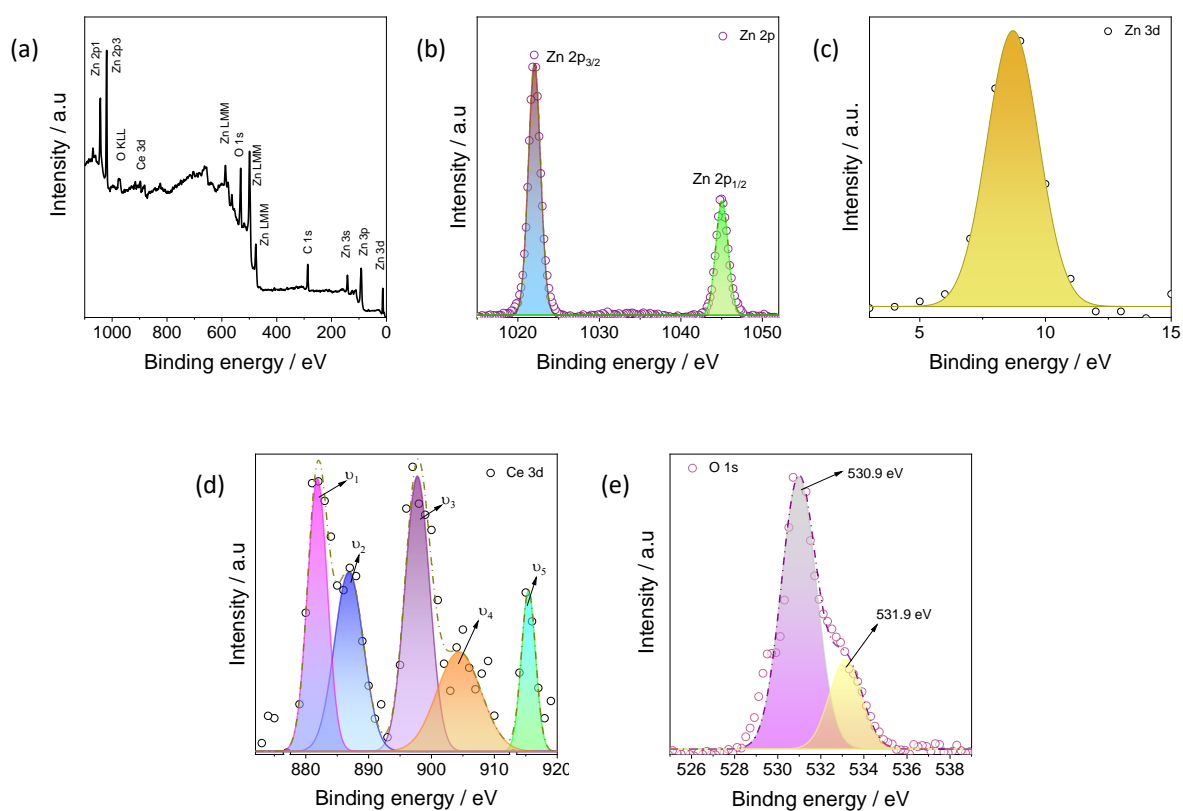


**Figure 6.13.** XPS of CZO3 (a) survey; (b) Zn 2; (c) Zn 3d; (d) Ce 3d and (e) O 1s.

XPS analysis provides intricate insights into the surface composition and chemical state of CZO3. The XPS survey in **Fig 6.13 (a)** underscores the presence of Zn, Ce, and O elements. The survey distinctly identifies the characteristic peaks associated with each element, along with their respective compositions.

Specifically, the  $Zn^{2+}$  state within the ZnO lattice manifests through significant peaks positioned at 1045 eV and 1022 eV, corresponding to Zn 2p<sub>1/2</sub> and Zn 2p<sub>3/2</sub>, respectively as shown in **Fig 6.13 (b)** (Pathak et al. 2020). Additionally, the peak observed at 8.77 eV is attributed to the Zn 3d state, as depicted in **Fig 6.13 (c)**. Deconvoluted spectra of Ce 3d in doped ZnO, depicted in **Fig 6.13 (d)**, reveal two sets of spin-orbitals corresponding to Ce 3d<sub>3/2</sub> ( $v_4, v_5$ ) and Ce 3d<sub>5/2</sub> ( $v_1, v_2, v_3$ ), indicating the presence of Ce in the +4 oxidation state. The observed binding energy doublets, such as  $v_3$  and  $v_5$  at 898.7 eV and 915.4 eV, respectively, originate from the final state of Ce (IV) 3d<sup>9</sup>4f<sup>0</sup>O<sup>2</sup>p<sup>6</sup>. Similarly, doublet  $v_2$  and  $v_4$  at 886.8 eV and 904.3 eV are attributed to the state of Ce (IV) 3d<sup>9</sup>4f<sup>1</sup>O<sup>2</sup>p<sup>5</sup>, while the peak at 881.8 eV is caused by Ce 3d<sup>9</sup>4f<sup>2</sup>O<sup>2</sup>p<sup>4</sup>. These distinctive peaks collectively confirm the doping of Ce into ZnO in the form of Ce (IV). Additionally, slight shifts in the Ce 3d binding energy compared to standard XPS energy peaks indicate modifications in the Ce-O bond length within ZnO, attributable to Ce<sup>+4</sup> doping. Notably, the absence of additional signals of other impurities underscores the successful synthesis of Ce<sup>+4</sup> doped ZnO (Faisal et al. 2013; Liang et al. 2015). The O 1s spectra, as observed in **Fig 6.13 (e)**, are fitted into two components: The low-energy component at 530.9 eV is attributed to Zn-O binding, while the high-energy component at 531.9 eV corresponds to oxygen species chemisorbed on the surface (Cervantes-López et al. 2017).

### 6.3.12 Density Functional Theory (DFT) Analysis

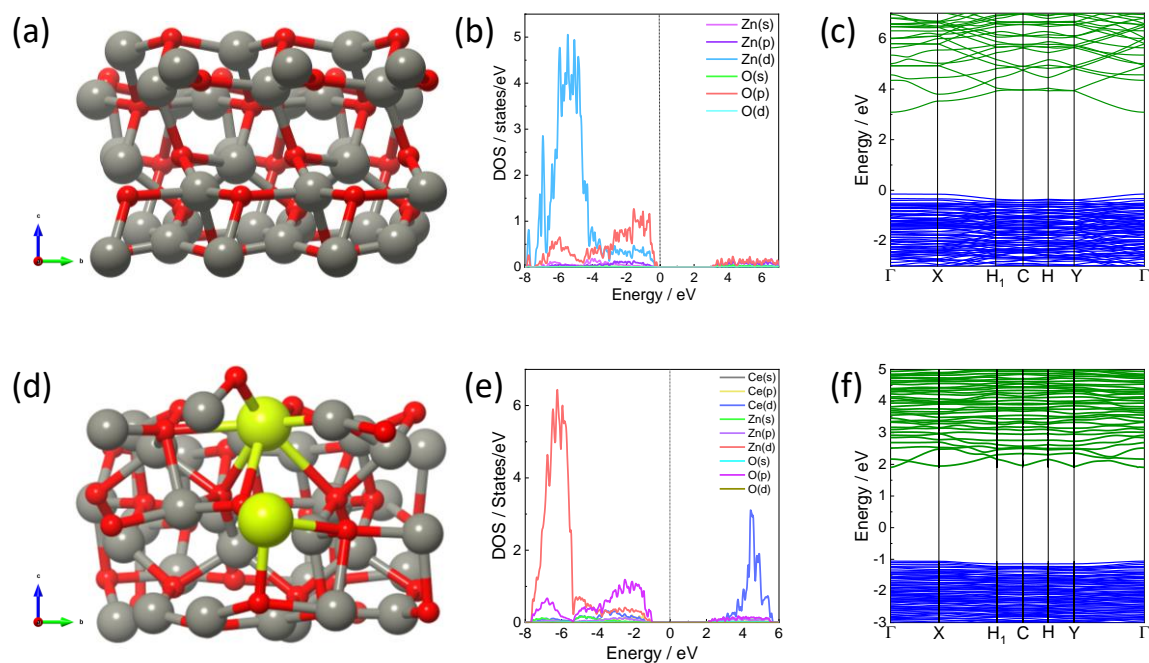


**Figure 6.14.** (a) optimized (101) slab for ZnO; (b) Density of States plot for ZnO; (c) Electronic band structure for ZnO; (d) optimized (101) slab for Ce-ZnO; (e) Density of States plot for Ce-ZnO; (f) Electronic band structure for Ce-ZnO.

The effectiveness of various sensor configurations can be evaluated to gain comprehensive insights into properties such as preferred adsorption sites, adsorption energy, and the detection of subtle changes in electronic properties induced by adsorption. The optimized geometry of cleaved pristine ZnO and Ce-doped ZnO is illustrated in **Fig 6.14 (a)** and **(d)**, respectively. It is evident from graph that cerium effectively substitutes two zinc.

Zn atoms rather than occupying interstitial sites, as confirmed by the density of states (DOS) analysis. As depicted in **Fig 6.14 (b)**, the material demonstrates a semiconducting nature, with Zn d-state and O p-state contributing to the valence band maxima, whereas conduction band minima consist of Zn s-state and Zn p-state and O p-state. Notably, the conducting band exhibits an absence of state contribution, reflecting the inferior conductivity behavior of pristine ZnO nanoparticles. In contrast, the introduction of Ce (**Fig 6.14 (d)**) results in a discernible difference in the DOS (**Fig 6.14 (e)**). In Ce-doped ZnO, Zn d-state and O p-state contribute to the valence band

maxima, while Zn s-state, Zn p-state, and a minimal amount of Ce p-state attribute to the shared valence band minima.

A significant deviation is observed in the presence of Ce d-state as the conduction band maxima, directly correlating with the experimentally observed enhanced response, indicative of the improved ZnO matrix upon Ce inclusion. This data aligns with the XPS results, corroborating the effectiveness of Ce doping. To elucidate the variation in band gap induced by Ce inclusion, band structure analysis was performed. This is crucial as exposure to light sources significantly enhances activity, improving electron mobility within the system.

As shown in **Fig 6.14 (c)** and **6.14 (f)**, both materials exhibit a semiconducting nature, yet the band gap for Ce-doped ZnO (2.903 eV) is notably smaller compared to pristine ZnO (3.199 eV) at gamma point. This reduction in band gap is attributed to the development of additional intermediate energy levels, leading to increased activity. Furthermore, to understand the exemplary sensing activity of Ce-doped ZnO towards cholesterol, adsorption energy was calculated to elucidate why Ce-ZnO demonstrates superior performance compared to ZnO.

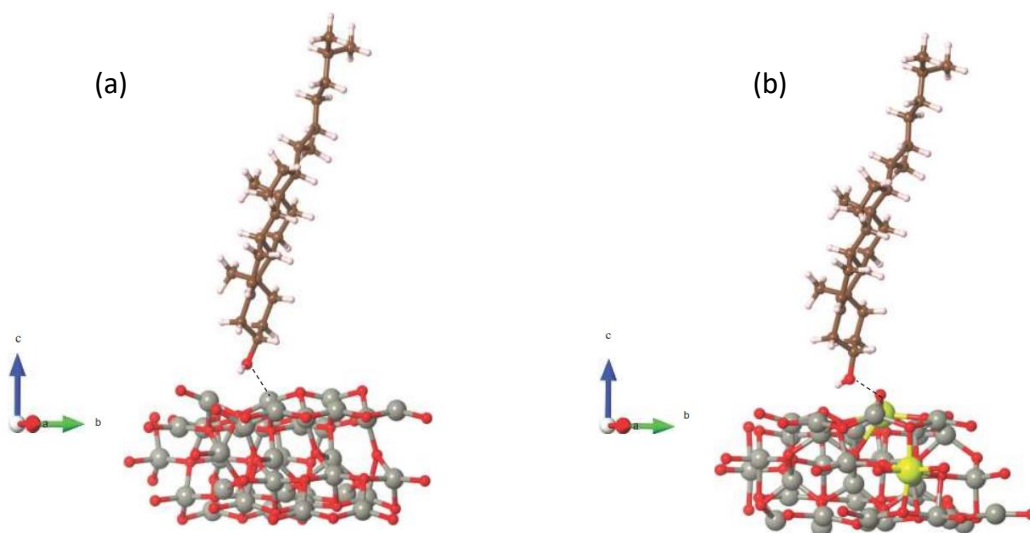


**Figure 6.15.** (a) Cholesterol adsorbed ZnO; (b) Cholesterol adsorbed Ce doped ZnO.

Utilizing **Eq. 6.1**, adsorption energy was calculated for both ZnO and Ce-doped ZnO. As illustrated in **Fig 6.15 (a-b)**, during cholesterol adsorption in pristine ZnO, the

molecule is attracted towards Zn atoms with an adsorption energy of -0.146 eV. In contrast, cholesterol adsorption onto Ce-doped ZnO results in higher adsorption onto Ce rather than Zn, with a significantly higher adsorption energy of -0.454 eV. This higher adsorption energy suggests a greater likelihood of cholesterol sensing by Ce-doped ZnO, which is confirmed by experimental analysis, showcasing the Ce (cerium) high affinity for attracting oxygen atoms in cholesterol derivatives enhances the activity of the ZnO matrix in cholesterol sensing applications.

### 6.3.13 Mechanism of PEC cholesterol biosensor of CZO3

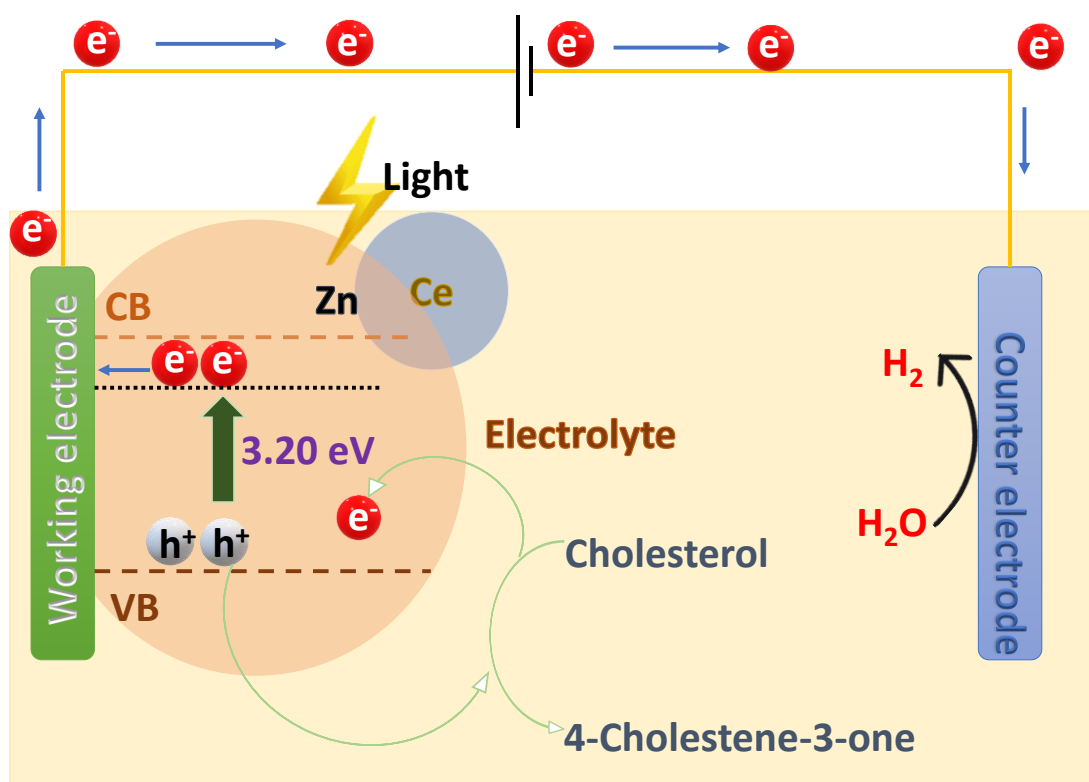


**Figure 6.16.** Mechanistic representation of PEC based Cholesterol biosensor

A PEC cell consists of three main components: platinum as the counter electrode (photocathode), CZO3@NF as the working electrode (photoanode), the KOH electrolyte is chosen for its compatibility with cholesterol and its non-adverse effects as shown in **Fig 6.16**. The diagram illustrates the typical mechanism of direct PEC oxidation of biomolecules. In PEC biosensing, the presence of target biomolecules

induces an increase in photocurrent, which is directly proportional to their concentration. We have also clarified that the doping of Ce results in a reduction of the band gap of the material as studied from UV and DFT studies. The PEC process comprises several critical steps: (a) light absorption by the CZO3 substrate leads to the generation of photoexcited charge carriers, specifically electrons ( $e^-$ ) and holes ( $h^+$ ); (b) these charge carriers are then separated, with photoelectrons migrating towards the WE and photoholes moving towards the electrolyte. Upon irradiation, photoexcited carriers are produced at the WE. Photoelectrons are transferred from the conduction band of the WE to the platinum electrode, while photoholes in the valence band of the WE participate in oxidation reactions with biological species in the electrolyte. For instance, cholesterol is oxidized to 4-Cholestene-3-one, facilitating the transfer of electrons to the photoanode. This process enhances the overall sensitivity and efficiency of the PEC biosensor, making it a robust tool for detecting biomolecules (Devadoss et al. 2015).

### 6.3.14 Electrochemical Analysis

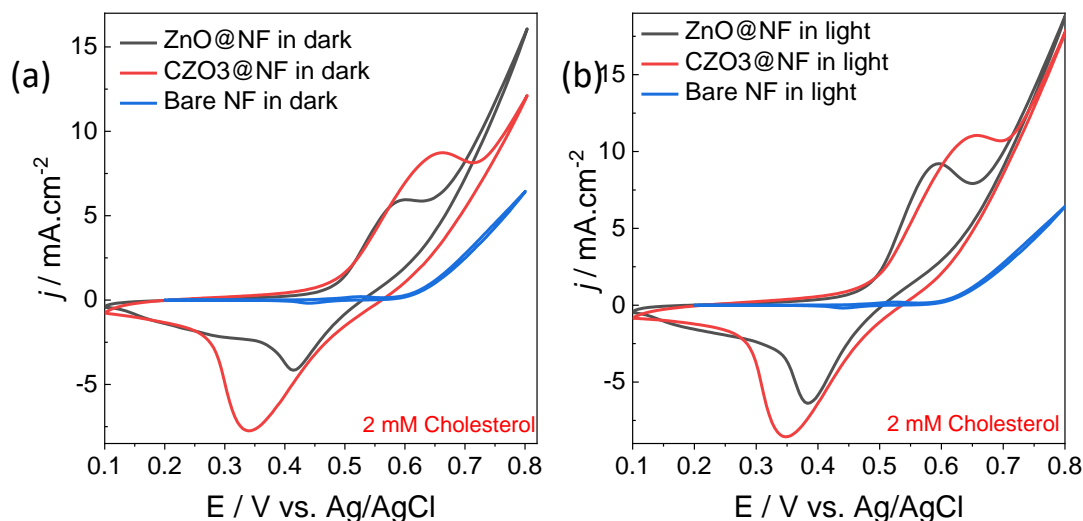


**Figure 6.17.** Comparison of CVs of CZO3@NF, ZnO@NF, and bare NF in 0.1 M KOH with the scan rate of 50 mV/s in (a) dark and (b) illuminated mode respectively.

In this investigation, CZO3/NF, bare NF, and ZnO/NF materials underwent scrutiny under conditions of cholesterol oxidation, employing a 2 mM cholesterol solution in 0.1 M KOH, with a scan rate of 50 mV/s. As depicted in **Fig 6.17 (a)** and **(b)** for dark and illuminated environments, respectively, the catalytic response of bare NF material

remains negligible during cholesterol oxidation in the absence of light within the specified potential range of 0.1 to 0.8 V vs Ag/AgCl. Conversely, both ZnO/NF and CZO3/NF materials exhibit discernible increases in anodic peak current, indicative of cholesterol oxidation in the dark mode. The CZO3/NF demonstrates an anodic current response nearly twice as pronounced as ZnO/NF. Furthermore, exposure to visible light reveals a substantial enhancement in CZO3/NF compared to ZnO/NF, exhibiting nearly triple the magnitude of improvement. This significant progress underscores the pivotal role played by the crystalline nature, heightened electron transport, expanded surface area inherent in CZO3/NF, and the band gap as mentioned in the DFT contributing to the effective oxidation of cholesterol to 4-Cholestene-3-one on the working electrode surface within a non-enzymatic biosensor context.

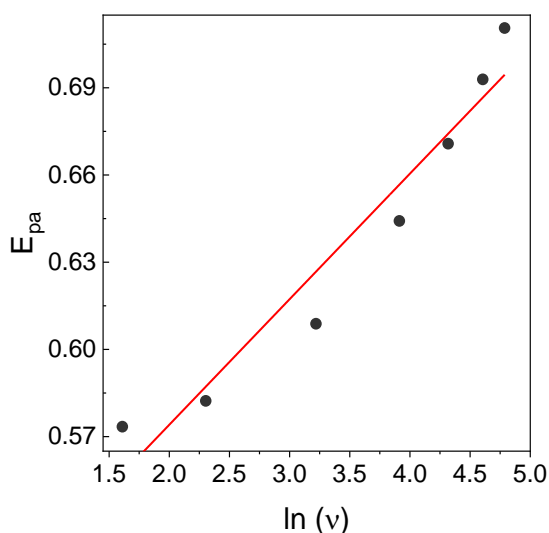


**Figure 6.18.** Laviron equation study of CZO3@NF

Additionally, the number of electrons necessary to oxidize cholesterol is determined utilizing the Laviron equation (**Eq. 4.3**). According to **Fig 6.18**, the application of the Laviron equation, calculated by plotting the slope of  $\ln(v)$  against the anodic peak potential ( $E$ ). The analysis reveals the exchange of 1.99 electrons during the electro-oxidation of cholesterol, thereby confirming the involvement of two electron transfers in this process.

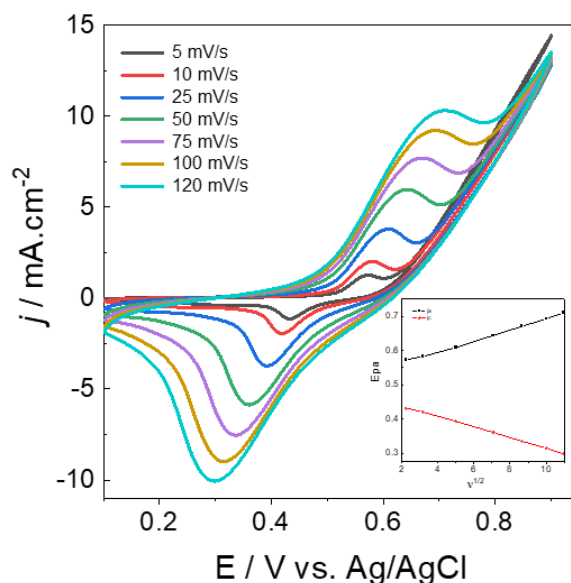


**Figure 6.19.** CVs of CZO3@NF in 0.1 M KOH with scan rates from 5-120 mV/s. The corresponding anodic peak current and cathodic peak current as a function of the square root of the scan rate (Inset).

Comprehensive CV analysis was conducted to elucidate the electrochemical characteristics of the CZO3/NF coating and represented in **Fig 6.19**, employing varied scan rates ranging from 5–120 mV/s. The primary objectives of this investigation encompassed the elucidation of modified electrode properties and dynamics, alongside discerning the influence of scan rate on both anodic and cathodic peak currents. Notably, the results reveal a concurrent increase in anodic and cathodic peaks with escalating scan rates. This observed behavior finds an explanation in the modulation of diffusion layer thickness, which dynamically adjusts with the scan rate. Slower scan rates foster the formation of thicker diffusion layers, impeding the access of electroactive species to the electrode surface and consequently diminishing both cathodic and anodic peak currents. Conversely, higher scan rates yield contrasting effects. As the scan rate escalates, the cathodic peak shifts towards the negative side, while the anodic peak shifts towards the positive side. Noteworthy is the observed linear correlation between the square root of the scan rate and the redox behavior of CZO3/NF, as depicted in the inset. This empirical evidence suggests that notwithstanding the diffusion layer's hindrance to electroactive species penetration, electron transfer persists via the outer sphere mechanism.

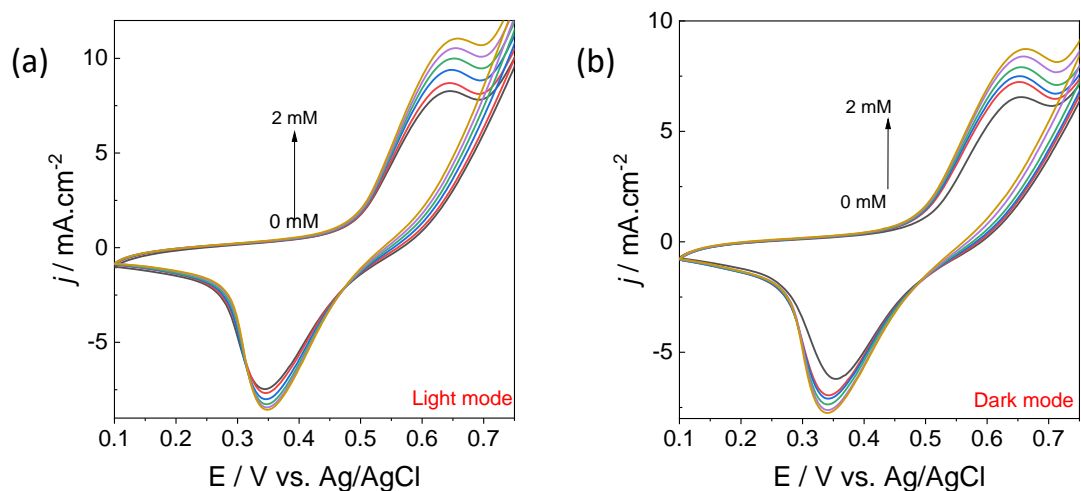


**Figure 6.20.** The successive addition of cholesterol in 0.1 M KOH at the scan rate of 50mV/s in (a) illuminated mode and (b) dark mode respectively.

The investigation depicted in **Fig 6.20 (a-b)** delves into the impact of cholesterol addition to a 0.1 M KOH solution under both illuminated and dark conditions, respectively. Notably, the findings unveil a gradual increase in the CV anodic peak with elevated cholesterol concentrations, indicative of electrocatalytic cholesterol oxidation. This observed phenomenon finds explanation in the expansion of the analyte's diffusion layer, resulting in the augmentation of the anodic peak.

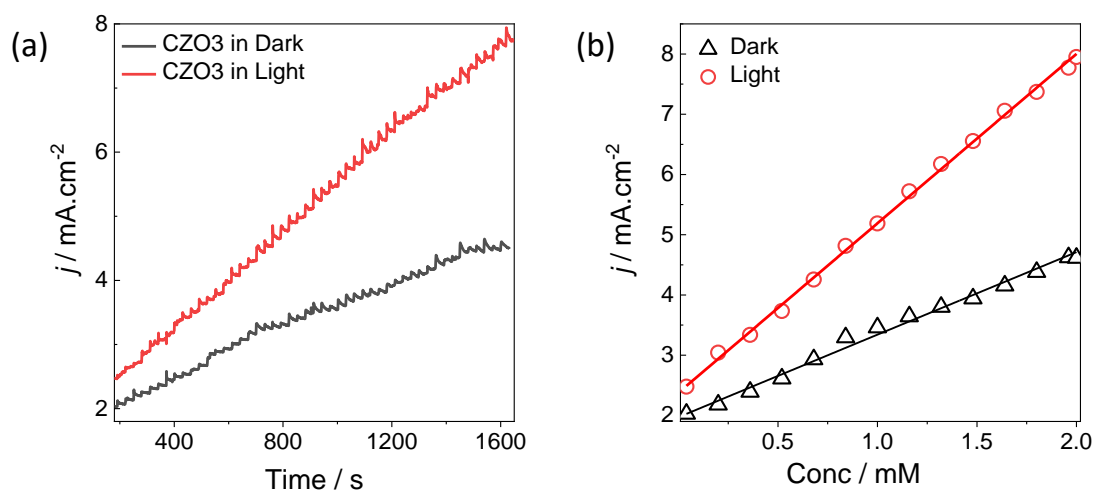


**Figure 6.21.** (a) The CA study of CZO3@NF in 0.1 M KOH with the successive addition of cholesterol in stirring condition in dark and illuminated mode respectively.

*Applied potential: 0.6 V; (b) Calibration plot of the CZO3@NF for the determination of the cholesterol in dark and illuminated mode respectively.*

The research outcomes suggest the potential applicability of the technology for the development of an amperometric sensor tailored for cholesterol measurement. Utilizing CZO3/NF for CA measurements, an enzyme-free cholesterol sensor was meticulously examined. Varied concentrations of cholesterol ranging from 40  $\mu\text{M}$  to 2 mM were introduced to assess the linear response of the sensor in both dark and illuminated modes, as depicted in **Fig 6.21 (a)**. The experiments were conducted under stirring conditions at a fixed potential of 0.6 V, with the amperometric response recorded at 30 s intervals. Each increment in cholesterol concentration elicited a proportional rise in the sensor's anodic peak, indicating the material's capability to detect added cholesterol. This response is attributed to the augmentation of the diffusion layer near the working electrode's surface, resulting in a higher-than-usual current. The calibration curve of the cholesterol sensor, illustrated in **Fig 6.21 (b)**, showcases a linear response across a concentration range of 40  $\mu\text{M}$  to 2 mM. Notably, the sensitivity values for dark and illuminated modes are recorded as 1370  $\mu\text{A mM}^{-1} \text{cm}^{-2}$  and 2812  $\mu\text{A mM}^{-1} \text{cm}^{-2}$ , respectively. Additionally, the LOQ values are 94  $\mu\text{M}$  and 58  $\mu\text{M}$ , while the LOD values are 28  $\mu\text{M}$  and 17  $\mu\text{M}$  for dark and illuminated modes, respectively, with a response time of 2 s.

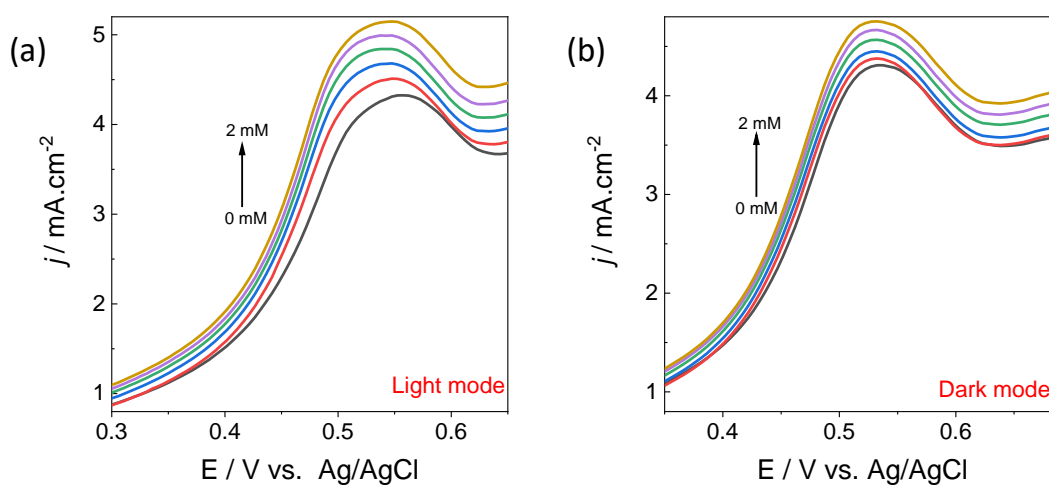


**Figure 6.22.** DPV study CZO3@NF with the successive addition of cholesterol in (a) illuminated and (b) dark mode respectively.

The DPV study conducted on CZO3/NF revealed notably enhanced repeatability, thereby affirming DPV analysis as a robust and effective analytical method. **Fig 6.22 (a-b)** from the investigation delineates a linear range for both illuminated and dark modes, spanning from 0.4 mM to 2 mM. Employing a scan rate of 5 mV/s, incremental additions of cholesterol to a solution of 0.1 M KOH in both modes elicited discernible variations in current, indicative of the sensitivity of the sensor to changes in cholesterol concentration. These findings underscore CZO3/NF's adaptive response to the cholesterol analyte, attributed to its crystalline structure and the presence of oxygen defects.

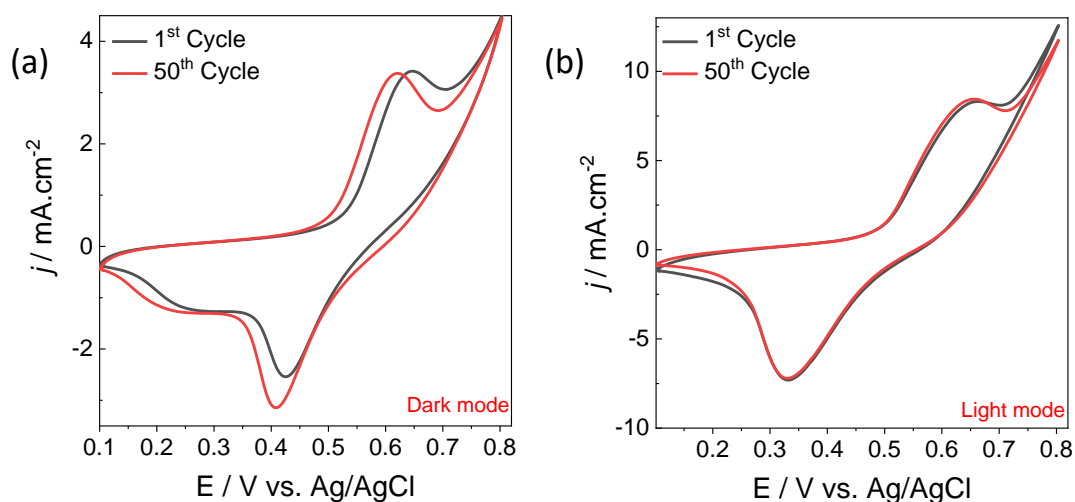


**Figure 6.23.** The CVs of CZO3@NF with 2 mM cholesterol for 50 cycles in 0.1 M KOH at the scan rate of 50 mV/s in (a) dark and (b) illuminated mode respectively.

The long-term durability of the CZO3/NF electrode in the presence of 2 mM cholesterol was scrutinized over 50 cycles, revealing exemplary stability in both illuminated and dark environments. In the dark mode, the electrode retained 98% of its characteristics after 50 cycles, demonstrating substantial structural and functional integrity, as depicted in **Fig 6.23 (a)**. This underscores its inherent stability and suitability for biosensor applications. Conversely, when exposed to light, the electrode exhibited 100% retention throughout the 50 cycles, as illustrated in **Fig 6.23 (b)**. Enhanced stability in the

illuminated mode can be attributed to light's pivotal role in expanding the surface area and promoting electron transfer. These results underscore the significance of light in CZO3/NF electrodes for augmenting surface area and facilitating effective electron transfer.

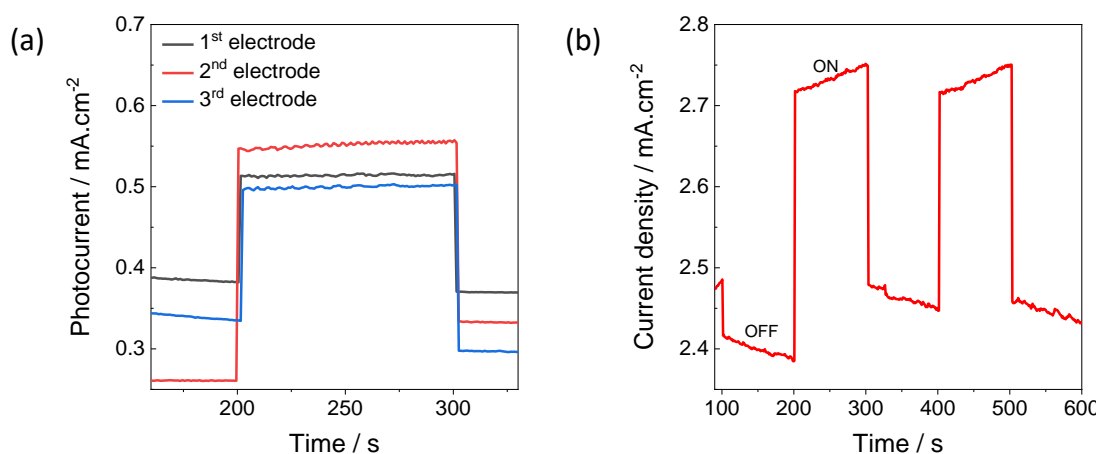


**Figure 6.24.** (a) Comparison of the activity of CZO3@NF with three different electrodes in dark and illuminated mode respectively; (b) Photocurrent activity of CZO3@NF in dark and illuminated mode.

To assess the repeatability of three distinct CZO3/NF electrodes, electrocatalytic oxidation studies were conducted using an illuminated mode with 1 mM cholesterol on each electrode under identical conditions, as depicted in **Fig 6.24 (a)**. The experimental findings demonstrate consistent and comparable electrocatalytic oxidation activity toward cholesterol across the electrodes treated with CZO3/NF. Furthermore, an in-depth examination of charge carrier separation and transfer was conducted by evaluating photocurrent versus time under ON-OFF conditions with 600 s visible light irradiation periods, as shown in **Fig 6.24 (b)**. The CZO3/NF electrode exhibited a discernible response to light, characterized by an increase in current density from 2.4 mA to 2.7 mA under a consistent bias voltage. This enhancement suggests a more efficient generation of photoinduced electrons and holes within the CZO3/NF sample.

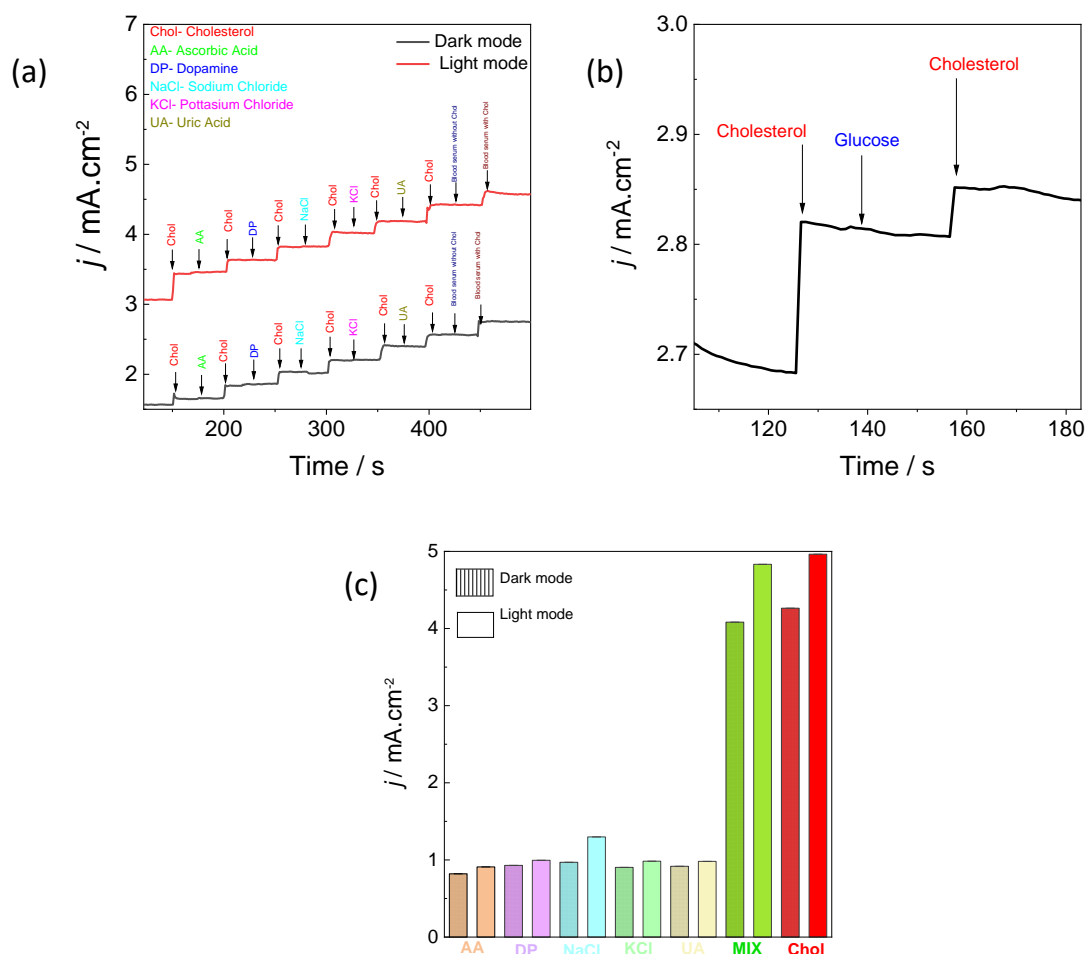


**Figure 6.25.** (a), (b) Interference study of CZO3@NF towards interference species in stirring condition in 0.1 M KOH; Applied potential 0.6 V; (c) DPV interference study for CZO3@NF at a scan rate of 5 mV/s with the pulse amplitude of 5 mV/s in dark and illuminated mode respectively.

The principal challenge encountered in the development of an electrochemical cholesterol sensor lies in effectively mitigating the presence of interfering compounds during cholesterol oxidation, highlighting the material's selectivity for cholesterol detection. CA experiments are conducted by introducing various substances, including AA, DP, NaCl, KCl, and UA into a 0.1 M KOH solution to investigate the selectivity of CZO3/NF. As illustrated in **Fig 6.25 (a-b)**, the interference species, at a concentration of 0.5 mM, elicit no discernible response from CZO3/NF in both dark and illuminated modes. In the case of glucose interference, no response was observed under dark

conditions. Therefore, we anticipate that glucose will similarly exhibit no response under illuminated conditions. Conversely, a distinct increase in current is observed upon the addition of 1 mM cholesterol. Consequently, this study underscores that interference species do not impede cholesterol oxidation activity even at higher concentrations, thus underscoring the heightened selectivity of CZO3/NF for cholesterol sensing.

An investigation, congruent with the Chronoamperometry (CA)-based study, was conducted employing Differential Pulse Voltammetry (DPV), with the findings delineated in **Fig 6.25 (c)**. Additionally, DPV analysis was executed on a mixture comprising 1 mM cholesterol and all interference species at a concentration of 0.5 mM. The absence of a significant alteration in the material's activity underscores that the presence of interfering species does not compromise the sensitivity of CZO3/NF to cholesterol. This underscores the exceptional selectivity and potential of CZO3/NF as a material for cholesterol oxidation.

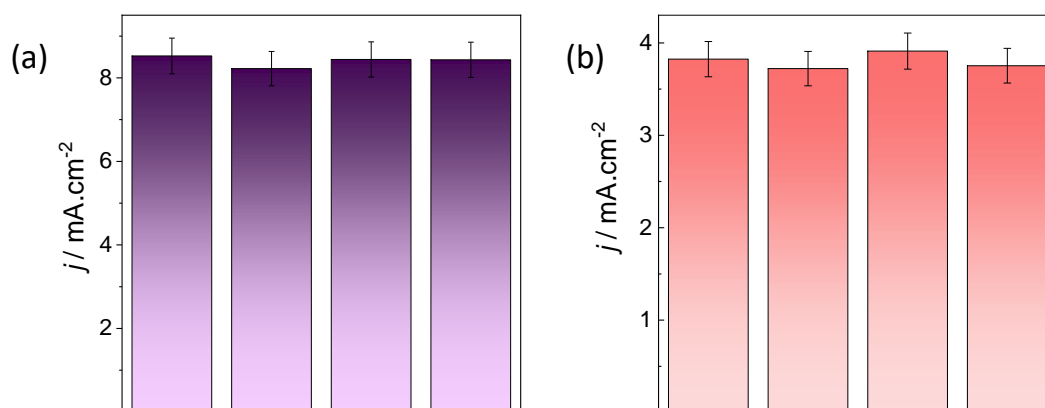


**Figure 6.26.** Reproducibility studies of CZO3 were conducted using CV analysis in 0.1 M KOH with 2 mM cholesterol to assess the material's consistency and performance in (a) illuminated and (b) dark mode respectively.

We have conducted a thorough assessment of the material's reproducibility under illuminated and in dark conditions by performing CV analysis. This evaluation involved subjecting multiple samples of the material to CV under identical experimental

conditions to ensure consistency. The results, illustrated in **Fig 6.26 (a-b)**, demonstrate that the electrocatalytic activity is nearly identical across all samples. This consistent performance underscores the high reproducibility of the material, affirming its reliability for practical applications. The uniform activity observed across the different samples highlights the material's stability and robustness in the given experimental setup.

### 6.3.15 High-Resolution Liquid Chromatography Mass Spectrometry (HR-LCMS) Analysis

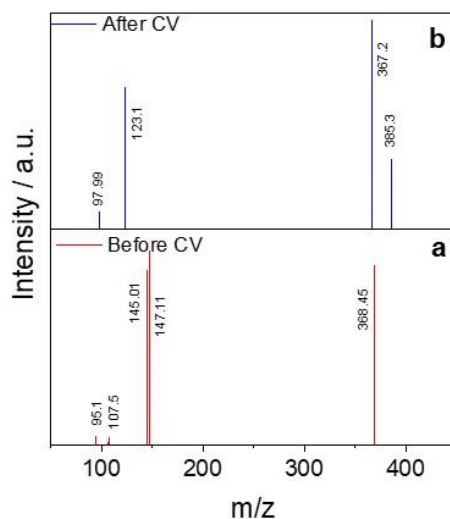


**Figure 6.27.** HR-LCMS study of (a) Cholesterol before adding to 3 electrode system CV setup, (b) 4-Cholesten-3-one formation after CV completion.

To corroborate this mechanism, the cholesterol solution underwent High-Resolution Liquid Chromatography Mass Spectrometry (HR-LCMS) analysis, both before and after interaction with the CZO3/NF material, as depicted in **Fig 6.27 (a-b)**. This analytical approach aimed to discern any alterations in the cholesterol sample subsequent to its interaction with the CZO3/NF material. The outcomes of the analysis unequivocally confirmed the conversion of cholesterol ( $m/z = 368.45$ ) into 4-cholestene-3-one ( $m/z = 385.3$ ).

Furthermore, the observed biosensing properties surpass and are comparable to those of previously published cholesterol biosensors, as depicted in **Table 6.4**. Notably, this represents the first successful demonstration and validation of a PEC-based non-

enzymatic cholesterol biosensor predicated on CZO3/NF, achieved through a comprehensive integration of theoretical and practical research methodologies.

*Table 6.4* showcases the observed biosensing characteristics of the proposed CZO3@NF electrode, revealing comparability and superiority to existing cholesterol biosensors documented in published literature.

Electrode	Sensitivity $\mu\text{A mM}^{-1} \text{ cm}^{-2}$	LOD $\mu\text{M}$	Linear Range	Ref.
MIP@TiO <sub>2</sub> IOPCs/CH <sub>3</sub> NH <sub>3</sub> PbBr <sub>3</sub>	-	$2.51 \times 10^{-4}$	$10^{-8}$ - $10^{-4}$ M	(Feng et al. 2022)
Copper (I) Sulfide nanoplates	-	0.1	0.01 - 6.8 mM	(Ji et al. 2014)
ZnO-Zn <sub>2</sub> In <sub>2</sub> O	81	-	0.001 - 9 mM	(Khan et al. 2021)
ZnO/SnO <sub>2</sub> /RuO <sub>2</sub>	11.3513	-	0.1nM ~ 0.01mM	(Alam et al. 2021)
CZO3@NF	1370	28	40 $\mu\text{M}$ - 2 mM	This work
	2812	17		

### 6.3.16 Real-Sample Analysis

CZO3/NF was deployed for quantifying cholesterol levels in human blood serum samples sourced from hospitals, with the serum retaining its original cholesterol concentrations for direct analysis under illuminated conditions. The acquired values closely aligned with the estimated values, as delineated in **Table 6.5**. This underscores the CZO3/NF electrode's proficiency in furnishing an acceptable range for cholesterol determination in real-world samples. Furthermore, **Table 6.5** elucidates studies conducted in a dark environment. The real sample chrono curves for illuminated and dark modes are depicted in **Fig 6.28 (a-e)**.

**a - Cholesterol**      **b- Blood serum with Cholesterol**

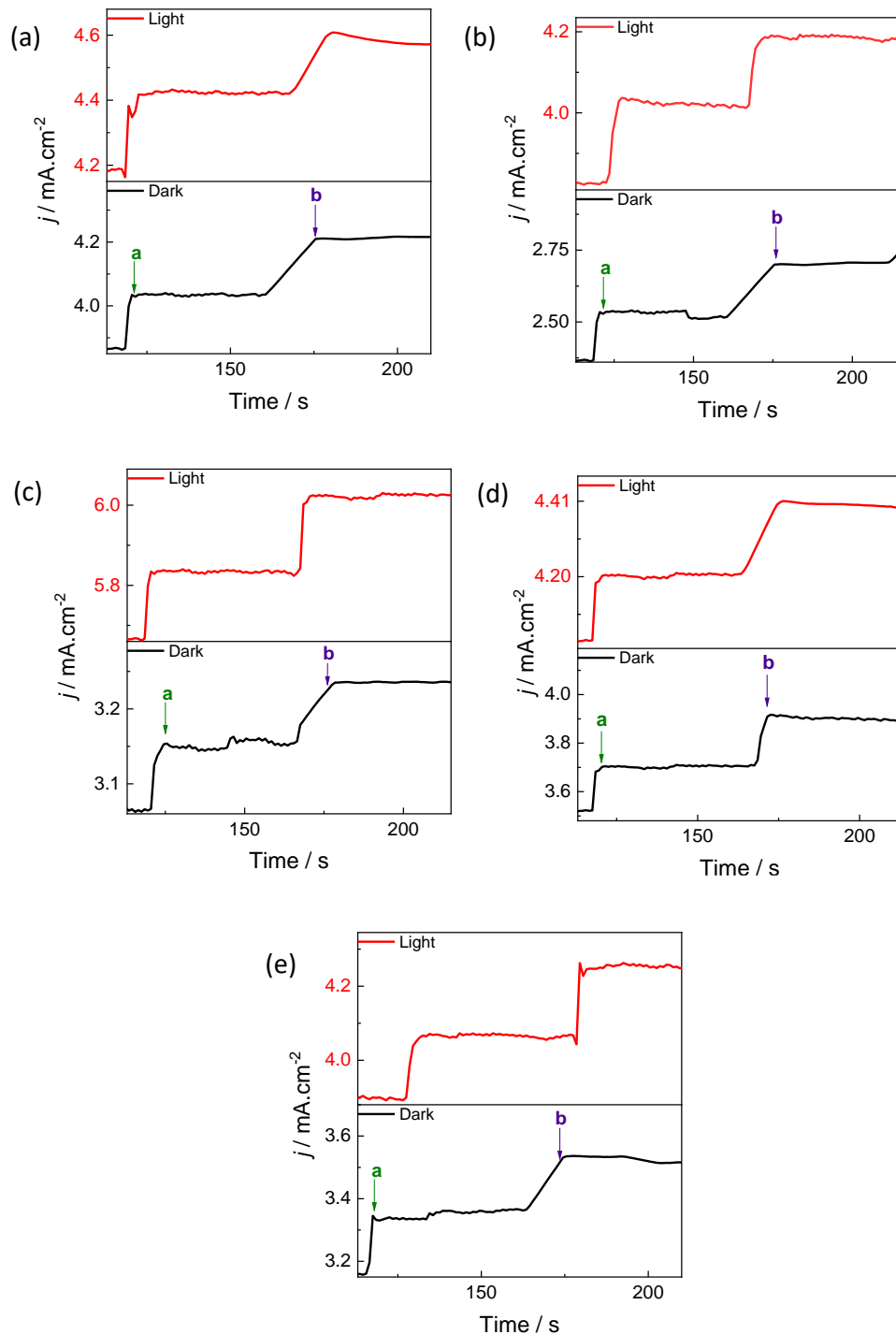


**Figure 6.28.** Real sample Chrono curves study for CZO3/NF for (a) Patient 1; (b) Patient 2; (c) Patient 3; (d) Patient 4; and (e) Patient 5 in both dark and illuminated mode respectively.

**Table 6.5** Analysis of human blood serum for cholesterol test in illuminated and dark mode.

Patient	Gender	Clinically tested (mg/dL)	Found (mg/dL) (Deviation)	
			Illuminated mode	Dark mode
1	M	141.72	144.38 (-2.66)	155 (-13.28)
2	F	48.18	48.98 (-0.8)	50.57 (-2.39)
3	M	194.86	195.5 (-0.64)	205.5 (-10.64)
4	M	146.15	133.75 (12.4)	164.75 (-18.6)
5	F	212.58	204.07 (8.51)	180.24 (32.34)

### 6.3.17 Eco-Friendly Properties

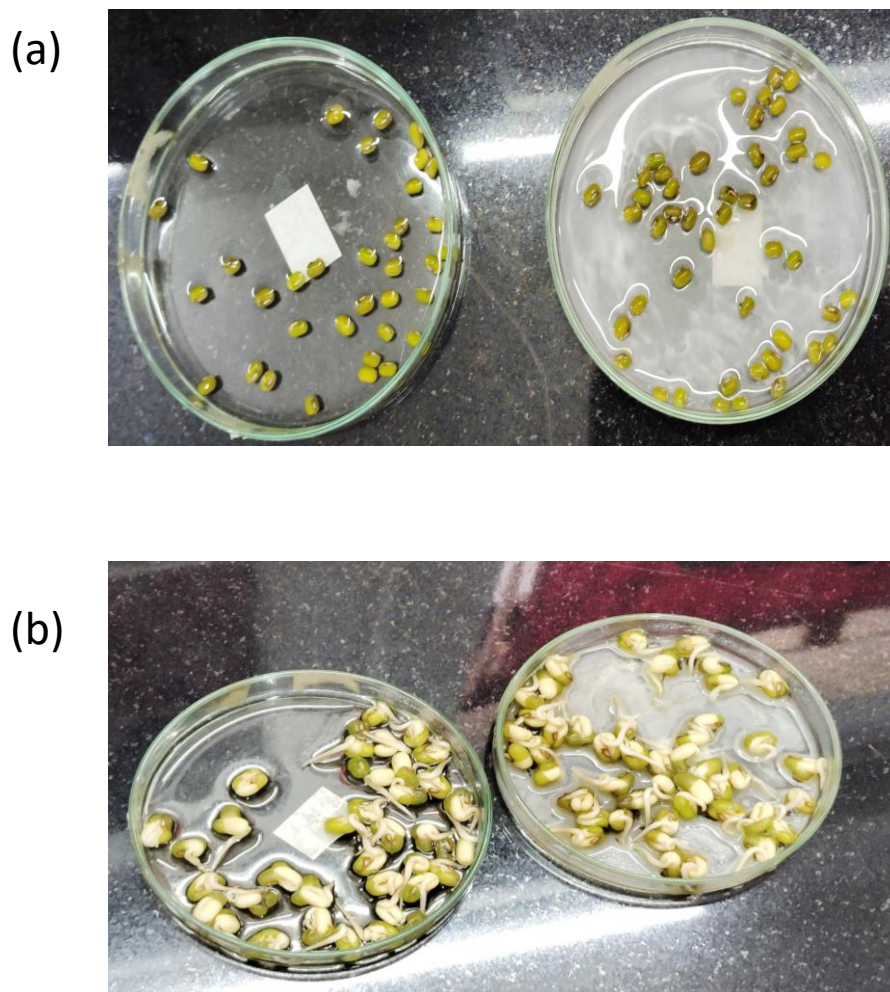


*Figure 6.29. Illustration of improved plant growth facilitated by the CZO<sub>3</sub> solution, with images depicting seed germination on (a) Day 1 and (b) Day 3.*

In this study, we examine the non-toxic nature of CZO<sub>3</sub> with respect to its environmental impact, specifically by promoting plant growth. The CZO<sub>3</sub> solution was prepared by dissolving the synthesized material in water, emphasizing its low ecological footprint, as illustrated in **Fig 6.29 (a-b)**. Green gram seeds were chosen as the model for this investigation. The seeds were immersed in the solution, and by day 3, germination was evident, marked by the emergence of small buds. This demonstrates the solution's simplicity and efficacy in fostering plant growth while minimizing harmful environmental effects.

## 6.4 Conclusions

- In summary, ZnO CZO1, CZO2, and CZO3 were synthesized utilizing a wet chemical technique and subsequently coated on NF substrate.
- Comprehensive analyses reveal that CZO3/NF outperformed other compositions studied, showcasing superior photocatalytic sensitivity, enhanced electron transfer rates, and an expanded surface area.
- The potential of ZnO and the optimal material CZO3 as biosensors for the detection of cholesterol was investigated via DFT calculations, which underlined CZO3 as superior to ZnO. This led to the selection of CZO3 for further evaluation of PEC performance.
- The PEC experiments conducted with the CZO3/NF electrode demonstrated a wide linear range spanning from 80  $\mu\text{M}$  to 2 mM, with a LOD of 17  $\mu\text{M}$ , rapid response time (2 s), exceptional reproducibility and stability, and an extraordinary sensitivity of 2.81 mA.mM<sup>-1</sup>.cm<sup>-2</sup>.
- Additionally, a suitable applied potential was meticulously chosen to mitigate interference from common biological species encountered in real specimens.
- It is proposed that the modified electrode holds promise for cholesterol sensing in human serum samples owing to its remarkable electrochemical activity, excellent biocompatibility, consistent morphology, cost-effectiveness, and non-toxic nature.

\*\*\*\*\*

## CHAPTER 7

---

---

**ENHANCED NON-ENZYMATIC CHOLESTEROL BIOSENSING USING  
Pd/C-DECORATED SnO<sub>2</sub>: SYNTHESIS, CHARACTERIZATION, AND  
ANALYTICAL PERFORMANCE IN CLINICAL BLOOD SPECIMENS**

---

---



---

---

***Abstract:** This chapter provides an in-depth description of the synthesis of SnO<sub>2</sub> and its subsequent decoration with Pd/C, along with a thorough characterization. This comprehensive analysis aims to enhance the simplicity and effectiveness of electrochemical cholesterol detection in human serum.*

---

---

## **7.1 Introduction**

Metal oxide semiconductor (MOS) technology is advantageous for analyte detection due to its low cost, portability, ease of maintenance, and stability. Among MOS materials, tin dioxide (SnO<sub>2</sub>) is particularly notable for its stable properties, high electron mobility, and excellent electrical characteristics. SnO<sub>2</sub>, an n-type semiconductor with a 3.6 eV band gap, possesses significant optical, electrical, and electrochemical properties, making it suitable for sensors, catalysts, photocatalysts, solar cells, gas sensors, and supercapacitors (Rai et al. 2018; Xin et al. 2018). However, pure SnO<sub>2</sub> encounters challenges such as high-power consumption, slow response, poor selectivity, and short recovery times. Combining SnO<sub>2</sub> with other nanocomposites is essential to overcome these limitations (Henkel et al. 2019; Zhang et al. 2018).

Noble metal nanoparticles like Au, Ag, Pt, Pd, and Ru are highly sought after for their unique properties in various fields (Wu et al. 2012). Among them, Pd-based catalysts stand out due to palladium's abundance and lower cost compared to platinum (Wen et al. 2010; Zhang et al. 2012). However, pure palladium and other metals often lack sensitivity, selectivity, and are prone to poisoning (Singh et al. 2010). To tackle these challenges, recent research has turned to bimetallic systems combining different metals to enhance sensor performance. These systems benefit from inter-metallic charge transfer and orbital hybridization, improving catalytic performance (Ferrando et al. 2008; Lim et al. 2009; Rodriguez and Goodman 1992; Stamenkovic et al. 2007). Hybrid noble and non-noble metal structures show synergistic effects, combining their properties for enhanced performance. These advances demonstrate the potential of bimetallic catalysts to address the limitations of pure metal systems, expanding their practical use (Bao et al. 2007; Prasad and Bhat 2016).

To overcome the limitations of both SnO<sub>2</sub> and pure metal catalysts, a combined approach leveraging the advantageous properties of SnO<sub>2</sub> and noble metal nanoparticles can be highly effective (Ji et al. 2019; Xue et al. 2019; Yang et al. 2019). This integration not only addresses the inherent shortcomings of each material but also enhances the overall performance of the sensors. For instance, incorporating noble metals with SnO<sub>2</sub> can improve sensitivity, selectivity, and response times due to the synergistic effects between the metal oxides and the noble metals (Prasad et al. 2015c). Therefore, the development of such hybrid nanocomposites represents a promising direction in the advancement of high-performance, cost-effective sensing technologies (Acharyya et al. 2023; Chao et al. 2021; Prasad and Bhat 2015c).

In this study, Pd/C-decorated SnO<sub>2</sub> was synthesized to develop a cost-effective electrocatalyst for cholesterol detection. The nanocomposite, consisting of palladium nanoparticles on a carbon support, demonstrated enhanced catalytic properties, stability, and sensitivity. Various electrochemical techniques such as including CV, CA, DPV, and LSV were employed to investigate its activity for cholesterol oxidation, revealing strong performance with rapid response, broad linear range, and low detection limit. These findings suggest the potential of Pd/C-decorated SnO<sub>2</sub> as a promising electrode for amperometric cholesterol sensing.

## 7.2 Experimental Method

### 7.2.1 Chemical reagents

Stannous chloride dihydrate ( $\text{SnCl}_2 \cdot 2\text{H}_2\text{O}$ ), sodium hydroxide ( $\text{NaOH}$ ) was all procured from Loba. 10 wt% palladium on carbon ( $\text{Pd/C}$ ) were obtained from Sigma-Aldrich. All materials were of high purity and were used without any further purification.

### 7.2.2 Synthesis of $\text{SnO}_2$ and $\text{SnO}_2\text{-Pd/C}$

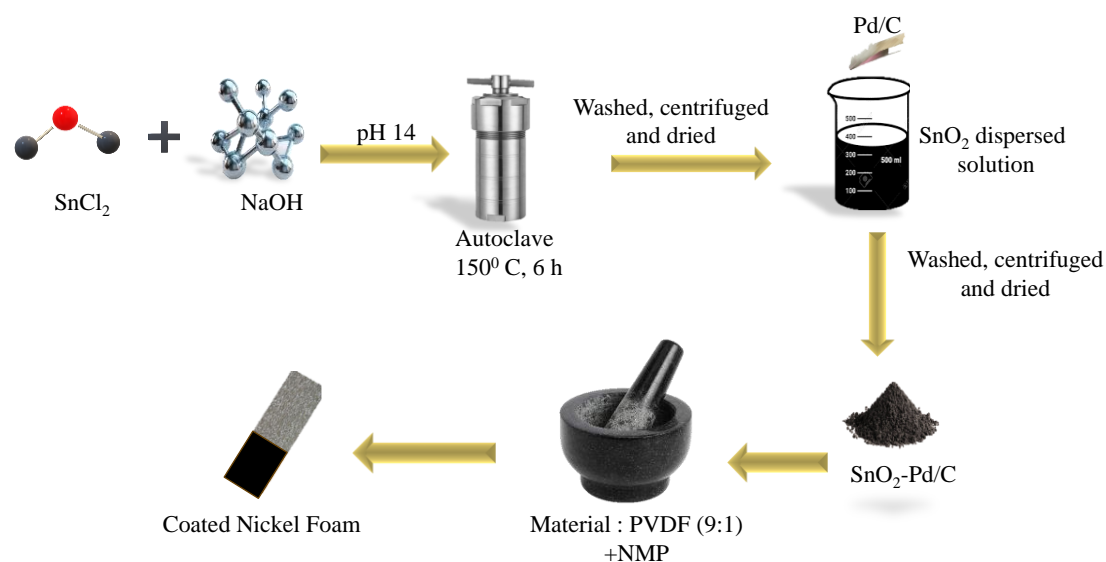


**Figure 7.1.** Schematic diagram of the synthesis of  $\text{SnO}_2\text{-Pd/C-NF}$

A measured quantity of 3g of  $\text{SnCl}_2 \cdot 2\text{H}_2\text{O}$  was dissolved in Milli-Q water and vigorously stirred to achieve homogeneity. Subsequently, 0.1 M  $\text{NaOH}$  was added until the solution turned milky white, followed by stirring for 5 minutes. 0.1 M Sodium citrate was then introduced and the solution was stirred for an hour before being transferring it into a Teflon-lined stainless-steel autoclave with a capacity of 200 mL. The mixture was heated at  $150^\circ\text{C}$  for 6 hours, after which the sample underwent centrifugation and was washed twice with water and ethanol. The resulting material was dried at  $100^\circ\text{C}$  for 24 hours and then calcined at  $500^\circ\text{C}$  for 2 hours.

To prepare  $\text{SnO}_2\text{-Pd/C}$ , 2g of calcined  $\text{SnO}_2$  was dispersed in 100 mL of water and vigorously stirred. Subsequently, 0.05 M  $\text{Pd/C}$  material was added and stirred for 3 hours, then sonicated for 30 min. The mixture was then centrifuged, washed twice with

water and ethanol, and dried at 80°C for 12 hours to yield the final product. The schematic diagram as shown in **Fig 7.1**.

## 7.3 Results and Discussions

### 7.3.1 X-Ray Diffraction (XRD) Analysis

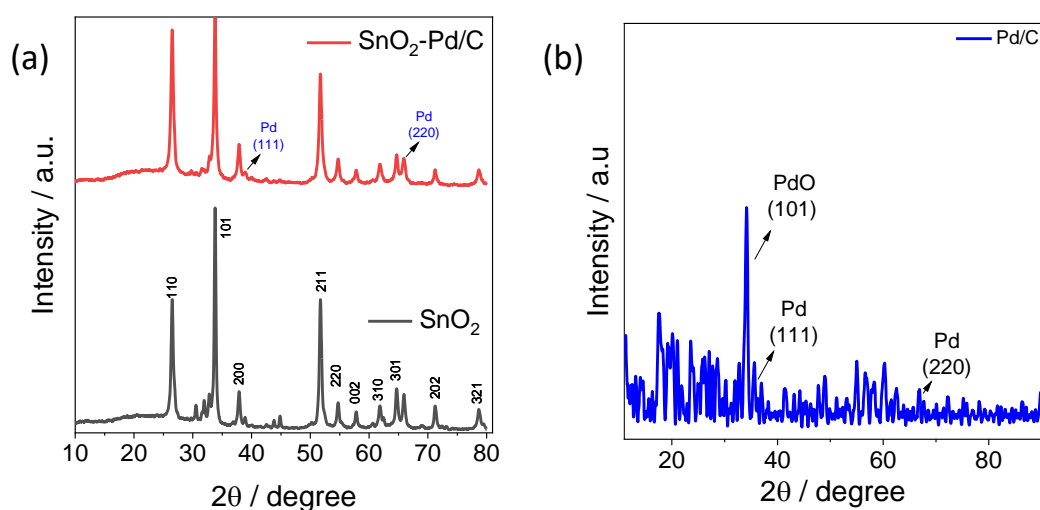


**Figure 7.2.** XRD analysis of (a) SnO<sub>2</sub>-Pd/C and pure SnO<sub>2</sub>; (b) 10 wt% Pd/C respectively.

XRD analysis of pristine SnO<sub>2</sub> and the SnO<sub>2</sub>-Pd/C composite, as shown in **Fig 7.2 (a)** displays distinctive diffraction peaks that correspond to the tetragonal crystal structure of SnO<sub>2</sub> (JCPDS-77-0450). The face-centered cubic phase of metallic Pd (JCPDS-05-0681) XRD analysis as illustrated in **Fig 7.2 (b)**. Notably, the SnO<sub>2</sub>-Pd/C sample exhibits small, low-intensity diffraction peaks indicative of Pd-based alloys. Pd (111) and Pd (220) facets are confirmed by the peaks at 2θ values of 38.03° and 65.86°, respectively as shown in **Fig 7.2 (b)** (Ipadeola et al. 2019). Due to the smaller quantity of Pd/C, these peaks are low in intensity, broader, and amorphous. Slight peak broadening suggests an increase in lattice defects attributed to the presence of Pd and carbon. Importantly, the absence of shifts in the XRD peaks indicates that Pd/C nanoparticles primarily interact with the surface of SnO<sub>2</sub> without altering its crystal structure, maintaining the structural integrity of SnO<sub>2</sub> while enhancing its surface properties for sensing. The XRD data confirms the successful synthesis of SnO<sub>2</sub>-Pd/C,

with distinct diffraction characteristics validating the presence and interaction of SnO<sub>2</sub> and Pd nanoparticles (Abdel Hameed 2017).

### 7.3.2 Raman Analysis

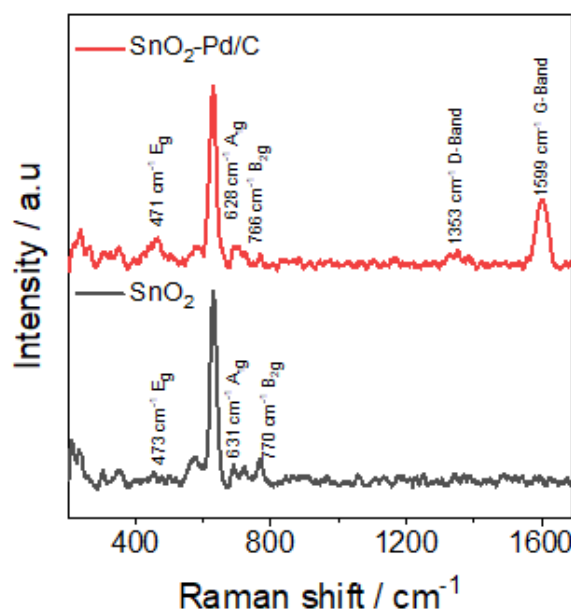


**Figure 7.3.** Raman analysis of SnO<sub>2</sub>-Pd/C-NF and pure SnO<sub>2</sub>-NF.

The standard rutile tetragonal structure of SnO<sub>2</sub> is evidenced by the Raman active modes E<sub>g</sub>, A<sub>1g</sub>, and B<sub>2g</sub>, which are observed at 473, 631, and 770 cm<sup>-1</sup>, respectively and is depicted in **Fig 7.3**. The A<sub>1g</sub> and B<sub>2g</sub> modes, being non-degenerate, reflect the contraction and expansion of Sn–O bonds, whereas the doubly degenerate E<sub>g</sub> mode pertains to the vibrational movement of oxygen atoms within the oxygen plane (Asaithambi et al. 2020; Mehraj et al. 2015). These observations confirm the successful formation of SnO<sub>2</sub>. In the SnO<sub>2</sub>-Pd/C composite, the Raman active modes of SnO<sub>2</sub> exhibit slight shifts, with E<sub>g</sub> at 471 cm<sup>-1</sup>, A<sub>1g</sub> at 628 cm<sup>-1</sup>, and B<sub>2g</sub> at 766 cm<sup>-1</sup> are shown in Fig. 1b. Additionally, the presence of peaks at 1353 cm<sup>-1</sup> and 1566 cm<sup>-1</sup> corresponding to the D and G bands of carbon, respectively, is noted. The lower intensity of the D band suggests that the carbon support possesses high quality, characterized by low defect density and high crystallinity. This high-quality carbon support contributes to enhanced electrical conductivity, stability, and potentially superior catalytic performance of the composite material (Zhang et al. 2019).

### 7.3.3 Cyclic Voltammetry (CV) and Electrochemical Active Surface Area (ECAS) study

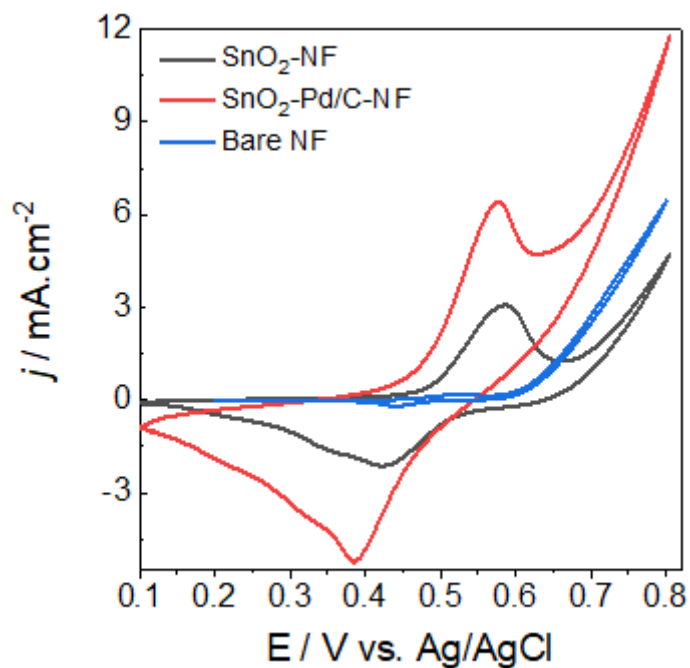


**Figure 7.4.** Cyclic Voltammetry comparison of bare NF,  $\text{SnO}_2\text{-NF}$ , and  $\text{SnO}_2\text{-Pd/C-NF}$ .

CV analyses were performed on the synthesized  $\text{SnO}_2\text{-NF}$  and  $\text{SnO}_2\text{-Pd/C-NF}$  samples within a potential window of 0.1 to 0.8 V vs.  $\text{Ag}/\text{AgCl}$  at a scan rate of 50  $\text{mV/s}$ , as shown in **Fig 7.4**. Notably,  $\text{SnO}_2\text{-Pd/C-NF}$  exhibited significantly enhanced activity compared to the other materials, with both its cathodic and anodic peaks exceeding those of its counterparts.

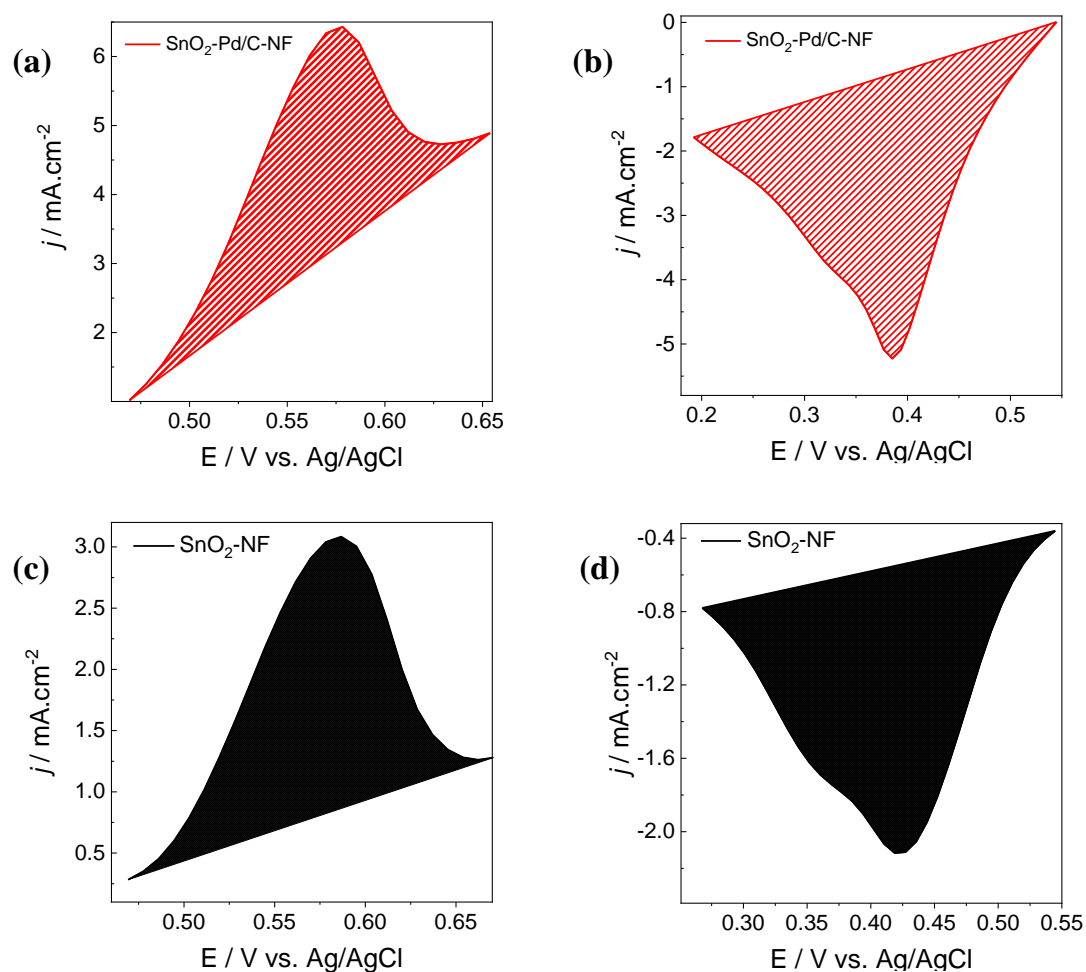


**Figure 7.5.** Oxidation and reduction peak analysis of (a), (b)  $\text{SnO}_2\text{-Pd/C-NF}$ ; (c), (d)  $\text{SnO}_2\text{-NF}$  respectively.

The selection of electrode material is further rationalized by elucidating the electrochemical surface-active sites, inferred from the redox peak currents, as depicted in **Fig 7.5 (a-d)**. The determination of surface-active sites, corresponding to the number of electrons transferred during the redox peaks (Yousefi et al. 2011), was achieved through the analysis of recorded CV data for the optimal materials. In this study, the oxidation peak was used to quantify the electron transfers, resulting in values of  $3.11 \times 10^{19}$  and  $2.4 \times 10^{19}$  for  $\text{SnO}_2\text{-Pd/C-NF}$  and  $\text{SnO}_2\text{-NF}$ , respectively as shown in **Fig 7.5 (a,c)**. Similarly, the reduction peak analysis yielded electron transfer values of  $8.22 \times 10^{19}$  and  $2.71 \times 10^{19}$  for  $\text{SnO}_2\text{-Pd/C-NF}$  and  $\text{SnO}_2\text{-NF}$ , respectively as shown in **Fig 7.5 (b,d)**. This analysis underscores the superiority of  $\text{SnO}_2\text{-Pd/C-NF}$ , given its

significantly higher electron transfer rates during both the oxidation and reduction peaks.

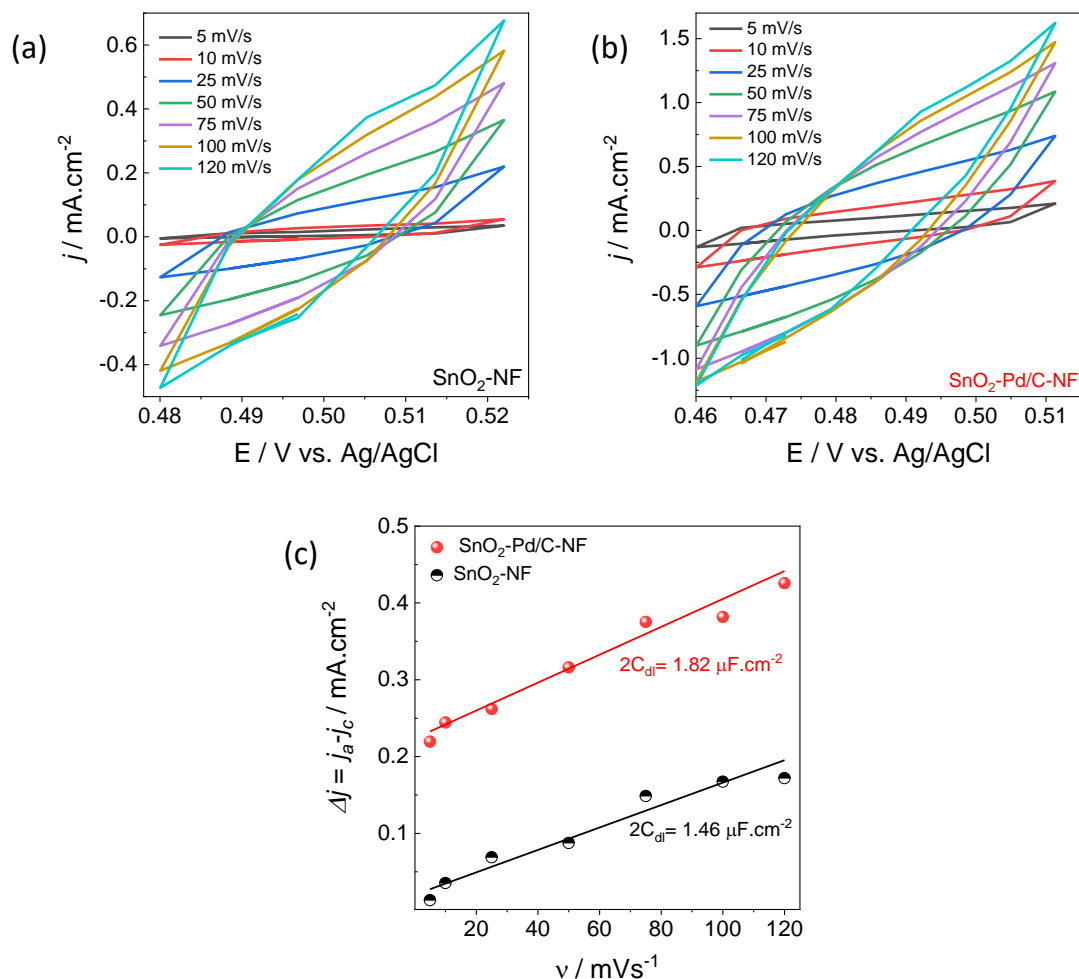


**Figure 7.6.** CV study for ECSA plot of (a)  $\text{SnO}_2\text{-NF}$ ; (b)  $\text{SnO}_2\text{-Pd/C-NF}$ ; (c) ECSA plot of  $\text{SnO}_2\text{-NF}$ ,  $\text{SnO}_2\text{-Pd/C-NF}$ .

As illustrated in **Fig 7.6 (a-b)**, the CVs compare the activity of  $\text{SnO}_2\text{-NF}$  and  $\text{SnO}_2\text{-Pd/C-NF}$  electrodes. In contrast to BET analysis, this study fully immerses the material in the electrolyte, enabling precise determination of the material's surface area activity (Anantharaj et al. 2018). According to **Fig 7.6 (c)**, the double-layer capacitance ( $2C_{dl}$ ) values for  $\text{SnO}_2\text{-Pd/C-NF}$  and  $\text{SnO}_2\text{-NF}$  are  $1.82 \mu\text{F.cm}^{-2}$  and  $1.46 \mu\text{F.cm}^{-2}$ , respectively. The electrochemically active surface areas for  $\text{SnO}_2\text{-Pd/C-NF}$  and  $\text{SnO}_2\text{-NF}$  were determined to be  $0.0227 \text{ cm}^2$  and  $0.0183 \text{ cm}^2$ , respectively. The significant

enhancement of active sites in SnO<sub>2</sub>-Pd/C-NF, compared to the other electrodes, unequivocally establishes SnO<sub>2</sub>-Pd/C-NF as the superior material.

### 7.3.4 Electrochemical Impedance Spectra (EIS) Study

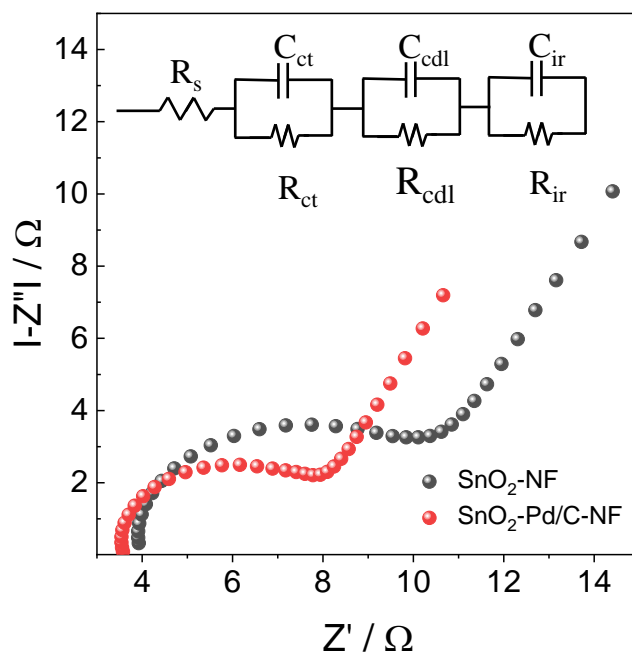


**Figure 7.7.** Nyquist Plot of SnO<sub>2</sub>-NF and SnO<sub>2</sub>-Pd/C-NF materials.

The conductivity and interference characteristics of SnO<sub>2</sub>-NF and SnO<sub>2</sub>-Pd/C-NF were rigorously examined through Electrochemical Impedance Spectroscopy (EIS), utilizing a standardized three-electrode configuration. The Nyquist plot was interpreted by fitting it to the equivalent circuit illustrated as depicted in **Fig 7.7**. This circuit encompasses solution resistance ( $R_s$ ), double-layer resistance ( $R_{cdl}$ ), charge transfer resistance ( $R_{ct}$ ), and internal resistance ( $R_{ir}$ ). The electrochemically derived parameters, detailed in **Table 7.1**, offer critical insights into the materials' performance. Remarkably, SnO<sub>2</sub>-Pd/C-NF exhibits significantly lower charge transfer resistance and solution resistance in comparison to the other materials, as indicated in **Table 7.1**. This finding unequivocally confirms the superior electrochemical activity of SnO<sub>2</sub>-Pd/C-NF relative to all other materials tested.

**Table 7.1.** EIS parameters for the fitted circuit

Samples	$R_s$ ( $\Omega$ )	$C_{ct}$ (F)	$R_{ct}$ ( $\Omega$ )	$C_{cdl}$ (F)	$R_{cdl}$ ( $\Omega$ )	$C_{ir}$ (F)	$R_{ir}$ ( $\Omega$ )
SnO <sub>2</sub> -NF	3.907	$2.209 \times 10^{-4}$	2.444	$6.611 \times 10^{-6}$	6.424	$1.68 \times 10^{-4}$	46.59
SnO <sub>2</sub> -Pd/C-NF	3.563	$4.213 \times 10^{-4}$	1.762	$1 \times 10^{-5}$	4.507	$2.438 \times 10^{-4}$	36.18

### 7.3.5 Field Emission Scanning Electron Microscopy (FE-SEM) Analysis

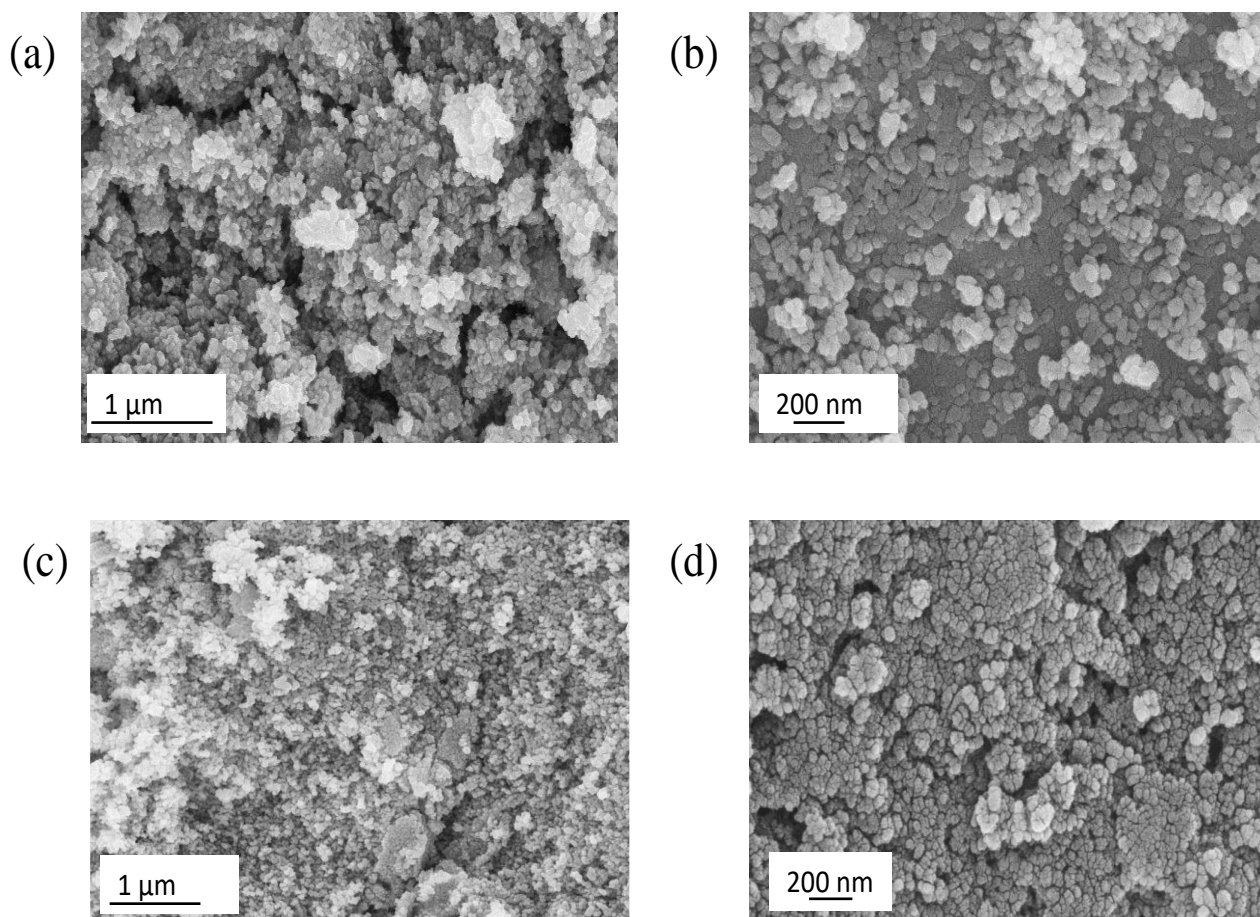


**Figure 7.8.** (a), (b) FE-SEM and magnified images of SnO<sub>2</sub> respectively; (c), (d) FE-SEM and magnified images of SnO<sub>2</sub>-Pd/C.

The FE-SEM analysis of the SnO<sub>2</sub> and SnO<sub>2</sub>-Pd/C materials provides critical insights into their morphological features, as illustrated in **Fig 7.8 (a-d)**, respectively. SnO<sub>2</sub> nanoparticles display a uniform and relatively less agglomerated structure with distinct particles as depicted in **Fig 7.8 (a-b)**. In contrast, the SnO<sub>2</sub>-Pd/C composite exhibits a higher degree of agglomeration as depicted in **Fig 7.8 (c-d)**. This increased agglomeration is primarily attributed to the presence of Pd, which acts as a catalyst and enhances the interactions between SnO<sub>2</sub> nanoparticles and the carbon support. Pd serves as nucleation sites for SnO<sub>2</sub> growth, promotes strong binding energies, and fosters a more interconnected network, all contributing to the observed agglomeration (Deivasegamani et al. 2017; Liu et al. 2021). This comprehensive FE-SEM analysis confirms the successful incorporation of Pd/C into the SnO<sub>2</sub> matrix, resulting in a modified and more interconnected structure.

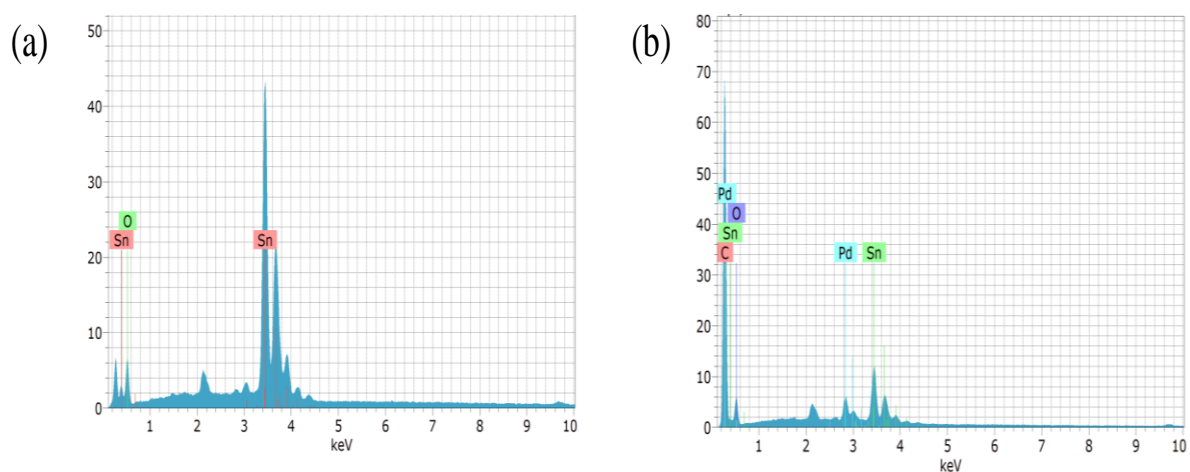


**Figure 7.9.** EDS analysis of (a) SnO<sub>2</sub>; (b) SnO<sub>2</sub>-Pd/C respectively.

Elemental composition validation via EDS corroborates the presence of Sn and O in the pure sample, alongside Pd and C within the nanocomposite system, as depicted in **Fig 7.9 (a-b)** respectively. This elemental analysis substantiates the successful formation of the SnO<sub>2</sub>-Pd/C composite.

### 7.3.6 High-Resolution Transmission Electron Microscopy (HR-TEM) Analysis

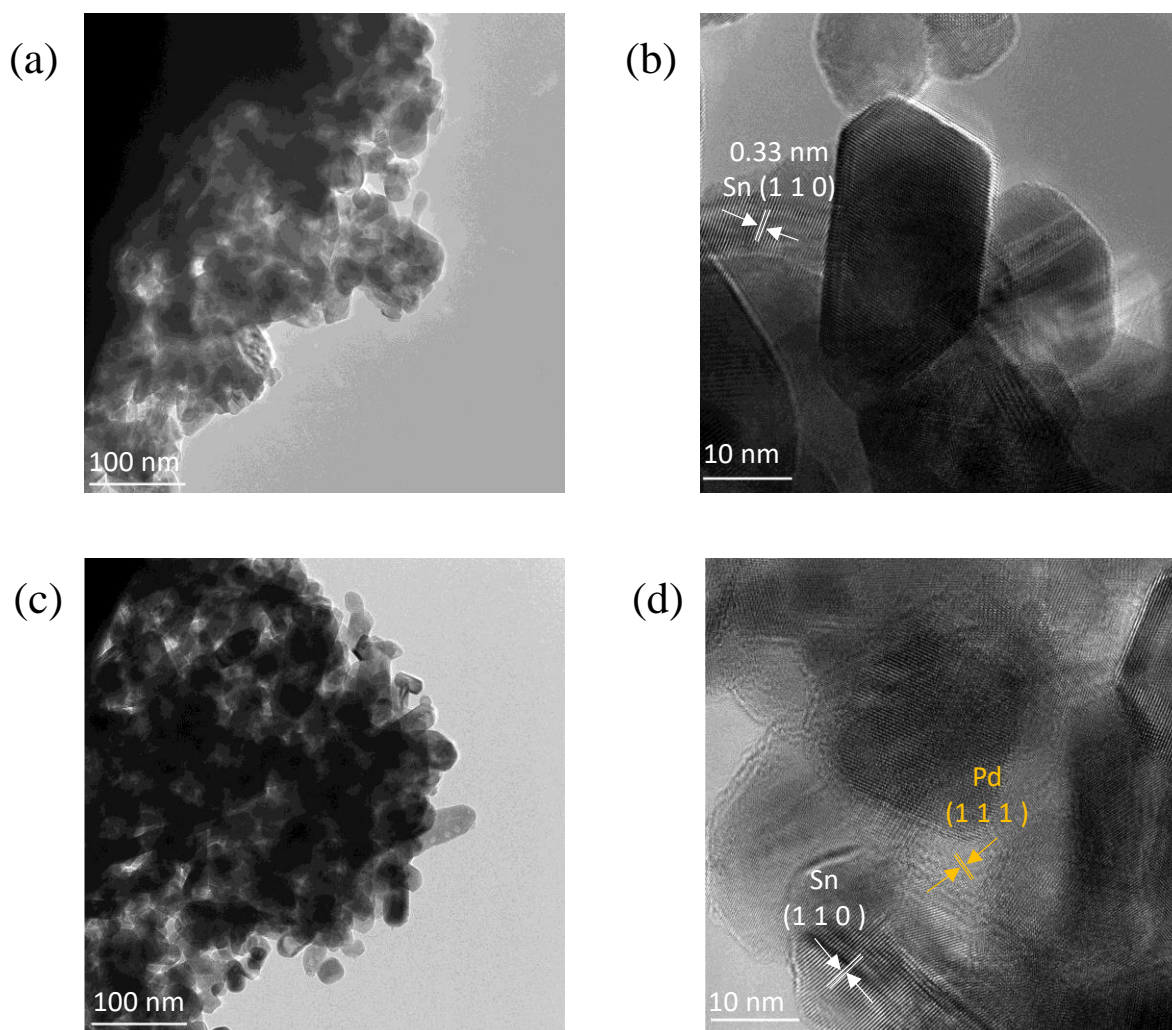


**Figure 7.10.** TEM and HR-TEM analysis of (a-b) SnO<sub>2</sub>; and (c-d) SnO<sub>2</sub>-Pd/C respectively.

The HR-TEM analysis of SnO<sub>2</sub> and SnO<sub>2</sub>-Pd/C materials provides significant insights into their structural and morphological properties, as illustrated in **Fig. 7.10 (a-b)** and **7.10 (c-d)**, respectively. The SnO<sub>2</sub> nanoparticles demonstrate a rod-like hexagonal morphology characterized by well-defined lattice fringes. These fringes exhibit an approximate spacing of 0.33 nm, which corresponds to the (110) plane, confirming the tetragonal structure of SnO<sub>2</sub> as per JCPDS-77-0450. This observation is indicative of the crystalline nature of the nanoparticles. In contrast, the SnO<sub>2</sub>-Pd/C composite shows increased agglomeration compared to pure SnO<sub>2</sub>, suggesting a strong interaction between the Pd/C and SnO<sub>2</sub> particles. The particle size lies between 5 to 60 nm. The

composite's smoother edges and greater aggregation imply the incorporation of carbon. The Pd and Sn elements are clearly identified by their characteristic lattice fringes, with the approximate interval of 0.33 nm corresponding to the (110) planes of the tetragonal SnO<sub>2</sub> structure and 0.234 nm corresponding to the (111) planes of the face-centered cubic phase of Pd, consistent with JCPDS-05-0681. This detailed HR-TEM analysis confirms the successful synthesis and decoration of Pd/C with SnO<sub>2</sub>, highlighting the enhanced structural properties of the composite.

### 7.3.7 X-ray photoelectron spectroscopy (XPS) Analysis

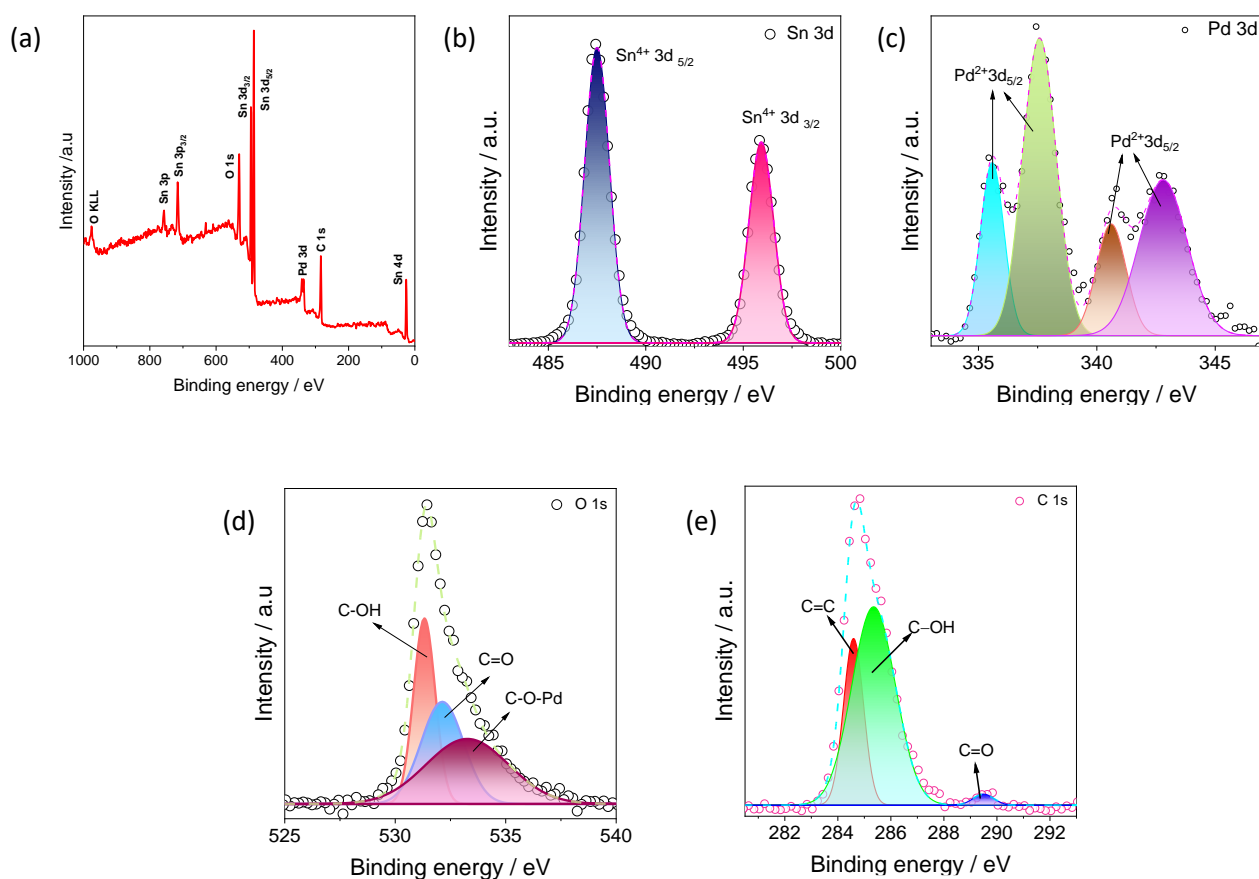


**Figure 7.11.** XPS of SnO<sub>2</sub>-Pd/C (a) Survey; (b) Sn 3d; (c) Pd 3d; (d) O 1s; (e) C 1s.

XPS was utilized to analyze the chemical environment of the SnO<sub>2</sub>-Pd/C composite material. The XPS spectra, illustrated in **Fig 7.11 (a)**, exhibit distinct binding energy peaks corresponding to oxygen (O), tin (Sn), palladium (Pd), and carbon (C). These peaks are well-defined and corroborate the elemental composition as determined by

energy-dispersive spectroscopy (EDS), thereby confirming the successful decoration of SnO<sub>2</sub> with Pd/C. The Sn 3d spectrum, presented in **Fig 7.11 (b)**, reveals two symmetric peaks at approximately 487.5 eV and 495.8 eV, which correspond to the Sn 3d<sub>5/2</sub> and Sn 3d<sub>3/2</sub> states, respectively. These peaks are characteristic of tin in the +4 oxidation state, which confirms the exclusive formation of the SnO<sub>2</sub> phase in the SnO<sub>2</sub>-Pd/C composite (Acharyya et al. 2023; Sahoo and Ramaprabhu 2017). The observed peak separation of 8 eV is attributed to the spin-orbit coupling of the Sn 3d states, reinforcing the assignment to SnO<sub>2</sub> (Acharyya et al. 2023).

In the Pd 3d spectrum, two pairs of asymmetric peaks are observed as shown in **Fig 7.11 (c)**. The binding energies at 335.5 eV and 337.5 eV correspond to the Pd 3d<sub>5/2</sub> state, whereas the binding energies at 340.6 eV and 342.7 eV correspond to the Pd 3d<sub>3/2</sub> state. The pronounced doublet peaks are indicative of the presence of metallic palladium Pd (0), whereas the subtler peaks correspond to palladium in the +2 oxidation state (Pd<sup>2+</sup>). The presence of these weaker peaks suggests the occurrence of Pd<sup>2+</sup> oxidation states, likely due to the formation of Pd-O bonds within the composite, indicative of partial oxidation (Wu et al. 2015). The O 1s spectrum, depicted in **Fig 7.11 (d)**, features three distinct peaks at 531.2 eV, 532.4 eV, and 533.4 eV. The peak observed at 532.4 eV corresponds to the standard binding energy of oxygen in O-C configurations. The observed peaks at 531.2 eV and 533.4 eV are indicative of C-OH bonds and C-O-Pd interactions within the SnO<sub>2</sub>-Pd/C composite, respectively. These findings illustrate the complex chemical environment of the material, emphasizing the intricate interactions between Pd/C and SnO<sub>2</sub> phases. (Ding et al. 2023; Sahoo and Ramaprabhu 2017).

The C 1s XPS spectra, shown in **Fig 7.11 (e)**, exhibit binding energy peaks at 284.8 eV, 286.7 eV, and 288.7 eV. These peaks are respectively assigned to C=C sp<sup>2</sup>, C-OH, and C=O functional groups within the carbon matrix of the composite (Ipadeola et al. 2019). The presence of these functional groups indicates the diverse chemical environment and potential interaction sites available in the carbon component of the SnO<sub>2</sub>-Pd/C composite.

### 7.3.8 Electrochemical Study

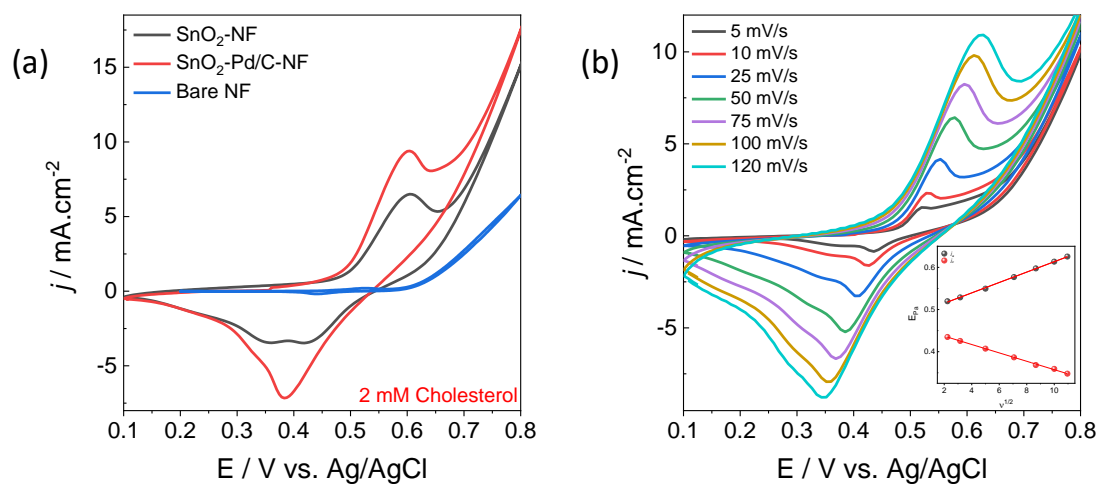


**Figure 7.12.** (a) Comparative CV analysis of SnO<sub>2</sub>-NF, SnO<sub>2</sub>-Pd/C-NF, and bare NF in 0.1 M KOH at a scan rate of 50 mV/s in presence of 2 mM cholesterol; (b) CV scan rate studies of SnO<sub>2</sub>-Pd/C-NF in 0.1 M KOH over a range of 5-120 mV/s. The inset illustrates the correlation between the anodic and cathodic peak currents with the square root of the scan rate.

As illustrated in **Fig 7.12 (a)**, the SnO<sub>2</sub>-Pd/C-NF composite was evaluated for its cholesterol oxidation properties in comparison with bare NF and SnO<sub>2</sub>-NF in a 2 mM cholesterol solution within 0.1 M KOH. The results demonstrated that, within the potential range of 0.1 to 0.8 V versus Ag/AgCl, bare NF showed no significant catalytic activity towards cholesterol oxidation. In contrast, the SnO<sub>2</sub>-NF material exhibited an increase in anodic peak current, indicative of its catalytic support for cholesterol oxidation. Notably, SnO<sub>2</sub>-Pd/C-NF showed a substantial enhancement in anodic peak current at  $E_{pa} = 0.59$  V upon the addition of cholesterol, displaying a threefold increase in responsiveness compared to SnO<sub>2</sub>-NF. This marked increase underscores the superior electrochemical activity of the SnO<sub>2</sub>-Pd/C-NF composite.

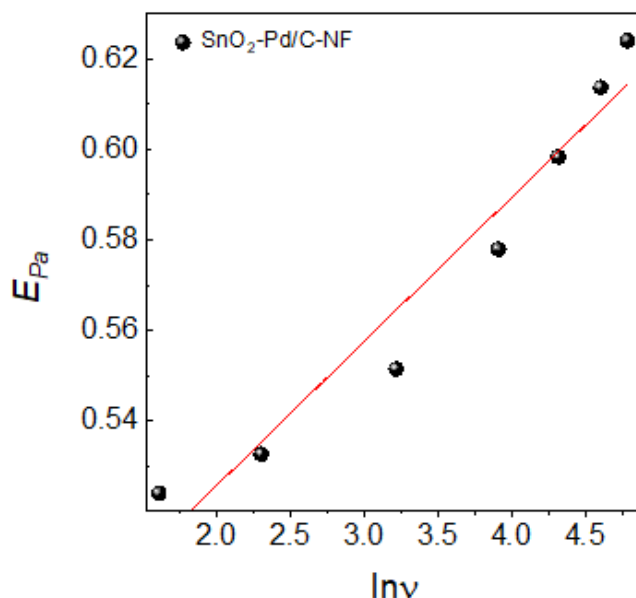
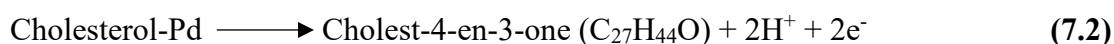


**Figure 7.13.** Laviron equation study of  $\text{SnO}_2\text{-Pd/C-NF}$

The underlying mechanism involves the adsorption of cholesterol onto the Pd sites, followed by its dehydrogenation to Cholest-4-en-3-one, with the concurrent release of protons and electrons contributing to the observed current change (Eq. 7.1, 7.2). This significant enhancement in electrochemical response highlights the effectiveness of the  $\text{SnO}_2\text{-Pd/C-NF}$  composite in cholesterol oxidation, providing a robust platform for biosensing applications.



As shown in Fig 7.13, the Laviron equation (Eq. 4.3) is derived from the slope of  $\ln(v)$  vs anodic peak potential during cholesterol addition. The analysis indicates that approximately 1.7 electrons, rounded to 2, are transferred during the electro-oxidation of cholesterol, confirming a two-electron process.

CV analysis as depicted in Fig 7.12 (b) was conducted on the  $\text{SnO}_2\text{-Pd/C-NF}$  electrode using scan rates ranging from 5-120 mV/s, aimed at exploring its electrochemical behavior and kinetic response. The investigation reveals a pronounced increase in both anodic and cathodic peak currents as the scan rate escalates. This phenomenon arises from the dynamic formation and depletion of a diffusion layer, which becomes thinner

with higher scan rates. At lower scan rates, a thicker diffusion layer impedes the access of electroactive species to the electrode surface, resulting in diminished peak currents. Conversely, elevated scan rates promote faster species transport, leading to higher peak currents. Moreover, the CV profiles illustrate a notable shift of the cathodic peak towards more negative potentials and the anodic peak towards more positive potentials with increasing scan rates. This shift signifies the electrode's redox dynamics and establishes a clear linear relationship between the peak currents and the square root of the scan rate as shown in **Fig 7.12 (b) (Inset)**. This observation underscores the diffusion-limited nature of the electrode process, where electron transfer predominantly occurs via an outer sphere mechanism facilitated by the reduction in diffusion layer thickness at higher scan rates (Rao et al. 2024; Rao and Bhat 2024).

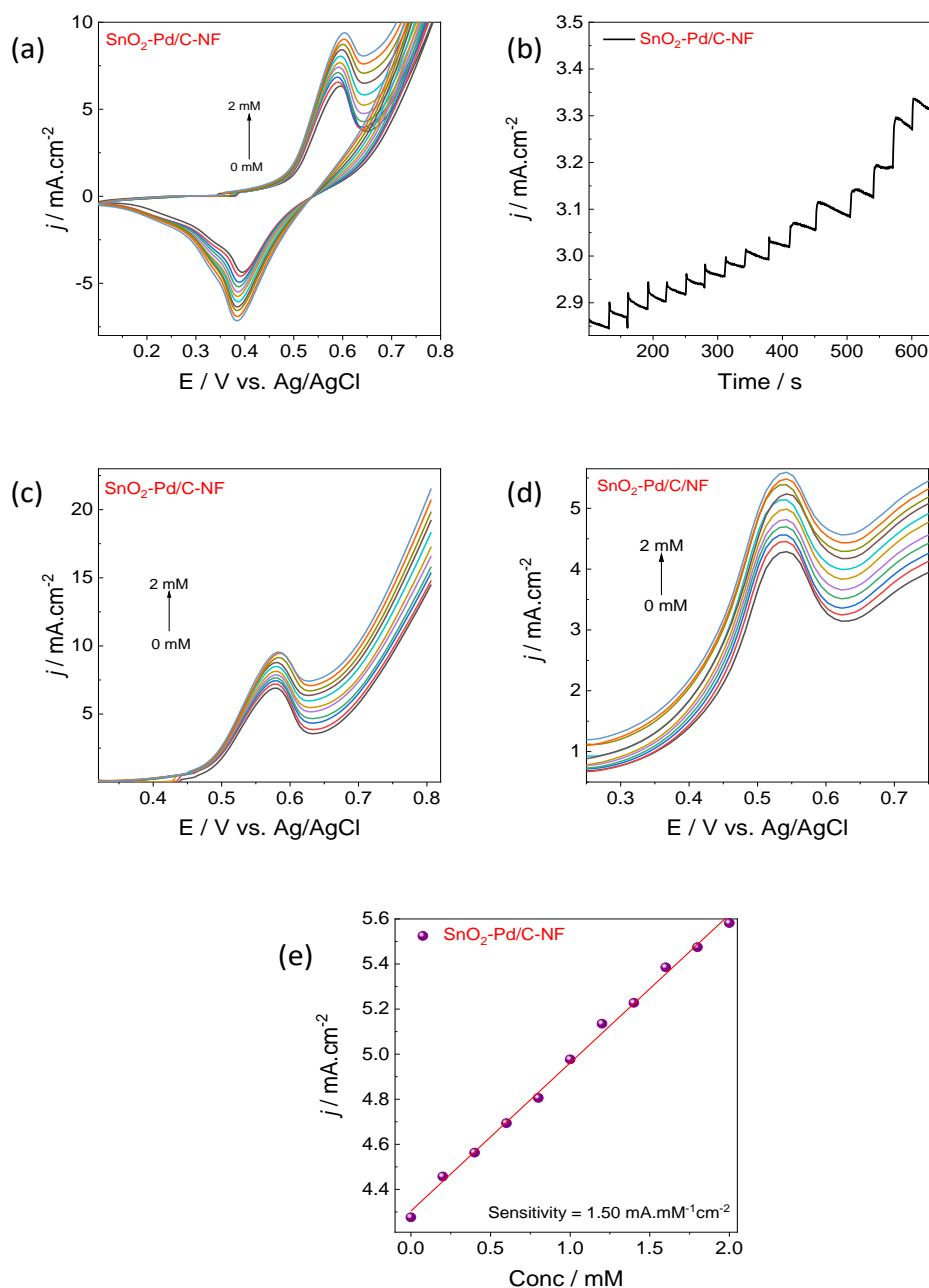


**Figure 7.14.** (a) CV analysis of SnO<sub>2</sub>-Pd/C-NF with successive additions of cholesterol in 0.1 M KOH at a scan rate of 50 mV/s; (b) CA study of SnO<sub>2</sub>-Pd/C-NF in 0.1 M KOH with successive additions of cholesterol under stirring conditions at an applied potential of 0.59 V; (c) LSV analysis of SnO<sub>2</sub>-Pd/C-NF with successive additions of cholesterol in 0.1 M KOH at a scan rate of 50 mV/s; (d) DPV analysis of SnO<sub>2</sub>-Pd/C-NF with successive additions of cholesterol in 0.1 M KOH at a scan rate of 10 mV/s; (e) Calibration curve for the determination of cholesterol using SnO<sub>2</sub>-Pd/C-NF.

According to **Fig 7.14 (a)**, the progressive addition of cholesterol analyzed through CV in 0.1 M KOH. As cholesterol concentration increases, a corresponding gradual augmentation in the anodic peak is observed, signifying the electrocatalytic oxidation process within the linear range extends from 200  $\mu\text{M}$  to 2 mM. This observed phenomenon is attributed to the increasing diffusion layer of cholesterol near the electrode surface, thereby amplifying the anodic peak current. Consequently, these findings underscore the efficacy of the  $\text{SnO}_2\text{-Pd/C/NF}$  electrode for precise amperometric sensing applications aimed at quantifying cholesterol levels.

Furthermore, the enzyme-free cholesterol sensor's analytical performance was rigorously assessed using CA measurements on the  $\text{SnO}_2\text{-Pd/C-NF}$  electrode. The study involved sequential additions of cholesterol across concentrations ranging from 200  $\mu\text{M}$  to 2 mM, conducted under constant stirring conditions with a fixed potential of 0.59 V. The recorded amperometric responses at 30 s intervals clearly illustrate incremental increases in current with each cholesterol addition, as depicted in **Fig 7.14 (b)**. This step-wise current augmentation directly correlates with the electrode's sensitivity to cholesterol, highlighting its capability to detect and quantify cholesterol levels based on changes in the analyte's diffusion layer near the electrode interface.

LSV is a versatile and widely used technique in electrochemistry that gives information on sensitivity, selectivity, and efficiency making it a valuable tool in the study of electrochemical biosensors. As illustrated in **Fig 7.14 (c)**, LSV analysis was carried out within the linear range of 200  $\mu\text{M}$  to 2 mM cholesterol in 0.1 M KOH, employing a scan rate of 50 mV/s. Each successive addition of cholesterol induced discernible changes in current, underscoring the electrode's responsiveness to varying cholesterol concentrations.

The DPV study demonstrated robust reproducibility, thereby establishing its reliability for analyzing the  $\text{SnO}_2\text{-Pd/C-NF}$  electrode. As illustrated in **Fig 7.14 (d)**, DPV analysis was conducted within the linear concentration range of 200  $\mu\text{M}$  to 2 mM cholesterol in 0.1 M KOH, employing a scan rate of 10 mV/s. Each successive addition of cholesterol-induced discernible changes in current, underscoring the electrode's responsiveness to varying cholesterol concentrations.

The calibration curve of the cholesterol sensor demonstrates a linear relationship over the concentration range of 200  $\mu\text{M}$  to 2 mM, as illustrated in **Fig 7.14 (e)**. This linearity enables the accurate determination of the sensor's sensitivity, LOD, and LOQ. The sensor exhibits a sensitivity of  $1560 \mu\text{A mM}^{-1} \text{cm}^{-2}$ , with limits of detection (LOD) and quantification (LOQ) determined to be 28  $\mu\text{M}$  and 34  $\mu\text{M}$ , respectively. The sensor also exhibits a rapid response time of 2 s, highlighting its efficiency and effectiveness in cholesterol detection.

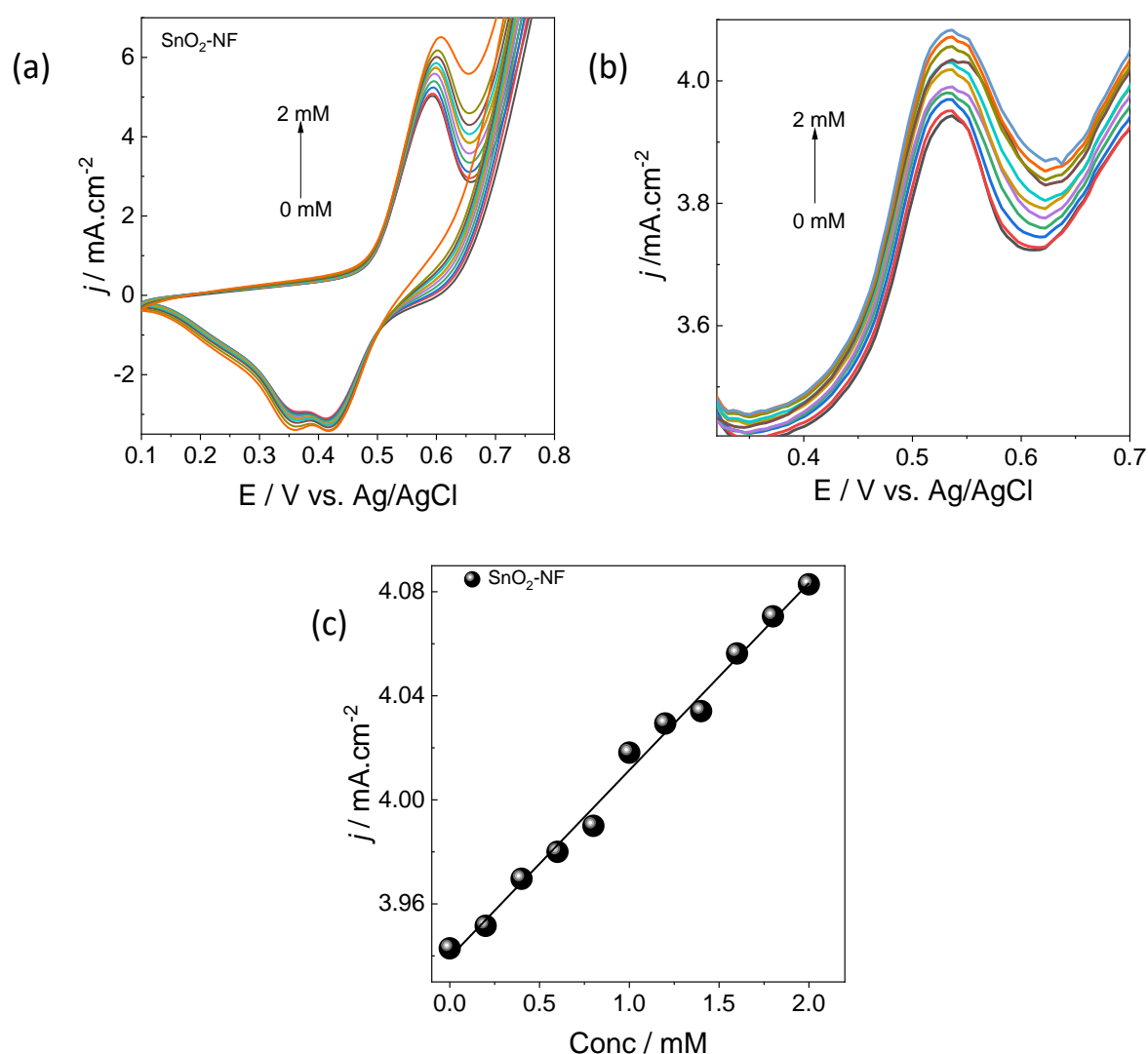


**Figure 7.15.** (a) CV analysis of SnO<sub>2</sub>-NF with successive additions of cholesterol in 0.1 M KOH at a scan rate of 50 mV/s; (b) DPV analysis of SnO<sub>2</sub>-NF with successive additions of cholesterol in 0.1 M KOH at a scan rate of 10 mV/s; (c) Calibration curve for the determination of cholesterol using SnO<sub>2</sub>-NF.

Additionally, CV successive analysis, DPV was performed on the base SnO<sub>2</sub>-NF within the linear range of 200 μM to 2 mM and are depicted in **Fig 7.15 (a-b)** respectively. The results paralleled those observed with the modified material, indicating that the base material is suitable for amperometric non-enzymatic cholesterol biosensors. This linearity enables the accurate determination of the sensor's sensitivity and it is found to be 546 μA mM<sup>-1</sup> cm<sup>-2</sup> and calibration graph as illustrated in **Fig 7.15 (c)**.

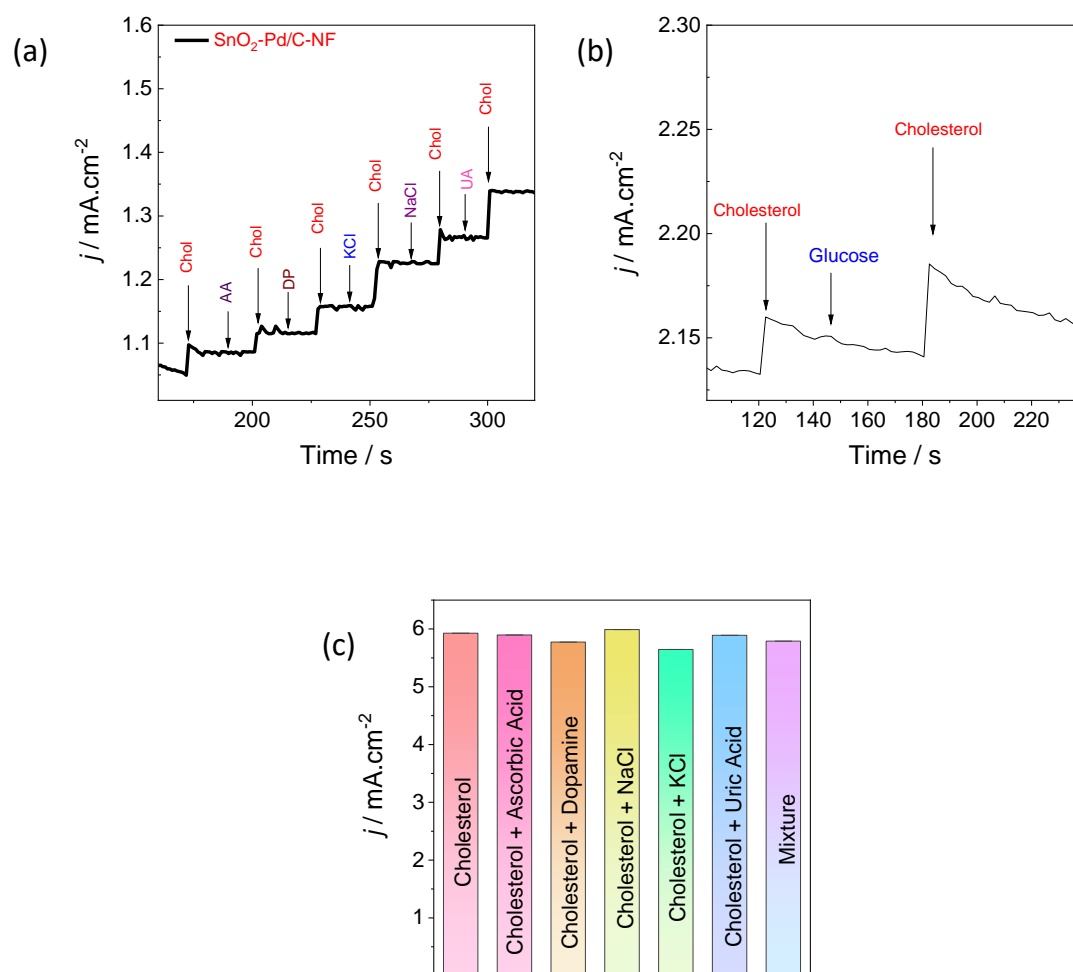


**Figure 7.16.** (a), (b) Interference study of SnO<sub>2</sub>-Pd/C-NF in the presence of interfering species under stirring conditions in 0.1 M KOH at an applied potential of 0.59 V; (c) DPV interference study for SnO<sub>2</sub>-Pd/C-NF at a scan rate of 5 mV/s with a pulse amplitude of 50 mV.

Developing an electrochemical cholesterol sensor poses a significant challenge due to the need to effectively eliminate interfering compounds during cholesterol oxidation, highlighting the material's selectivity in detecting cholesterol. In this study, various substances such as AA, DP, NaCl, KCl, UA and Glucose were added to a 0.1 M KOH solution to evaluate the selectivity of SnO<sub>2</sub>-Pd/C-NF. As depicted in **Fig 7.16 (a-b)**, these interference species at a concentration of 0.5 mM did not elicit a response from SnO<sub>2</sub>-Pd/C-NF, whereas a distinct current increase was observed upon the addition of 2 mM cholesterol. This observation underscores that even at higher concentrations, the interference species do not impact the cholesterol oxidation activity of SnO<sub>2</sub>-Pd/C-NF, demonstrating its exceptional selectivity for cholesterol sensing.

Similar to the CA investigation, an interference study using DPV was conducted to assess the selectivity of the SnO<sub>2</sub>-Pd/C-NF material for cholesterol sensing, as illustrated in **Fig 7.16 (c)**. The study involved analyzing the response of the material to individual interference species, including ascorbic acid (AA), dopamine (DP), NaCl, KCl, and uric acid (UA), each mixed with cholesterol at a concentration of 0.5 mM. The results indicated that these interference species did not alter the activity of SnO<sub>2</sub>-Pd/C-NF, as evidenced by the consistent response observed in DPV analysis. Moreover, the mixture containing 2 mM cholesterol and all interference species showed no significant deviation in the material's electrochemical activity, reaffirming its robust sensitivity towards cholesterol oxidation. These findings underscore the high selectivity and potential of SnO<sub>2</sub>-Pd/C-NF as a reliable material for cholesterol detection applications. The SnO<sub>2</sub>-Pd/C composite material excels as a non-enzymatic cholesterol biosensor due to its unique structural and functional properties. SnO<sub>2</sub> provides stability and high surface area, while Pd/C enhances catalytic activity and conductivity. This synergy results in remarkable sensitivity, selectivity, and stability with improved electrochemical activity due to the composite's large surface area, lower solution resistance, and enhanced charge transfer capabilities.

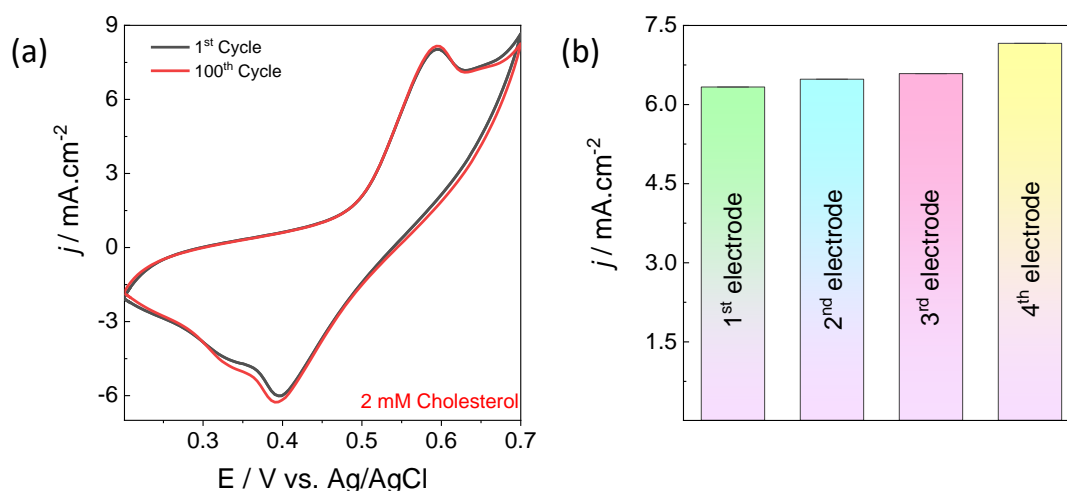


**Figure 7.17.** (a) The CVs of SnO<sub>2</sub>-Pd/C-NF with 2 mM Cholesterol for 100 cycles in 0.1 M KOH at the scan rate of 50 mV/s; (b) Comparison of the activity of SnO<sub>2</sub>-Pd/C-NF with four different electrodes in 0.1 M KOH at the scan rate of 50 mV/s.

The long-term stability of the SnO<sub>2</sub>-Pd/C-NF electrode was systematically assessed by monitoring its response over 100 consecutive cycles in a 2 mM cholesterol solution. The results, as depicted in **Fig 7.17 (a)**, demonstrate an impressive 100% retention of anodic current. This finding underscores the electrode's exceptional stability and durability, making it highly suitable for extended analytical use. Furthermore, the consistent performance with negligible degradation highlights the electrode's robustness and reliability, affirming its potential for repeated use in diverse applications with minimal loss of sensitivity.

The reproducibility of the SnO<sub>2</sub>-Pd/C-NF electrode's performance was rigorously evaluated by fabricating and testing four identical electrodes under controlled conditions. Each electrode underwent CV analysis to assess its electrochemical activity. The results revealed that all four electrodes exhibited highly consistent electrochemical behavior, with minimal variation in their anodic current responses. This uniformity in performance, as depicted in **Fig 7.17 (b)**, underscores the high reproducibility of the synthesis and fabrication process for the SnO<sub>2</sub>-Pd/C-NF material. The consistent performance across multiple electrodes highlights the material's reliability and robustness, ensuring dependable analytical results for practical applications.

### 7.3.9 Post-Cholesterol Oxidation Characterization

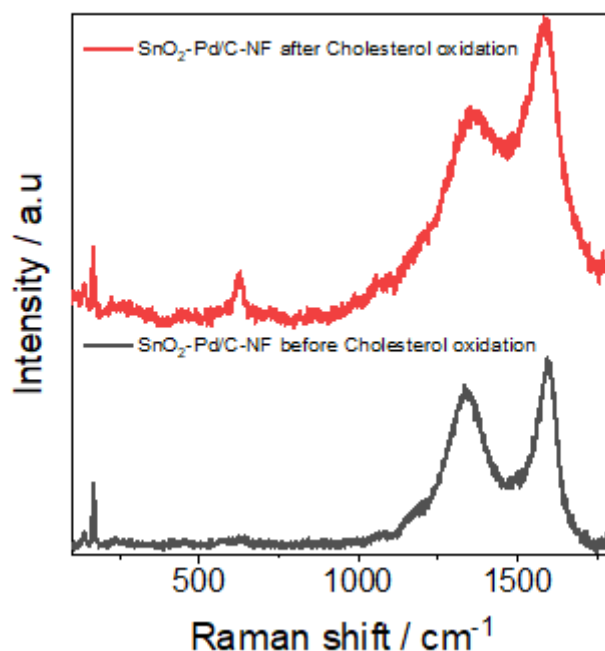


**Figure 7.18.** Before and after cholesterol oxidation Raman analysis of SnO<sub>2</sub>-Pd/C-NF respectively.

The SnO<sub>2</sub>-Pd/C-NF material was evaluated for cholesterol sensing, with Raman spectroscopy employed to assess structural changes resulting from cholesterol oxidation. As shown in **Fig 7.18**, the analysis revealed no significant changes in the peaks before and after cholesterol exposure, indicating that the SnO<sub>2</sub>-Pd/C-NF material retains its structural and chemical integrity throughout the sensing process. This stability implies that the material's morphology remains unchanged, which is essential for consistent performance in repeated use. Additionally, the broadening of peaks observed in the Raman spectra can be attributed to the overlap between the characteristic peaks of the nickel foam and the D and G bands of carbon.

### 7.3.10 High-Resolution Liquid Chromatography Mass Spectrometry (HR-LCMS)

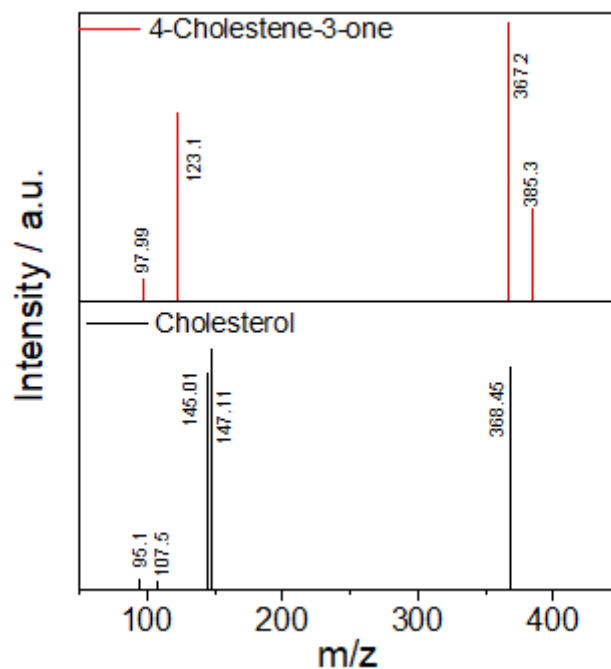


*Figure 7.19. HR-LCMS study of Cholesterol before CV and 4-Cholestene-3-one formation after CV completion.*

To validate this mechanism, the cholesterol solution underwent High-Resolution Liquid Chromatography Mass Spectrometry (HR-LCMS) analysis before and after exposure to the SnO<sub>2</sub>-Pd/C-NF material, as depicted in **Fig 7.19**. This analytical approach aimed to detect any changes in the cholesterol sample following its interaction with the SnO<sub>2</sub>-Pd/C-NF material. The results of the analysis conclusively confirmed the transformation of cholesterol (m/z = 368.45) into 4-cholestene-3-one (m/z = 385.3). This finding provides robust evidence supporting the catalytic activity of SnO<sub>2</sub>-Pd/C-NF in facilitating the oxidation of cholesterol.

Moreover, the observed biosensing properties of the SnO<sub>2</sub>-Pd/C-NF material exhibit superior performance compared to previously reported cholesterol biosensors, as illustrated in **Table 7.2**. The synthesis method described represents a novel and streamlined approach, yielding enhanced activity surpassing that of other materials documented in the literature.

**Table 7.2** delineates the biosensing characteristics observed for the SnO<sub>2</sub>-Pd/C-NF electrode, demonstrating its comparative and superior performance in cholesterol detection when compared to existing biosensors documented in the published literature.

<b>Electrode</b>	<b>Sensitivity</b>	<b>LOD</b>	<b>Linear Range</b>	<b>Ref.</b>
Au-f-MWCNT-Ppy	10.12 $\mu\text{A mM}^{-1} \text{cm}^{-2}$	$0.1 \times 10^{-3} \text{ M}$	2 – 8 mM	(Alagappan et al. 2020)
MIP-MWCNTs/Au NPs/SPCE	5 $\mu\text{A} \cdot \mu\text{M}^{-1} \text{cm}^{-2}$	0.01 $\mu\text{M}$	0.01–8 $\mu\text{M}$	(Jalalvand 2022)
MnO <sub>2</sub> /Graphite	-	0.42 nM	$12 \times 10^{-10}$ - $240 \times 10^{-10} \text{ M}$	(Rison et al. 2020)
ZnO/SnO <sub>2</sub> /RuO <sub>2</sub>	11.35 $\mu\text{A} \cdot \mu\text{M}^{-1} \text{cm}^{-2}$	-	0.1nM ~ 0.01mM	(Alam et al. 2021)
SnO <sub>2</sub> -Pd/C-NF	1560 $\mu\text{A} \cdot \text{mM}^{-1} \text{cm}^{-2}$	28 $\mu\text{M}$	200 $\mu\text{M}$ to 2 mM	This work

### 7.3.11 Real Sample Analysis

The SnO<sub>2</sub>-Pd/C-NF electrode was utilized for the quantification of cholesterol in human blood serum samples sourced from hospitals, featuring concentrations spanning 2 mM to 15 mM. By directly analyzing unaltered serum, the electrode delivered values closely mirroring estimated concentrations. **Table 7.3** highlights these findings, affirming the electrode's efficacy in accurately determining cholesterol levels in real-world clinical samples.

**Table 7.3** Analysis of human blood sample

Patient	Gender	Clinically tested (mg/mL)	Found (mg/dL) (SnO <sub>2</sub> -Pd/C-NF)	Deviation
1	F	105.4	101.86	3.54
2	M	178.92	178.03	0.89
3	M	292.3	279	13.3
4	F	315.3	315.9	- 0.6
5	F	418.9	423.4	- 4.5

### 7.4 Conclusions

- SnO<sub>2</sub>-Pd/C was successfully synthesized using a two-step method, involving the hydrothermal preparation of SnO<sub>2</sub> followed by Pd/C decoration and coating on Nickel Foam (NF).
- The resulting biosensor demonstrated remarkable sensitivity of 1560 μA·mM<sup>-1</sup>·cm<sup>-2</sup>, significantly surpassing the sensitivity of SnO<sub>2</sub>-NF alone, which was measured at 546 μA·mM<sup>-1</sup>·cm<sup>-2</sup>.
- The LOD for the Pd/C-decorated SnO<sub>2</sub> composite was determined to be 28 μM, with a LOQ of 34 μM in a 0.1 M KOH solution. The sensor exhibited a linear response across a concentration range of 200 μM to 2 mM.
- The SnO<sub>2</sub>-Pd/C-NF biosensor retained 97% of its performance over a 30-day period, demonstrating excellent cyclic stability and long-term reliability.

- The sensor's robust performance in human serum samples underscores its practical applicability and effectiveness under standard conditions.
- The superior performance of the SnO<sub>2</sub>-Pd/C-NF composite highlights its potential for non-enzymatic cholesterol biosensing in future clinical and biochemical applications.

\*\*\*\*\*

## **CHAPTER 8**

---

---

### **SUMMARY AND CONCLUSIONS**

---

---



---

---

***Abstract:** This section encapsulates the principal findings of the thesis, delivers concluding insights, and outlines prospective avenues for future research.*

---

---

## **8.1 Summary**

Technology plays a vital role in modern life, streamlining processes and addressing complex challenges. In healthcare, advanced diagnostics greatly enhance treatment efficacy, and the advent of reliable biosensors has the potential to improve testing precision, surpassing traditional limitations. This thesis, titled "Synthesis of Nanomaterials and their Applications in Biosensors," explores the sophisticated domain of biosensing with a particular focus on utilizing metal oxide nanomaterials for glucose and cholesterol monitoring. The research commences with the meticulous synthesis and comprehensive characterization of various nanomaterials, including V-doped TiO<sub>2</sub>, Ce-doped ZnO, and Pd/C-decorated SnO<sub>2</sub>. Advanced analytical techniques such as XRD, FE-SEM, HR-TEM, XPS, UV-Visible Spectroscopy, Raman Spectroscopy, and PL Spectroscopy are employed to elucidate their structural, morphological, and optical properties. The electrochemical characteristics are investigated using methodologies including CV, CA, DPV, LSV, and EIS.

Our thesis explores the critical role of technology, focusing on the application of metal oxide-based biosensors in daily life. Biosensors, essential for timely medical interventions, leverage metal oxides due to their exceptional electron transport capabilities, catalytic properties, and chemical durability. These materials possess a large surface area, robust catalytic activity, and stability, making them ideal for rapid and precise detection of biological molecules. Metal oxides exhibit high sensitivity and selectivity, enabling detection of low concentrations of substances, crucial for accurate diagnostics. Their catalytic properties, as seen in TiO<sub>2</sub> and ZnO, enhance biosensor performance by improving signal transduction and sensitivity. The robustness and chemical stability of metal oxides ensure long-term reliability, even in harsh conditions. Additionally, their cost-effectiveness and widespread availability facilitate the development of affordable biosensors for healthcare and environmental monitoring. Functionalization with biological molecules further enhances their sensitivity and specificity, enabling tailored biosensors for diverse applications. High electron mobility

in metal oxides like SnO<sub>2</sub> and ZnO promotes efficient electron transport, improving overall biosensor performance.

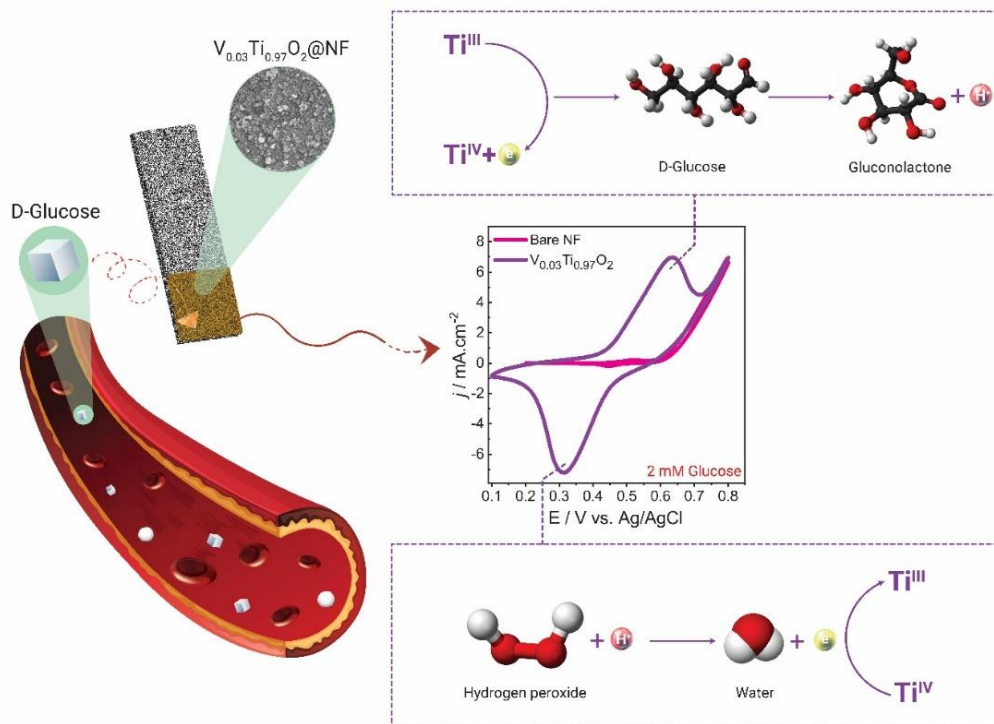


**Figure 8.1.** Graphical representation of the mechanism of  $V_{0.03}Ti_{0.97}O_2@NF$  sensing glucose.

TiO<sub>2</sub> and doped TiO<sub>2</sub> ( $M_xTi_{1-x}O_2$ ,  $M = V, Ni, Co$ ) ( $x = 0.00, 0.01, 0.02$  and  $0.03$ ) nanoparticles were synthesized using the hydrothermal method and subjected to a thorough structural analysis. These materials were coated on Nickel foam (NF) substrates and investigated using electrochemical techniques. The graphical representation as shown in **Fig. 8.1**.

Among these materials,  $V_{0.03}Ti_{0.97}O_2@NF$  demonstrated exceptional electrochemical performance. This superior performance was attributed to its well-defined crystalline structure, mesoporous morphology, significant surface area, enhanced electron mobility, and efficient charge transfer characteristics. The study also explored their potential as glucose sensors through DFT simulations. Specifically,  $V_{0.03}Ti_{0.97}O_2@NF$  exhibited heightened chemical reactivity, notably forming strong chemical bonds with glucose oxygen atoms.

In electrochemical glucose sensing applications,  $V_{0.03}Ti_{0.97}O_2@NF$  displayed remarkable sensitivity, quantified at  $1129.31 \mu A mM^{-1}cm^{-2}$ , with a LOD of  $1.8 \mu M$  and rapid response time of 2.1 s in 0.1 M KOH solution. These findings underscore the material's efficacy in accurate glucose analysis, particularly in human blood samples. The rapid synthesis, cost-effectiveness, and potential for diverse medical applications highlight  $V_{0.03}Ti_{0.97}O_2@NF$  as a promising candidate for commercialization in glucose biosensing technologies.

Building upon our initial findings, we extended our investigation to explore the influence of higher vanadium doping levels in  $TiO_2$ . Synthesizing materials with progressively increased vanadium concentrations (0.03, 0.05, 0.07, and 0.09), we identified  $V_{0.07}Ti_{0.93}O_2$  as a particularly promising candidate for glucose biosensing applications. This material exhibited notable characteristics including enhanced sensitivity, with a measured value of  $1482.8 \mu A mM^{-1}cm^{-2}$ , a LOD of 488 mM, and a rapid response time of 2 s. These findings underscore the potential of  $V_{0.07}Ti_{0.93}O_2$  as an effective non-enzymatic glucose biosensor, highlighting its suitability for advanced biomedical applications.

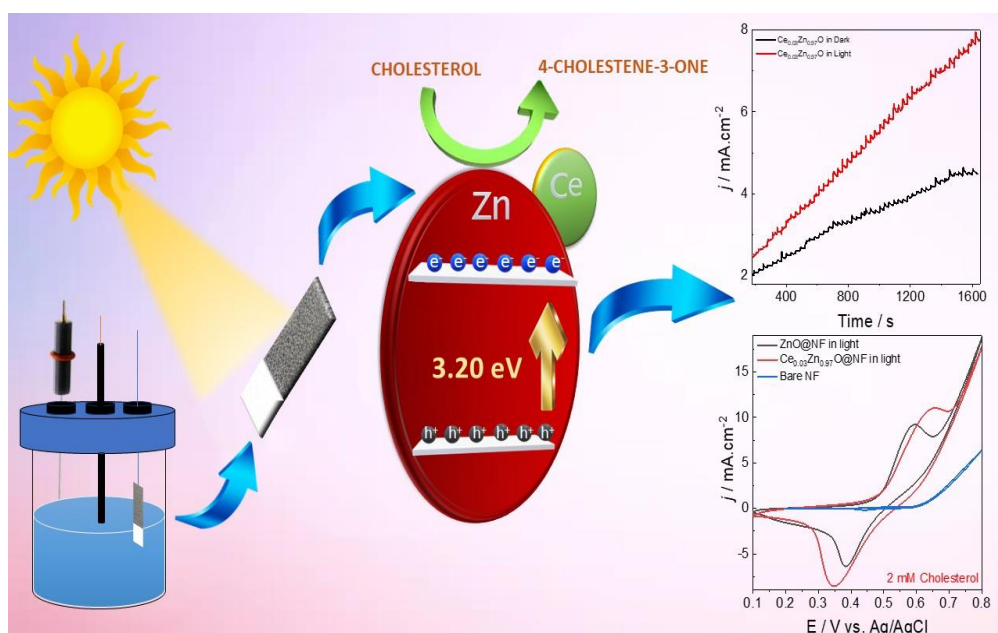


**Figure 8.2.** Graphical representation of the  $CZO3@NF$  sensing cholesterol.

In this comprehensive study, we synthesized cerium-doped zinc oxide ( $\text{Ce}_x\text{Zn}_{1-x}\text{O}$ ,  $x = 0.00, 0.01, 0.02, \text{ and } 0.03$ ) using the wet chemical method to investigate the potential of these materials in PEC biosensors for enzyme-free cholesterol detection. The research focused particularly on  $\text{Ce}_{0.03}\text{Zn}_{0.97}\text{O}$  (CZO3) supported on NF as the active material. The graphical representation as shown in **Fig. 8.2**.

The results revealed significant enhancements in sensitivity for cholesterol detection, with CZO3/NF achieving an activity of  $2.812 \text{ mA}\cdot\text{mM}^{-1}\cdot\text{cm}^{-2}$  under illuminated conditions. This represents a twofold increase in sensitivity compared to the performance in dark mode, which was measured at  $1.37 \text{ mA}\cdot\text{mM}^{-1}\cdot\text{cm}^{-2}$ . The LOD for cholesterol was determined to be  $17 \mu\text{M}$  under light and  $28 \mu\text{M}$  in the dark, while the LOQ was measured at  $54 \mu\text{M}$  under light and  $98 \mu\text{M}$  in the dark, within a  $0.1 \text{ M KOH}$  solution. These measurements indicate a linear detection range extending from  $80 \mu\text{M}$  to  $2 \text{ mM}$ , highlighting the sensor's capability for precise quantification over a broad range of concentrations.

To further understand the impact of cerium doping on the electronic properties of ZnO, ab-initio calculations based on DFT were conducted on the 101 surfaces of both pristine ZnO and CZO3. These calculations demonstrated that doping with cerium significantly affects the band gap of ZnO, thereby enhancing its electronic and catalytic properties. The study found that CZO3 exhibits superior activity compared to pristine ZnO, underscoring its improved performance and greater potential for sensing applications.

Additionally, the CZO3/NF PEC biosensor displayed remarkable cyclic stability, maintaining 97% of its initial performance over a 60-day period, which is a critical attribute for long-term biosensing applications. The sensor's robust performance was further validated through tests with human serum samples, where it consistently exhibited reliable and stable detection capabilities in both dark and illuminated conditions. This comprehensive investigation highlights the superior sensitivity, stability, and practical applicability of CZO3/NF PEC biosensors, making them highly promising candidates for advanced biosensing applications, particularly in medical diagnostics. The findings underscore the significant potential of cerium-doped ZnO in enhancing the performance of biosensors, offering valuable insights for the development of next-generation diagnostic tools.

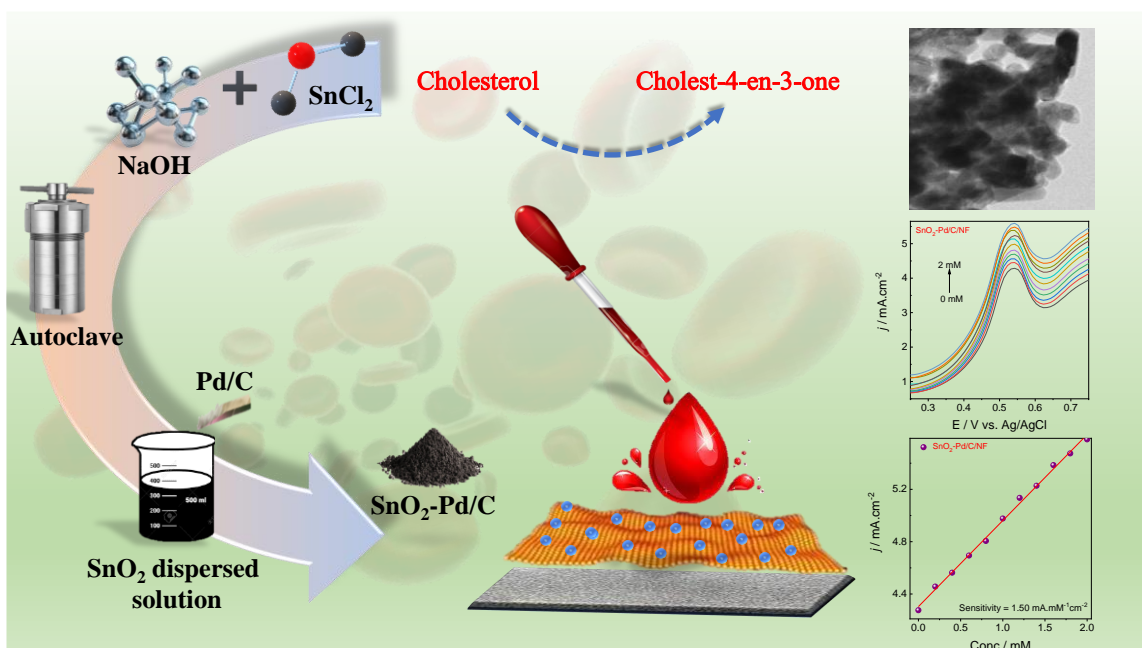


**Figure 8.3.** Graphical representation of the  $\text{SnO}_2\text{-Pd/C-NF}$  sensing cholesterol.

This study details the synthesis of  $\text{SnO}_2\text{-Pd/C}$  via a meticulous two-step process. Initially,  $\text{SnO}_2$  was synthesized using the hydrothermal method, after which it was decorated with Pd/C to enhance its properties. The focus of this research is on the development of a non-enzymatic cholesterol biosensor, employing  $\text{SnO}_2\text{-Pd/C}$  on NF as the active material. The graphical representation as shown in **Fig. 8.3**.

The findings indicate significant improvements in the sensitivity for cholesterol detection, with an observed activity of  $1560 \mu\text{A.mM}^{-1}.\text{cm}^{-2}$ , which represents a threefold increase compared to the activity observed with  $\text{SnO}_2\text{-NF}$ , which was  $546 \mu\text{A.mM}^{-1}.\text{cm}^{-2}$ . Furthermore, the biosensor demonstrated a LOD of  $28 \mu\text{M}$  and a LOQ of  $34 \mu\text{M}$  in a  $0.1 \text{ M KOH}$  solution. The material also exhibited a broad linear detection range, spanning from  $200 \mu\text{M}$  to  $2 \text{ mM}$ . This range ensures the biosensor's applicability in various cholesterol detection scenarios, highlighting its versatility and effectiveness.

The  $\text{SnO}_2\text{-Pd/C-NF}$  biosensor also exhibited excellent cyclic stability, maintaining 97% of its performance over a 30-day period. This high level of stability is crucial for practical applications, as it underscores the biosensor's potential for reliable and long-term use in biosensing applications. Additionally, the biosensor demonstrated robust sensing capabilities when tested with human serum samples, showcasing consistent

performance under standard conditions. These findings underscore the significant advancements in the sensitivity and stability of the SnO<sub>2</sub>-Pd/C-NF biosensor, highlighting its potential for non-enzymatic cholesterol detection in clinical settings. The study's comprehensive approach to synthesis and characterization provides a solid foundation for future research and development in the field of biosensing, particularly for applications requiring high sensitivity, stability, and reliability.

## 8.2 Conclusions

In conclusion, this thesis has demonstrated the significant potential of metal oxide-based nanomaterials for developing highly sensitive, stable, and efficient biosensors for glucose and cholesterol detection. The meticulous synthesis and comprehensive characterization of V-doped TiO<sub>2</sub>, Ce-doped ZnO, and Pd/C-decorated SnO<sub>2</sub> have underscored their exceptional electrochemical properties, making them promising candidates for advanced biosensing applications. The superior electron transport capabilities, robust catalytic properties, and chemical stability of these metal oxides enable precise and rapid detection of target molecules, crucial for accurate diagnostics in healthcare.

Our exploration into vanadium-doped TiO<sub>2</sub> revealed V<sub>0.07</sub>Ti<sub>0.93</sub>O<sub>2</sub> as an optimal material for glucose biosensing, exhibiting remarkable sensitivity and rapid response times, thus validating its potential for practical medical applications. Similarly, the study on cerium-doped ZnO demonstrated that Ce<sub>0.03</sub>Zn<sub>0.97</sub>O enhances photoelectrochemical cholesterol detection, showcasing significant improvements in sensitivity and stability. Furthermore, the development of the SnO<sub>2</sub>-Pd/C-based biosensor highlighted notable advancements in non-enzymatic cholesterol detection, with substantial improvements in sensitivity and cyclic stability, thereby reinforcing its applicability in clinical settings.

The findings of this research contribute valuable insights into the optimization of metal oxide nanomaterials for biosensing technologies. The demonstrated versatility, efficiency, and cost-effectiveness of these materials provide a solid foundation for their integration into mainstream diagnostic technologies. The scalability and adaptability of metal oxide-based biosensors hold immense promise for widespread adoption in healthcare, environmental monitoring, and various industrial processes.

In essence, this thesis heralds a new era in biosensor technology, addressing the limitations of traditional diagnostic methods and offering enhanced sensitivity, specificity, and durability. The continued exploration and optimization of these nanomaterials will undoubtedly drive further innovations, solidifying their role as pivotal components in the future of biomedical diagnostics and beyond.

**Table 8.1.** Comparison of all fabricated biosensors related to the thesis.

Analyte Used		Glucose		Cholesterol	
SI. No	Parameters	V <sub>0.03</sub> Ti <sub>0.97</sub> O <sub>2</sub>	V <sub>0.07</sub> Ti <sub>0.93</sub> O <sub>2</sub>	Ce <sub>0.03</sub> Zn <sub>0.97</sub> O (CZO3)	SnO <sub>2</sub> -Pd/C
1	Sensitivity (μAmM <sup>-1</sup> cm <sup>-2</sup> )	1129.31	1482.8	2812 (Light) 1370 (Dark)	1560
2	LOD (μM)	1.8	488	17 (Light) 28 (Dark)	28
3	LOQ (μM)	6.2	-	54 (Light) 98 (Dark)	34
4	Selectivity	Yes	-	Yes	Yes
5	Linear range	20 μM - 2 mM	0.2-2 mM	80 μM - 2 mM	0.2-2 mM

### 8.3 Future Work

Future work will focus on enhancing the performance and versatility of metal oxide-based biosensors through several key strategies. One area of emphasis will be the development of new metal oxide composites and hybrid materials to improve sensitivity, selectivity, and response times. Researchers will also investigate advanced techniques for functionalizing biosensors to strengthen their interactions with target molecules and expand the range of detectable substances. Integrating these biosensors with microfluidic systems and wearable devices will be explored to enable real-time,

point-of-care diagnostics. Additionally, efforts will be made to scale up production, ensuring that these biosensors remain cost-effective and accessible for widespread use in healthcare and environmental monitoring.

Another important aspect of future work will involve the use of screen-printed electrodes, which offer a low-cost, reproducible, and scalable platform for developing disposable biosensors. This approach will facilitate the creation of portable and user-friendly diagnostic tools, enhancing the overall utility and impact of metal oxide-based biosensors. Extensive in vivo testing and clinical trials will be conducted to validate the practical applications of these biosensors in real-world settings. By addressing these areas, future research will pave the way for the adoption of advanced biosensors in mainstream diagnostic and monitoring practices, significantly improving healthcare outcomes and environmental monitoring capabilities.

\*\*\*\*\*

---

---

## REFERENCES

---

---

Abdel Hameed, R. M. (2017). "Facile preparation of Pd-metal oxide/C electrocatalysts and their application in the electrocatalytic oxidation of ethanol." *Applied Surface Science*, 411, 91–104.

Abid, N., Khan, A. M., Shujait, S., Chaudhary, K., Ikram, M., Imran, M., Haider, J., Khan, M., Khan, Q., and Maqbool, M. (2022). "Synthesis of nanomaterials using various top-down and bottom-up approaches, influencing factors, advantages, and disadvantages: A review." *Advances in Colloid and Interface Science*, 300, 102597.

Acharyya, S., Bhowmick, P. K., and Guha, P. K. (2023). "Selective identification and quantification of VOCs using metal nanoparticles decorated SnO<sub>2</sub> hollow-spheres based sensor array and machine learning." *Journal of Alloys and Compounds*, 968, 171891.

Agnihotri, A. S., Varghese, A., and M, N. (2021). "Transition metal oxides in electrochemical and bio sensing: A state-of-art review." *Applied Surface Science Advances*, 4, 100072.

Ahmad, M., Nisar, A., and Sun, H. (2022). "Emerging Trends in Non-Enzymatic Cholesterol Biosensors: Challenges and Advancements." *Biosensors*, 12(11), 955.

Ahmad, R., Tripathy, N., Ahn, M.-S., Bhat, K. S., Mahmoudi, T., Wang, Y., Yoo, J.-Y., Kwon, D.-W., Yang, H.-Y., and Hahn, Y.-B. (2017). "Highly Efficient Non-Enzymatic Glucose Sensor Based on CuO Modified Vertically-Grown ZnO Nanorods on Electrode." *Sci Rep*, 7(1), 5715.

Alagappan, M., Immanuel, S., Sivasubramanian, R., and Kandaswamy, A. (2020). "Development of cholesterol biosensor using Au nanoparticles decorated f-MWCNT covered with polypyrrole network." *Arabian Journal of Chemistry*, 13(1), 2001–2010.

Alam, M. M., Uddin, M. T., Asiri, A. M., Rahman, M. M., and Islam, M. A. (2021). "Electrochemical detection of cholesterol in a buffer solution with a glassy carbon electrode doctored by ZnO/SnO<sub>2</sub>/RuO<sub>2</sub> nanomaterials."

Alarcon-Angeles, G., Álvarez-Romero, G. A., and Merkoçi, A. (2018). "Electrochemical Biosensors: Enzyme Kinetics and Role of Nanomaterials." *Encyclopedia of Interfacial Chemistry*, Elsevier, 140–155.

Alhadrami, H. A. (2018). "Biosensors: Classifications, medical applications, and future prospective." *Biotech and App Biochem*, 65(3), 497–508.

Amiripour, F., Ghasemi, S., and Azizi, S. N. (2021). "A novel non-enzymatic glucose sensor based on gold-nickel bimetallic nanoparticles doped aluminosilicate framework prepared from agro-waste material." *Applied Surface Science*, 537, 147827.

Amri, F., Septiani, N. L. W., Rezki, M., Iqbal, M., Yamauchi, Y., Golberg, D., Kaneti, Y. V., and Yulianto, B. (2021). "Mesoporous TiO<sub>2</sub> -based architectures as promising

sensing materials towards next-generation biosensing applications.” *J. Mater. Chem. B*, 9(5), 1189–1207.

Anand, T. P., Chellaram, C., Murugaboopathi, G., Parthasarathy, V., and Vinurajkumar, S. (2013). “Applications of Biosensors in Food Industry.” *Biosci., Biotechnol. Res. Asia*, 10(2), 711–714.

Anantharaj, S., Ede, S. R., Karthick, K., Sam Sankar, S., Sangeetha, K., Karthik, P. E., and Kundu, S. (2018). “Precision and correctness in the evaluation of electrocatalytic water splitting: revisiting activity parameters with a critical assessment.” *Energy Environ. Sci.*, 11(4), 744–771.

Anh, T. T. N., Lan, H., Tam, L. T., Pham, V.-H., and Tam, P. D. (2018). “Highly Sensitive Nonenzymatic Cholesterol Sensor Based on Zinc Oxide Nanorods.” *Journal of Elec Materi*, 47(11), 6701–6708.

Asaithambi, S., Sakthivel, P., Karuppaiah, M., Hayakawa, Y., Loganathan, A., and Ravi, G. (2020). “Improved photocatalytic performance of nanostructured SnO<sub>2</sub> via addition of alkaline earth metals (Ba<sup>2+</sup>, Ca<sup>2+</sup> and Mg<sup>2+</sup>) under visible light irradiation.” *Appl. Phys. A*, 126(4), 265.

Bai, J., and Zhou, B. (2014). “Titanium Dioxide Nanomaterials for Sensor Applications.” *Chem. Rev.*, 114(19), 10131–10176.

Bao, J., Chen, W., Liu, T., Zhu, Y., Jin, P., Wang, L., Liu, J., Wei, Y., and Li, Y. (2007). “Bifunctional Au-Fe<sub>3</sub>O<sub>4</sub> Nanoparticles for Protein Separation.” *ACS Nano*, 1(4), 293–298.

Bao, J., Qi, Y., Huo, D., Hou, J., Geng, X., Samalo, M., Liu, Z., Luo, H., Yang, M., and Hou, C. (2019). “A Sensitive and Selective Non-Enzymatic Glucose Sensor based on AuNPs/CuO NWs-MoS<sub>2</sub> Modified Electrode.” *J. Electrochem. Soc.*, 166(13), B1179–B1185.

Bechambi, O., Touati, A., Sayadi, S., and Najjar, W. (2015). “Effect of cerium doping on the textural, structural and optical properties of zinc oxide: Role of cerium and hydrogen peroxide to enhance the photocatalytic degradation of endocrine disrupting compounds.” *Materials Science in Semiconductor Processing*, 39, 807–816.

Beitollahi, H., Tajik, S., Garkani Nejad, F., and Safaei, M. (2020). “Recent advances in ZnO nanostructure-based electrochemical sensors and biosensors.” *J. Mater. Chem. B*, 8(27), 5826–5844.

Belluzo, M., Ribone, M., and Lagier, C. (2008). “Assembling Amperometric Biosensors for Clinical Diagnostics.” *Sensors*, 8(3), 1366–1399.

Bhalla, N., Jolly, P., Formisano, N., and Estrela, P. (2016). “Introduction to biosensors.” *Essays in Biochemistry*, (P. Estrela, ed.), 60(1), 1–8.

Blöchl, P. E. (1994). “Projector augmented-wave method.” *Phys. Rev. B*, 50(24), 17953–17979.

Bontempelli, G., Dossi, N., and Toniolo, R. (2016). “Linear Sweep and Cyclic<sup>\*</sup>.” *Reference Module in Chemistry, Molecular Sciences and Chemical Engineering*, Elsevier, B9780124095472122000.

Cervantes-López, J. L., Rangel, R., Espino, J., Martínez, E., García-Gutiérrez, R., Bartolo-Pérez, P., Alvarado-Gil, J. J., and Contreras, O. E. (2017). “Photoluminescence on cerium-doped ZnO nanorods produced under sequential atomic layer deposition–hydrothermal processes.” *Appl. Phys. A*, 123(1), 86.

Chakraborty, M., and Hashmi, M. S. J. (2017). “An Overview of Biosensors and Devices.” *Encyclopedia of Smart Materials*, Elsevier, 1–23.

Chao, G., Zhang, L., Tian, J., Fan, W., and Liu, T. (2021). “Pd–SnO<sub>2</sub> heterojunction catalysts anchored on graphene sheets for enhanced oxygen reduction.” *Composites Communications*, 25, 100703.

Chaudhary, S., Umar, A., Bhasin, K., and Baskoutas, S. (2018). “Chemical Sensing Applications of ZnO Nanomaterials.” *Materials*, 11(2), 287.

Chiu, W.-T., Chang, T.-F. M., Sone, M., Hosoda, H., Tixier-Mita, A., and Toshiyoshi, H. (2021). “Developments of the Electroactive Materials for Non-Enzymatic Glucose Sensing and Their Mechanisms.” *Electrochem*, 2(2), 347–389.

Chiu, W.-T., Chang, T.-F. M., Sone, M., Tixier-Mita, A., and Toshiyoshi, H. (2020). “Electrocatalytic activity enhancement of Au NPs-TiO<sub>2</sub> electrode via a facile redistribution process towards the non-enzymatic glucose sensors.” *Sensors and Actuators B: Chemical*, 319, 128279.

Das, D., Das, A., Reghunath, M., and Nanda, K. K. (2017). “Phosphine-free avenue to Co<sub>2</sub>P nanoparticle encapsulated N,P co-doped CNTs: a novel non-enzymatic glucose sensor and an efficient electrocatalyst for oxygen evolution reaction.” *Green Chem.*, 19(5), 1327–1335.

Davis, G. (1985). “Electrochemical techniques for the development of amperometric biosensors.” *Biosensors*, 1(2), 161–178.

Deivasegamani, R., Karunanidhi, G., Santhosh, C., Gopal, T., Saravana Achari, D., Neogi, A., Nivetha, R., Pradeep, N., Venkatraman, U., Bhatnagar, A., Jeong, S. K., and Grace, A. N. (2017). “Chemoresistive sensor for hydrogen using thin films of tin dioxide doped with cerium and palladium.” *Microchim Acta*, 184(12), 4765–4773.

Dekanski, A., Stevanović, J., Stevanović, R., Nikolić, B. Ž., and Jovanović, V. M. (2001). “Glassy carbon electrodes.” *Carbon*, 39(8), 1195–1205.

- Devadoss, A., Sudhagar, P., Terashima, C., Nakata, K., and Fujishima, A. (2015). "Photoelectrochemical biosensors: New insights into promising photoelectrodes and signal amplification strategies." *Journal of Photochemistry and Photobiology C: Photochemistry Reviews*, 24, 43–63.
- Ding, K., Di, M., Yan, M., Li, M., Li, W., and Wang, H. (2023). "A Palladium based Composite Electrocatalyst of Pd/SnO<sub>2</sub>-CSS Showing an Excellent Electrocatalytic Activity for Ethanol Oxidation Reaction (EOR)." *JNMES*, 26(3), 215–226.
- Ding, Y., Wang, Y., Su, L., Zhang, H., and Lei, Y. (2010). "Preparation and characterization of NiO–Ag nanofibers, NiO nanofibers, and porous Ag: towards the development of a highly sensitive and selective non-enzymatic glucose sensor." *J. Mater. Chem.*, 20(44), 9918.
- Djaja, N. F., and Saleh, R. (2013). "Characteristics and Photocatalytic Activities of Ce-Doped ZnO Nanoparticles." *MSA*, 04(02), 145–152.
- Dong, Q., Ryu, H., and Lei, Y. (2021). "Metal oxide based non-enzymatic electrochemical sensors for glucose detection." *Electrochimica Acta*, 370, 137744.
- Duan, X., Liu, K., Xu, Y., Yuan, M., Gao, T., and Wang, J. (2019). "Nonenzymatic electrochemical glucose biosensor constructed by NiCo<sub>2</sub>O<sub>4</sub>@Ppy nanowires on nickel foam substrate." *Sensors and Actuators B: Chemical*, 292, 121–128.
- Elgrishi, N., Rountree, K. J., McCarthy, B. D., Rountree, E. S., Eisenhart, T. T., and Dempsey, J. L. (2018). "A Practical Beginner's Guide to Cyclic Voltammetry." *J. Chem. Educ.*, 95(2), 197–206.
- Estadulho, G. L. D., Alencar, L. M., Guima, K.-E., Trindade, M. A. G., and Martins, C. A. (2021). "3D-Printed Templates Converted into Graphite, Ruthenium, or Copper Are Used as Monolithic Sensors." *ACS Appl. Electron. Mater.*, 3(8), 3482–3488.
- Evans, D. H., and Kelly, M. J. (1982). "Theory for double potential step chronoamperometry, chronocoulometry, and chronoabsorptometry with a quasi-reversible electrode reaction." *Anal. Chem.*, 54(11), 1727–1729.
- Fahmy Taha, M., Ashraf, H., and Caesarendra, W. (2020). "A Brief Description of Cyclic Voltammetry Transducer-Based Non-Enzymatic Glucose Biosensor Using Synthesized Graphene Electrodes." *ASI*, 3(3), 32.
- Faisal, M., Ismail, A. A., Ibrahim, A. A., Bouzid, H., and Al-Sayari, S. A. (2013). "Highly efficient photocatalyst based on Ce doped ZnO nanorods: Controllable synthesis and enhanced photocatalytic activity." *Chemical Engineering Journal*, 229, 225–233.
- Feng, D., Huang, P., Miao, Y., Liang, A., Wang, X., Tang, B., Hou, H., Ren, M., Gao, S., Geng, L., and Luo, A. (2022). "Novel photoelectrochemical sensor for cholesterol

based on  $\text{CH}_3\text{NH}_3\text{PbBr}_3$  perovskite / $\text{TiO}_2$  inverse opal heterojunction coated with molecularly imprinted polymers.” *Sensors and Actuators B: Chemical*, 368, 132121.

Ferrando, R., Jellinek, J., and Johnston, R. L. (2008). “Nanoalloys: From Theory to Applications of Alloy Clusters and Nanoparticles.” *Chem. Rev.*, 108(3), 845–910.

Fifere, N., Airinei, A., Timpu, D., Rotaru, A., Sacarescu, L., and Ursu, L. (2018). “New insights into structural and magnetic properties of Ce doped ZnO nanoparticles.” *Journal of Alloys and Compounds*, 757, 60–69.

Fox, C. S. (2004). “Trends in Cardiovascular Complications of Diabetes.” *JAMA*, 292(20), 2495.

Ge, L., Liu, Q., Hao, N., and Kun, W. (2019). “Recent developments of photoelectrochemical biosensors for food analysis.” *J. Mater. Chem. B*, 7(46), 7283–7300.

Ghorui, U. K., Adhikary, B., and Mondal, A. (2023). “Hydroxyl radical assisted enzyme-free electrochemical detection and oxidation of cholesterol by a galvanically deposited layer-by-layer ZnO/ $\text{WO}_3$  thin film nanocomposite.” *New J. Chem.*, 47(20), 9779–9796.

Gouvea, C. (2011). “Biosensors for health applications.” *Biosensors for Health, Environment and Biosecurity*, P. A. Serra, ed., InTech.

Grattarola, M., and Massobrio, G. (1998). *Bioelectronics handbook: MOSFETs, biosensors, and neurons*. New York: McGraw-Hill.

Grätzel, M. (2001). “Photoelectrochemical cells.” *Nature*, 414(6861), 338–344.

Griffin, G. D., Stratis-Cullum, D. N., and McKnight, T. E. (2014). “Biosensors<sup>☆</sup>.” *Reference Module in Biomedical Sciences*, Elsevier, B9780128012383024880.

Grochowska, K., Ryl, J., Karczewski, J., Śliwiński, G., Cenian, A., and Siuzdak, K. (2019). “Non-enzymatic flexible glucose sensing platform based on nanostructured  $\text{TiO}_2$  – Au composite.” *Journal of Electroanalytical Chemistry*, 837, 230–239.

Guo, C., Zhang, X., Huo, H., Xu, C., and Han, X. (2013). “ $\text{Co}_3\text{O}_4$  microspheres with free-standing nanofibers for high performance non-enzymatic glucose sensor.” *Analyst*, 138(22), 6727.

Hagfeldt, A., Boschloo, G., Sun, L., Kloo, L., and Pettersson, H. (2010). “Dye-Sensitized Solar Cells.” *Chem. Rev.*, 110(11), 6595–6663.

Haleem, A., Javaid, M., Singh, R. P., Suman, R., and Rab, S. (2021). “Biosensors applications in medical field: A brief review.” *Sensors International*, 2, 100100.

Ham, M.-H., Choi, J. H., Boghossian, A. A., Jeng, E. S., Graff, R. A., Heller, D. A., Chang, A. C., Mattis, A., Bayburt, T. H., Grinkova, Y. V., Zeiger, A. S., Van Vliet, K. J., Hobbie, E. K., Sligar, S. G., Wraight, C. A., and Strano, M. S. (2010). "Photoelectrochemical complexes for solar energy conversion that chemically and autonomously regenerate." *Nature Chem*, 2(11), 929–936.

Han, H., Sudhagar, P., Song, T., Jeon, Y., Mora-Seró, I., Fabregat-Santiago, F., Bisquert, J., Kang, Y. S., and Paik, U. (2013). "Three dimensional-TiO<sub>2</sub> nanotube array photoanode architectures assembled on a thin hollow nanofibrous backbone and their performance in quantum dot-sensitized solar cells." *Chem. Commun.*, 49(27), 2810.

Henkel, K., Haeberle, J., Müller, K., Janowitz, C., and Schmeißer, D. (2019). "Preparation, properties and electronic structure of SnO<sub>2</sub>." *Single Crystals of Electronic Materials*, Elsevier, 547–572.

Ipadeola, A. K., Barik, R., Ray, S. C., and Ozoemena, K. I. (2019). "Bimetallic Pd/SnO<sub>2</sub> Nanoparticles on Metal Organic Framework (MOF)-Derived Carbon as Electrocatalysts for Ethanol Oxidation." *Electrocatalysis*, 10(4), 366–380.

Jalalvand, A. R. (2022). "Fabrication of a novel molecularly imprinted biosensor assisted by multi-way calibration for simultaneous determination of cholesterol and cholestanol in serum samples." *Chemometrics and Intelligent Laboratory Systems*, 226, 104587.

Jang, K., Park, K. R., Kim, K. M., Hyun, S., Ahn, C., Kim, J. C., Lim, S., Han, H., and Mhin, S. (2021). "Electrochemical performance of the spinel NiCo<sub>2</sub>O<sub>4</sub> based nanostructure synthesized by chemical bath method for glucose detection." *Applied Surface Science*, 545, 148927.

Ji, H., Zeng, W., and Li, Y. (2019). "Gas sensing mechanisms of metal oxide semiconductors: a focus review." *Nanoscale*, 11(47), 22664–22684.

Ji, R., Wang, L., Wang, G., and Zhang, X. (2014). "Synthesize Thickness Copper (I) Sulfide nanoplates on Copper Rod and It's Application as Nonenzymatic Cholesterol Sensor." *Electrochimica Acta*, 130, 239–244.

Jiang, Sun, Zhao, Huo, and Cui. (2019). "A Flexible Portable Glucose Sensor Based on Hierarchical Arrays of Au@Cu(OH)<sub>2</sub> Nanograss." *Sensors*, 19(22), 5055.

Jo, H. J., Shit, A., Jhon, H. S., and Park, S. Y. (2020). "Highly sensitive non-enzymatic wireless glucose sensor based on Ni–Co oxide nanoneedle-anchored polymer dots." *Journal of Industrial and Engineering Chemistry*, 89, 485–493.

Jolly, P., Formisano, N., and Estrela, P. (2015a). "DNA aptamer-based detection of prostate cancer." *Chemical Papers*, 69(1).

Jolly, P., Formisano, N., Tkáč, J., Kasák, P., Frost, C. G., and Estrela, P. (2015b). “Label-free impedimetric aptasensor with antifouling surface chemistry: A prostate specific antigen case study.” *Sensors and Actuators B: Chemical*, 209, 306–312.

Jung, Y.-I., Noh, B.-Y., Lee, Y.-S., Baek, S.-H., Kim, J. H., and Park, I.-K. (2012). “Visible emission from Ce-doped ZnO nanorods grown by hydrothermal method without a post thermal annealing process.” *Nanoscale Res Lett*, 7(1), 43.

Junita, J., Jayalakshmi, D., and Rodney, J. D. (2023). “Combustion-derived BaNiO<sub>3</sub> nanoparticles as a potential bifunctional electrocatalyst for overall water splitting.” *International Journal of Hydrogen Energy*, 48(38), 14287–14298.

Kamat, A., Huth, A., Klein, O., and Scholl, S. (2010). “Chronoamperometric Investigations of the Electrode–Electrolyte Interface of a Commercial High Temperature PEM Fuel Cell.” *Fuel Cells*, 10(6), 983–992.

Kang, Z., Yan, X., Wang, Y., Zhao, Y., Bai, Z., Liu, Y., Zhao, K., Cao, S., and Zhang, Y. (2016). “Self-powered photoelectrochemical biosensing platform based on Au NPs@ZnO nanorods array.” *Nano Res.*, 9(2), 344–352.

Karimi-Maleh, H., Cellat, K., Arıkan, K., Savk, A., Karimi, F., and Şen, F. (2020). “Palladium–Nickel nanoparticles decorated on Functionalized-MWCNT for high precision non-enzymatic glucose sensing.” *Materials Chemistry and Physics*, 250, 123042.

Karunakaran, C., Rajkumar, R., and Bhargava, K. (2015). “Introduction to Biosensors.” *Biosensors and Bioelectronics*, Elsevier, 1–68.

Kashale, A. A., Rasal, A. S., Kamble, G. P., Ingole, V. H., Dwivedi, P. K., Rajoba, S. J., Jadhav, L. D., Ling, Y.-C., Chang, J.-Y., and Ghule, A. V. (2019). “Biosynthesized Co-doped TiO<sub>2</sub> nanoparticles based anode for lithium-ion battery application and investigating the influence of dopant concentrations on its performance.” *Composites Part B: Engineering*, 167, 44–50.

Khaliq, N., Rasheed, M. A., Cha, G., Khan, M., Karim, S., Schmuki, P., and Ali, G. (2020). “Development of non-enzymatic cholesterol bio-sensor based on TiO<sub>2</sub> nanotubes decorated with Cu<sub>2</sub>O nanoparticles.” *Sensors and Actuators B: Chemical*, 302, 127200.

Khan, S., Rasheed, M. A., Shah, A., Mahmood, A., Waheed, A., Karim, S., Khan, M., and Ali, G. (2021). “Preparation of oxidized Zn–In nanostructures for electrochemical non-enzymatic cholesterol sensing.” *Materials Science in Semiconductor Processing*, 135, 106101.

Khosroshahi, Z., Karimzadeh, F., Kharaziha, M., and Allafchian, A. (2020). “A non-enzymatic sensor based on three-dimensional graphene foam decorated with Cu-xCu<sub>2</sub>O

nanoparticles for electrochemical detection of glucose and its application in human serum.” *Materials Science and Engineering: C*, 108, 110216.

Kim, H., Lee, Y., Song, D., Kwon, Y., Kim, E.-J., and Cho, E. (2020). “Cu<sub>3</sub>P/PAN derived N-doped carbon catalyst with non-toxic synthesis for alkaline hydrogen evolution reaction.” *Sustainable Energy Fuels*, 4(10), 5247–5253.

Kresse, G., and Furthmüller, J. (1996). “Efficiency of ab-initio total energy calculations for metals and semiconductors using a plane-wave basis set.” *Computational Materials Science*, 6(1), 15–50.

Kunnamareddy, M., Rajendran, R., Sivagnanam, M., Rajendran, R., and Diravidamani, B. (2021). “Nickel and sulfur codoped TiO<sub>2</sub> nanoparticles for efficient visible light photocatalytic activity.” *J Inorg Organomet Polym*, 31(6), 2615–2626.

Lee, Y.-J., and Park, J.-Y. (2010). “Nonenzymatic free-cholesterol detection via a modified highly sensitive macroporous gold electrode with platinum nanoparticles.” *Biosensors and Bioelectronics*, 26(4), 1353–1358.

Lefrou, C., Nogueira, R. P., Huet, F., and Takenouti, H. (2010). “Electrochemistry.” *Shreir’s Corrosion*, Elsevier, 13–51.

Levitan, I., Fang, Y., Rosenhouse-Dantsker, A., and Romanenko, V. (2010). “Cholesterol and Ion Channels.” *Cholesterol Binding and Cholesterol Transport Proteins*; Subcellular Biochemistry, J. R. Harris, ed., Dordrecht: Springer Netherlands, 509–549.

Li, H., Guo, C.-Y., and Xu, C.-L. (2015). “A highly sensitive non-enzymatic glucose sensor based on bimetallic Cu–Ag superstructures.” *Biosensors and Bioelectronics*, 63, 339–346.

Liang, Y., Guo, N., Li, L., Li, R., Ji, G., and Gan, S. (2015). “Preparation of porous 3D Ce-doped ZnO microflowers with enhanced photocatalytic performance.” *RSC Adv.*, 5(74), 59887–59894.

Lim, B., Jiang, M., Camargo, P. H. C., Cho, E. C., Tao, J., Lu, X., Zhu, Y., and Xia, Y. (2009). “Pd-Pt Bimetallic Nanodendrites with High Activity for Oxygen Reduction.” *Science*, 324(5932), 1302–1305.

Liu, B., and Liu, J. (2019). “Sensors and biosensors based on metal oxide nanomaterials.” *TrAC Trends in Analytical Chemistry*, 121, 115690.

Liu, C., Suematsu, K., Uchiyama, A., Watanabe, K., Guo, Y., Wang, D., and Shimano, K. (2021). “Impact of Pd nanoparticle loading method on SnO<sub>2</sub> surface for natural gas detection in humid atmosphere.” *J Mater Sci*, 56(25), 13975–13988.

- Liu, C., Xu, J., Cui, S., and Yu, H. (2018). "Photocatalytic activity of Ce-doped ZnO nanoparticles." *Mater. Tehnol.*, 52(3), 349–353.
- Liu, S., Liu, S.-L., Long, Y.-Z., Liu, L.-Z., Zhang, H.-D., Zhang, J.-C., Han, W.-P., and Liu, Y.-C. (2014). "Fabrication of p-type ZnO nanofibers by electrospinning for field-effect and rectifying devices." *Applied Physics Letters*, 104(4), 042105.
- Liu, S., Yu, B., and Zhang, T. (2013). "A novel non-enzymatic glucose sensor based on NiO hollow spheres." *Electrochimica Acta*, 102, 104–107.
- Lu, H., Liu, Z., Yan, X., Li, D., Parent, L., and Tian, H. (2016). "Electron work function—a promising guiding parameter for material design." *Sci Rep*, 6(1), 24366.
- Luo, J., Jiang, S., Zhang, H., Jiang, J., and Liu, X. (2012). "A novel non-enzymatic glucose sensor based on Cu nanoparticle modified graphene sheets electrode." *Analytica Chimica Acta*, 709, 47–53.
- Malhotra, B. D., and Ali, Md. A. (2018). "Nanomaterials in Biosensors." *Nanomaterials for Biosensors*, Elsevier, 1–74.
- Mehraj, S., Ansari, M. S., and Alimuddin. (2015). "Annealed SnO<sub>2</sub> thin films: Structural, electrical and their magnetic properties." *Thin Solid Films*, 589, 57–65.
- Mohamad Nor, N., Ridhuan, N. S., and Abdul Razak, K. (2022). "Progress of Enzymatic and Non-Enzymatic Electrochemical Glucose Biosensor Based on Nanomaterial-Modified Electrode." *Biosensors*, 12(12), 1136.
- Mohankumar, P., Ajayan, J., Mohanraj, T., and Yasodharan, R. (2021). "Recent developments in biosensors for healthcare and biomedical applications: A review." *Measurement*, 167, 108293.
- Monošík, R., Stred'anský, M., and Šturdík, E. (2012). "Biosensors - classification, characterization and new trends." *Acta Chimica Slovaca*, 5(1), 109–120.
- Nagarajan, A., Sethuraman, V., Sridhar, T. M., and Sasikumar, R. (2023). "Development of Au@NiO decorated polypyrrole composite for non-Enzymatic electrochemical sensing of cholesterol." *Journal of Industrial and Engineering Chemistry*, 120, 460–466.
- Nandini, S., Nalini, S., Reddy, M. B. M., Suresh, G. S., Melo, J. S., Niranjana, P., Sanetuntikul, J., and Shanmugam, S. (2016). "Synthesis of one-dimensional gold nanostructures and the electrochemical application of the nanohybrid containing functionalized graphene oxide for cholesterol biosensing." *Bioelectrochemistry*, 110, 79–90.
- Narwal, V., Deswal, R., Batra, B., Kalra, V., Hooda, R., Sharma, M., and Rana, J. S. (2019). "Cholesterol biosensors: A review." *Steroids*, 143, 6–17.

- Nasrollahzadeh, M., Sajadi, S. M., Sajjadi, M., and Issaabadi, Z. (2019). "An Introduction to Nanotechnology." *Interface Science and Technology*, Elsevier, 1–27.
- Pathak, T. K., Coetsee-Hugo, E., Swart, H. C., Swart, C. W., and Kroon, R. E. (2020). "Preparation and characterization of Ce doped ZnO nanomaterial for photocatalytic and biological applications." *Materials Science and Engineering: B*, 261, 114780.
- Peter, L. M. (1990). "Dynamic aspects of semiconductor photoelectrochemistry." *Chem. Rev.*, 90(5), 753–769.
- Phetsang, S., Jakmunee, J., Mungkornasawakul, P., Laocharoensuk, R., and Ounnunkad, K. (2019). "Sensitive amperometric biosensors for detection of glucose and cholesterol using a platinum/reduced graphene oxide/poly(3-aminobenzoic acid) film-modified screen-printed carbon electrode." *Bioelectrochemistry*, 127, 125–135.
- Prasad, J. R., and Bhat, B. R. (2016). "Nickel Oxide—Multi Walled Carbon Nanotube Composite as Non-Enzymatic Electrochemical Glucose Sensor." *adv sci lett*, 22(1), 219–222.
- Prasad, R., and Bhat, B. R. (2015a). "Self-assembly synthesis of Co<sub>3</sub>O<sub>4</sub> /multiwalled carbon nanotube composites: an efficient enzyme-free glucose sensor." *New J. Chem.*, 39(12), 9735–9742.
- Prasad, R., and Bhat, B. R. (2015b). "Multi-wall carbon nanotube–NiO nanoparticle composite as enzyme-free electrochemical glucose sensor." *Sensors and Actuators B: Chemical*, 220, 81–90.
- Prasad, R., and Bhat, B. R. (2015c). "Multi-wall carbon nanotube–NiO nanoparticle composite as enzyme-free electrochemical glucose sensor." *Sensors and Actuators B: Chemical*, 220, 81–90.
- Prasad, R., Ganesh, V., and Bhat, B. R. (2016). "Nickel-oxide multiwall carbon-nanotube/reduced graphene oxide a ternary composite for enzyme-free glucose sensing." *RSC Adv.*, 6(67), 62491–62500.
- Prasad, R., Gorjizadeh, N., Rajarao, R., Sahajwalla, V., and Bhat, B. R. (2015a). "Plant root nodule like nickel-oxide–multi-walled carbon nanotube composites for non-enzymatic glucose sensors." *RSC Adv.*, 5(56), 44792–44799.
- Prasad, R., Gorjizadeh, N., Rajarao, R., Sahajwalla, V., and Bhat, B. R. (2015b). "Plant root nodule like nickel-oxide–multi-walled carbon nanotube composites for non-enzymatic glucose sensors." *RSC Adv.*, 5(56), 44792–44799.
- Prasad, R., Gorjizadeh, N., Rajarao, R., Sahajwalla, V., and Bhat, B. R. (2015c). "Plant root nodule like nickel-oxide–multi-walled carbon nanotube composites for non-enzymatic glucose sensors." *RSC Adv.*, 5(56), 44792–44799.

- Qi, C., Zhang, C., and Yang, Z. (2022). "Engineering Co<sub>3</sub>O<sub>4</sub> with Co defects for highly sensitive nonenzymatic detection of glucose." *Colloids and Surfaces A: Physicochemical and Engineering Aspects*, 654, 130096.
- Rahman, Md. M., Ahammad, A. J. S., Jin, J.-H., Ahn, S. J., and Lee, J.-J. (2010). "A Comprehensive Review of Glucose Biosensors Based on Nanostructured Metal-Oxides." *Sensors*, 10(5), 4855–4886.
- Rai, D. P., Laref, A., Shankar, A., Sandeep, Sakhya, A. P., Khenata, R., and Thapa, R. K. (2018). "Spin-induced transition metal (TM) doped SnO<sub>2</sub> a dilute magnetic semiconductor (DMS): A first principles study." *Journal of Physics and Chemistry of Solids*, 120, 104–108.
- Rajendran, S., Manoj, D., Raju, K., Dionysiou, Dionysios. D., Naushad, Mu., Gracia, F., Cornejo, L., Gracia-Pinilla, M. A., and Ahamad, T. (2018). "Influence of mesoporous defect induced mixed-valent NiO (Ni<sup>2+</sup>/Ni<sup>3+</sup>)-TiO<sub>2</sub> nanocomposite for non-enzymatic glucose biosensors." *Sensors and Actuators B: Chemical*, 264, 27–37.
- Rao, L., and Bhat, B. R. (2024). "Enhancing glucose detection: Vanadium-doped TiO<sub>2</sub> (V<sub>0.07</sub>Ti<sub>0.93</sub>O<sub>2</sub>) as non-enzymatic biosensor." *J Mater Sci: Mater Electron*, 35(16), 1102.
- Rao, L., Rodney, J. D., Shivakumar, Dalimba, U. K., Udayashankar, N. K., Kim, B. C., and Bhat, B. R. (2024). "Elucidating mechanisms and DFT analysis of monometallic Vanadium incorporated nanoporous TiO<sub>2</sub> as advanced material for enzyme-free electrochemical blood glucose biosensors with exceptional performance tailored for point-of-care applications." *Microchemical Journal*, 204, 111172.
- Ratnam, K. V., Manjunatha, H., Janardan, S., Babu Naidu, K. C., and Ramesh, S. (2020). "Nonenzymatic electrochemical sensor based on metal oxide, MO (M= Cu, Ni, Zn, and Fe) nanomaterials for neurotransmitters: An abridged review." *Sensors International*, 1, 100047.
- Ratsoma, M. S., Poho, B. L. O., Makgopa, K., Raju, K., Modibane, K. D., Jafta, C. J., and Oyedotun, K. O. (2023). "Application of Nickel Foam in Electrochemical Systems: A Review." *J. Electron. Mater.*, 52(4), 2264–2291.
- Reinert, A. A., Payne, C., Wang, L., Ciston, J., Zhu, Y., and Khalifah, P. G. (2013). "Synthesis and Characterization of Visible Light Absorbing (GaN)<sub>1-x</sub>(ZnO)<sub>x</sub> Semiconductor Nanorods." *Inorg. Chem.*, 52(15), 8389–8398.
- Rengaraj, A., Haldorai, Y., Kwak, C. H., Ahn, S., Jeon, K.-J., Park, S. H., Han, Y.-K., and Huh, Y. S. (2015). "Electrodeposition of flower-like nickel oxide on CVD-grown graphene to develop an electrochemical non-enzymatic biosensor." *J. Mater. Chem. B*, 3(30), 6301–6309.

- Revathi, C., and Rajendra Kumar, R. T. (2019). “Enzymatic and Nonenzymatic Electrochemical Biosensors.” *Fundamentals and Sensing Applications of 2D Materials*, Elsevier, 259–300.
- Rezaei, B., and Irannejad, N. (2019). “Electrochemical detection techniques in biosensor applications.” *Electrochemical Biosensors*, Elsevier, 11–43.
- Rison, S., Akshaya, K. B., Bhat, V. S., Shanker, G., Maiyalagan, T., Joice, E. K., Hegde, G., and Varghese, A. (2020). “MnO<sub>2</sub> Nanoclusters Decorated on Graphene Modified Pencil Graphite Electrode for Non-Enzymatic Determination of Cholesterol.” *Electroanalysis*, 32(10), 2128–2136.
- Rodriguez, J. A., and Goodman, D. W. (1992). “The Nature of the Metal-Metal Bond in Bimetallic Surfaces.” *Science*, 257(5072), 897–903.
- Rogers, K. R. (2006). “Recent advances in biosensor techniques for environmental monitoring.” *Analytica Chimica Acta*, 568(1–2), 222–231.
- Ronkainen, N. J., Halsall, H. B., and Heineman, W. R. (2010). “Electrochemical biosensors.” *Chem. Soc. Rev.*, 39(5), 1747.
- Sahoo, M., and Ramaprabhu, S. (2017). “Solar synthesized tin oxide nanoparticles dispersed on graphene wrapped carbon nanotubes as a Li ion battery anode material with improved stability.” *RSC Adv.*, 7(23), 13789–13797.
- Santoro, K., and Ricciardi, C. (2016). “Biosensors.” *Encyclopedia of Food and Health*, Elsevier, 430–436.
- Sassolas, A., Prieto-Simón, B., and Marty, J.-L. (2012). “Biosensors for Pesticide Detection: New Trends.” *AJAC*, 03(03), 210–232.
- Schneider, J., Matsuoka, M., Takeuchi, M., Zhang, J., Horiuchi, Y., Anpo, M., and Bahnemann, D. W. (2014). “Understanding TiO<sub>2</sub> Photocatalysis: Mechanisms and Materials.” *Chem. Rev.*, 114(19), 9919–9986.
- Scholz, F. (2015). “Voltammetric techniques of analysis: the essentials.” *ChemTexts*, 1(4), 17.
- Sehit, E., and Altintas, Z. (2020). “Significance of nanomaterials in electrochemical glucose sensors: An updated review (2016-2020).” *Biosensors and Bioelectronics*, 159, 112165.
- Serra, P. A. (Ed.). (2011). *Biosensors for Health, Environment and Biosecurity*. InTech.
- Shu, J., and Tang, D. (2017). “Current Advances in Quantum-Dots-Based Photoelectrochemical Immunoassays.” *Chemistry An Asian Journal*, 12(21), 2780–2789.

- Si, P., Ding, S., Yuan, J., Lou, X. W. (David), and Kim, D.-H. (2011). "Hierarchically Structured One-Dimensional TiO<sub>2</sub> for Protein Immobilization, Direct Electrochemistry, and Mediator-Free Glucose Sensing." *ACS Nano*, 5(9), 7617–7626.
- Simões, F. R., and Xavier, M. G. (2017). "Electrochemical Sensors." *Nanoscience and its Applications*, Elsevier, 155–178.
- Singh, B., Laffir, F., McCormac, T., and Dempsey, E. (2010). "PtAu/C based bimetallic nanocomposites for non-enzymatic electrochemical glucose detection." *Sensors and Actuators B: Chemical*, 150(1), 80–92.
- Singh, P., Sreekumar, A., and Badhulika, S. (2023). "Tin oxide-polyaniline nanocomposite modified nickel foam for highly selective and sensitive detection of cholesterol in simulated blood serum samples." *Nanotechnology*, 34(43), 435501.
- Stamenkovic, V. R., Mun, B. S., Arenz, M., Mayrhofer, K. J. J., Lucas, C. A., Wang, G., Ross, P. N., and Markovic, N. M. (2007). "Trends in electrocatalysis on extended and nanoscale Pt-bimetallic alloy surfaces." *Nature Mater*, 6(3), 241–247.
- Su, Y., Guo, H., Wang, Z., Long, Y., Li, W., and Tu, Y. (2018). "Au@Cu<sub>2</sub>O core-shell structure for high sensitive non-enzymatic glucose sensor." *Sensors and Actuators B: Chemical*, 255, 2510–2519.
- Sulimovici, S. I., and Boyd, G. S. (1970). "The Cholesterol Side-Chain Cleavage Enzymes in Steroid Hormone-Producing Tissues." *Vitamins & Hormones*, Elsevier, 199–234.
- T., D., Rao, K. V., Bikshalu, K., Malapati, V., and Sadasivuni, K. K. (2018). "Non-enzymatic sensing of glucose using screen-printed electrode modified with novel synthesized CeO<sub>2</sub>@CuO core shell nanostructure." *Biosensors and Bioelectronics*, 111, 166–173.
- Thévenot, D. R., Toth, K., Durst, R. A., and Wilson, G. S. (2001). "Electrochemical biosensors: recommended definitions and classification | International Union of Pure and Applied Chemistry: Physical Chemistry Division, Commission I.7 (Biophysical Chemistry); Analytical Chemistry Division, Commission V.5 (Electroanalytical Chemistry).1." *Biosensors and Bioelectronics*, 16(1–2), 121–131.
- Thi Phong Thu, D., Thi Xuan, C., Oanh, V. T., Viet, N. X., Tu, L. M., Loan, T. T., Van Tuan, C., Ha, N. H., Thi Thanh Le, D., and Hoa, N. D. (2024). "One-Step Method for the Direct Growth of NiO Nanoflowers on Pencil Graphite Electrode for Highly Sensitive Non-Enzymatic Glucose Sensing." *J. Electrochem. Soc.*, 171(1), 017505.
- Thuy, N. M., Van, D. Q., and Hai, L. T. H. (2012). "The Visible Light Activity of the TiO<sub>2</sub> and TiO<sub>2</sub>:V<sup>4+</sup> Photocatalyst." *Nanomaterials and Nanotechnology*, 2, 14.

- Tian, K., Baskaran, K., and Tiwari, A. (2018). "Nonenzymatic glucose sensing using metal oxides – Comparison of CuO, Co<sub>3</sub>O<sub>4</sub>, and NiO." *Vacuum*, 155, 696–701.
- Umar, A., Ahmad, R., Kumar, R., Ibrahim, A. A., and Baskoutas, S. (2016). "Bi<sub>2</sub>O<sub>2</sub>CO<sub>3</sub> nanoplates: Fabrication and characterization of highly sensitive and selective cholesterol biosensor." *Journal of Alloys and Compounds*, 683, 433–438.
- Umar, A., and Hahn, Y.-B. (2008). "Ultraviolet-Emitting ZnO Nanostructures on Steel Alloy Substrates: Growth and Properties." *Crystal Growth & Design*, 8(8), 2741–2747.
- Vinoth, V., Subramaniam, G., Anandan, S., Valdés, H., and Manidurai, P. (2021). "Non-enzymatic glucose sensor and photocurrent performance of zinc oxide quantum dots supported multi-walled carbon nanotubes." *Materials Science and Engineering: B*, 265, 115036.
- Viswanathan, P., Park, J., Kang, D.-K., and Hong, J.-D. (2019). "Polydopamine-wrapped Cu/Cu(II) nano-heterostructures: An efficient electrocatalyst for non-enzymatic glucose detection." *Colloids and Surfaces A: Physicochemical and Engineering Aspects*, 580, 123689.
- Waleed, H., Rasheed, H. U., Nisar, A., Zafar, A., Liu, Y., Karim, S., Yu, Y., Sun, H., Hussain, S., Faiz, Y., Ali, T., Safdar, A., Ahmad, N., Faiz, F., and Ahmad, M. (2024). "Tuning electrocatalytic activity of Co<sub>3</sub>O<sub>4</sub> nanosheets using CdS nanoparticles for highly sensitive non-enzymatic cholesterol biosensor." *Materials Science in Semiconductor Processing*, 173, 108154.
- Wang, J. (2005). "Carbon-Nanotube Based Electrochemical Biosensors: A Review." *Electroanalysis*, 17(1), 7–14.
- Wang, J. (2008). "Electrochemical glucose biosensors." *Electrochemical Sensors, Biosensors and their Biomedical Applications*, Elsevier, 57–69.
- Wang, X., Lin, F., Zhou, X., Miao, Y., Feng, D., Huang, P., Ren, M., Geng, L., Luo, A., and Deng, Y. (2023). "Molecularly imprinted polymer coating-assisted CsPbBr<sub>3</sub> perovskite quantum dots/TiO<sub>2</sub> inverse opal heterojunctions for the photoelectrochemical detection of cholesterol." *Analyst*, 148(15), 3666–3676.
- Wen, D., Guo, S., Dong, S., and Wang, E. (2010). "Ultrathin Pd nanowire as a highly active electrode material for sensitive and selective detection of ascorbic acid." *Biosensors and Bioelectronics*, 26(3), 1056–1061.
- Wen, J., Guo, H., Ma, X., Wei, Z., He, X., Zhang, L., Li, B., Wang, T., and Cheng, Y. (2020). "Mesoporous Ce-doped ZnO hollow microspheres for oxidation of 1,2-dichlorobenzene." *Catal. Sci. Technol.*, 10(11), 3739–3747.

Wu, G., Wu, Y., Liu, X., Rong, M., Chen, X., and Chen, X. (2012). “An electrochemical ascorbic acid sensor based on palladium nanoparticles supported on graphene oxide.” *Analytica Chimica Acta*, 745, 33–37.

Wu, P., Huang, Y., Kang, L., Wu, M., and Wang, Y. (2015). “Multisource Synergistic Electrocatalytic Oxidation Effect of Strongly Coupled PdM (M = Sn, Pb)/N-doped Graphene Nanocomposite on Small Organic Molecules.” *Sci Rep*, 5(1), 14173.

Xiao, P., Zhang, Y., and Cao, G. (2011). “Effect of surface defects on biosensing properties of TiO<sub>2</sub> nanotube arrays.” *Sensors and Actuators B: Chemical*, 155(1), 159–164.

Xin, T., Diao, F., Li, C., Feng, H., Liu, G., Zou, J., Ding, Y., Liu, B., and Wang, Y. (2018). “Synergistic effect of hierarchical SnO<sub>2</sub> nanorods/Fe<sub>2</sub>O<sub>3</sub> hexahedrons with enhanced performance as lithium ion battery anodes.” *Materials Research Bulletin*, 99, 196–203.

Xu, M., Song, Y., Ye, Y., Gong, C., Shen, Y., Wang, L., and Wang, L. (2017). “A novel flexible electrochemical glucose sensor based on gold nanoparticles/polyaniline arrays/carbon cloth electrode.” *Sensors and Actuators B: Chemical*, 252, 1187–1193.

Xue, D., Wang, P., Zhang, Z., and Wang, Y. (2019). “Enhanced methane sensing property of flower-like SnO<sub>2</sub> doped by Pt nanoparticles: A combined experimental and first-principle study.” *Sensors and Actuators B: Chemical*, 296, 126710.

Yadav, H. M., Park, J.-D., Kang, H.-C., and Lee, J.-J. (2021). “Recent Development in Nanomaterial-Based Electrochemical Sensors for Cholesterol Detection.” *Chemosensors*, 9(5), 98.

Yang, L., Zhang, S., Liu, X., Tang, Y., Zhou, Y., and Wong, D. K. Y. (2020). “Detection signal amplification strategies at nanomaterial-based photoelectrochemical biosensors.” *J. Mater. Chem. B*, 8(35), 7880–7893.

Yang, X., Fu, H., Tian, Y., Xie, Q., Xiong, S., Han, D., Zhang, H., and An, X. (2019). “Au decorated In<sub>2</sub>O<sub>3</sub> hollow nanospheres: A novel sensing material toward amine.” *Sensors and Actuators B: Chemical*, 296, 126696.

Ye, J.-S., Chen, C.-W., and Lee, C.-L. (2015). “Pd nanocube as non-enzymatic glucose sensor.” *Sensors and Actuators B: Chemical*, 208, 569–574.

Yousefi, M., Amiri, M., Azimirad, R., and Moshfegh, A. Z. (2011). “Enhanced photoelectrochemical activity of Ce doped ZnO nanocomposite thin films under visible light.” *Journal of Electroanalytical Chemistry*, 661(1), 106–112.

Yu, J.-H., Nam, S.-H., Lee, J. W., Kim, D. I., and Boo, J.-H. (2016). “Synthesis and characterization of vanadium doped TiO<sub>2</sub> for the visible light-driven photocatalytic

activity.” *2016 International Renewable and Sustainable Energy Conference (IRSEC)*, Marrakech: IEEE, 785–788.

Yu, L., Shen, Y., Chen, L., Zhang, Q., Hu, X., and Xu, Q. (2023). “Molecularly imprinted ultrasensitive cholesterol photoelectrochemical sensor based on perfluorinated organics functionalization and hollow carbon spheres anchored organic-inorganic perovskite.” *Biosensors and Bioelectronics*, 237, 115496.

Zhang, D., Zhang, C., Liu, J., Chen, Q., Zhu, X., and Liang, C. (2019). “Carbon-Encapsulated Metal/Metal Carbide/Metal Oxide Core–Shell Nanostructures Generated by Laser Ablation of Metals in Organic Solvents.” *ACS Appl. Nano Mater.*, 2(1), 28–39.

Zhang, W., Yuan, R., Chai, Y.-Q., Zhang, Y., and Chen, S.-H. (2012). “A simple strategy based on lanthanum–multiwalled carbon nanotube nanocomposites for simultaneous determination of ascorbic acid, dopamine, uric acid and nitrite.” *Sensors and Actuators B: Chemical*, 166–167, 601–607.

Zhang, Y., Li, N., Xiang, Y., Wang, D., Zhang, P., Wang, Y., Lu, S., Xu, R., and Zhao, J. (2020). “A flexible non-enzymatic glucose sensor based on copper nanoparticles anchored on laser-induced graphene.” *Carbon*, 156, 506–513.

Zhang, Z., Xu, M., Liu, L., Ruan, X., Yan, J., Zhao, W., Yun, J., Wang, Y., Qin, S., and Zhang, T. (2018). “Novel SnO<sub>2</sub>@ZnO hierarchical nanostructures for highly sensitive and selective NO<sub>2</sub> gas sensing.” *Sensors and Actuators B: Chemical*, 257, 714–727.

Zhao, W.-W., Xu, J.-J., and Chen, H.-Y. (2015). “Photoelectrochemical bioanalysis: the state of the art.” *Chem. Soc. Rev.*, 44(3), 729–741.

Zheng, B., Liu, G., Yao, A., Xiao, Y., Du, J., Guo, Y., Xiao, D., Hu, Q., and Choi, M. M. F. (2014). “A sensitive AgNPs/CuO nanofibers non-enzymatic glucose sensor based on electrospinning technology.” *Sensors and Actuators B: Chemical*, 195, 431–438.

Zhou, Z., Zhu, Z., Cui, F., Shao, J., and Zhou, H. S. (2020). “CuO/Cu composite nanospheres on a TiO<sub>2</sub> nanotube array for amperometric sensing of glucose.” *Microchim Acta*, 187(2), 123.

Zhu, J., Zhu, Z., Lai, Z., Wang, R., Guo, X., Wu, X., Zhang, G., Zhang, Z., Wang, Y., and Chen, Z. (2002). “Planar Amperometric Glucose Sensor Based on Glucose Oxidase Immobilized by Chitosan Film on Prussian Blue Layer.” *Sensors*, 2(4), 127–136.

Zhuang, Z., Su, X., Yuan, H., Sun, Q., Xiao, D., and Choi, M. M. F. (2008). “An improved sensitivity non-enzymatic glucose sensor based on a CuO nanowire modified Cu electrode.” *Analyst*, 133(1), 126–132.

## LIST OF PAPER PUBLISHED AND COMMUNICATED

1. **Rao, L.**, Rodney, J. D., Shivakumar, Dalimba, U. K., Udayashankar, N. K., Kim, B. C., and Bhat, B. R. (2024). “Elucidating mechanisms and DFT analysis of monometallic Vanadium incorporated nanoporous TiO<sub>2</sub> as advanced material for enzyme-free electrochemical blood glucose biosensors with exceptional performance tailored for point-of-care applications.” *Microchemical Journal*, 204, 111172.
2. **Rao, L.**, and Bhat, B. R. (2024). “Enhancing glucose detection: Vanadium-doped TiO<sub>2</sub> (V<sub>0.07</sub>Ti<sub>0.93</sub>O<sub>2</sub>) as non-enzymatic biosensor.” *J Mater Sci: Mater Electron*, 35(16), 1102.
3. **Rao, L.**, Rodney, J. D., Joy, A., Shivangi Nileshbhai, C., James, A., S, S., Joyline Mascarenhas, F., Udayashankar, N. K., Anjukandi, P., Chul Kim, B., and Ramachandra Bhat, B. (2024). “Cerium-Modulated Zinc Oxide for enhanced Photoelectrochemical Non-Enzymatic biosensing of Cholesterol: An experimental and First Principle Analysis.” *Chemical Engineering Journal*, 500, 156639.
4. **Rao, L.**, Rodney, J.D., S, S., Mascarenhas, J.F., Nayak, M.P., Kim, B.C., Bhat, B.R., Synthesis and Characterization of Pd/C-Decorated SnO<sub>2</sub> for Advanced Non-Enzymatic Cholesterol Biosensing: Analytical Application in Clinical Blood Specimens. (Under review – *Microchemical Journal*)

## PAPER PRESENTED IN THE CONFERENCE AND WORKSHOP ATTENDED:

1. Lavanya Rao and B Ramachandra Bhat (2023). “Enhancing Glucose Detection: Non-Enzymatic Biosensing Utilizing Vanadium-Doped TiO<sub>2</sub> (V<sub>0.07</sub>Ti<sub>0.93</sub>O<sub>2</sub>)” International Conference on Condensed Matter and Device Physics (ICCMDP 2023). 27-29 September 2023, Department of Physics, School of Energy Technology (SoET), Pandit Deendayal Energy University (PDEU), Gandhinagar, Gujarat, India.

2. Participated in the webinar on “Voltammetric Techniques For (BIO) SENSING AND ENERGY STORAGE APPLICATIONS” conducted on 24<sup>th</sup> June 2023 by the Physics department, Velammal Institute of Technology, Chennai, INDIA.
3. Participated in the Three-week Online Workshop on Electrochemical Data Analysis during 05-23 June 2023 jointly organized by the Department of Physics, Guru Nanak Dev University Amritsar, India and SIAS Research Forum.
4. Participated in the One Day National Webinar on “Frontiers in Chemistry”, 28<sup>th</sup> September 2020 by the Department of Chemistry, NITK, Surathkal, Mangalore, INDIA.
5. Five-day National E-Workshop on “Advanced materials for Energy Storage and Conversion devices” 28-29 February 2020, CSIR -Advanced Materials And Process Research Institute (AMPRI), Bhopal, India.

#### OTHER PUBLICATIONS:

1. James, A., Rodney, J. D., Manojbabu, A., Joshi, S., **Rao, L.**, Bhat, B. R., and Udayashankar, N. K. (2024). “Cobalt-doped LaFeO<sub>3</sub> for photo-Fenton degradation of organic pollutants and visible-light-assisted water splitting.” *J Mater Sci: Mater Electron*, 35(2), 190.
2. James, A., Rodney, J. D., **Rao, L.**, Bhat, B. R., and Udayashankar, N. K. (2023). “Bi-functional LaM<sub>x</sub>Fe<sub>1-x</sub>O<sub>3</sub> (M = Cu, Co, Ni) for photo-fenton degradation of methylene blue and photoelectrochemical water splitting.” *International Journal of Hydrogen Energy*, 48(46), 17536–17552.
3. Jauhar, Ro. Mu., Ramachandran, K., Deepapriya, S., Joshi, S., Ghfar, A. A., **Rao, L.**, Bhat, B. R., Udayashankar, N. K., Siva, V., Govindan, R., Kim, B. C., and Rodney, J. D. (2024b). “Growth of octahedral structured AgBiS<sub>2</sub> single crystals and its insights on the high performance electrocatalytic hydrogen generation. *International Journal of Hydrogen Energy*, 77, 291–300.
4. Jauhar, R. M., Ramachandran, K., Rodney, J. D., Deepapriya, S., Joshi, S., **Rao, L.**, Bhat, B. R., N K, U., Siva, V., Kim, B. C., Senthil Pandian, M., and Raji, G.

(2024a). “Bridgman - Stockbarger Derived Edge Sites Enriched Silver Bismuth Sulphide Single Crystals and its Insights on the High-Performance Electrocatalytic Hydrogen Generation.” (Revised - International Journal of Hydrogen Energy)

5. Mascarenhas, F. J., Rodney, J. D., **Rao, L.**, Kim, B. C., Kim, B. C., and Bhat, B. R. (2024). “Iron Decorated Cobalt Manganese Sulphide Nanoflowers as a Battery Type Electrode Material for High Performance Supercapacitor.” (Under review - Journal of Energy Storage)
6. Mascarenhas, F. J., Rodney, J. D., **Rao, L.**, Kim, B. C., and Bhat, B. R. (2024). “Electrodeposited CoMnS/NiCo<sub>2</sub>S<sub>4</sub> nanocomposite for high performance supercapacitors.” *Electrochimica Acta*, 507, 145133.
7. Rodney, J. D., Joshi, S., Ray, S., **Rao, L.**, Deepapriya, S., Carva, K., Bhat, B. R., Udayashankar, N. K., Perumal, S., Katlakunta, S., Raj, C. J., and Kim, B. C. (2024). “Electrocatalytic synergies of melt-quenched Ni-Sn-Se-Te nanoalloy for direct seawater electrolysis.” *Chemical Engineering Journal*, 499, 155775.

#### **PATENT GRANTED:**

1. Rodney, J. D., Joshi, S., **Rao, L.**, Deepapriya, S., Bhat, B.R., Udayashankar, N.K., Raj, J., “METAL CHALCOGENIDE-BASED NANOALLOY COMPOSITIONS FOR SEAWATER SPLITTING AND METHOD THEREOF” (Patent Number: 520232, Date of grant: 05/03/2024)

\*\*\*\*\*

---

---

**CERTIFICATE FROM THE INSTITUTE HUMAN ETHICS COMMITTEE,  
NITK SURATHKAL**

---

---



NATIONAL INSTITUTE OF TECHNOLOGY KARNATAKA SURATHKAL  
P. O. SRINIVASNAGAR MANGALORE 575 025  
KARNATAKA, INDIA

Office of Dean (Research and Consultancy)

Ph: +91-824-2474067

Email: dean.rc@nitk.edu.in

---

NITK/Bioethics/2023/02

24.04.2023

**Certificate**

This is to certify that Professor B R Bhat of the Department of Chemistry had submitted a proposal on **"SYNTHESIS OF NANOPARTICLES AND ITS APPLICATION IN BIOSENSORS"** to the institute human ethics committee of the NITK Surathkal.

The ethics committee has studied this proposal and after the due discussions,

**The committee has permitted Professor B R Bhat to undertake this work at the NITK Surathkal.**

**Prof. Satybodh M. Kulkarni**

संचालक/प्रमुख (आर एंड सी) / Dean (R&C)  
राष्ट्रीय प्रौद्योगिकी संस्थान कर्नाटक, सुरथकल  
National Institute of Technology Karnataka, Surathkal  
पी.ओ. श्रीनिवासनगर, मंगलूर-575025, कर्नाटक, भारत  
P.O.Srinivasnagar, Mangalore-575025, Karnataka, India

---

---

## CURRICULUM VITAE

---

---

### **Lavanya Rao V R**

Research Scholar

Catalysis and Materials Chemistry Laboratory

Department of Chemistry

National Institute of Technology Karnataka

Srinivas Nagar, Surathkal

Mangalore – 575025, Karnataka, India.

Email- raolavanyahv11@gmail.com

Phone: 8310658439



---

---

### **SUMMARY**

---

---

I am a dedicated researcher with expertise in electrochemical biosensors, water splitting, and energy storage. My work focuses on developing advanced nanomaterials to enhance biosensor sensitivity, improve hydrogen production efficiency, and create high-performance electrode materials for energy storage. I have an extensive publication and have filed patent, consistently advancing technology in these critical areas.

---

---

### **PERSONAL DETAILS**

---

---

**Date of Birth** : 11/01/1996  
**Gender** : Female  
**Languages** : English, Kannada, Hindi and Tulu  
**Nationality** : Indian  
**Profile ID** : 0009-0002-1871-0070 (**ORCID**)  
58147831500 (**Scopus**)  
oSypcNkAAAAJ (**Google Scholar**)

---

---

## EDUCATIONAL QUALIFICATIONS

---

---

**Doctor of Philosophy (2019-2024)** in Chemistry from National Institute of Technology Karnataka, Suarathkal. (Thesis: Synthesis of Nanomaterials and their Applications in Biosensor- Submitted)

**Master of Science (2016-2018)** in Organic Chemistry from Mangalore University Konaje, Mangalore. (Thesis: Synthesis and characterisation of  $\alpha$ -hydroxy phosphate).  
**CGPA: 7.02**

**Bachelor of Science (2013 – 2016)** from Vivekananda College of Art and Science, Puttur. (Subjects: Physics, Mathematics, and Chemistry). **Percentage: 92.67 %**

---

---

## RESEARCH EXPERIENCE

---

---

As an Intern worked on the project “Synthesis and Characterization of  $\alpha$ -Hydroxyphosphate” at TATA Company, Advinus Therapeutics Limited, located in the Peenya Industrial Area, Bengaluru, Karnataka, India (560058).

---

---

## RESEARCH INTEREST

---

---

Electrochemical Biosensor, Water Splitting, Photoelectrochemical Water Splitting, Synthesis Techniques, Nanomaterials, Material Characterization, Electrochemical Techniques, Supercapacitor.

---

---

## RESEARCH SKILLS

---

---

**Material Synthesis:** Nanomaterials, Transition based Nanomaterials, Doped Nanomaterials, Nanocomposite, Chalcogenides, Green Synthesis.

**Material Characterization Techniques:** X-Ray Diffraction (XRD), Raman spectroscopy, UV-Visible spectroscopy, Photoluminescence (PL), Field Emission Scanning Electron Microscopy (FE-SEM), High-Resolution Transmission Electron

Microscopy (HR-TEM), Energy Dispersive X-Ray Spectroscopy (EDX), X-ray Photoelectron Spectroscopy (XPS).

**Electrochemical Techniques:** Cyclic Voltammetry (CV), Chronoamperometry (CA), Chronopotentiometry (CP), Electrochemical Impedance Spectroscopy (EIS), Differential Pulse Voltammetry (DPV) Galvanostatic Charge Discharge (GCD).

**Modern Computational Tools:** Microsoft Office tools (Word, Excel and Powerpoint), Xpert Highscore Software, ImageJ, Graphic Design Software (Adobe Illustrator, Blender), OriginPro, ZsimWin.

---

---

## RESEARCH PUBLICATIONS

---

---

1. **Rao, L.,** Rodney, J. D., Shivakumar, Dalimba, U. K., Udayashankar, N. K., Kim, B. C., and Bhat, B. R. (2024). “Elucidating mechanisms and DFT analysis of monometallic Vanadium incorporated nanoporous TiO<sub>2</sub> as advanced material for enzyme-free electrochemical blood glucose biosensors with exceptional performance tailored for point-of-care applications.” *Microchemical Journal*, 204, 111172.
2. **Rao, L.,** and Bhat, B. R. (2024). “Enhancing glucose detection: Vanadium-doped TiO<sub>2</sub> (V<sub>0.07</sub>Ti<sub>0.93</sub>O<sub>2</sub>) as non-enzymatic biosensor.” *J Mater Sci: Mater Electron*, 35(16), 1102.
3. **Rao, L.,** Rodney, J. D., Joy, A., Shivangi Nileshbhai, C., James, A., S, S., Joyline Mascarenhas, F., Udayashankar, N. K., Anjukandi, P., Chul Kim, B., and Ramachandra Bhat, B. (2024). “Cerium-Modulated Zinc Oxide for enhanced Photoelectrochemical Non-Enzymatic biosensing of Cholesterol: An experimental and First Principle Analysis.” *Chemical Engineering Journal*, 500, 156639.
4. **Rao, L.,** Rodney, J.D., S, S., Mascarenhas, J.F., Nayak, M.P., Kim, B.C., Bhat, B.R., Synthesis and Characterization of Pd/C-Decorated SnO<sub>2</sub> for Advanced Non-Enzymatic Cholesterol Biosensing: Analytical Application in Clinical Blood Specimens. (Under review – *Microchemical Journal*)

5. James, A., Rodney, J. D., Manojbabu, A., Joshi, S., **Rao, L.**, Bhat, B. R., and Udayashankar, N. K. (2024). "Cobalt-doped LaFeO<sub>3</sub> for photo-Fenton degradation of organic pollutants and visible-light-assisted water splitting." *J Mater Sci: Mater Electron*, 35(2), 190.
6. James, A., Rodney, J. D., **Rao, L.**, Bhat, B. R., and Udayashankar, N. K. (2023). "Bi-functional LaM<sub>x</sub>Fe<sub>1-x</sub>O<sub>3</sub> (M = Cu, Co, Ni) for photo-fenton degradation of methylene blue and photoelectrochemical water splitting." *International Journal of Hydrogen Energy*, 48(46), 17536–17552.
7. Jauhar, Ro. Mu., Ramachandran, K., Deepapriya, S., Joshi, S., Ghfar, A. A., **Rao, L.**, Bhat, B. R., Udayashankar, N. K., Siva, V., Govindan, R., Kim, B. C., and Rodney, J. D. (2024b). "Growth of octahedral structured AgBiS<sub>2</sub> single crystals and its insights on the high performance electrocatalytic hydrogen generation. *International Journal of Hydrogen Energy*, 77, 291–300.
8. Jauhar, R. M., Ramachandran, K., Rodney, J. D., Deepapriya, S., Joshi, S., **Rao, L.**, Bhat, B. R., N K, U., Siva, V., Kim, B. C., Senthil Pandian, M., and Raji, G. (2024a). "Bridgman - Stockbarger Derived Edge Sites Enriched Silver Bismuth Sulphide Single Crystals and its Insights on the High-Performance Electrocatalytic Hydrogen Generation." (Revised - International Journal of Hydrogen Energy)
9. Mascarenhas, F. J., Rodney, J. D., **Rao, L.**, Kim, B. C., Kim, B. C., and Bhat, B. R. (2024). "Iron Decorated Cobalt Manganese Sulphide Nanoflowers as a Battery Type Electrode Material for High Performance Supercapacitor." (Under review - Journal of Energy Storage)
10. Mascarenhas, F. J., Rodney, J. D., **Rao, L.**, Kim, B. C., and Bhat, B. R. (2024). "Electrodeposited CoMnS/NiCo<sub>2</sub>S<sub>4</sub> nanocomposite for high performance supercapacitors." *Electrochimica Acta*, 507, 145133.
11. Rodney, J. D., Joshi, S., Ray, S., **Rao, L.**, Deepapriya, S., Carva, K., Bhat, B. R., Udayashankar, N. K., Perumal, S., Katlakunta, S., Raj, C. J., and Kim, B. C. (2024). "Electrocatalytic synergies of melt-quenched Ni-Sn-Se-Te nanoalloy for direct seawater electrolysis." *Chemical Engineering Journal*, 499, 155775.

---

---

## **PATENT GRANTED**

---

---

1. Rodney, J. D., Joshi, S., **Rao, L.**, Deepapriya, S., Bhat, B.R., Udayshankar, N.K., Raj, J., “METAL CHALCOGENIDE-BASED NANOALLOY COMPOSITIONS FOR SEAWATER SPLITTING AND METHOD THEREOF” (Patent Number: 520232, Date of grant: 05/03/2024).

---

---

## **PAPER PRESENTED IN THE CONFERENCE AND WORKSHOP ATTENDED:**

---

---

1. Lavanya Rao and B Ramachandra Bhat (2023). “Enhancing Glucose Detection: Non-Enzymatic Biosensing Utilizing Vanadium-Doped  $\text{TiO}_2$  ( $\text{V}_{0.07}\text{Ti}_{0.93}\text{O}_2$ )” International Conference on Condensed Matter and Device Physics (ICCMDP 2023). 27-29 September 2023, Department of Physics, School of Energy Technology (SoET), Pandit Deendayal Energy University (PDEU), Gandhinagar, Gujarat, India.
2. Participated in the webinar on “Voltammetric Techniques For (BIO) SENSING AND ENERGY STORAGE APPLICATIONS” conducted on 24<sup>th</sup> June 2023 by the Physics department, Velammal Institute of Technology, Chennai, INDIA.
3. Participated in the Three-week Online Workshop on Electrochemical Data Analysis during 05-23 June 2023 jointly organized by the Department of Physics, Guru Nanak Dev University Amritsar, India and SIAS Research Forum.
4. Participated in the One Day National Webinar on “Frontiers in Chemistry”, 28<sup>th</sup> September 2020 by the Department of Chemistry, NITK, Surathkal, Mangalore, INDIA.
5. Five-day National E-Workshop on “Advanced Materials for Energy Storage and Conversion devices” 28-29 February 2020, CSIR -Advanced Materials And Process Research Institute (AMPRI), Bhopal, India.

---

---

## SCHOLARSHIPS AND ACHIEVEMENTS

---

---

1. INSPIRE Central Government Scholarship (SHE SCHOLARSHIP) 2013-2018
2. Sir C.V. Raman Scholarship 2013-2016
3. Karnataka Science and Technology Scholarship 2013-2016

2<sup>nd</sup> Rank holder in the subject of Chemistry in Bachelor of Science under Mangalore University during the academic year 2013-2016.

---

---

## DECLARATION

---

---

I hereby declare that all the information given above is true to the best of my knowledge.

\*\*\*\*\*